学位論文

Electronic states of narrow-gap semiconductors under multi-extreme conditions

（多重極限環境下における ナローギャップ半導体の電子状態）

平成 29 年 12 月博士（理学）申請

東京大学大学院理学系研究科
物理学専攻

秋葉　和人

Abstract

Materials can be classified into metals or insulators from the viewpoint of the electric conduction. Exploration of exotic electronic phases beyond the conventional framework of the band theory has been a challenging subject in condensed matter physics.

More than 50 years ago, emergence of the excitonic insulator phase, a quantum condensed state of electron–hole pairs, was theoretically proposed as a new ground state at the boundary between metal and insulator. Although numbers of experimental attempts have been devoted to search the realization of the excitonic insulator phase, the concrete evidence have never been reported up to the present.

The boundary region between metal and insulator comes to attract renewed interests in viewpoints of topology in condensed matter physics. The topological materials are characterized by their non-trivial band topology and high mobility carriers obeying the relativistic Dirac equation. Since Dirac equation originally describes the motion of particles with high velocity close to the light speed, transport properties of topological materials attract general interest beyond the field of condensed matter physics. Actually, numbers of unconventional behaviors have been reported experimentally, yet the essence stemming from the non-trivial topology of the band structure remains unclear since the interpretation of experimental results is often hindered by their complex electronic structures.

Common to these topics, model materials having simple and controllable band structure are needed. As candidates for such materials, two narrow-gap semiconductors, black phosphorus (BP) and lead telluride (PbTe), were investigated in this thesis.

We utilized static magnetic fields up to 14 T and pulsed magnetic fields up to 55 T. The electrical transport measurements under pressure were performed in static fields with piston-cylinder-type pressure cell. Resistivity, magnetization, and ultrasonic measurement techniques under pulsed high magnetic fields were utilized in this study.

BP is known as a high mobility semiconductor with narrow direct band gap. The band gap is suppressed by applying hydrostatic pressure, and is expected to collapse at a certain pressure. This suggests that the band structure can be tuned continuously from semiconductor to semimetal, which is an ideal playground to explore the exotic states in the vicinity of the semiconductor-semimetal (SC-SM) transiton. Since only carriers near the narrowest band gap govern the physical properties, BP under pressure is regarded as a quite simple playground. Although several previous studies demonstrated the metallization under pressure, the details of the electronic states around the SC-SM transition was unclear. Thus, we intend to clarify the electronic structure in the vicinity of the SC-SM transition.

We investigated the electrical transport properties in pressurized BP under high magnetic fields. In semiconducting states below 1 GPa, we observed the magneto-phonon resonance (MPR), which is a quantum transport phenomenon showing up in high mobility semiconductors. Through the analysis of the MPR, we identified a reduction of the cyclotron mass with applying pressure, which is understood as a result of the band gap reduction. At higher pressures, we observed clear Shubnikov-de Haas (SdH) oscillations, which directly demonstrate the pressure-induced SC-SM transiton. We revealed the light cyclotron masses and small carrier densities in the semimetallic state, which are comparable with conventional elemental semimetals, bismuth and graphite. Further, the Fermi

surface of semimetallic BP becomes monotonically larger as pressure increases, which indicates the tunability of carrier density by hydrostatic pressure. The origin of large and non-saturating magnetoresistance in semimetallic BP was discussed by the semiclassical two-carrier model. We found that the magnetoresistance cannot be fully reproduced by the Drude model. Therefore, additional mechanisms such as change in carrier relaxation time in magnetic fields have to be considered. In addition, the nearly compensated nature and large difference of the mobilities between electrons and holes were clarified from the two-carrier analyses. To explore the exotic electronic states near the SC-SM transition, we measured the temperature dependence of the resistivity down to 43 mK in magnetic fields. Although apparent semimetal-to-insulator-like change was observed in the temperature dependence of the longitudinal and transverse magnetoresistance, these phenomena were reasonably reproduced as trivial effects within the conventional theory for metals in high magnetic fields.

PbTe is known as a degenerate direct-gap semiconductor, which has moderate carrier density of $\sim 10^{18}$ cm^{-3} at low temperature. Substitution of Sn for Pb and application of hydrostatic pressure reduce the band gap, and cause the topological phase transition to the topological crystalline insulator (TCI). Recent theoretical study suggested that the ratio of Zeeman energy to cyclotron energy (ZC ratio) can be used as a quantitative index to determine the degree of similarity to the Dirac electron system, namely, "Diracness" of materials. ZC ratio is known to be unity in a system with ideal two-band Dirac Hamiltonian. Theoretical calculation expected that the ZC ratio increases by substitution of Sn, and becomes unity at the zero-gap state, namely, the topological phase transition point. This suggests the ralization of ideal Dirac electron system in this material. PbTe is suitable to testify above new criterion to identify the "Diracness" for its simple band structure and strong spin-orbit effect. Besides, we can seek the unconventional behavior by tuning the band topology from a trivial semiconductor to TCI *via* the zero-gap state by manipulating external parameters. Based on motivations mentioned above, we investigated various physical properties of PbTe and $Pb_{1-x}Sn_xTe$ in magnetic fields.

We studied the electrical transport, magnetization, and elastic properties in PbTe, and observed clear SdH, de Haas-van Alphen (dHvA), and acoustic dHvA oscillations. We explained that the large second harmonic observed in the quantum oscillations is due to the prominent spin-splitting in PbTe. We analyzed the spin-splitted quantum oscillation based on the conventional Lifshitz-Kosevich formula, and found the oscillation pattern was reproduced by the ZC ratio. The simple band structure of PbTe and high-field measurements up to 55 T enabled us to unambiguously determine the ZC ratio of 0.52. From these results, we clarified that PbTe is in the spin-polarized quantum limit state above $\sim$35 T. We also observed large and non-saturating magnetoresistance effect in both transverse and longitudinal configurations, which origin was remained as an open question. In transport measurements under pressure, we observed slight upturn of the ZC ratio in one sample, which indicates that the Diracness of PbTe is enhanced by pressure.

Acknowledgments

First of all, I would like to express my sincerest gratitude to my supervisor, Prof. M. Tokunaga for his considerable support and a lot of insightful discussion during my master's and doctor's courses. His passionate, sincere attitude toward science have always stimulated my motivation to study.

To accomplish this work, I have received full cooperation from following people: Dr. A. Miyake for overall experimental support; Prof. Y. Akahama for providing black phosphorus samples; Prof. K. Matsubayashi and Prof. Y. Uwatoko for supporting high-pressure experiments; Mr. H. Arai and Prof. Y. Fuseya for supporting theoretical aspects; Prof. H. Sakai, Mr. K. Katayama, Mr. T. Sakamoto, Prof. N. Hanasaki, and Prof. S. Takaoka for preparing PbTe and $Pb_{1-x}Sn_xTe$ samples; Prof. Y. Nakanishi and Prof. M. Yoshizawa for supporting ultrasonic measurements under pulsed high magnetic fields; and Dr. A. Matsuo, Mr. K. Kawaguchi, and Prof. K. Kindo for providing opportunities to utilize high magnetic field environment. I am grateful to their indispensable supports and discussion.

I also appreciate all members of International MegaGauss Science Laboratory, The Institute for Solid State Physics, The University of Tokyo (Kindo, Tokunaga, Kohama, Takeyama, Matsuda, and Osada groups) for variable discussion and fun time in daily life.

I would like to appreciate JSPS Research Fellowship for Young Scientists for financial support over two years in my doctoral course.

Finally, I express my gratitude for my family and friends for their support and encouragement.

Kazuto Akiba

秋葉和人

Contents

Abstract **i**

Acknowledgments **iii**

List of figures **vii**

List of tables **viii**

1 General Introduction **1**
1.1 Exotic States Near the Metal-Insulator Transition 1
1.2 Topological Materials 6
1.3 General Issues and Solutions 9

2 Experimental Methods **10**
2.1 Essentials of the Electrical Transport Measurements 10
2.2 Resistivity Measurements under Pressure 13
2.3 Generation of Pulsed Magnetic Fields 16
2.4 Cryostat System in High-Field Measurements 20
2.5 Resistivity Measurements in Pulsed Magnetic Fields 22
2.6 Magnetization Measurements in Pulsed Magnetic Fields 24
2.7 Ultrasonic Measurements in Pulsed Magnetic Fields 26
2.8 Samples 32
2.8.1 Black Phosphorus 32
2.8.2 PbTe and $Pb_{1-x}Sn_xTe$ 32

3 Black Phosphorus **34**
3.1 Basic Properties of Black Phosphorus 34
3.1.1 Crystal Structure 34
3.1.2 Energy Band Structure 35
3.1.3 Physical Properties at Ambient Pressure 36
3.1.4 Physical Properties under Pressure 40
3.2 Purpose of the Study 43
3.3 Results and Discussion 44
3.3.1 Temperature Dependence of the Resistivity at Various Pressures . 44
3.3.2 Quantum Transport Phenomena in Semiconducting Black Phosphorus —Magneto-Phonon Resonance— 46
3.3.3 Quantum Transport Phenomena in Semimetallic Black Phosphorus —Shubnikov-de Haas Oscillation— 50

3.3.4 Analyses of the In-Plane Transport Properties Based on the Two-Carrier Model . . . 58
3.3.5 Exploration of Unconventional Electronic Phases on the Boundary between Semiconducting and Semimetallic States . . . 63
3.4 Summary . . . 66

4 Lead Telluride **67**
4.1 Basic Properties of PbTe . . . 67
4.1.1 Crystal and Energy Band Structure . . . 67
4.1.2 Physical Properties of PbTe . . . 67
4.1.3 Physical Properties of $Pb_{1-x}Sn_xTe$ . . . 72
4.1.4 Topological Properties of $Pb_{1-x}Sn_xTe$ . . . 73
4.1.5 Ferroelectric Transition in $Pb_{1-x}Sn_xTe$ . . . 77
4.1.6 Physical Properties of Pressurized PbTe . . . 78
4.2 Purpose of the Study . . . 79
4.3 Results and Discussion . . . 80
4.3.1 Pristine PbTe at Ambient Pressure . . . 80
4.3.2 $Pb_{0.7}Sn_{0.3}Te$ . . . 99
4.4 Summary . . . 104

5 Concluding Remarks **105**
5.1 Summary of This Thesis . . . 105
5.2 Future Prospects . . . 107

Publications **108**

A Computer Programs Composed for This Study **109**
A.1 Numerical Lock-In . . . 109
A.2 Data Acquisition with Tektronix DPO5104B . . . 115
A.3 Numerical Analysis of Ultrasonic Measurements . . . 125

List of Figures

1.1 Quantum limit state in high magnetic fields. 2
1.2 Excitonic insulator phase in solids. 4
1.3 Topological materials. 7

2.1 Basis of the electrical transport measurements. 10
2.2 Resistivity measurements under high pressure. 15
2.3 Structure of pulse magnets. 17
2.4 Generation of pulsed magnetic fields. 18
2.5 Cryostat system in high-field measurements. 20
2.6 Resistivity measurements under pulsed magnetic fields. 22
2.7 Magnetization measurements in pulsed magnetic fields. 24
2.8 Pulse-echo method. 27
2.9 Digital technique for ultrasonic measurements in pulsed magnetic fields. . 28
2.10 Calculation flow diagram of the ultrasonic measurements. 30
2.11 Samples investigated in this study. 33

3.1 Crystal structure of black phosphorus. 35
3.2 Energy band structure of black phosphorus. 37
3.3 Transport properties of black phosphorus at ambient pressure. 38
3.4 High pressure phases of black phosphorus. 41
3.5 Transport properties of black phosphorus under pressure. 42
3.6 Pressure dependence of the optical phonon frequencies in black phosphorus. 42
3.7 Temperature dependence of the resistivity under pressure. 44
3.8 Estimation of band gap from the temperature dependence of the resistivity. 45
3.9 Magneto-phonon resonance at ambient pressure. 47
3.10 Magneto-phonon resonance under pressure. 48
3.11 SdH oscillations at 1.64 GPa under $B \parallel a$. 49
3.12 SdH oscillations at various pressures and their FFT spectra. 51
3.13 Pressure dependence of the FFT frequencies and cyclotron masses. 52
3.14 Longitudinal magnetoresistance ρ_{zz} and Landau-level fan diagram. 53
3.15 SdH oscillations and their FFT spectra under B along the b- and c-axis. . 55
3.16 Summary of the pressure dependence of the oscillation frequencies along three field directions. 56
3.17 First-principle calculation of the band structure and Fermi surface. 57
3.18 Two-carrier analyses at the semiconducting state. 59
3.19 Two-carrier analyses near and above the SC-SM transition. 61
3.20 Temperature dependence of resistivity under magnetic fields. 63
3.21 Resistivity measurements using dilution refrigerator. 65

4.1 Crystal and energy band structures of PbTe. 68

4.2 SdH oscillations in PbTe. 69
4.3 Spin-splitting in PbTe. 70
4.4 Composition dependence of the lattice constant and band structure in $Pb_{1-x}Sn_xTe$. 72
4.5 Topological surface states in $Pb_{0.6}Sn_{0.4}Te$. 73
4.6 Composition dependence of the inverse masses, g-factors and ZC ratios in $Pb_{1-x}Sn_xTe$. 74
4.7 Ferroelectric transition in $Pb_{1-x}Sn_xTe$. 76
4.8 Pressure induced topological phase transition in PbTe. 77
4.9 Transport properties of #T sample. 80
4.10 Angular dependence of the SdH oscillations. 82
4.11 Magnetization of #T sample. 84
4.12 Origin of the large second harmonic observed in #T sample. 85
4.13 Simulation of the SdH oscillations based on the LK formula. 87
4.14 Angular dependence of the ZC ratio. 88
4.15 Landau-level structures at several ZC ratios. 89
4.16 Resistivity, magnetization, and elastic properties in pulsed high magnetic fields. 91
4.17 SdH oscillations of PbTe under pressure. 92
4.18 Analysis of the SdH oscillations under pressure. 94
4.19 Transport properties of #S sample. 96
4.20 Transport properties of #S sample under pulsed magnetic fields. 97
4.21 Selection rule of carrier scattering in longitudinal magnetoresistance. . . . 98
4.22 Transport properties of #T30 sample. 100
4.23 Landau-level fan diagram of #T30 sample. 101
4.24 Ultrasonic measurements of #T30 sample under pulsed magnetic fields. . 102
4.25 Fan diagrams constructed from various quantum oscillation phenomena. . 102

List of Tables

1.1 Carrier densities and cyclotron masses of several semimetals and narrow-gap semiconductors. 3
1.2 Comparison of the characteristic parameters between the electron-proton and electron-hole systems. 5

2.1 Capacitor banks utilized for pulsed field generation. 16
2.2 Representative combinations of pulse magnets and capacitor banks. 16
2.3 Physical properties of PbTe (#T, S) and $Pb_{0.7}Sn_{0.3}Te$ (#T30) samples. . 32

3.1 Structural parameters of black phosphorus 34
3.2 Physical quantities estimated from the transport measurements on p- and n-type BP. 39
3.3 Cyclotron and effective masses of black phosphorus. 39
3.4 Optical phonon modes in black phosphorus 40

4.1 Cyclotron masses normalized by the electron mass, ZC ratios, and effective g-factors of PbTe estimated in a previous study. 71

Chapter 1

General Introduction

1.1 Exotic States Near the Metal-Insulator Transition

Materials in the world can be classified into either insulator of metal from the viewpoint of the electric conduction. Insulators are characterized by the energy gap between the valence and conduction bands, and Fermi level (ϵ_F) is inside the band gap. Ideally, such materials do not have electrical conductivity at 0 K. The others are called metals, in which ϵ_F is inside either the valence or conduction band. As a result, metals have finite charge carriers even at 0 K. If we assume that the band structure can be continuously controlled from insulator to metal by external parameters, what kind of electronic state is expected in the marginal region between these two phases? Semiconductor and semimetal are simple answers for above question based on the conventional band theory. Semiconductor is characterized by moderate band gap $G > 0$ as shown in Fig. 1.1(a), and shows finite conductivity by thermally excited carriers at low temperatures. Typical examples of the single-element semiconductor are Si, P (black), Ge *etc.* If a overlap $G < 0$ between valence and conduction bands arises at ϵ_F as shown in Fig. 1.1(b), the system is called semimetal, in which electrons and holes coexist even at 0 K. The typical examples for compensated semimetals are bismuth and graphite, which have almost the same numbers of electrons and holes with extremely small effective masses.

In semiconductors and semimetals, the physical properties are mainly determined by the band structure only near the band gap or band overlap in the reciprocal space. Here, we overview the general character of such a low-carrier system based on the simple $\boldsymbol{k} \cdot \boldsymbol{p}$ perturbation. We start from the one-electron Schrödinger equation,

$$\left[-\frac{\hbar^2}{2m_0} \boldsymbol{\nabla}^2 + V(\boldsymbol{r}) \right] \Psi_{n,\boldsymbol{k}}(\boldsymbol{r}) = E_n(\boldsymbol{k}) \Psi_{n,\boldsymbol{k}}(\boldsymbol{r}). \tag{1.1}$$

Here, $\hbar = h/(2\pi)$, m_0, $V(\boldsymbol{r})$, $\Psi_{n,\boldsymbol{k}}(\boldsymbol{r}) = e^{i\boldsymbol{k}\cdot\boldsymbol{r}} u_{n,\boldsymbol{k}}(\boldsymbol{r})$, and $E_n(\boldsymbol{k})$ represent reduced Planck constant, bare mass of electron, periodic potential, Bloch function of nth band , and nth eigen energy, respectively. For simplicity, the spin-orbit interaction is omitted in Eq. (1.1). By substituting $\Psi_{n,\boldsymbol{k}}(\boldsymbol{r})$ in Eq. (1.1), we can obtain the expression with $u_{n,\boldsymbol{k}}(\boldsymbol{r})$ as

$$\left[-\frac{\hbar^2}{2m_0} \boldsymbol{\nabla}^2 + V(\boldsymbol{r}) + \frac{\hbar^2 k^2}{2m_0} - \frac{\hbar}{m_0} \boldsymbol{k} \cdot \boldsymbol{p} \right] u_{n,\boldsymbol{k}}(\boldsymbol{r}) = E_n(\boldsymbol{k}) u_{n,\boldsymbol{k}}(\boldsymbol{r}), \tag{1.2}$$

where $\boldsymbol{p} = i\hbar\nabla$. We assume that the exact solution of Eq. (1.2) is known in case of $\boldsymbol{k} = \boldsymbol{0}$:

$$\mathscr{H}(\boldsymbol{0}) u_{n,\boldsymbol{0}}(\boldsymbol{r}) = \left[-\frac{\hbar^2}{2m_0} \boldsymbol{\nabla}^2 + V(\boldsymbol{r}) \right] u_{n,\boldsymbol{0}}(\boldsymbol{r}) = E_n(\boldsymbol{0}) u_{n,\boldsymbol{0}}(\boldsymbol{r}). \tag{1.3}$$

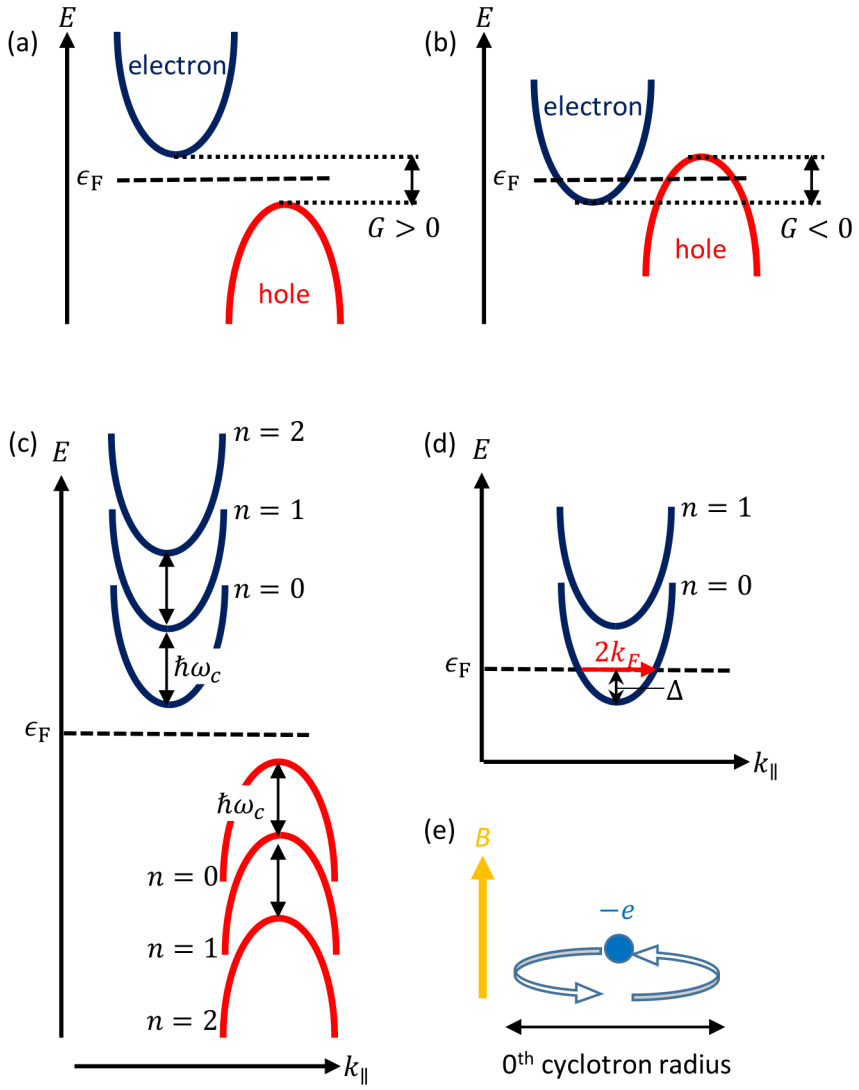

Figure 1.1: Schematic energy band structure of (a) semiconductors with energy gap $G > 0$ and (b) semimetals with band overlap $G < 0$. (c) Landau quantization of the energy band in magnetic fields. $k_\parallel$ represents the wavenumber along the magnetic field direction. (d) Quantum limit state realized in high magnetic fields. Red arrow represents the nesting vector with wavenumber $2k_F$ characterizing the density wave state in the quantum limit state. (e) Cyclotron orbit of electron in the quantum limit state.

	Bi ($B \parallel$ Trigonal) [1,2]		graphite ($B \parallel c$) [3,4]		InSb [5]	PbSe [6]
carrier	electron	hole	electron	hole	electron	electron
n (cm^{-3})	2.88×10^{17}	3.00×10^{17}	$\sim 3 \times 10^{18}$	$\sim 3 \times 10^{18}$	2×10^{14}	2.9×10^{17}
m^*/m_0	0.0125	0.0678	0.038	0.057	0.0146	0.0410

Table 1.1: Carrier densities (n) and cyclotron masses (m^*) of typical semimetals (Bi and graphite) and narrow-gap semiconductors (InSb and PbSe). The cyclotron masses are normalized by the bare mass of electron (m_0).

Then, we regard $\mathscr{H}'(\boldsymbol{k}) = \hbar^2 k^2/(2m_0) - \hbar \boldsymbol{k} \cdot \boldsymbol{p}/m_0$ as a perturbation to $\mathscr{H}(\boldsymbol{0})$ and evaluate the energy band structure in the vicinity of $\boldsymbol{k} = \boldsymbol{0}$. Assuming that $u_{n,\boldsymbol{0}}(\boldsymbol{r})$ are non-degenerated, $E_n(\boldsymbol{k})$ up to the order of k^2 is expressed as

$$E_n(\boldsymbol{k}) = E_n(\boldsymbol{0}) + \frac{\hbar^2 k^2}{2m_0} + \hbar^2 \sum_{m \neq n} \frac{\langle n| \boldsymbol{k} \cdot \boldsymbol{v} |m\rangle \langle m| \boldsymbol{k} \cdot \boldsymbol{v} |n\rangle}{E_n(\boldsymbol{0}) - E_m(\boldsymbol{0})} \tag{1.4}$$

$$= E_n(\boldsymbol{0}) + \sum_{\mu\nu} \frac{\hbar^2}{2} k_\mu \left[\frac{\delta_{\mu\nu}}{m_0} + 2 \sum_{m \neq n} \frac{\langle n| v_\mu |m\rangle \langle m| v_\nu |n\rangle}{E_n(\boldsymbol{0}) - E_m(\boldsymbol{0})} \right] k_\nu \tag{1.5}$$

$$= E_n(\boldsymbol{0}) + \frac{\hbar^2}{2} \boldsymbol{k} \hat{\alpha} \boldsymbol{k}. \tag{1.6}$$

Here, $\boldsymbol{v} = \boldsymbol{p}/m$ and $\mu, \nu = x, y, z$. 3×3 matrix $\hat{\alpha}$ is called inverse mass tensor, and each component is defined as

$$\alpha_{\mu\nu} = \frac{\delta_{\mu\nu}}{m_0} + 2 \sum_{m \neq n} \frac{\langle n| v_\mu |m\rangle \langle m| v_\nu |n\rangle}{E_n(\boldsymbol{0}) - E_m(\boldsymbol{0})}. \tag{1.7}$$

In case that specific two bands are located quite close at $\boldsymbol{k} = \boldsymbol{0}$ and the matrix elements of velocity operator are finite, the contribution from the second term in Eq. (1.7) becomes large because of the small denominator, and as a result, $\alpha_{\mu\nu}$ takes large value. This results in the small carrier effective mass $m_{\mu\nu}$ defined as inverse matrix of $\hat{\alpha}$, as seen in many narrow-gap semiconductors and semimetals.

In such a system with low carrier density and small effective mass, we can observe anomalously large response to the external magnetic fields, and have been extensively studied as playgrounds for novel physics. In general, the energy band of a solid is quantized into the Landau subbands E_n^L with integer $n = 0, 1, 2, \ldots$ ignoring the effect of spin as

$$E_n^L = \left(n + \frac{1}{2} \right) \hbar \omega_c + \frac{\hbar^2 k_z^2}{2m_z}, \tag{1.8}$$

where $\omega_c = eB/m^*$, k_z, and m_z represent the cyclotron frequency with cyclotron mass m^*, wavenumber along the magnetic field, and effective mass along the magnetic field, respectively. The Landau quantization is schematically shown in Fig. 1.1(c). In the case of semimetals or narrow-gap semiconductors, m^* can be much smaller than that of normal materials as mentioned above. m^*/m_0 of representative materials are shown in Table 1.1. As a result, the quantity $E_{n+1}^L - E_n^L = \hbar\omega_c$, namely, the separation between the adjacent Landau subbands can be greatly modified by increasing B. That is why semimetals or narrow-gap semiconductors show remarkable "quantum effect" under moderate magnetic fields. Actually, the quantum oscillation phenomena such as

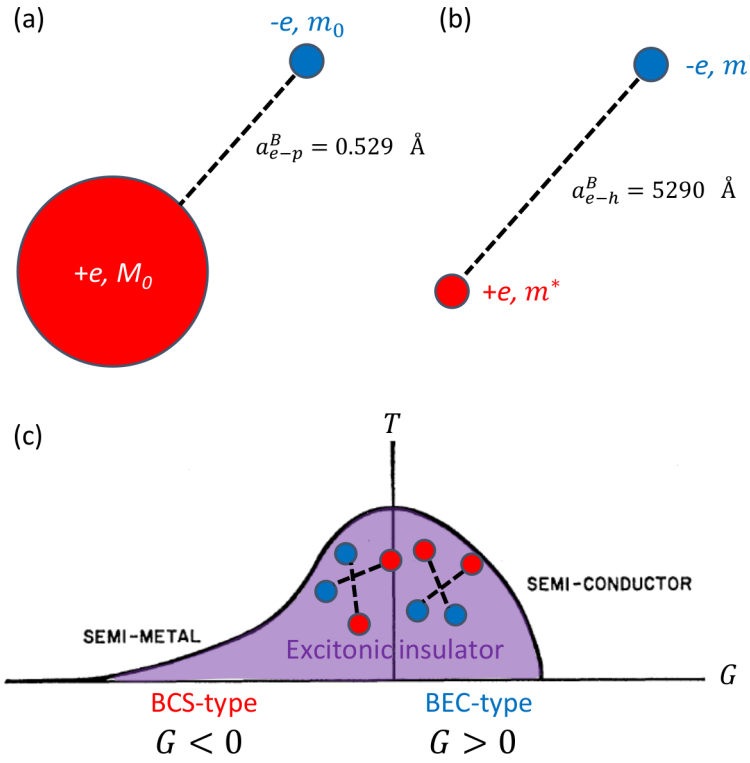

Figure 1.2: (a) Hydrogen atom and (b) exciton in solids. $a^B_{e\text{-}p,e\text{-}h}$ represent the binding radii in Bohr model (see text for details). (c) Phase diagram of the excitonic insulator phase in the T–G plane [12]. T and G represent the temperature and band gap (overlap), respectively.

Shubnikov-de Haas [7, 8] and de Haas-van Alphen [9, 10] oscillations were firstly discovered in bismuth. The magneto-phonon resonance in high mobility semiconductor, which is shown later in Sec. 3.3.2, can be cited as another example. We can consider an extreme case called "quantum limit state", in which all carriers are confined to the lowest Landau level E^L_0 in high-field limit as shown in Fig. 1.1(d). Although the realization of the quantum limit state requires extremely high magnetic field more than 10000 T in typical metals with $\Delta \sim 1$ eV in Fig. 1.1(d) and $m^* \sim m_0$, it can be realized below 100 T in some semimetals and degenerate semiconductors for their small Δ and m^*. Owing to the recent improvement of high-field generation techniques, magnetic fields up to 100 T came to be generated in several pulsed high-field facilities. In the quantum limit state, the orbital motion in the plane perpendicular to the field direction is confined to the cyclotron orbit with the smallest radius as shown in Fig. 1.1(e), and thus, only translational motion along the magnetic field direction is allowed. Owing to such a "quasi-one-dimensional" band character, the system under quantum limit state has an instability toward the density wave state, which has carrier modulation with Fermi wavenumber $2k_F$ [11] along the magnetic field direction.

Under the coexistence of electrons and holes, we can expect more fruitful physics which originates from the Coulomb correlation between them. Here, we overview the fundamental interest in electron-hole system by comparing it with electron-proton system [13]. The simplest element in electron-proton systems is a hydrogen atom ${}^1_1$H [Fig. 1.2(a)]. The energy of electron orbit E^{Bohr}_n and its radius a^{Bohr}_n for the hydrogen atom

system	$E^B(eV)$	a^B (Å)	E^C at 10 T (eV)
electron-proton (e-p)	13.6	0.529	1.16×10^{-3}
electron-hole (e-h)	1.36×10^{-5}	5290	5.80×10^{-2}

Table 1.2: Comparison of the characteristic parameters between the electron-proton and electron-hole systems. In electron-hole system, the effective mass and dielectric constant are assumed to be $0.02m_0$ and $100\epsilon_0$, respectively.

are expressed by well-known Bohr model with integer $n = 1, 2, \ldots$ as

$$E_n^{Bohr} = -\frac{e^2}{8\pi\epsilon_0 a_n}, \tag{1.9}$$

$$a_n^{Bohr} = \frac{\epsilon_0 h^2 n^2}{\pi e^2 \mu}. \tag{1.10}$$

Here, e, ϵ_0, and h represent the elemental charge of electron, dielectric constant of vacuum, and Planck constant, respectively. $\mu = M_0 m_0/(M_0 + m_0)$ is the conversion mass of proton (M_0) and electron (m_0) mass, and is approximated $\mu \sim m_0$ in case of hydrogen atom ($M_0 \gg m_0$). Based on Eqs. (1.9) and (1.10), the ground state of $^1_1$H has the binding energy $E^B_{e\text{-}p} = |E_0^{Bohr}| = 13.6$ eV and radius $a^B_{e\text{-}p} = a_0^{Bohr} = 0.529$ Å. Here, we assume the application of the magnetic field of 10 T to hydrogen atom. The energy scale of the magnetic field is represented by cyclotron energy $E^C_{e\text{-}p} = e\hbar B/m_0 = 1.16 \times 10^{-3}$ eV, which is found to be merely perturbative effect on $E^B_{e\text{-}p}$. If we try to achieve the situation that the energy scale of the magnetic field is larger than that of Coulomb interaction ($E^B_{e\text{-}p} < E^C_{e\text{-}p}$), B exceeds $\sim$ 100000 T, which is far beyond the technical limit of high-field generation. Such a extremely high magnetic field is expected to exist on a neutron star in the universe. Then, we consider an exciton in crystals, a bounding state of electron and hole by Coulomb attraction [Fig. 1.2(b)]. We assume large dielectric constant [ϵ_0 is substituted by $100\epsilon_0$ in Eqs. (1.9) and (1.10)] and small effective masses of $m^* = 0.02m_0$ for both electron and hole, which are similar with those of bismuth. In this case, the conversion mass becomes $\mu = 0.01m_0$, and the binding energy is $E^B_{e\text{-}h} = 10^{-6}E^B_{e\text{-}p} = 1.36 \times 10^{-5}$ eV, which is quite lower than that of hydrogen atom due to the large binding radius $a^B_{e\text{-}h} = 10^4 a^B_{e\text{-}p} = 5290$ Å. On the other hand, the effect of the magnetic field becomes relatively larger than that in a hydrogen atom due to the small m^*. The cyclotron energy is estimated as $E^C_{e\text{-}h} = e\hbar B/m^* = 5.80 \times 10^{-2}$ eV at $B = 10$ T, which is no longer a perturbation on $E^B_{e\text{-}h}$. Actually, the situation $E^B_{e\text{-}h} < E^C_{e\text{-}h}$ is satisfied under the magnetic field of ~ 0.002 T, which indicates that the electron-hole system under the magnetic field at 10 T corresponds to the extremely-high-field limit in electron-proton system. Thus, the physics of electron-hole system in high magnetic fields can contain common essence with that of electron-proton system on a neutron star, which stimulate a general interest of physics beyond the framework of condensed matter physics. The comparison of the characteristic parameters between electron-proton and electron-hole systems are summarized in Table 1.2.

One of the novel ground states expected in the electron-hole system with the condition $E^B_{e\text{-}h} > |G|$ is "excitonic insulator phase". The concept of the condensed phase of excitons has firstly been proposed more than 50 years ago [14]. Since exciton is electrically neutral, the realization of such a phase is assumed to accompany insulation of the system. Theoretically, excitonic insulator phase is expected to exist in the vicinity of the semiconductor-semimetal boundary as shown in Fig. 1.2(c). In the semimetallic

region ($G < 0$), excitonic insulator phase is known to be formulated by analogy with the BCS theory in superconductivity. In semiconducting region ($G > 0$), on the other hand, it is regarded as a Bose-Einstein condensation (BEC) state of excitons. Thus, the investigation of excitonic insulator phase is expected to bring important knowledge of essential phenomena in condensed matter physics, such as BCS, BEC, and their crossover phenomena. Theoretically, the application of magnetic fields to semimetals or semiconductors is known to enhance the binding energy of excitons due to the shrinkage effect of the cyclotron orbit [15,16]. In addition, since the band overlap generally becomes smaller as the magnetic field increases, the condition $E^B_{e\text{-}h} > |G|$ is expected to be satisfied on the way to increase the magnetic field. Fenton predicted the realization of the excitonic insulator phase in high magnetic fields based on the advantages mentioned above [17]. Actually, recent experimental studies of graphite suggested the realization of excitonic insulator phase in high magnetic field [18–20]. Other than graphite, there are several reports on the possible realization of the excitonic insulator in other materials, such as bismuth [21–23], Ta_2NiSe_5 [24, 25], $1T$-$TiSe_2$ [26–28], $TmSe_{1-x}Te_x$ [29], and excited semiconductor [30]. However, the concrete thermodynamic evidence and understanding of the physical properties have been still lacking. Thus, a simple model material has been desired, in which the band structure can be continuously tuned between semiconductor and semimetal.

1.2 Topological Materials

The boundary between a metal and an insulator has recently been focused on in a context of topology in solids. Materials with non-trivial band topology are called "topological materials", which do not belong to the categories based on the conventional band theory. The exploration of novel physical properties in this kind of materials is now one of the main streams in condensed matter physics. One of the outstanding features of the topological materials is the presence of "Dirac fermions" which obey the relativistic Dirac equation and have extremely high mobility. Dirac equation has been originally used to describe the motion of high-velocity particles in high energy physics or particle physics. Hence, if we can observe the behavior of such a high energy particle in topological materials, the knowledge can be beneficial in other fields of physics. The first prediction and experimental discovery of "topological insulators" [35, 36], which possess Dirac fermions at their surfaces, initiate the research of topological nature in solids. More recently, "three-dimensional (3D) topological semimetals" such as Dirac semimetals [31, 37] and Weyl semimetals [38–40] have been actively investigated owing to their exotic character, in which Dirac fermions contribute the bulk physical properties.

The identification of the topological materials mostly relies on the experimental or computational verification of linear energy dispersion relation, which is a consequence from the Dirac equation. Actually, 3D topological semimetals such as Cd_3As_2 and Na_3Bi has been confirmed the linearity of the dispersion relation by both ARPES experiments and band calculations [37, 41, 42]. As an example, the case of Cd_3As_2 is shown in Fig. 1.3(a) and (b). Many other materials have been proposed as candidates of topological materials based on the above criteria.

The point of interest is novel transport properties which emerge as a result of the relativistic equation of motion in these materials. One of the intriguing properties expected in the topological materials is the non-trivial Berry's phase accompanied with the singularity of the energy band structure. Mikitik *et al.* theoretically suggested that a closed

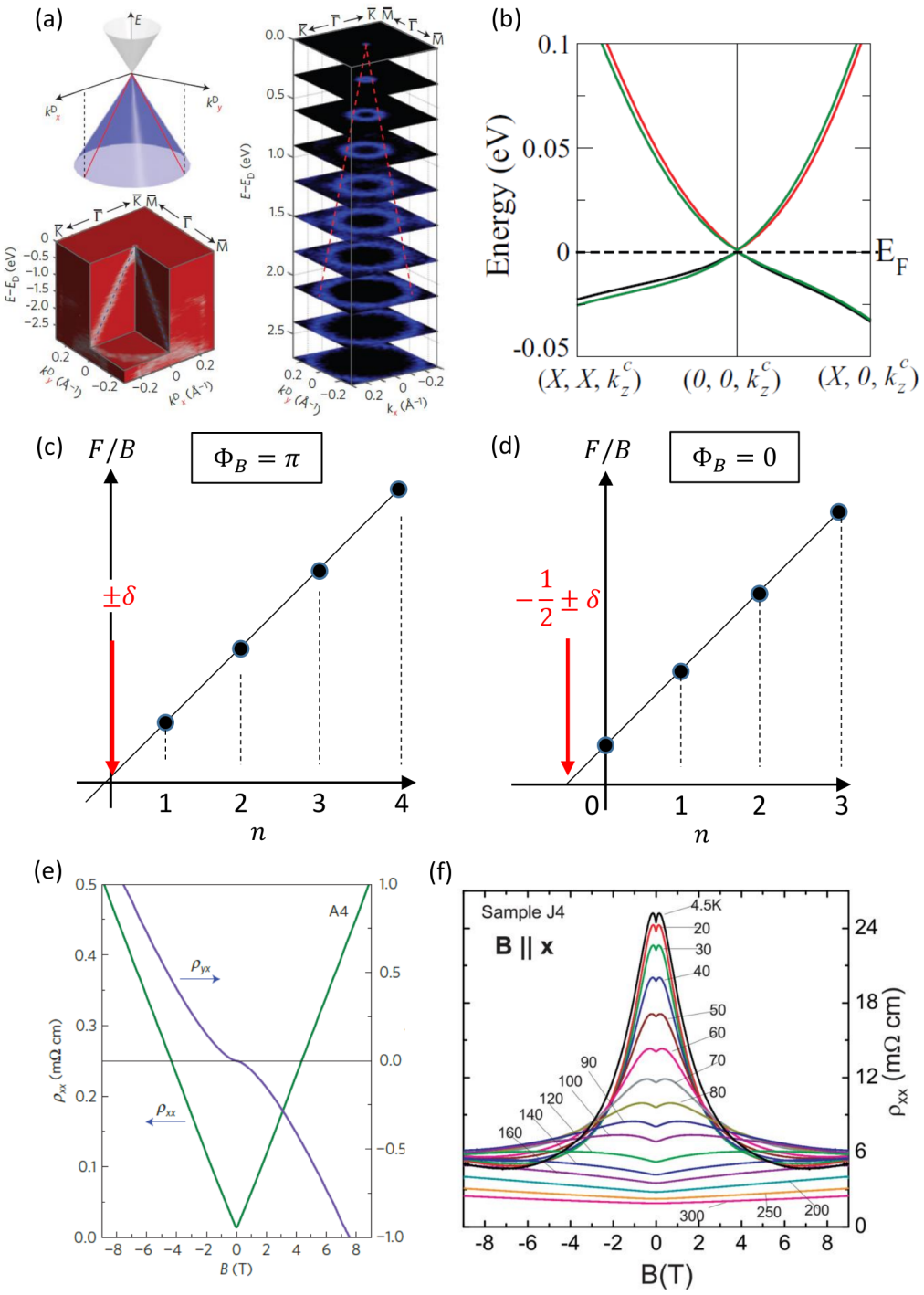

Figure 1.3: Linear energy dispersion relation in topological semimetal Cd_3As_2 appeared in (a) ARPES measurement [31] and (b) band calculation [32]. (c) Landau-level fan diagrams in case that closed orbit in momentum space accompanies Berry's phase $\Phi_B =$ (c)π and (d)0. δ is 1/8 for 3D and 0 for 2D system. (e) Linear magnetoresistance observed in Cd_3As_2 [33]. (f) Negative longitudinal magnetoresistance observed in Na_3Bi [34].

orbit in momentum space which surrounds a Dirac point in a two-dimensional (2D) surface state or band-contact line in a 3D bulk has non-trivial Berry's phase $\Phi_B = \pi$ [43]. They also pointed out that whether a material has the non-trivial Berry's phase can be discernable by focusing on the phase of quantum oscillations. Based on their suggestion, many experimental attempts have been made to detect the non-trivial Berry's phase in topological insulators and 3D topological semimetals. The observation of SdH oscillation and construction of Landau-level fan diagram, as shown in Figs. 1.3(c) and (d), are frequently-used method for the identification of the Berry's phase [44]. In case of the SdH oscillation, the conductivity σ_{xx} is firstly plotted against the inversed magnetic field $(1/B)$. Then, a *peak* position $(1/B_n)$ is assigned to an *integer* Landau index n. Through above assignment, the Landau-level fan diagram ($1/B_n$ against n) is constructed. Here, oscillation component of the SdH oscillation $\Delta\sigma_{xx}$ is assumed by

$$\Delta\sigma_{xx} = \cos\left[2\pi\left(\frac{F}{B} + \gamma \pm \delta\right)\right], \tag{1.11}$$

where F is the frequency of oscillation. $\gamma = 1/2 - \Phi_B/(2\pi)$ is called Onsager phase factor with Berry's phase Φ_B, which originates from the Bohr-Sommerfeld quantization rule for closed orbit in momentum space surrounding the area S_n:

$$S_n = \frac{2\pi eB}{\hbar}(n + \gamma). \tag{1.12}$$

δ take $\pm 1/8$ and 0 for three-dimensional (3D) and two-dimensional (2D) systems, respectively. Based on Eq. (1.11), the system has a non-trivial Berry's phase $\Phi_B = \pi$ when the horizontal intercept takes $\pm 1/8$ (3D bulk) or 0 (2D surface) [Fig. 1.3(c)]. In contrast, trivial Berry's phase $\Phi_B = 0$ is identified when the horizontal intercept takes $-1/2 \pm 1/8$ (3D bulk) or $-1/2$ (2D surface) [Fig. 1.3(d)]. In case that only single kind of carrier contributes the transport properties, the condition $\sigma_{xx} \ll |\sigma_{xy}|$ is generally fulfilled when the quantum oscillations are observable. Thus, the dips in σ_{xx} correspond to those in ρ_{xx}, and the analysis for ρ_{xx} is also valid. However, we should be careful in multi-carrier cases in which $\sigma_{xx} \ll |\sigma_{xy}|$ is not necessarily satisfied [45]. In this case, the analysis based on ρ_{xx} can lead to wrong result. In numbers of research, non-trivial Berry's phase detected through this analysis has been proposed as an evidence of a topological material. However, the precise determination of the phase factor of quantum oscillation accompanies many difficulties since most of the actual materials have multiple kinds of carriers. Owing to the complexity accompanying with the analyses, there exists several cases that the estimated Berry's phase varies by research groups even in the same material [46].

Also, there are many reports which suggest the observation of unconventional transport properties owing to the presence of the Dirac fermions. One example is large linear transverse magnetoresistance in high magnetic fields. This behavior has been theoretically proposed by Abrikosov [47, 48] under the situation that the energy dispersion has linear dependence upon the momentum and the carriers are all confined to the lowest Landau subband (namely, under the quantum limit state). Later, Wang *et al.* theoretically showed the possible emergence of the linear and non-saturating magnetoresistance even when other subbands cross the Fermi level and the thermal broadening is comparable to the separation of Landau subbands in the presence of the topological surface state [49]. Experimentally, the observation of large linear magnetoresistance, for example in Cd_3As_2 [Fig. 1.3(e)] [33], and many other materials have been reported until now. In [33], the possible contribution of topologically protected back scattering has

also been suggested as a mechanism of the phenomenon. On the other hand, Parish *et al.* proposed that macroscopic disorder can cause the non-saturating magnetoresistance based on the calculation, which does not suppose the existence of linear dispersion [50]. Kisslinger *et al.* also suggested a mechanism without the existence of linear dispersion that linear magnetoresistance should emerge when the system has low density charge carriers, distorted current path, and high magnetic field [51].

Another example of the intriguing phenomena is the negative longitudinal magnetoresistance (magnetic field is applied parallel to the electric current). This behavior is believe to stem from the Adler-Bell-Jackiw chiral anomaly (or merely chiral anomaly) in quantum field theory [52]. We can find numbers of reports which insist on the observation of the chiral anomaly, for example, in Na_3Bi as shown in Fig. 1.3(f) [34]. On the other hand, the negative longitudinal magnetoresistance is also shown to occur without topological nature. Arnold *et al.* suggested that the strong inhomogeneity of electric current in a magnetic field due to the high-mobility of the carriers can cause apparent negative magnetoresistance [53]. This effect is referred as the current jetting effect.

Considering the situations mentioned above, the universal nature of topological materials has not fully been clarified at the moment.

1.3 General Issues and Solutions

Although the exotic states in narrow-gap semiconductors and semimetals have been searched for more than 50 years, there is only limited experimental knowledge about that. To overcome such stagnation, a model material is needed, in which the carrier density is sensitively controllable by external parameters over the wide range from semiconductor to semimetal.

With respect to the study of topological materials, on the other hand, there are numerous reports which claim the observation of novel phenomena stemming from their non-trivial topology. At present, however, it is very difficult to distinguish whether observed physical properties originate from the universal nature of topological materials. To clarify truly special behavior in the topological materials, it is crucially important to faithfully analyze the obtained results based on the well-known theoretical framework, and then, elucidate the phenomena which are essentially unable to explain in the traditional framework. The nature stemming from their non-trivial topology should be latent in them. Common to both topics, the material investigated should have electronic structure as simple as possible to eliminate the ambiguity in extracting the nature or comparing with the theoretical framework. Otherwise, the essence can be obscured by the complexity. Besides, controllable band structure by external parameters is desirable, which enables us systematic investigation with tuning the carrier density or topology of the band structure as desired.

Based on these problem consciousness and philosophy, we focus on the narrow-gap semiconductors, black phosphorus and lead telluride as ideal model materials satisfying above properties. In the subsequent chapters, we explain the experimental methods of investigations, background of each material, and newly obtained results.

Chapter 2

Experimental Methods

2.1 Essentials of the Electrical Transport Measurements

In this section, we review the rudimentary knowledge of the electrical transport measurements. Electrical resistance (or merely resistance) R represents the degree of difficulty in flowing the electrical current I through a material, and defined using the voltage drop V as

$$\boldsymbol{V}(B) = \hat{R}(B)\boldsymbol{I} \tag{2.1}$$

$$= \begin{pmatrix} R_{xx} & R_{xy} & R_{xz} \\ R_{yx} & R_{yy} & R_{yz} \\ R_{zx} & R_{zy} & R_{zz} \end{pmatrix} \begin{pmatrix} I_x \\ I_y \\ I_z \end{pmatrix}. \tag{2.2}$$

Here, we explicitly showed the dependence on magnetic flux density (B) following the realistic situation. To measure the resistance, we shaped the sample into rectangle and attached gold wires (typically 30 μm-diameter) to the sample with conductive paste. We mainly utilized carbon epoxies, MRX-713J (Tamura Corporation) and DOTITE XC-12 (Fujikura Kasei Co.,Ltd.) to attach the gold wires to the sample. It is desirable that the contacts on the sample has sufficient mechanical strength and small contact resistance. High contact resistance on current path limits the maximum of the current in the measurement at low temperature due to the possible heating.

Figure. 2.1(a) shows typical setting for the five-terminal method utilized in this study. Two pairs of contacts ($I_\pm$ and $V_\pm$) are used for current injector and voltage

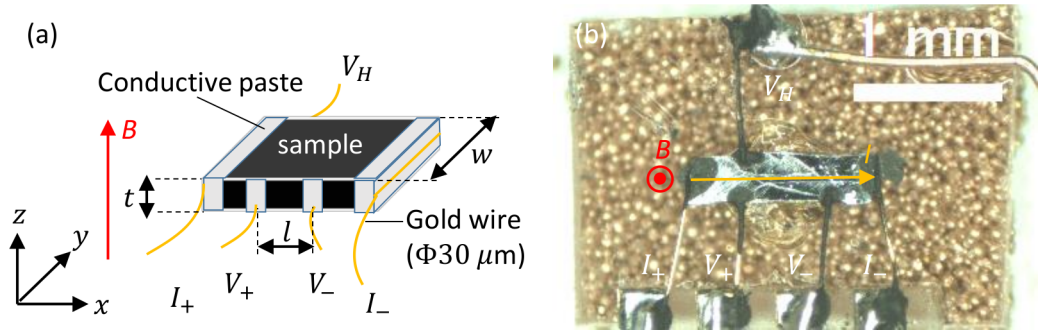

Figure 2.1: (a) Five-terminal method for electrical transport measurements. (b) An example of actual setting for five-terminal measurement on PbTe.

probe, respectively. Another contact (V_H) is formed on the facing side of either V_+ or V_- for the measurement of Hall resistance. In the five-terminal method, we can measure the resistance and Hall resistance simultaneously on a sample (we abbreviated V_H contact and adopted four-terminal method for only resistance measurement). Five- (or four-) terminal method allows us, in principle, to measure the resistance of the sample $V_{sample}(I, B) = R_{sample}(B)I$ without contact resistance or resistance of wires, and thus, it is advantageous to precisely measure the small resistance. An example of actual setting for PbTe is shown in Fig. 2.1(b). Generally, there is a temperature gradient (ΔT) on lead wires connecting between the sample and a voltmeter at room temperature. Thus, the thermal voltage $V_{therm}(\Delta T)$ by Seebeck effect is included in obtained voltage drop. In case of a measurement under time-dependent magnetic fields, in addition, the change of magnetic flux running through an open loop of the circuit causes induced voltage $V_{EM}(B)$. Especially in pulsed magnetic field, $V_{EM}(B)$ can be comparable or even larger than the voltage drop by the sample. The voltage drop obtained by five-terminal method $V(I, B)$ is generally represented as

$$V(I, B) = V_{sample}(I, B) + V_{therm}(\Delta T) + V_{EM}(B), \tag{2.3}$$

taking above extrinsic effects into consideration. We have to extract only $V_{sample}(I, B)$ from Eq. (2.3).

We firstly consider the case of DC measurement with a fixed current ($I = I_0$ is independent of time). Since $V_{therm}(\Delta T)$ and $V_{EM}(B)$ do not depend on I, and $V_{sample}(\pm I, B) = \pm V_{sample}(I, B)$, $V(\pm I_0, B)$ is represented as

$$V(\pm I_0, B) = \pm V_{sample}(I_0, B) + V_{therm}(\Delta T) + V_{EM}(B). \tag{2.4}$$

As is clear from Eq. (2.4), $R_{sample}(B)$ is obtained by

$$R_{sample}(B) = \frac{V(+I_0) - V(-I_0)}{2I_0}. \tag{2.5}$$

In case of AC measurement [$I = I_0 \sin(2\pi ft)$ is oscillatory current with frequency f], $V(I, B)$ is expressed as

$$V(I, B) = V_{sample}(I_0, B) \sin(2\pi ft) + V_{therm}(\Delta T) + V_{EM}(B). \tag{2.6}$$

Here, we consider the amount $V_L(I, B) = V(I, B) \sin(2\pi ft)$, which is represented as

$$V_L(I, B) = \frac{V_{sample}(I_0, B)}{2} - \frac{V_{sample}(I_0, B)}{2} \cos(4\pi ft) + [V_{therm}(\Delta T) + V_{EM}(B)] \sin(2\pi ft). \tag{2.7}$$

We can extract $V_{sample}(I_0, B)$ from Eq. (2.7) by attenuating the oscillating components, and obtain $R_{sample}(B)$. The details of the analysis in AC measurements will be described in Sec. 2.5.

By the five-terminal DC or AC measurement, we can obtain $R_{sample}(B)$ and $R^H_{sample}(B)$ using potential difference $V_+ - V_-$ and $V_+ - V_H$ in Fig. 2.1(b), respectively. Here, the sign of $R^H_{sample}(B)$ was defined to correspond to that of carrier assuming single-carrier conduction. When the shape of the sample and the geometry of the contacts are perfect, $R_{sample}(B)$ and $R^H_{sample}(B)$ are exactly the resistance $R_{xx}(B)$ and Hall resistance $R_{yx}(B)$, respectively. In realistic case, however, $R_{sample}(B)$ and $R^H_{sample}(B)$ contain finite residual components due to the misalignment of the contacts:

$$R_{sample}(B) = R_{xx}(B) + \delta R_{yx}(B), \tag{2.8}$$

$$R^H_{sample}(B) = \delta R_{xx}(B) + R_{yx}(B). \tag{2.9}$$

Here, δ represents small dimensionless constant. To separate these components, we focus on the following properties of $R_{xx}(B)$ and $R_{yx}(B)$ [see Fig. 1.3(e) for example]:

$$R_{xx}(\pm B) = R_{xx}(B), \tag{2.10}$$
$$R_{yx}(\pm B) = \pm R_{yx}(B). \tag{2.11}$$

Thus, we can obtain $R_{xx}(B)$ and $R_{yx}(B)$ using $R_{sample}(\pm B)$ and $R^H_{sample}(\pm B)$ as

$$R_{xx}(B) = \frac{R_{sample}(B) + R_{sample}(-B)}{2}, \tag{2.12}$$
$$R_{yx}(B) = \frac{R^H_{sample}(B) - R^H_{sample}(-B)}{2}. \tag{2.13}$$

Using $R_{xx}(B)$ and $R_{yx}(B)$, we can finally obtain the resistivity $[\rho_{xx}(B)]$ and Hall resistivity $[\rho_{yx}(B)]$, which are independent of the shape of the sample as

$$\rho_{xx}(B) = R_{xx}(B)\frac{wt}{l}, \tag{2.14}$$
$$\rho_{yx}(B) = R_{yx}(B)\frac{wt}{w} \tag{2.15}$$
$$= R_{yx}(B)t. \tag{2.16}$$

Here, w, t, and l are defined in Fig. 2.1(a).

2.2 Resistivity Measurements under Pressure

In this section, we explain the setup of resistivity measurements under pressure performed in this study. We utilized two kinds of piston-cylinder-type pressure cells with different diameters of sample space to realize high pressure environment. One has the diameter of 5 mm (max ∼2.5 GPa), and the other 4 mm (max ∼3 GPa). The former and latter are provided by Uwatoko group (ISSP, The University of Tokyo) and C&T Factory Co., Ltd., respectively. The overall view of the piston-cylinder-type pressure cell is shown in Fig. 2.2(a). The cylinder is composed of inner shell (NiCrAl alloy) and outer cylinder (CuBe alloy). Such a double-layered cylinder (called hybrid cylinder) is known to improve the efficiency of pressure generation and maximum pressure [54]. The applied load is held by upper and lower lock nuts made of CuBe. Figure 2.2(b) shows an illustration of the sample cell which is pressurized in the cylinder. Copper wires are twisted and passed through a plug made of NiCrAl or CuBe (the number of wires varies according to the measurement). The wires and plug are tightly glued by STYCAST 2850FT in order to prevent the leakage of the pressure medium outside the cell. The sample and pressure sensor are enclosed in the cell made of Teflon with appropriate pressure medium. We utilized glycerine, Daphne7373, or Daphne7474 as pressure mediums (the second and last ones are provided by Idemitsu Kosan Co., Ltd.). The sample cell is inserted into the hybrid cylinder together with two seal rings made of CuBe, piston, and two backups both made of tungsten carbide. The sample space is pressurized using an oil hydraulic press and push rod up to maximum load of ∼6 ton. Pure lead (Pb) was used for a pressure sensor. It is well known that the pressure (P, GPa) dependence of the superconducting transition temperature (T_c, K) of Pb at zero magnetic fields obeys the following empirical formula [55]:

$$T_c = 7.19 - 0.384P. \tag{2.17}$$

We measured temperature dependence of resistivity of Pb at low temperature everytime after we changed the load, and determined the actual pressure in the sample space. Here, we paid sufficient attention to exclude the effect of the remnant magnetic field of superconducting magnet when we determine T_c: Even if the control panel of the magnet indicates 0 T, slight remnant magnetic field can exist. Thus, we checked the value of remnant magnetic field and compensated it every time before determining the pressure.

For the measurements of black phosphorus, we used two different setups to direct the field direction with respect to the stacking direction. The detailed sketches are shown in Fig. 2.2(c) and (d). For in-plane field configuration, sample was placed on a flexible glassfiber sheet placed parallel to the field direction as shown in Fig. 2.2(c). For out-of-plane configuration, a tube made of Fiber-Reinforced Plastics (FRP) or machinable ceramics (MACOR) was put in the Teflon cell: the outer diameter of the tube is almost the same with the inner diameter of the Teflon tube so that the stacking direction is automatically aligned to the field direction when the tube was inserted into the Teflon cell. The sample was mounted on a chip of paper or glass to prevent the sample from falling into the borehole of the tube [the lower inset of Fig. 2.2(d)].

We performed resistivity measurements under pressure and magnetic field using Physical Property Measurement System (PPMS, Quantum Design), which can generate low temperature down to 1.8 K and static magnetic fields up to 14 T. We measured resistivity ρ_{xx} (and Hall resistivity ρ_{yx}) of the sample, and resistivity of Pb pressure sensor simultaneously using typical resistivity option implemented in PPMS. Several jigs

developed by ElectroLAB [shown with ※ in Fig. 2.2(a)] were attached to the pressure cell to combine it with the PPMS.

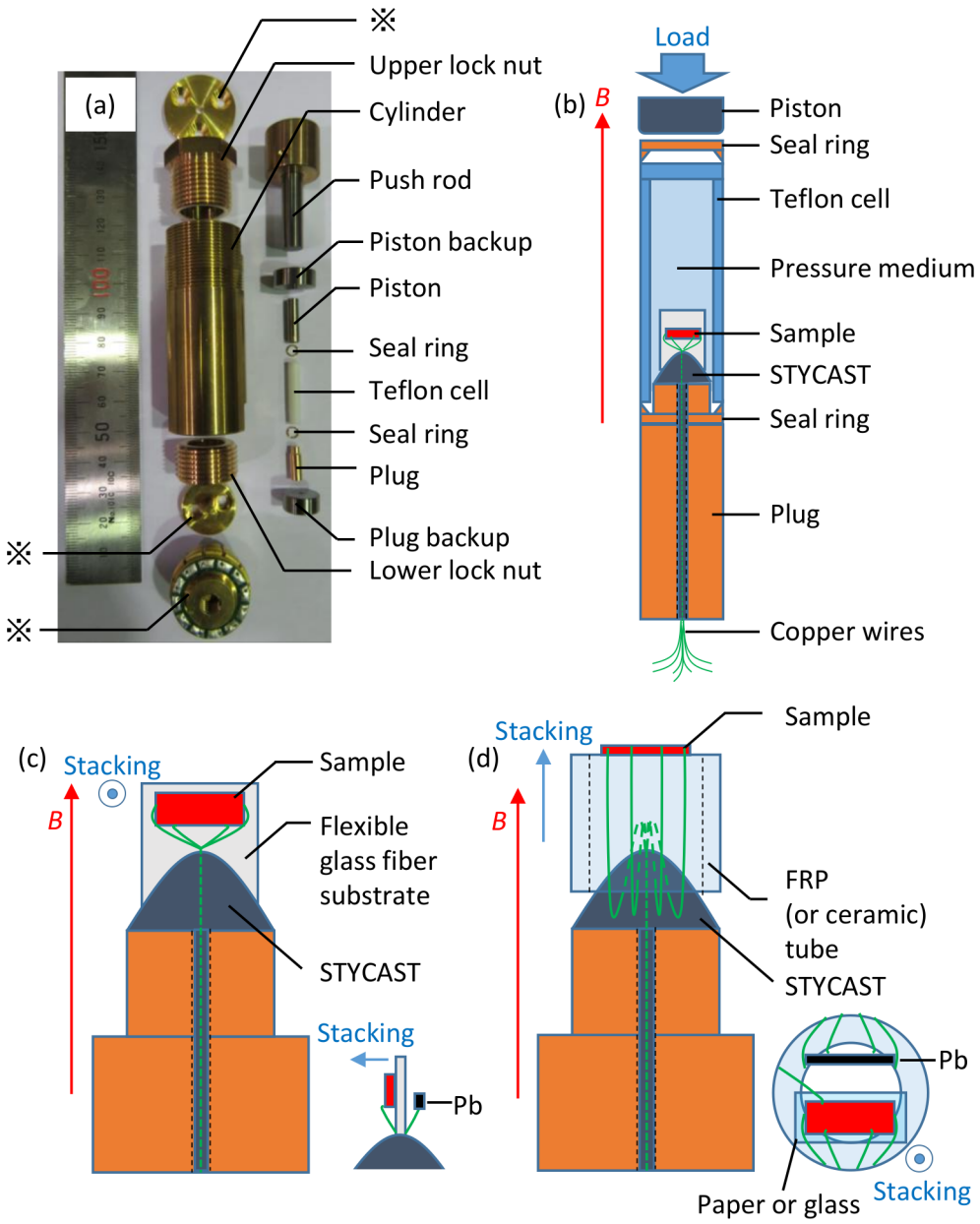

Figure 2.2: (a) The overall view of piston-cylinder-type pressure cell utilized in this study. "※" represent jigs for PPMS measurement. (b) Detailed view of the sample cell. The magnetic field is applied along the cell. (c) The magnified view of the configuration for B (c) perpendicular to and (d) parallel to the stacking direction of layered material. The lower insets in (c) and (d) show magnified views around the sample from different viewpoints.

installation site	V_{max} (kV)	C (mF)	$W_{max} = CV_{max}^2/2$ (kJ)
Building C, ISSP	10	18	900
Building K, ISSP	20	2.5	500

Table 2.1: Capacitor banks utilized for pulsed field generation. V_{max}, C, and W_{max} represent the maximum charging voltage, capacitance, and maximum accumulation energy, respectively.

magnet type	bore (mm)	driving bank	$T_0/2$ (ms)	B_{max} (T)
mid pulse	18	Building C	38	55 (9 kV discharging)
60 T	18	Building C	38	60 (9 kV discharging)
short pulse	15	Building K	4	75 (15 kV discharging)

Table 2.2: Representative combinations of pulse magnets and capacitor banks. $T_0/2$ and B_{max} represent the pulse duration time and maximum magnetic field, respectively.

2.3 Generation of Pulsed Magnetic Fields

In this section, we briefly review how to generate pulsed high magnetic fields. In this study, we utilized non-destructive pulse magnets developed in Kindo group (ISSP, The University of Tokyo) [56]. These magnets are basically multilayered solenoids made by specially developed Cu-Ag alloy wires. A picture and schematic view of the magnet are shown in Figs. 2.3(a) and (b), respectively. Magnets with different self-inductance (L) were manufactured by changing the number of turns and layers, diameter, and length of solenoids. In addition, a capacitor bank with large accumulation energy is necessary for high magnetic field generation. We utilized two kinds of capacitor banks with different capacitance (C) in ISSP, as shown in the Table 2.1. We can control the properties of magnetic fields (such as pulse duration or maximum field) by changing the combination between the magnet and capacitor bank, as shown in Table 2.2.

The circuit for pulsed magnetic field generation is schematically shown in Fig. 2.4(a). Here, R and V_0 represent the resistance of the magnet and DC voltage supply for charging capacitor bank, respectively. Strictly speaking, R is the combined resistance of magnets and whole current path, but the latter is sufficiently smaller than the former. The capacitor bank can be charged or discharged depending on the state of the switch. Now, we consider the situation that the charge CV_0 is discharged to the magnet at $t = 0$. Then, we can describe the time (t) dependence of this circuit according to Kirchhoff's law as

$$L\frac{di(t)}{dt} + Ri(t) = \frac{q(t)}{C}. \tag{2.18}$$

Here, $i(t)$ and $q(t)$ represent the current passing through the circuit and charge stored in the capacitor bank at t, respectively. Moreover, we can rewrite Eq. (2.18) using the relationship $i(t) = -dq(t)/dt$ as

$$\frac{d^2q(t)}{dt^2} + \frac{R}{L}\frac{dq(t)}{dt} + \frac{1}{LC}q(t) = 0. \tag{2.19}$$

By assuming the solution of Eq. (2.19) as $q(t) = e^{\lambda t}$, we can obtain the representation for constant λ as

$$\lambda = -D \pm \sqrt{D^2 - \frac{1}{LC}}. \tag{2.20}$$

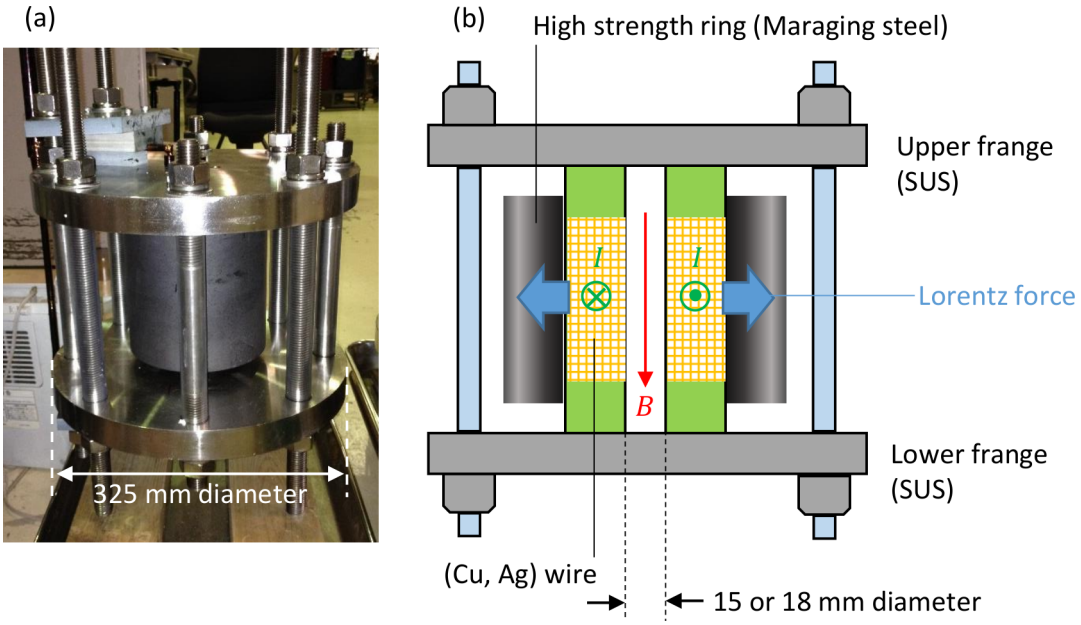

Figure 2.3: (a) Picture of typical pulse magnet utilized in this study. (b) Cross-sectional view of the pulse magnet.

Here, $D = R/(2L)$. In this study, we generated magnetic fields under the condition $D^2 - 1/(LC) < 0$ [namely, $q(t)$ can be described as damped oscillation]. For this case, we can write down the general form of $q(t)$ with constants A and B as

$$q(t) = e^{-Dt}\left[A\cos(\omega t) + B\sin(\omega t)\right]. \tag{2.21}$$

Here, $\omega = \sqrt{1/(LC) - D^2}$. A and B are determined by initial condition at $t = 0$ [$q(0) = CV_0$ and $dq(t)/dt|_{t=0} = 0$], and thus, $q(t)$ is written as

$$q(t) = e^{-Dt}\left[CV_0\cos(\omega t) + \frac{CDV_0}{\omega}\sin(\omega t)\right]. \tag{2.22}$$

Then, $i(t)$ is obtained as

$$i(t) = -\frac{dq(t)}{dt} \tag{2.23}$$

$$= Dq(t) + e^{-Dt}\left[\omega CV_0\sin(\omega t) - CDV_0\cos(\omega t)\right] \tag{2.24}$$

$$= \frac{e^{-Dt}V_0}{L\omega}\sin(\omega t). \tag{2.25}$$

From Eq. (2.25), we can see that the period of oscillation (T_0) is represented as $T_0 = 2\pi\sqrt{LC/(1 - LCD^2)}$ and the amplitude of oscillation decreases as time goes by due to the coefficient $\exp(-Dt)$. For example, we can plot $i(t)$ as Fig. 2.4(b) by substituting typical parameters ($V_0 = 9000$ V, $C = 18$ mF, $L = 8.7$ mH, and $R = 0.2$ Ω) into Eq. (2.25), and determine $T_0 = 79.2$ ms. Only the highest current peak (t from 0 to $T_0/2 = 39.6$ ms) is used for the field generation, and capacitor bank is connected to the earth at $t \sim T_0/2$. In simplified case that the length of the solenoid is sufficiently long, and it is put in the vacuum, the magnetic flux density (B) generated inside the solenoid is proportional to i: $B(t) = \mu_0 n i(t)$. Here, μ_0 and n represent the magnetic

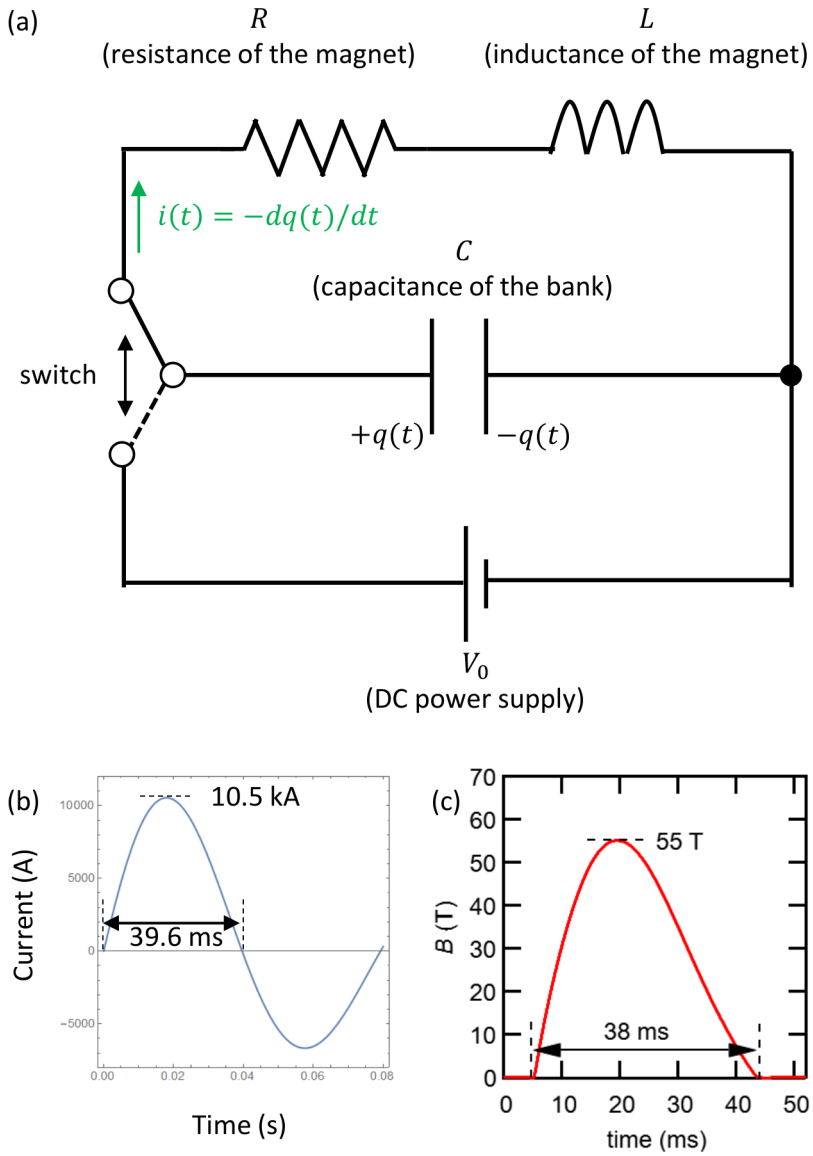

Figure 2.4: (a) Simplified circuit diagram for pulsed magnetic field generation. (b) Simulated electric current $i(t)$ flowing through the circuit shown in (a). We assumed $V_0 = 9000$ V, $C = 18$ mF, $L = 8.7$ mH, and $R = 0.2$ Ω. (c) Actual field property of mid pulse magnet in Table. 2.2.

permeability of vacuum and number of turns per unit length, respectively. Although $B(t)$ cannot be represented such a simple form in realistic case, actual field property shown in Fig. 2.4(c) coincide well with the simulated $i(t)$.

We can simulate the Joule heat (W_J) generated at the magnet assuming above parameters. W_J is represented by integrated form as

$$W_J = \int_0^t dt' R i^2(t'). \tag{2.26}$$

Assuming $R = 0.2\ \Omega$ is independent of time, we obtain $W_J \sim 437$ kJ by substituting $t = 39.6$ ms. Comparing with the input energy $W_0 = CV_0^2/2 = 729$ kJ, which is initially stored in the capacitor bank, 60 % of the total energy is converted to heat at the magnet. Since the repetition of such a huge heating can cause a fatal damage on the magnet, magnet is always cooled by liquid nitrogen during the operations, and we arrange appropriate time interval after field generation until the resistance of the magnet returns to the equilibrium value in liquid nitrogen. We also roughly estimate the Lorentz force (F_L) acting on the Cu-Ag wire. We adopt simple formula for F_L,

$$F_L = IBl\sin(\theta). \tag{2.27}$$

Here, I, l, and θ are current flowing through the wire, the length of wire, and the angle between B and I. We assume a segment of the wire near the center of the magnet, and that maximum current is passing through into it: the flowing current and generated magnetic field are approximately $I = 10.5$ kA and $B = 55$ T, respectively. Then, F_L acting on the Cu-Ag wire with length of 1 cm reaches $F_L \sim 5.8 \times 10^3$ N $= 5.9 \times 10^2$ kgw. Also note that F_L always acts outward of the magnet, regardless of the current direction. To prevent the breakdown of the magnet by such a huge electromagnetic stress, the wire itself and insulating layer put on the surface of the wire should be sufficiently tough. In addition, multilayered coil is enclosed by a high strength ring made of Maraging steel to reinforce the strength against the Lorentz force, as shown in Figs. 2.3(a) and (b). The maximum fields are determined by the strength of the wire and insulating layer. In other words, the development of the high strength and conductive wire is important to improve the maximum magnetic field.

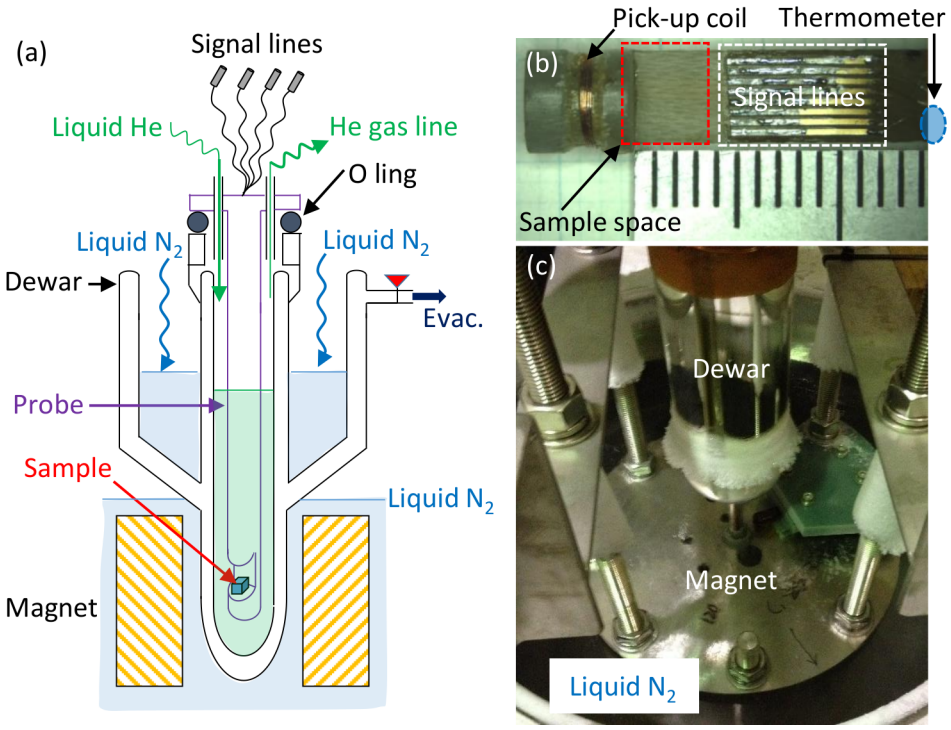

Figure 2.5: (a) Structural drawing of the cryostat system in high-field measurements. (b) Magnified view of the sample space on the tip of a resistivity measurement probe. The body of the probe is made of FRP with diameter of 5 mm. (c) Cryostat system installed in a pulse magnet.

2.4 Cryostat System in High-Field Measurements

In this section, we review the cryostat used in high-field measurements. In order to measure physical properties of materials in pulsed magnetic fields, we used several home-made measurement probes and glass dewers shown in Fig. 2.5(a).

We used several probes specialized for electrical transport, magnetization, and ultrasound measurements. Although the details of the probes depend on the purpose of the measurement, all of them basically satisfy the following essential requirements:

1. Capable of holding the sample in a cryostat andS at the center of the pulse magnet.

2. Possess several lead wires to transmit the electrical signal from and to the sample space.

3. Possess a thermometer to measure the temperature around the sample.

4. Possess a field pick-up coil to measure the magnetic field applied to the sample.

An example of the sample space on the tip of resistivity measurement probe is shown in Fig. 2.5(b). Since typical space in cryostats for pulse magnets is a cylinder with diameter of 10 mm, the measurement probe is made sufficiently thin and long to satisfy the requirement 1. Additionally, we have to exclude metallic components around the sample as possible to avoid heating by eddy current. We used non-metallic materials such as FRP as a body of the probe. In regards to requirement 2, we should pay attention to

eliminate looped paths in the electrical wiring. Otherwise, the signal from the sample can be hidden in significant induced voltage by pulsed fields. We used Cernox thermometers (CX-1030-BG-HT, Lake Shore Cryotronics, Inc.) to satisfy the requirement 3. In regards to requirement 4, we wound copper wire several times just below the sample space. The voltage induced between both ends of the pick-up coil (V_p) is proportional to the amount $NS \times dB/dt$. Here, N, B, and S represent the number of turns of the coil, magnetic flux density passing through the coil, and cross-section of the coil, respectively. In principle, we can calculate B from the time integration of V_p assuming N and S are known. However, S varies by thermal deformation at low temperature, which can cause a error determining B. Thus, we evaluate the actual S referring to physical phenomena at low temperature which occur at well-defined magnetic field value. We used the spin-flop transition in MnF_2 (9.24 T) or SdH oscillation of Kish graphite below 10 T (the last oscillation occurs at 7.40 T) to calibrate the pick-up coil.

The measurement probe is inserted into the dewer made of glass. The sample space is isolated from the air outside, as shown in Fig. 2.5(a). Thermal insulation layer of the dewer is evacuated by vacuum pump, which enables us to maintain low temperature with cryogen. For precise temperature control from 4.2 to 300 K, we used additional tubular heater with several turns of manganin wire, which covers just around the sample space of the probes. The current flowing through the manganin wire was controlled by temperature controller (Lake Shore Model 335 or Cryo-con Model 32) to maintain the desired temperature. The sample installed into the dewer is inserted into the magnet as shown in Fig. 2.5(c).

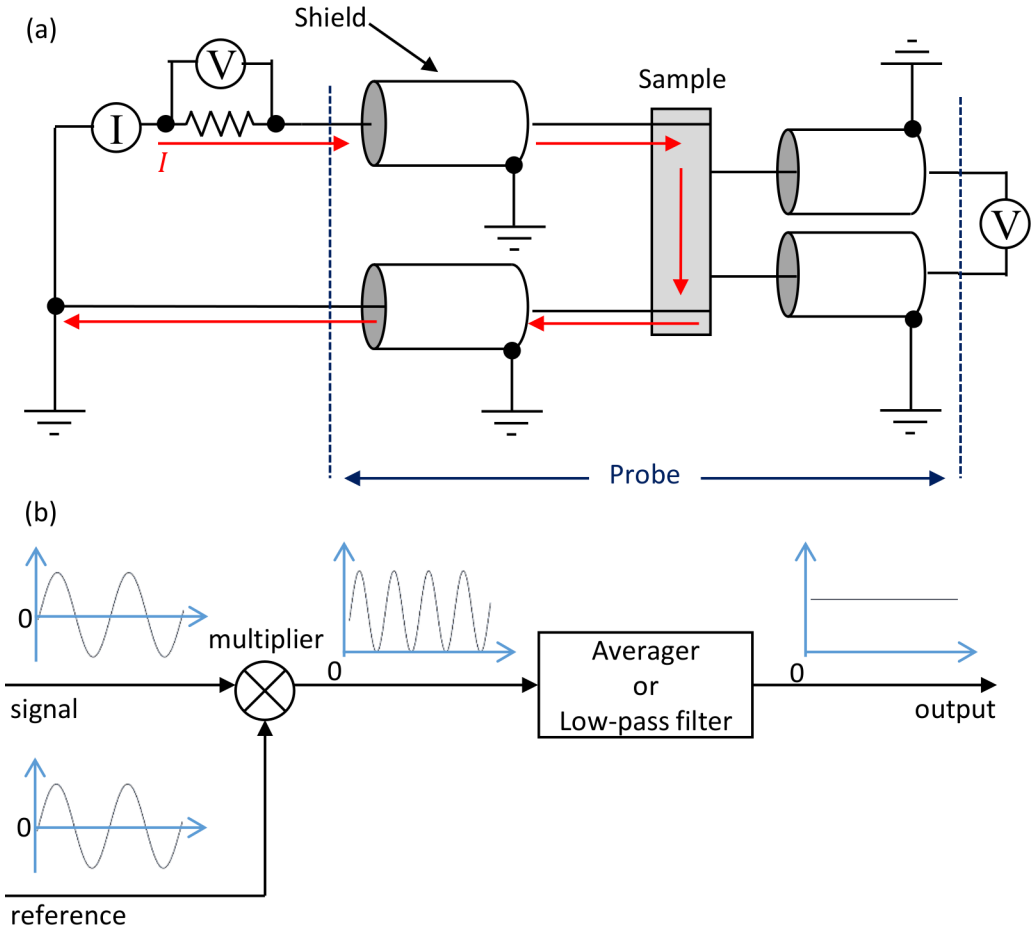

Figure 2.6: (a) Circuit diagram for four-terminal resistivity measurements. (b) Calculation flow diagram of numerical lock-in technique.

2.5 Resistivity Measurements in Pulsed Magnetic Fields

In this section, we mention how to measure the electrical transport properties under pulsed magnetic fields. Basically, we adopted four-terminal (for only ρ_{xx} measurement) or five-terminal (for simultaneous measurement of ρ_{xx} and ρ_{yx}) method in this study. The circuit diagram of the four-terminal resistivity measurement is shown in Fig. 2.6(a). The resistor put near the current source is used to monitor the current I passing through the curcuit, and is called shunt resistor. Shunt resistor can be abbreviated in case of constant-current measurement.

We chose either AC or DC current for the measurements considering the conditions of the measurement. Since the analysis of the DC measurement is quite straightforward, we do not explain the details here.

In AC measurements, we obtain the resistivity of the sample from the response to the AC current. We briefly explain the principle of the numerical analysis utilized in this study. We assume that the AC current $[I = I_0 \sin(2\pi f t)]$ with the frequency of $f = \omega/2\pi$ is injected to the sample, and the response obtained by an oscilloscope with the sampling rate of M_s is represented by

$$V[I, B(t_n)] = V_{\text{sample}}[I_0, B(t_n)] \sin(2\pi f t_n) + \alpha(t_n), \tag{2.28}$$

following Eq. (2.6). Here, $t_n = n/M_s$ with natural numbers n. $\alpha(t_n)$ in Eq. (2.28) represents the extrinsic contributions which do not depend on I, and is assumed to change sufficiently slower than the first term. In pulsed magnetic fields used in this study, which have typical time durations of ~ 40 ms, f should be taken sufficiently large (typically ~ 100 kHz) to obtain the precise field dependence. Also, M_s should be enough larger than f: in most measurements, we set $M_s = 5$ MHz. We multiply a referential wave $\sin(2\pi f t_n)$ by the right hand side of Eq. (2.28) on a computer, and then, we obtain $V_{\rm L}[I, B(t_n)]$ as

$$V_{\rm L}[I, B(t_n)] = \frac{V_{\rm sample}[I_0, B(t_n)]}{2} - \frac{V_{\rm sample}[I_0, B(t_n)]}{2}\cos(4\pi f t_n) + \alpha(t_n)\sin(2\pi f t_n). \tag{2.29}$$

To obtain the field dependence of the sample voltage $V_{\rm sample}[I_0, B(t_n)]$ we concern, there are two possible procedures. One is to apply a digital low-pass filter to attenuate the periodic terms of Eq. (2.29). In this method, however, we should pay attention not to attenuate intrinsic structures such as quantum oscillation with high frequency and so forth. Second is to sum $V_{\rm L}[I, B(t_n)]$ over the interval of $T = 1/f$. We can eliminate the periodic terms by summing over Eq. (2.29), and obtain the relationship

$$\sum_{n=1}^{N} V_{\rm L}[I, B(t_n)] = \sum_{n=1}^{N} \frac{V_{\rm sample}[I_0, B(t_n)]}{2}, \tag{2.30}$$

where $N = M_s/f$ represents the number of data point contained in T. Here, we assume that the magnetic field dependence of $V_{\rm sample}[I_0, B(t_n)]$ is ignorable within the time interval $T = 1/f$. Then, Eq. (2.30) is represented as

$$\sum_{n=1}^{N} V_{\rm L}[I, B(t_n)] = \frac{V_{\rm sample}[I_0]}{2} N, \tag{2.31}$$

and finally, we obtain the relationship

$$V_{\rm sample}[I_0] = 2\sum_{n=1}^{N} \frac{V_{\rm L}(t_n)}{N}. \tag{2.32}$$

We regard that $V_{\rm sample}[I_0]$ represented by Eq. (2.32) is the signal at the magnetic field value $\sum_{n=1}^{N} B(t_n)/N$, and thus, we obtain the field dependence of $V_{\rm sample}[I_0]$ by performing the summation represented by Eq. (2.32) over the whole measured time. We implemented above routines as a computer program written on Igor Pro (WaveMetrics, Inc.). The source code is shown in App. A.1, and the calculation flow diagram is given in Fig. 2.6(b). This principle is also commonly used in commercial lock-in amplifiers. Recent progress in digitizer enabled us to perform fast multi-channel analyses of the data in high dynamic range, which could not be done with using commercial products. Therefore, we utilized numerical lock-in analyses after recording all the oscillating voltage signals. Generally, AC measurement provides more accurate data than DC measurement does, since the random noise (such as Johnson noise or white noise) is attenuated by filtering or averaging in above processes. However, the accuracy of AC measurement can be impaired by unintentional contamination of stray capacitance or inductance, which causes delay or advance in phase of signals. When the phase difference between a sample and shunt resistor is too large, we utilize the standard DC measurement instead.

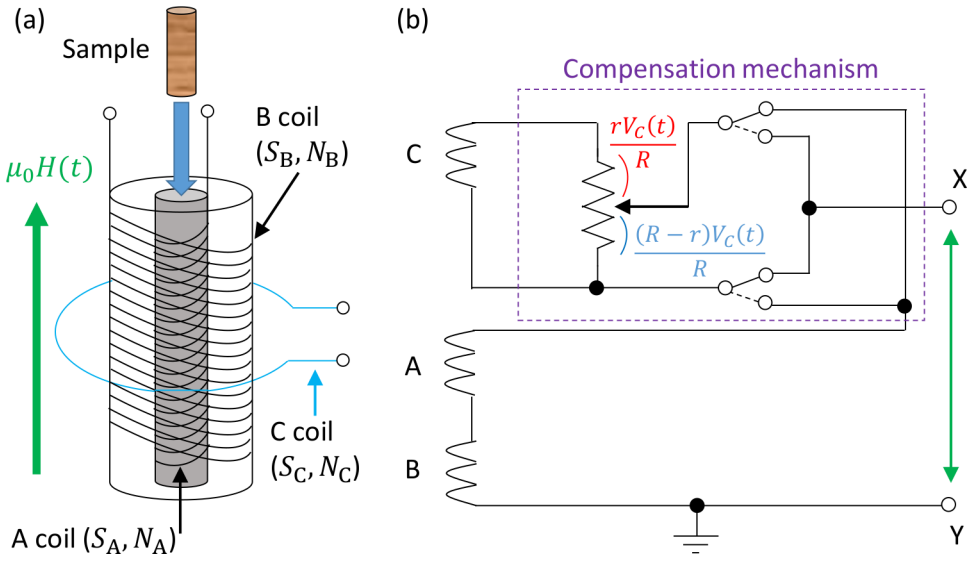

Figure 2.7: (a) Magnetization pick-up coil in pulsed magnetic field. (b) Circuit diagram for magnetization measurement.

2.6 Magnetization Measurements in Pulsed Magnetic Fields

In this section, we overview the magnetization measurement technique in pulsed magnetic fields. If the magnetization of a sample varies, the magnetic flux around the sample is also modified. Basically, we detect the time derivative of magnetic flux density $B(t)$ as an induced voltage in a pick-up coil with the number of turn N and cross-sectional area S as,

$$V(t) = -N\frac{d\Phi(t)}{dt} = -NS\frac{dB(t)}{dt}, \tag{2.33}$$

$$B(t) = \mu_0[H(t) + M(t)] \tag{2.34}$$

Here, $\Phi(t)$ is the magnetic flux which penetrates the coil, and $H(t)$ and $M(t)$ represent the magnetic field and magnetization, respectively. In high magnetic fields, $H(t)$ is much larger than $M(t)$. Therefore, it is important to accurately extract the signal of the sample from huge background.

We utilized a pair of coils (referred as A and B coils) which are turned in opposite direction with each other and typically 4 mm in length. They are connected in series and placed coaxially as shown in Fig. 2.7(a). Here, product of N and S of the both coils are set to be nearly the same, *i.e.*, $N_A S_A \sim N_B S_B$, where the number of turns and areas are $N_{A(B)}$ and $S_{A(B)}$ for A (B) coil, respectively. Therefore, spatially homogeneous contribution from $H(t)$ is cancelled out by two coils, while inhomogeneous contribution from $M(t)$ is selectively detected. We review the principle of measurement more in detail.

Firstly, we consider the situation that there is no sample in the coaxial coils, and the magnetic field $H(t)$ is applied parallel to the coil axis. Then, the voltage V_{AB} arose between the starting point of A coil and the ending point of B coil is represented as follows:

$$V_{\mathrm{AB}} = -\mu_0\frac{\mathrm{d}H(t)}{\mathrm{d}t}(N_{\mathrm{A}}S_{\mathrm{A}} - N_{\mathrm{B}}S_{\mathrm{B}}). \tag{2.35}$$

In the ideal condition, $N_A S_A = N_B S_B$, namely, $V_{AB} = 0$ is strictly fulfilled. However, even if we carefully prepare the coils to fulfill above condition at room temperature, it should be disturbed by a deformation of coils by lowering the temperature or slight non-uniformity of the magnetic field. In order to compensate above effects, we add another coils having the number of turn $N_C = 1$–3 and area of S_C [referred as C coil in Fig. 2.7(a)]. The both ends of C coil are connected to the variable resistor R as shown in Fig. 2.7(b): it divides the voltage $V_{\rm C}(t) = -\mu_0 S_{\rm C} N_{\rm C} {\rm d}H(t)/{\rm d}t$ generated by C coil into $(R-r)V_{\rm C}(t)/R$ and $rV_{\rm C}(t)/R$. Then, $\pm rV_{\rm C}(t)/R$ is added to V_{AB}. we adjust the variable resistor to satisfy the condition

$$-\mu_0 \frac{{\rm d}H(t)}{{\rm d}t}(N_{\rm A}S_{\rm A} - N_{\rm B}S_{\rm B}) \pm \mu_0 N_{\rm C} S_{\rm C} \frac{r}{R}\frac{{\rm d}H(t)}{{\rm d}t} = 0. \tag{2.36}$$

Here, the double sign in Eq. (2.36) is selectable by the switch in the compensation mechanism shown in Fig. 2.7(b).

We assume that a sufficiently long columnar sample with an area of S_p is inserted in the A coil and $H(t)$ is applied to them under the condition represented by Eq. (2.36). Then, the magnetic flux which penetrate A, B, and C coils [$\Phi_{A,B,C}(t)$] are represented as

$$\Phi_{\rm A,\,B,\,C}(t) = \mu_0 M(t) S_{\rm p} + \mu_0 H(t) S_{\rm A,\,B,\,C}. \tag{2.37}$$

Using Eq. (2.36), the voltage $V_{in}(t)$ which appears between X and Y in Fig. 2.7(b) is represented as

$$V_{\rm in}(t) = -N_{\rm A}\frac{{\rm d}\Phi_{\rm A}(t)}{{\rm d}t} + N_{\rm B}\frac{{\rm d}\Phi_{\rm B}(t)}{{\rm d}t} \pm N_{\rm C}\frac{r}{R}\frac{{\rm d}\Phi_{\rm C}(t)}{{\rm d}t} \tag{2.38}$$

$$= -\mu_0 S_{\rm p}\left(N_{\rm A} - N_{\rm B} \pm \frac{r}{R}N_{\rm C}\right)\frac{{\rm d}M(t)}{{\rm d}t}. \tag{2.39}$$

As we can see from Eq. (2.39), $V_{\rm in}(t)$ is proportional to ${\rm d}M(t)/{\rm d}t$ of the sample. In principle, we can obtain $M(t)$ by integrating Eq. (2.39) when Eq. (2.36) is strictly satisfied. Practically, however, there remains residual background which could not be eliminated with this procedures. Thus, we measure the background signal without the sample [V_{out}(t)], and obtain the final data $V_{in}(t) - V_{out}(t)$.

In addition, we also carry out a correction for sample length: above formulation is only true when the sample are sufficiently longer than the pick-up coils. The correction coefficient was determined by magnetization measurements of a set of standard samples, like Ni-powder, having different length.

2.7 Ultrasonic Measurements in Pulsed Magnetic Fields

In this section, we explain the method of ultrasonic measurements under pulsed magnetic fields. We utilized a common technique called pulse-echo method in this study. In this method, ultrasonic pulse is injected to a sample using a ultrasound transducer attached to a surface of the sample, and transmitted pulse is detected by another transducer attached to the confronted surface [Fig. 2.8(a)]. Drive pulse with a frequency of f = 10-100 MHz is used for ultrasound generation. The pulse are generated repeatedly with the typical repetition frequency of f_R = 50-100 kHz in order to obtain precise time (field) dependence within a duration time of pulsed magnetic fields. The number of cycles in a drive pulse is typically set to $N_c = 10$. We utilized piezoelectric $LiNbO_3$ single crystals with thickness of 0.1 mm as transducers. The direction of displacement can be controlled according to the orientation of the crystal. We used crystals with 36° Y-cut (41° X-cut) for longitudinal (transverse) oscillation. Gold is evaporated on the surface of the transducers as electrical input/output and ground terminals. The appearance of the transducers utilized in this study are shown in Fig. 2.8(b). The transducers are attached to the surface of the samples with either THIOKOL LP31, LP32, and LP33 (Toray Industries, Inc.), or one-component RTV rubber KE44 and KE45 (Shin-Etsu Chemical Co., Ltd.). An example of actual setting is shown in Fig. 2.8(c). Generated pulse repeats reflecting at the edge of the sample, and thus, a series of "echo" is observed at the receiving-side transducer. Hereafter, we call the echo which travels through the sample $(2n + 1)$ times as E_n, where $n = 0, 1, 2, \cdots$. For example, the echo which is generated on the transducer and arrived directly to the other transducer is called E_0. From the time interval T_i between the adjacent echos and known sample thickness L, we can evaluate the sound velocity of the sample as $v = 2L/T_i$. Also, it is known that the amplitude of the nth pulse A_n is represented as

$$A_n \propto \exp(-\beta t), \tag{2.40}$$

using the attenuation coefficient β per unit time. We can also express A_n with attenuation coefficient α per unit length as

$$A_n \propto \exp\left[-\alpha(2n+1)L\right]. \tag{2.41}$$

When v increases (decreases) with magnetic field, time interval between the adjacent echos decreases (increases), correspondingly. In addition, the envelope of the echo amplitude varies by the field dependence of ultrasonic attenuation. In order to evaluate these changes in pulsed magnetic fields, we utilized measurement apparatus developed in Yoshizawa-Nakanishi group (Iwate University), or new digital technique which is implemented as a computer program by the author. The details of the former technique are described in [57, 58]. In the latter technique, we record the whole echo spectrum during the pulse field generation (typically 50 ms), and then analyze the data on a computer. We can reanalyze the data at any time by saving raw data to a storage device. The simplified diagram of the latter system is shown in Fig. 2.9.

Here, we briefly review the principle of the analysis. We assume that E_n is represented by the following form:

$$E_n(t, \phi_n) = A_n \sin(2\pi f t - \phi_n). \tag{2.42}$$

Whereas, we need a reference wave $y_R(t, \Theta)$, which has the same frequency f with that of injected ultrasound:

$$y_R(t, \Theta) = \sin(2\pi f t - \Theta). \tag{2.43}$$

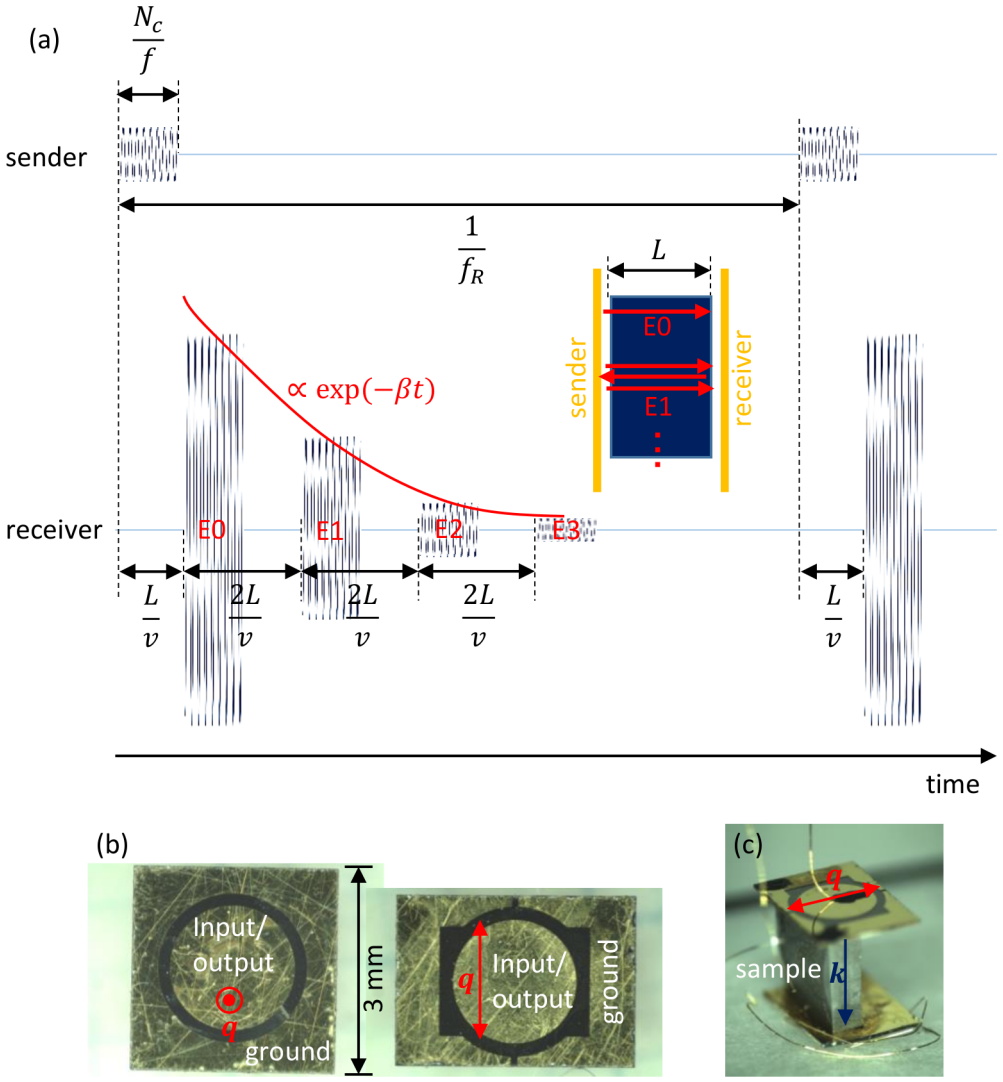

Figure 2.8: (a) Schematic diagram of the pulse-echo method. The upper trace represents the electrical signal applied to sender transducer, and the lower acquired electrical signal from receiver transducer. (b) Ultrasound transducer for longitudinal (left) and transverse (right) sound wave. $\boldsymbol{q}$ represents the direction of displacement. (c) An example of actual setting for ultrasonic measurement with transverse sound wave. $\boldsymbol{k}$ represents the direction of propagation of ultrasound wave.

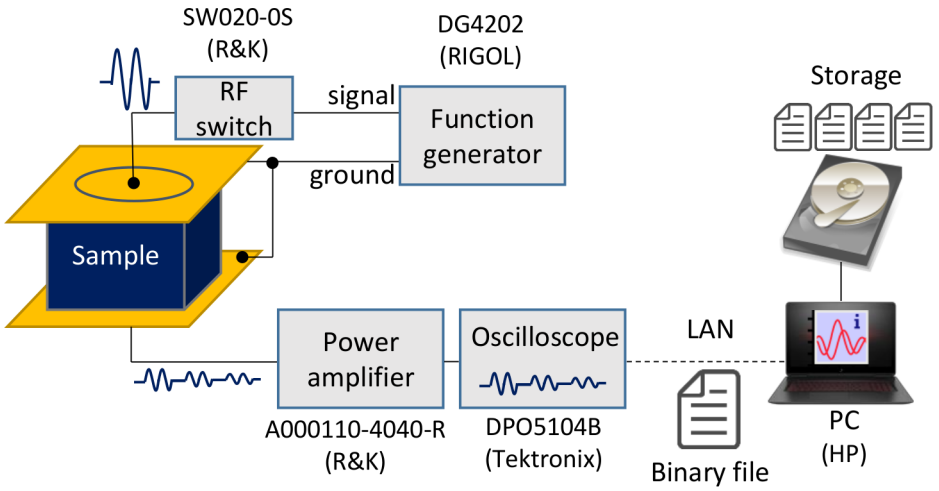

Figure 2.9: Schematic diagram of the digital technique for ultrasonic measurement in pulsed magnetic field.

For simplicity, we assume $\Theta = 0$ and focus on a relative phase shift against the reference. Firstly, we consider two quantities, $y_R(t,0)E_n(t,\phi_n)$ and $y_R(t,\pi/2)E_n(t,\phi_n)$: they are expressed as

$$y_R(t,0)E_n(t,\phi_n) = \frac{A_n}{2}\left[\cos(\phi_n) - \cos(4\pi f t - \phi_n)\right], \tag{2.44}$$

and

$$y_R(t,\pi/2)E_n(t,\phi_n) = \frac{A_n}{2}\left[\sin(\phi_n) - \cos(4\pi f t - \frac{\pi}{2} - \phi_n)\right]. \tag{2.45}$$

We can see that Eqs. (2.44) and (2.45) contain non-periodic and periodic terms. In order to extract the former terms which is directly connected with ϕ_n, a low-pass filter or boxcar averaging is applied. As a result, we obtain

$$y_R(t,0)E_n(t,\phi_n) \to \frac{A_n}{2}\cos(\phi_n) \equiv R \tag{2.46}$$

from Eq. (2.44), and

$$y_R(t,\pi/2)E_n(t,\phi_n) \to \frac{A_n}{2}\sin(\phi_n) \equiv I \tag{2.47}$$

from Eq. (2.45). Then, we can obtain the amplitude A_n and phase ϕ_n of E_n as

$$A_n = 2\sqrt{R^2 + I^2}, \tag{2.48}$$

$$\phi_n = \arctan(I/R). \tag{2.49}$$

Above procedures are summarized as a flow diagram shown in Fig. 2.10. In measurement apparatus developed in Yoshizawa-Nakanishi group, above procedures are functionalized by combinations of analog circuit elements. In new digital technique, they are all implemented as a computer program. In digital technique, the sampling rate of oscilloscope should be sufficiently larger than the frequency of ultrasound: we usually set it to ~ 1 GHz or more. Because the number of the total data point becomes enormous (roughly 1 GHz $\times$ 50 ms $= 5 \times 10^7$ points for one wave), it is practically important to deal with such big data without long processing time. To reduce the size of data and accelerate the data transfer, we treat acquired data in binary format, and directly transfer it

through the LAN cable. The data acquisition was mainly carried out with DPO5104B (Tektronix), and data acquisition was performed with Virtual Instrument Software Architecture (VISA). In addition, we improved the processing speed by employing parallel computing algorithms to the main calculation part. Typical processing time for raw echo trace having 6.5×10^7 data points is ~ 30 sec with Intel Core i7 7700HQ CPU (8 threads). We confirmed that the processing time with 8 threads can be approximately 1/4 compared to that with single thread. The program for the data acquisition and data analysis are shown in Apps. A.2 and A.3, respectively, which are written on IgorPro.

From A_n and ϕ_n, we can obtain the magnetic field dependence of the ultrasound attenuation coefficient and sound velocity.

Using Eq. (2.41), the ratio A_n/A_{n+1} is represented as

$$\frac{A_n}{A_{n+1}} = \exp(2\alpha L). \tag{2.50}$$

Thus, the attenuation coefficient per unit length is represented using A_n/A_{n+1} as

$$\alpha[\mathrm{dB/unit\,length}] = \frac{20}{2L} \log\left(\frac{A_n}{A_{n+1}}\right). \tag{2.51}$$

Here, if we assume [cm] as a unit of L, α has a unit of [dB/cm], correspondingly. In this study, we mainly focus on the magnetic field dependence of $\alpha(B)$ on the basis of that in zero-magnetic field $\alpha(0)$. We refer $d\alpha = \alpha(B) - \alpha(0)$ and define as

$$d\alpha = \frac{20}{(2n+1)L} \log\left(\frac{A_n(0)}{A_n(B)}\right). \tag{2.52}$$

Next, we consider the sound velocity. There exists following relationship between the sound velocity $v(B)$, ultrasonic frequency f, and the time interval $T(B)$ between E_n and E_{n+1}:

$$v(B) = \frac{2L}{T(B)}, \tag{2.53}$$

$$T(B) = T(0) + dT(B), \tag{2.54}$$

$$dT(B) = \frac{1}{f}\frac{\phi_{n+1}(B) - \phi_n(B)}{2\pi}. \tag{2.55}$$

In this formulation, $dT < 0$ in case $v(B)$ increases. If we assume the field dependence of L (magnetostriction) is sufficiently small, then, the change of the sound velocity from zero-magnetic field $dv = v(B) - v(0)$ is given by taking total derivative of Eq. (2.53):

$$dv = -v(0)\frac{dT}{T(0)} \tag{2.56}$$

$$= -v(0)\frac{\phi_{n+1}(B) - \phi_n(B)}{2\pi f T(0)}. \tag{2.57}$$

Therefore, the ratio $dv/v(0)$ is represented as

$$\frac{dv}{v(0)} = -\frac{\phi_{n+1}(B) - \phi_n(B)}{2\pi f T(0)}, \tag{2.58}$$

which means that $dv/v(0)$ is proportional to the phase difference between the adjacent echos. Here, we use the relationship about $\phi_n(B)$,

$$\phi_n(B) = (2n+1)\phi_0(B), \tag{2.59}$$

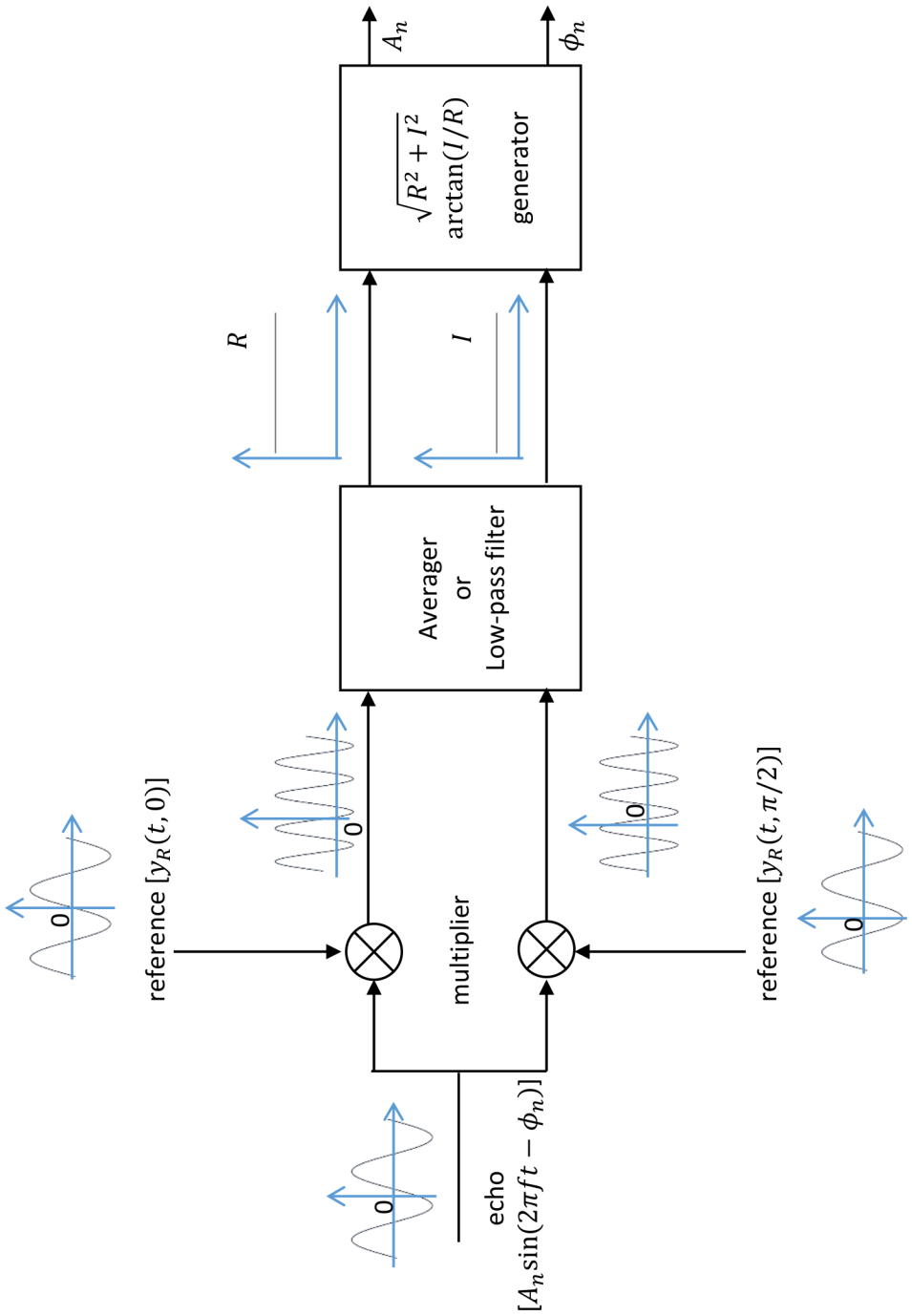

Figure 2.10: Calculation flow diagram of the ultrasonic measurements.

and simplify Eq. (2.58) as

$$\frac{dv}{v(0)} = -\frac{\phi_n(B)}{(2n+1)\pi f T(0)}. \tag{2.60}$$

From Eq. (2.60), we can see that $dv/v(0)$ is represented only with $\phi_n(B)$.

We can also convert $dv/v(0)$ into the field dependence of the elastic constant $dC/C(0)$. The elastic constant $C(B)$ is represented using $v(B)$ and density of the sample ρ as

$$C(B) = \rho v^2(B). \tag{2.61}$$

Taking the total derivative of Eq. (2.61), we can obtain the similar relationship with Eq. (2.57) as

$$dC = 2\rho v(0) dv \tag{2.62}$$

$$= -2\rho v^2(0) \frac{\phi_{n+1}(B) - \phi_n(B)}{2\pi f T(0)}. \tag{2.63}$$

Therefore, the ratio $dC/C(0)$ is represented by

$$\frac{dC}{C(0)} = -2 \times \frac{\phi_{n+1}(B) - \phi_n(B)}{2\pi f T(0)} \tag{2.64}$$

$$= -2\frac{dv}{v(0)}. \tag{2.65}$$

sample name	synthesis method	n (10^{18}cm^{-3})	μ (10^4 cm^{2}V^{-1}s^{-1})
PbTe (#T)	vapor transport	3.7 (hole)	37
PbTe (#S)	Bridgmann	0.99 (hole)	28
$Pb_{0.7}Sn_{0.3}Te$ (#T30)	vapor transport	51 (hole)	0.095

Table 2.3: Physical properties of PbTe and $Pb_{0.7}Sn_{0.3}Te$ samples. n and μ represent the carrier density and mobility, respectively.

2.8 Samples

2.8.1 Black Phosphorus

Single crystals of black phosphorus sample were synthesized under high pressure and temperature, and supplied by Prof. Y. Akahama (University of Hyogo). The synthesis method is basically the same with that mentioned in [59]. Appearance of the single crystal utilized in this study is shown in Fig. 2.11(a), and all measured samples were cut from this crystals. Clear Laue spots were observed as shown in Fig. 2.11(b), which assure the high quality of the sample. Figure. 2.11(c) shows simulated Laue spots assuming the orthorhombic $Cmca$ space group, which show good agreement with the observed pattern. The simulation of the Laue patterns was performed using QLaue.

2.8.2 PbTe and $Pb_{1-x}Sn_xTe$

Single crystals of PbTe were synthesized by the vapor transport (referred as #T) or Bridgmann method (referred as #S) by Prof. H. Sakai, Mr. K. Katayama, Mr. T. Sakamoto, Prof. N. Hanasaki, and Prof. S. Takaoka (Osaka University). Appearances of #T and #S samples are shown in Figs. 2.11(d) and (e), respectively. Figure 2.11(f) shows the Laue pattern of #T sample, which is well reproduced by simulated pattern shown in Fig. 2.11(g) assuming the cubic $Fm\bar{3}m$ structure. We also confirm clear Laue patterns and correspondence with the simulation in regards to #S sample. Both samples are easily cleaved along the cubic crystal axis, and showed linear and positive ρ_{yx}, which indicate that only single hole carrier contributes the physical properties. The typical carrier densities and mobilities of the samples determined by the Hall resistivity measurements at 2 K are summarized in Table 2.3. The carrier density of #T sample are approximately 3.8 times larger than that of #S sample, while the mobilities were not so different with each other.

Single crystal $Pb_{0.7}Sn_{0.3}Te$ (#T30) were synthesized by the vapor transport method. The composition is determined by energy dispersive X-ray spectroscopy (EDX) measurements. The observed Laue pattern was reproduced assuming $Fm\bar{3}m$ structure. The carrier density and mobility determined by the Hall resistivity measurements are listed in Table 2.3. #T30 also showed linear and positive ρ_{yx}, and thus, the conduction carrier is assumed to be a single kind of hole. The carrier density is more than 10 times higher, and the mobility is much lower than that in pristine PbTe.

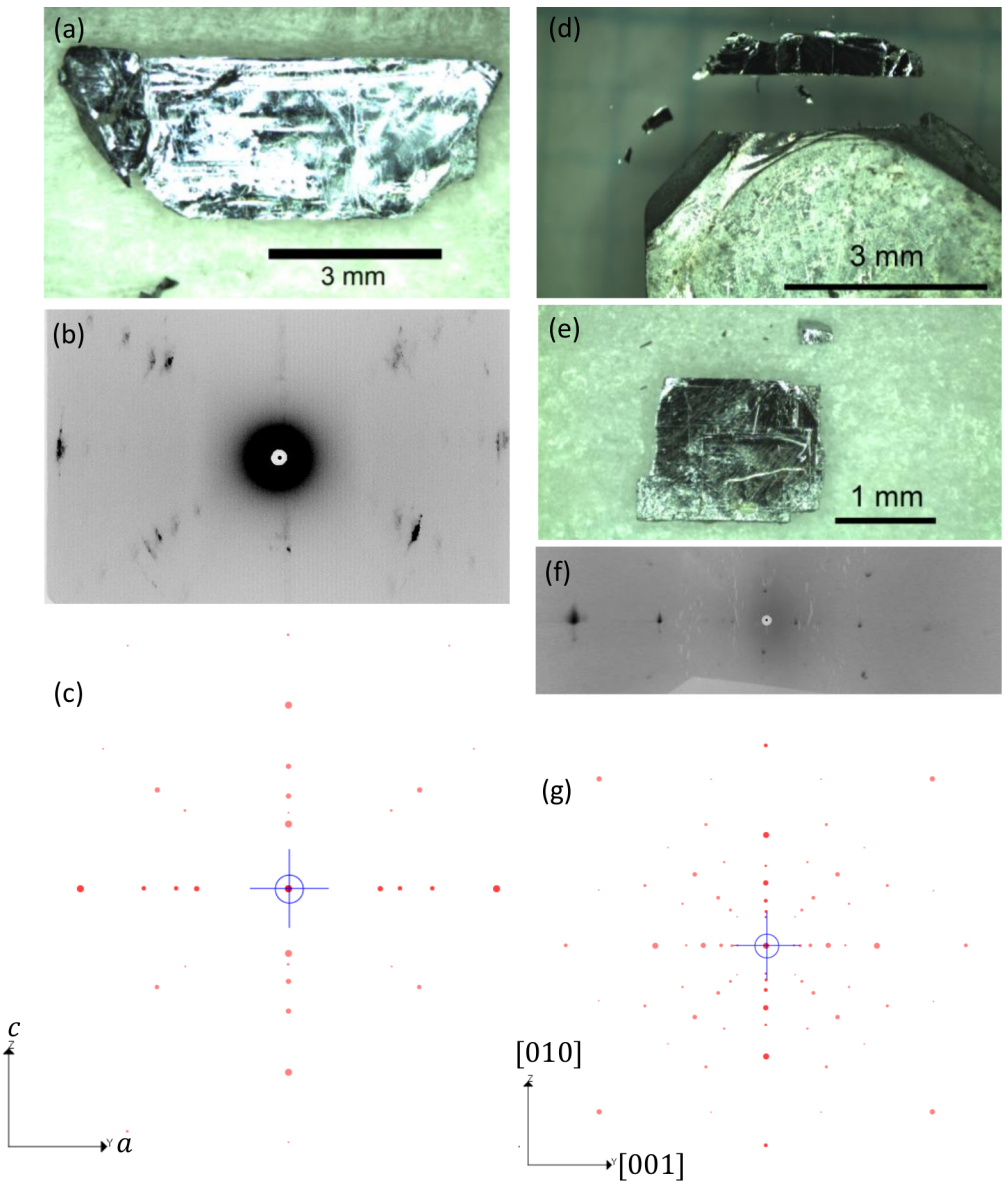

Figure 2.11: (a) Single crystal of black phosphorus. (b) Laue diffraction pattern of black phosphorus sample. (c) Simulated Laue pattern assuming $Cmca$ space group. (d) Single crystal PbTe (#T). (e) Single crystal PbTe (#S). (f) Laue diffraction pattern of #T sample. (g) Simulated Laue pattern assuming $Fm\bar{3}m$ space group.

Chapter 3

Black Phosphorus

3.1 Basic Properties of Black Phosphorus

Phosphorus is known to form various allotropes at ambient condition. Black phosphorus (BP), one of the targets in this study, is the most stable allotropes among them, and is known as an elemental narrow-gap semiconductor with a characteristic layered structure. Since the first discovery of BP by P. W. Bridgmann under high pressure and high temperature condition in 1914 [60], it has attracted many researcher's attention not only for its bulk properties as a semiconductor with high mobility, but also for recent application as a thin film device. In this section, we review the previous studies of BP and clarify the purpose of this study.

3.1.1 Crystal Structure

At first, we review the crystal structure of BP. The crystal structure is shown in Fig. 3.1(a), which belongs to an orthorhombic crystal system with a space group of $Cmca$ [61, 62]. BP consists of characteristic puckered honeycomb layers, in which phosphorus atoms are covalently bonded to zigzag and armchair chains along the a- and c-axes, respectively [Fig. 3.1(b)]. The monolayer is called "phosphorene" and recently shed light because of the application to a thin film device owing to its high mobility and appropriate band gap [63]. In bulk BP, these layers are alternatively stacked along the b-axis like Bernal graphite, which is commonly referred to as AB stacking. In contrast with the firm covalent bonds in the ac plane, the interlayer coupling along the b-axis is weak van der Waals interaction. The lattice constants determined by the X-ray diffraction study

parameter	value (unit)
a	3.3136 (Å)
b	10.478 (Å)
c	4.3763 (Å)
d_1	2.224 (Å)
d_2	2.244 (Å)
α_1	96.34 (°)
α_2	102.09 (°)

Table 3.1: Structural parameters of BP. a, b, and c represent the lattice constants. The definitions of $d_{1,2}$ and $\alpha_{1,2}$ are shown in Fig. 3.1(b). The values are taken from [61].

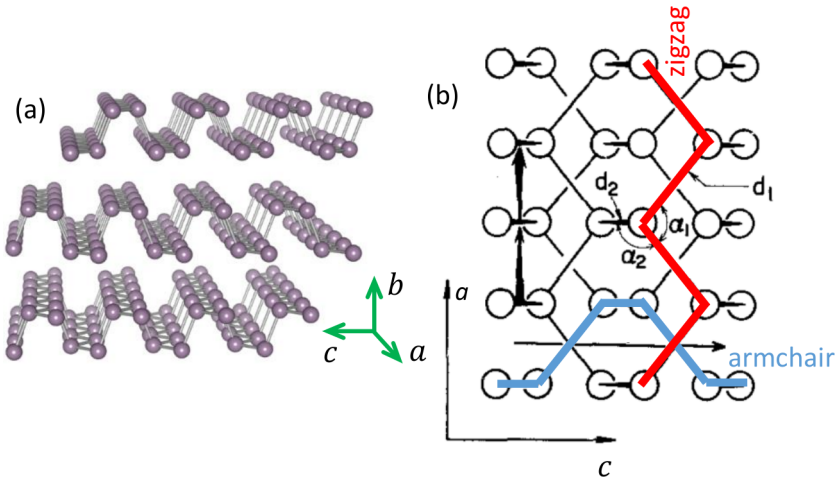

Figure 3.1: (a) Crystal structure of bulk BP and corresponding crystal axes. (b) Schematic view of the in-plane crystal structure. [64]. The values of $d_{1,2}$ and $\alpha_{1,2}$ are listed in Table 3.1.

on single crystalline BP [61] are listed in Table 3.1. Here, the lengths d_1 and d_2 are the nearest and next nearest neighbor distances, respectively, and α_1 and α_2 are bond angles shown in Fig. 3.1(b).

3.1.2 Energy Band Structure

Next, we review the energy band structure of BP at ambient pressure. Before we enter the details of band structure of bulk, we firstly focus on phosphorene constructing BP. Since the primitive cell of the monolayer phosphorene has four P atoms, there are twenty valence electrons contributing the physical properties. They occupy the lowest ten energy bands, and the residual bands remain fully empty: thus, monolayer phosphorene is a semiconductor. Figure 3.2(a) shows the energy band structure of monolayer phosphorene calculated by the Linear Combinations of Atomic Orbitals (LCAO) method, in which a direct gap of ∼2 eV opens at the Γ point in two-dimensional Brillouin zone illustrated in Fig. 3.2(d) [65]. As is clear at the X point, the energy bands are divided into eight pairs. The two pairs with the lowest energy, the next three pairs below the energy gap, and the rest three pairs above the energy gap can be roughly regarded as $3s$, $3p$ bonding, and $3p$ anti-bonding orbitals, respectively.

The band gap is known to decrease taking interlayer hopping of the carriers into consideration by stacking these layers. Figure 3.2(b) and (c) show the energy band structure of bilayer and five-layer phosphoren calculated by LCAO method [65], which clearly depicts the reduction of the band gap at the Γ point with increasing number of layers. Note that, in multilayer case, band structures are projected on a two-dimensional Brillouin zone showin in Fig. 3.2(d). The reduction of the band gap has been experimentally confirmed by optical reflection measurements on few-layer phosphorene [66]. As a result of infinite stacking, bulk BP has a narrow direct band gap of ∼0.3 eV at the Z point in the three-dimensional Brillouin zone [Fig. 3.2(e) and (f)]. A remarkable point on the band structure of bulk BP is that the dispersion along the Γ-Z line is relatively steeper than those along the other directions. In a previous study, this point has been qualitatively explained by taking the orbital characters of wave functions in valence and conduction bands into account [67]. This brings an unique character to the

physical properties of bulk BP that the effective mass, which is roughly proportional to the reciprocal of curvature of the energy dispersion, is relatively light even along the interlayer direction. Takao *et al.* [67] and Asahina *et al.* [68] calculated the effective mass of electron and hole, and predicted large anisotropy and unconventionally light effective mass along the interlayer direction. This has been experimentally confirmed, which will be reviewed later with the previous results of cyclotron resonance experiments. Note that in graphite, which is also a layered material, the effective mass along the interlayer direction is approximately 200 times larger than that within a layer [3].

3.1.3 Physical Properties at Ambient Pressure

Experimental progress on BP has been made with improvements of synthesis technique. In the early stage of study (1950–60s), Keyes [69] and Warschauer [70] reported the electrical transport properties of p-type polycrystalline BP synthesized under high pressure (1.1–1.4 GPa) and high temperature (200–260 °C). They assumed that the resistivity ρ has Arrhenius-type temperature dependence above room temperature as

$$\rho = \rho_0 \exp\left(\frac{\Delta_g}{2k_B T}\right), \tag{3.1}$$

and estimated the intrinsic band gap at ∼0.35 eV. Here, ρ_0, Δ_g, k_B, and T represent a constant, intrinsic band gap, Boltzmann constant, and temperature, respectively.

On the other hand, it has also been known that needle-like small single crystals can be obtained from a solution of white phosphorus in liquid bismuth [61]. Maruyama *et al.* synthesized single crystals of BP with typical dimensions of $5 \times 0.1 \times 0.07$ mm^3 (needle direction corresponds to the a-axis) by the bismuth flux method, and measured transport and optical properties [71]. They reported that the intrinsic band gap is estimated to be 0.31 eV from the temperature dependence of the resistivity, which is consistent with the studies on polycrystalline BP mentioned above and calculations by Takao *et al.* [67] and Asahina *et al* [68].

In 1980s, Shirotani *et al.* [72] and Endo *et al.* [59] succeeded in the synthesis of large single crystals of BP under pressure with refined high pressure apparatuses, which enabled precise and various investigations in BP.

Akahama *et al.* investigated detailed transport properties using undoped p- and Te-doped n-type large single crystals synthesized under pressure [73]. Since our study focus on the undoped BP, here we mainly review the transport properties of undoped p-type samples. Figure 3.3(a) shows the resistivities along the three principal axes as a function of inverse temperature. Apparent anisotropy of resistivity was observed at room temperature: the resistivities along the a- and b- axes are higher than that along the c-axis. The increase of resistivities with decreasing temperature observed above 100 K is due to the reduction of thermally excited carriers *via* the intrinsic band gap, which is well explained by Eq. (3.1). The band gap of 0.335 eV reported in their study is similar to the previous reports mentioned above. We can also recognize that the resistivities rapidly increases below 20 K in Fig. 3.3(a), which is ascribed to the reduction of thermally excited carriers *via* the impurity gap.

In their study, the hole density and mobility were evaluated based on simple single-

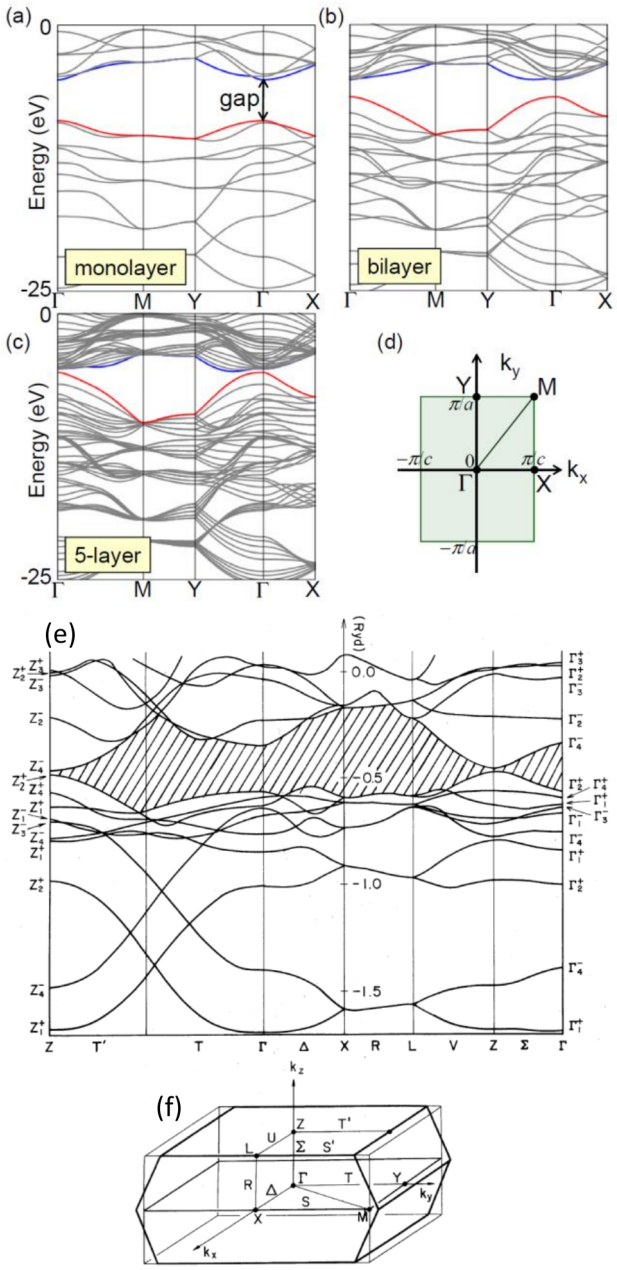

Figure 3.2: Energy band structure of (a) monolayer, (b) bilayer, and (c) five-layer phosphorene obtained by LCAO method [65]. (d) Two-dimensional Brillouin zone of monolayer phosphorene [65]. (e) Energy band structure of bulk BP obtained by the tight binding method [67]. (f) Three-dimensional Brillouin zone of bulk BP [67].

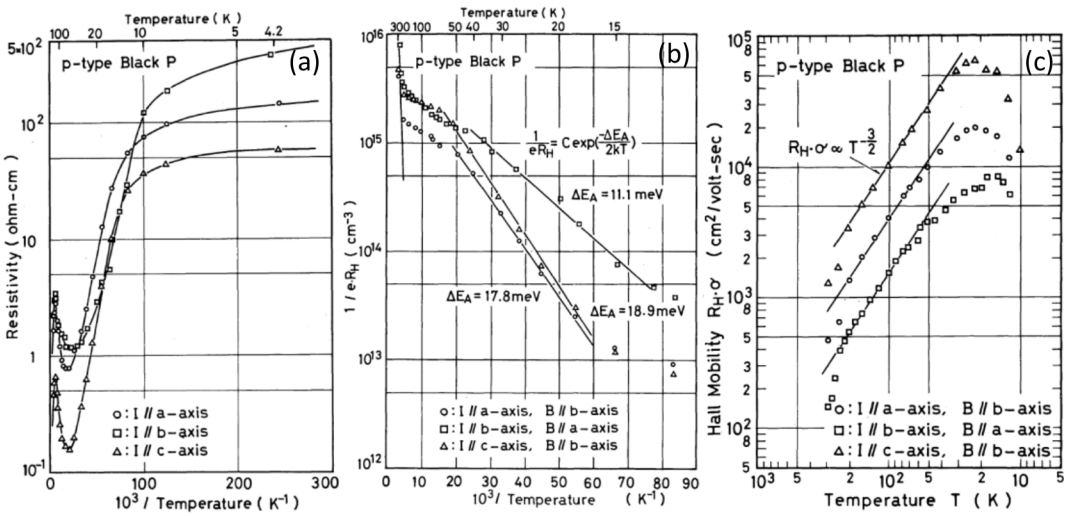

Figure 3.3: (a) Resistivities along the three crystal axes as a function of inversed temperature [73]. (b) $1/(eR_H)$ and (c) $R_H\sigma$ of p-type BP single crystal estimated by single-carrier model [73]. See text for detailed explanations.

carrier model in the intermediate temperature range:

$$R_H = \frac{\gamma}{ep}, \tag{3.2}$$

$$\sigma = \frac{1}{\rho} = ep\mu_h, \tag{3.3}$$

$$\frac{1}{eR_H} = \frac{p}{\gamma}, \tag{3.4}$$

$$R_H\sigma = \gamma\mu_h, \tag{3.5}$$

where μ_h and p are hole drift mobility and density, respectively. γ is a constant and taken to $3\pi/8$ assuming that acoustic phonons dominantly contribute to the carrier scattering. As Eqs. (3.4) and (3.5) represent, $1/(eR_H)$ and $R_H\sigma$ are proportional to the hole density and mobility, respectively. Figure 3.3(b) shows the temperature dependence of $1/(eR_H)$ as a function of temperature. The hole density was estimated to 2–5 $\times$ 10^{15} cm^{-3} just below room temperature, where the temperature dependence of $1/(eR_H)$ becomes weak. From the slopes of temperature dependence shown in Fig. 3.3(b), the impurity gap was estimated to 11–19 meV. Figure 3.3(c) shows the temperature dependence of $R_H\sigma$ as a function of temperature. From 200 to 50 K, $R_H\sigma$ obeys $T^{-3/2}$ law, which indicates the dominance of the acoustic phonon scattering in this temperature range [74]. At low temperature below 15 K, $R_H\sigma$ turns to decrease, which is attributed to an effect of impurity scattering. The maximum of $R_H\sigma$ for current direction along the c-axis is the highest, which reaches 6.5 $\times$ 10^4 cm^{2}V^{-1}s^{-1} at $\sim$20 K, as shown in Fig. 3.3(b). The results obtained by Akahama *et al.* are summarized in Table 3.2 including the results on n-type BP. Above results certified the low-carrier density and high-mobility natures of carriers in semiconducting BP.

Successful synthesis of large single crystals also enables us to perform precise optical measurements. Narita *et al.* [75] and Takeyama *et al.* [76] investigated the cyclotron resonance of single crystalline BP, and experimentally determined the effective masses along the three principal axes. The cyclotron masses in a magnetic field parallel to the a-

	p-type			n-type		
crystal axis	a	b	c	a	b	c
$R_H\sigma$ at 200 K ($\mathrm{cm^2V^{-1}s^{-1}}$)	1300	540	3300	460	400	2300
maximum of $R_H\sigma$ ($\times 10^3$ $\mathrm{cm^2V^{-1}s^{-1}}$)	20	8.5	65	2.2	1.0	16
activation energy of impurity level	$\sim$18 meV			$\sim$39 meV		
carrier concentration	2–5$\times 10^{15}$ $\mathrm{cm^{-3}}$			2–3$\times 10^{16}$ $\mathrm{cm^{-3}}$		

Table 3.2: Physical quantities estimated from the transport measurements on p- and n-type BP [73]. Hall mobility $R_H\sigma$ at 200 K and their maxima are separately shown along the three principal axes.

	cyclotron masses					
	hole			electron		
	m_a^*/m_0	m_b^*/m_0	m_c^*/m_0	m_a^*/m_0	m_b^*/m_0	m_c^*/m_0
Exp. [75] (at 20 K)	0.146	0.222	0.427	0.103	0.291	0.362
Exp. [76] (at 30 K)	0.166	0.238	0.436	0.120	0.330	0.380
	effective masses					
	hole			electron		
	m_a/m_0	m_b/m_0	m_c/m_0	m_a/m_0	m_b/m_0	m_c/m_0
Exp. [75] (at 20 K)	0.648	0.280	0.076	1.03	0.128	0.083
Exp. [76] (at 30 K)	0.625	0.304	0.091	1.14	0.127	0.096
Calc. [68]	0.81	0.36	0.09	1.16	0.17	0.09

Table 3.3: Cyclotron masses in magnetic fields applied along the a, b, and c axes ($m^*_{a,b,c}$) and effective masses along the a, b, and c axes ($m_{a,b,c}$). Experimental values are taken from [75] and [76], and calculation from [68].

(m_a^*), b- (m_b^*), and c- (m_c^*) plane are represented as geometrical averages: $m_a^* = \sqrt{m_b m_c}$, $m_b^* = \sqrt{m_c m_a}$, and $m_c^* = \sqrt{m_a m_b}$. Here, $m_{a,b,c}$ represent the effective masses along the three crystal axes. Therefore, $m_{a,b,c}$ are calculated as $m_a = m_b^* m_c^*/m_a^*$, $m_b = m_c^* m_a^*/m_b^*$, and $m_c = m_a^* m_b^*/m_c^*$. Narita *et al.* investigated the cyclotron resonance in both p- and n-type samples and reported only single resonance peak for each type. Whereas, Takeyama *et al.* reported different results on p-type BP. They observed basically single resonance peak (CR1) in most of the samples, while some samples show additional resonance peak (CR2). They found that the effective masses determined from CR1 and CR2 correspond to that of hole and electron determined by Narita *et al.*, respectively, which suggests the coexistence of electrons and holes in a sample. Since CR2 peaks often disappeared by partially masking the surface of the samples, they regarded that small n-type regions can mix in a p-type sample in the synthesis processes. The results of their studies are summarized in Table 3.3. Although BP has a layered structure along the b-axis, m_b is not the heaviest but m_a for both carrier types, as mentioned in Sec. 3.1.2. Table 3.3 also shows good correspondence between experiments and theoretical calculation by Asahina *et al* [68].

Phonon structure has been also investigated both experimentally and theoretically. Group theoretically, the orthorhombic structure has 12 phonon modes at the Γ point, $2A_g + B_{1g} + B_{2g} + 2B_{3g} + A_u + 2B_{1u} + 2B_{2u} + B_{3u}$ [77, 78]. The first 6 modes ($2A_g$, B_{1g}, B_{2g}, and $2B_{3g}$) are Raman active, and 2 modes (one of the B_{1u} and one of the B_{2u}) are infrared active ones. The rest modes are optically inactive ones. Sugai *et al.*

		phonon frequency at the Γ point (cm^{-1})	
		Exp.	Calc.
mode	type	Sugai *et al.* [78]	Kaneta *et al.* [80]
A_g^1	R	365	356
A_g^2	R	470	480
B_{1g}	R	197	194
B_{2g}	R	442	439
B_{3g}^1	R	233	228
B_{3g}^2	R	440	439
B_{1u} (T)	IR	136	129
B_{1u} (L)	IR	138	135
B_{2u} (T)	IR	468	461
B_{2u} (L)	IR	470	462

Table 3.4: Comparison between experimental and theoretical frequencies of optical phonons at the Γ point. "R" and "IR" in "type" column represent Raman active and infrared active, respectively.

performed Raman scattering and infrared reflection spectroscopy at room temperature, and reported the observation of 6 Raman active modes and 2 infrared active modes with transverse (T) and longitudinal (L) splitting [78]. Theoretically, Kaneta *et al.* calculated the lattice dynamics of BP using valence force field model (VFFM) [79] and adiabatic bond charge model (BCM) [80]. They found that BCM can successfully reproduces the experimental results including infrared active modes which could not be explained by VFFM. Identified optical phonon frequencies at Γ point are listed in Table 3.4, which shows good correspondence between the experiment and calculation.

3.1.4 Physical Properties under Pressure

Next, we focus on the pressure effects on the physical properties of BP. BP is known to transform into various structures under pressure. The pressure-temperature phase diagram is summarized in Fig. 3.4(a). The first structural transition from orthorhombic to rhombohedral ($A7$) structure takes place at ∼5 GPa [81]. The $A7$ structure is known as ambient structures of Bi, Sb, and As [82], which is the same family elements with P in the periodic table. Thus, $A7$ phosphorus is considered to be a semimetal. Then, $A7$ structure undergoes a transition to a metallic simple cubic (SC) structure at ∼10 GPa [81]. SC phase is known to be stable up to ∼100 GPa [83]. The SC phase shows superconductivity at low temperature. The pressure dependence of superconducting transition temperature has been investigated [84].

The detailed pressure dependence of the lattice constants has been investigated by Cartz *et al.* by neutron diffraction [85] and Kikegawa *et al.* by X-ray diffraction [86]. The both studies report that the lattice constants b and c decrease with almost the same degree as pressure increases, while a is almost independent of the applied pressure, at least up to 3 GPa [Fig. 3.4(b)]. These results indicate that there exists a large compressive anisotropy between armchair and zigzag directions in a layer. The average linear compressibilities along the three principal axes are estimated as $K_a = 0.7 \times 10^{-4}$, $K_b = 119 \times 10^{-4}$, and $K_c = 124 \times 10^{-4}$ GPa^{-1} in [85].

The pressure dependence of the intrinsic band gap has been discussed by several

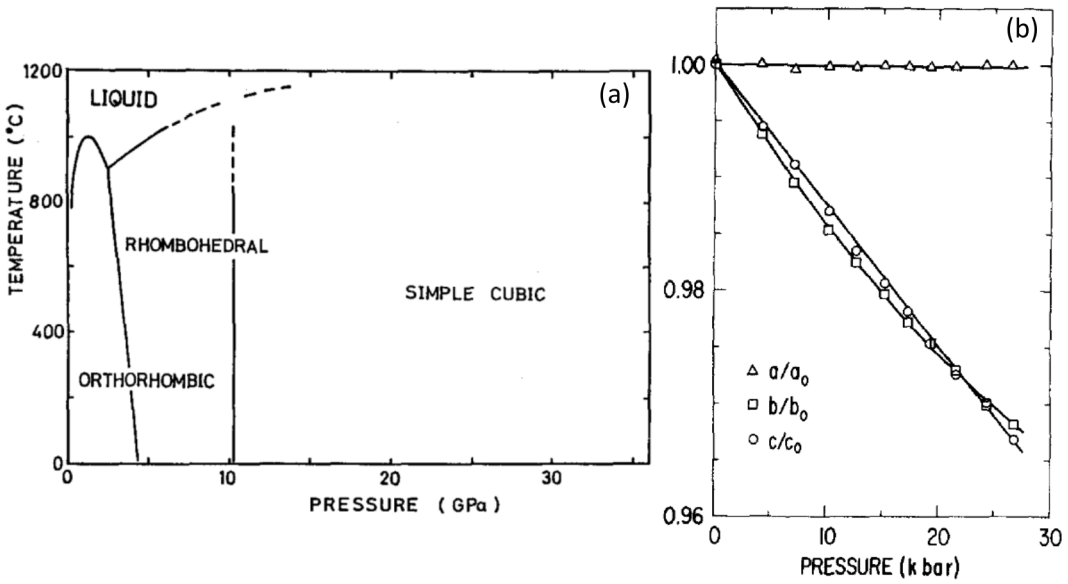

Figure 3.4: (a) Temperature-pressure phase diagram of BP [64]. (b) Pressure dependence of the lattice constants [85].

reports. Earlier, Keyes reported the pressure dependence of the resistivity up to 0.8 GPa and pointed out that the band gap decreases by applying pressure [69]. He commented on a possible band overlapping above 2 GPa by simply extrapolating pressure dependence of the band gap to higher pressure.

Okajima *et al.* also reported the pressure dependence of resistivity under pressure up to 15 GPa [87], which is higher than that in Keyes *et al.* Two resistivity anomalies were observed at ∼4.2 and 10.8 GPa in their measurement, which are ascribed to correspond to the structural phase transitions from orthorhombic to $A7$ phase and $A7$ to SC phase, respectively. Further, they estimated the pressure dependence of the intrinsic band gap assuming the Arrhenius-type thermal excitation, and pointed out that the band gap remained finite at around 2 GPa at which Keyes *et al.* assumed to occur band overlapping, and band gap became zero at around 4 GPa [Fig. 3.5(a)], at which resistivity anomaly corresponding to $A7$ to SC phase transition observed.

On the other hand, Akahama *et al.* reported the temperature dependence of the resistivity at various pressures and estimated pressure dependence of the intrinsic band gap, as shown in Fig. 3.5(b) and (c) [88]. Unlike the results of Okajima *et al.*, the band gap decreases proportional to the applied pressure, and becomes zero at around 1.7 GPa, which supports Keyes's suggestion. This indicates that the semiconductor-metal transition takes place without structural phase transition in the orthorhombic phase. Akahama *et al.* later investigated the pressure dependence of optical properties by infrared absorption, and obtained identical pressure dependence of the band gap [89].

In addition, the pressure dependence of the phonon frequencies has been reported by Sugai *et al.* on needle-like samples [77], and Vanderborgh *et al.* on polycrystalline samples [90]. Both groups reported the pressure dependence of the phonon frequencies for A_g^1, B_{2g}, and A_g^2 modes in the orthorhombic phase. In their results, energies of B_{2g}, and A_g^2 branches are almost independent of the applied pressure, while energy of A_g^1 branch showed tendency of gradual increase as pressure increases (Fig. 3.6).

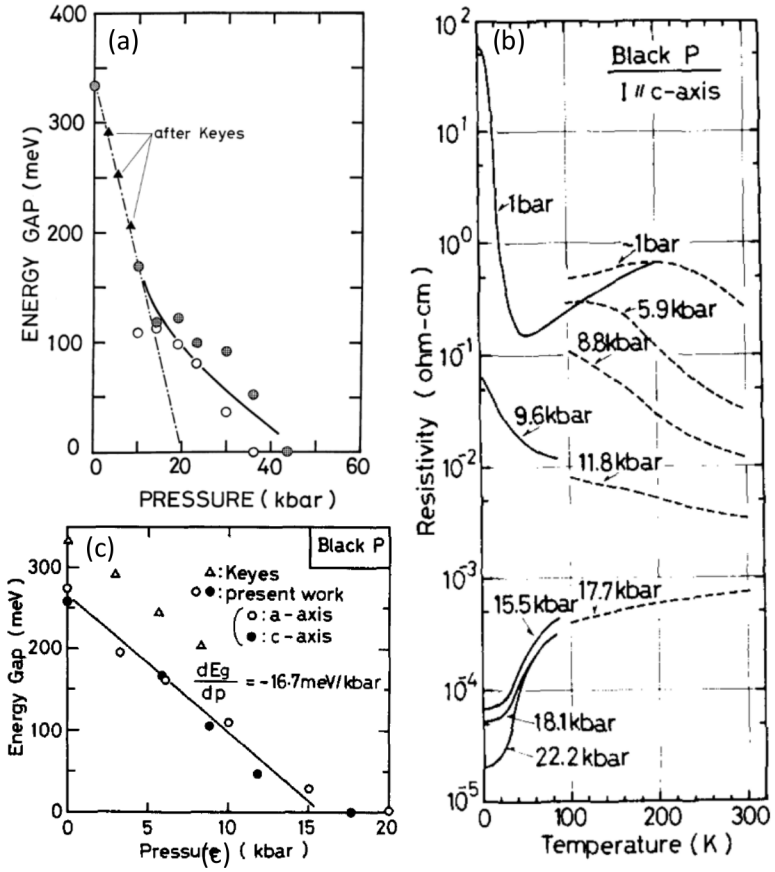

Figure 3.5: (a) Pressure dependence of the intrinsic band gap estimated from the temperature dependence of the resistivity by Okajima *et al* [87]. (b) Temperature dependence of the resistivity at various pressures reported by Akahama *et al* [88]. (c) Pressure dependence of the intrinsic band gap estimated from the temperature dependence of the resistivity by Akahama *et al* [88].

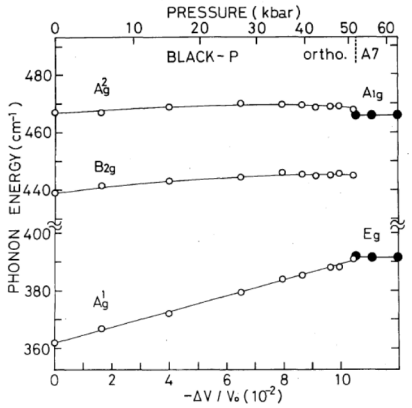

Figure 3.6: Pressure dependence of the optical phonon frequencies [77].

3.2 Purpose of the Study

The various properties including the transport, optical, and phonon properties have been investigated at ambient pressure, as mentioned in the previous section. In regards to the physical properties under pressure, however, there is relatively few available information about the electronic states. Although observation of the SdH oscillation can provide the most direct evidence for metallization and a wealth of information on the Fermi surface, there has been no such a report. If the metallization is realized under pressure, anticipated metallic phase should be semimetallic to fulfill a charge neutrality condition. Thus, pressurized BP can be a novel candidate for elemental semimetals after bismuth and graphite. The possible realization of unconventional electronic phases due to the strong carrier correlation has been discussed in previous literatures in bismuth and graphite, and thus, BP can be a possible stage to realize such a phases. In case of BP, the carrier density can be continuously controlled by tuning applied pressure, which is unique character for BP and favorable for exploring the unconventional electronic phase in the vicinity of semiconductor-semimetal transition. In order to clarify the electronic state of BP under pressure and testify the possible pressure-induced semiconductor-semimetal transition in pressurized BP, we investigated the detailed transport properties in the pressure range from ambient pressure to 2.5 GPa.

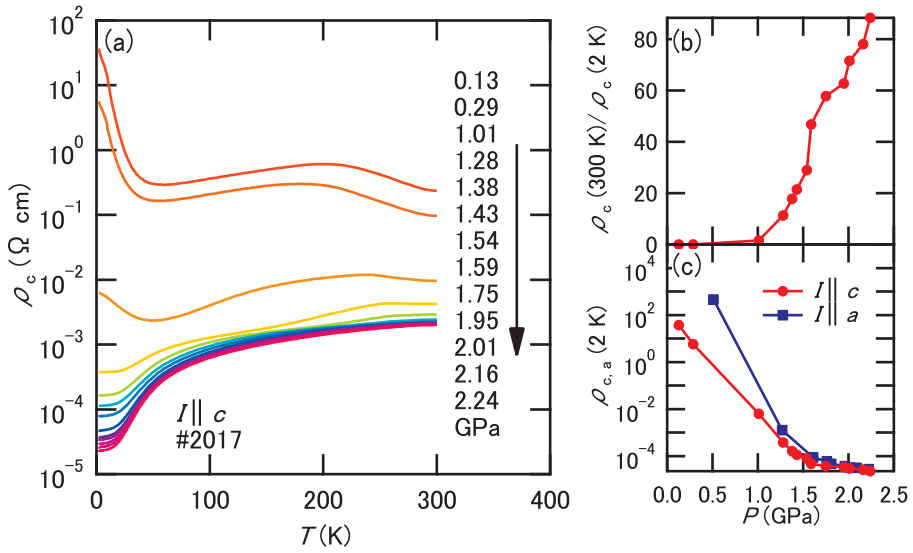

Figure 3.7: (a) Temperature dependence of the resistivity along the c-axis (ρ_c) at various pressures. Measurements were performed on #2017 sample. (b) Pressure dependence of the resistivity ratio [ρ_c(300 K) / ρ_c(2 K)] between 300 K and 2 K. (c) Pressure dependence of the resistivity along the c- (ρ_c) and a- (ρ_a) axes at 2 K.

3.3 Results and Discussion

3.3.1 Temperature Dependence of the Resistivity at Various Pressures

Firstly, we introduce the results of the temperature dependence of the resistivity on two samples (referred as #2015 and #2017), and explain the behaviors by following the previous studies. The #2015 and #2017 samples are identical with those investigated in [91] and [92], respectively, and both were cut from the same single crystal bulk described in Sec. 2.8.

Figure 3.7(a) shows the temperature dependence of the resistivity of #2017 sample along the c-axis (ρ_c) at various pressures up to 2.24 GPa. The behaviors of ρ_c at 0.13, 0.29, and 1.01 GPa are explained well by assuming that BP is an extrinsic semiconductor [89]. As an example, we focus on the behavior of ρ_c at 0.13 GPa. In the temperature region between 300 to 200 K, which corresponds to region I in Fig. 3.8(a), ρ_c increases as temperature goes down. This behavior can be understood as a reduction of thermally activated carriers across the intrinsic band gap Δ_g. We can estimate Δ_g assuming the temperature dependence of ρ_c to follow Eq. (3.1). The fitted curve assuming Eq. (3.1) is shown in Fig. 3.8(a) as a dashed line, which reproduces the experimental results well. The estimated Δ_g is approximately 0.15 eV, which is slightly smaller than the previous studies [73, 88]. The Δ_g appears to vary with sample pieces as shown in Fig. 3.8(b). This dispersion might come from the limited fitting region for the estimation of Δ_g. In the temperature region between 200 to 50 K, which corresponds to region II in Fig. 3.8(a), ρ_c decreases as temperature goes down in contrast to the region I. This is ascribed to the enhancement of the mobility, which is reported in previous study (Fig. 3.3). In the temperature region between 50 to 10 K, which corresponds to the region III in Fig. 3.8(a), ρ_c drastically increases with lowering the temperature. This can be regarded as the reduction of carriers due to the suppression of the thermal activation *via* the energy gap between the valence and impurity bands Δ_i. We estimated the Δ_i

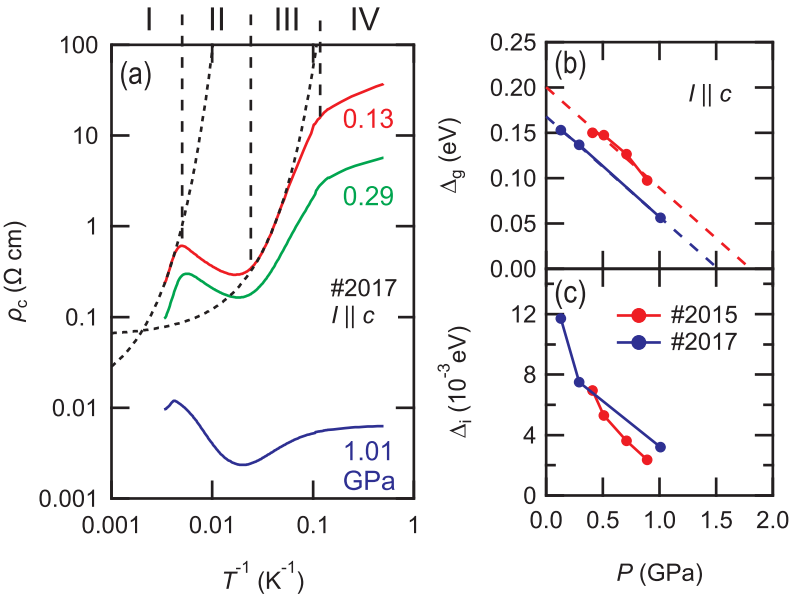

Figure 3.8: (a) ρ_c of #2017 sample as a function of inverse temperature (T^{-1}) at several pressures. Dashed lines are fitting curves assuming the Arrhenius-type temperature dependence (see text). The energy gap between (b) valence and conduction bands (Δ_g) and (c) valence and impurity bands (Δ_i) estimated by curve fittings.

by similar function with Eq. (3.1):

$$\rho_c = \rho_0 \exp\left(\frac{\Delta_i}{2k_B T}\right), \tag{3.6}$$

and obtain $\Delta_i \sim 10$ meV at 0.13 GPa, which is consistent with other studies [73, 93]. The fitted curve reproduces the experimental behavior as shown in Fig. 3.8(a). In the temperature region below 10 K, which is referred as region IV in Fig. 3.8(a), ρ_c tends to saturate, which might be governed by the variable range hopping conduction between impurity levels. At 0.29 and 1.01 GPa, we can also recognize similar temperature dependence and define region I to IV for each ρ_c vs. T^{-1} curves. As we can see in Figs. 3.7(a) and 3.8(a), gap-like behaviors observed in region I and III are suppressed as the pressure increases, which can be understood as a reduction of both Δ_g and Δ_i. The pressure dependences of Δ_g and Δ_i estimated from curve fittings in the region I and III are shown in Figs. 3.8(b) and (c), respectively. We can recognize the common behavior between #2015 and #2017 samples that both Δ_g and Δ_i monotonically decrease as pressure increases. We can roughly estimate by linear extrapolation [shown as dashed lines in Fig. 3.8(b)] that Δ_g becomes zero at around 1.5 GPa, which suggests the realization of pressure-induced semiconductor-semimetal (SC-SM) transition. This critical pressure coincides with the previous report by Akahama *et al.* [88, 89]. Above 1.38 GPa, the temperature dependence becomes totally metallic over the entire temperature range as shown in Fig. 3.7(a). Here, we note that the temperature dependence of the resistivity seems to be strongly affected by the quality of the samples, since other groups have reported qualitatively different results and slightly low SC-SM transition pressure [93, 94]. Figure 3.7(b) shows the the pressure dependence of the resistivity ratio between 300 K and 2 K [ρ_c(300 K)/ρ_c(2 K)]. We can see the change of slope at around 1.2 GPa, at which magnetoresistance starts to increase (as shown in later section): this is consistent with

the previous report [93]. We also observed the pressure dependence of the anisotropy in the in-plane resistivities. Figure 3.7(c) shows ρ_c ($I \parallel c$) and ρ_a ($I \parallel a$) at 2 K. While ρ_a is more than 10 times larger than ρ_c near the ambient pressure, the difference between ρ_a and ρ_c becomes small as pressure increases.

3.3.2 Quantum Transport Phenomena in Semiconducting Black Phosphorus —Magneto-Phonon Resonance—

In this section, we focus on the quantum transport phenomena under magnetic fields observed in the semiconducting state. Figure 3.9(a) shows the field dependence of ρ_{xx} at 77 K with a magnetic field of up to 55 T applied along the a-axis and current along the c-axis. The ρ_{xx} shows positive magnetoresistance accompanied by some hump structures below 30 T. These structures are periodic in terms of B^{-1} as shown in Fig. 3.9(b). This periodic structure has been ascribed to the magneto-phonon resonance (MPR) [95]. The MPR is the resonant scattering of carriers by optical phonons and observed as an enhancement of resistance when the following resonance condition is fulfilled:

$$\hbar\omega_O = N\hbar\omega_c \quad (N = 1,\, 2,\, 3, \dots), \tag{3.7}$$

where $\hbar\omega_O$ is the energy of the optical phonon and $\omega_c = eB/m^*$ is the cyclotron frequency [96]. e and m^* represent the elemental charge and cyclotron mass, respectively. Observation of the MPR indicates the existence of well-defined Landau levels in BP, *i.e.*, $\omega_c\tau = \mu B > 1$ above 4 T (τ and μ denote the relaxation time and mobility of carriers, respectively). Therefore, $\mu > 0.25\ \mathrm{T}^{-1} = 2500\ \mathrm{cm}^2\ \mathrm{V}^{-1}\ \mathrm{s}^{-1}$ at 77 K, which is consistent with previous reports (Table 3.2). Figure 3.9(c) shows the temperature dependence of the second derivatives of resistivity ($-d^2\rho_{xx}/dB^2$). The MPR is the most remarkable at 50 K, and then suppressed as the temperature increases or decreases. The suppression of oscillating component by decreasing temperature is ascribed to the suppression of thermal excitation of the optical phonons which cause the carrier scattering. Hence, the MPR becomes hardly visible at 4.2 K. On the other hand, the suppression by increasing temperature is regarded as the effect of thermal broadening of Landau subbands: there is no well-defined Landau subband structure due to the shortening of τ, and thus, resonant scattering does not occur anymore in higher temperature. The trend mentioned above is clearly shown in the FFT spectrum in Fig. 3.9(d): FFT spectrum at 50 K has the highest magnitude at around 23 T. We can also recognize that the position of the peak (the period of the MPR) is almost independent of the temperature. Here, Eq. (3.7) can be transformed to the relationship between the inversed field and the integer index as

$$B^{-1} = \frac{e}{m^*\omega_O}N, \tag{3.8}$$

and the FFT frequency identified in Fig. 3.9(d) corresponds to the coefficient $e/(m^*\omega_O)$. Thus, temperature-insensitive FFT frequency peak seen in Fig. 3.9(d) results from the temperature-insensitive m^*. Actually, the temperature coefficient of the effective masses along the three principal axes have been reported as $dm_{a,b,c}/dT = 10^{-5}$–10^{-4} [76], which is consistent with our results.

Next, we discuss pressure dependence of the MPR. Figure 3.10(a) shows pressure dependence of the second derivative $-d^2\rho_c/dB^2$ at 77 K, in which the period of oscillation becomes long with applied pressure. To understand this behavior, we focus on the relationship between peak/dip position of MPR (B^{-1}) and integer index (N) shown in Fig. 3.10(b). Here, integer (half-integer) indices correspond to the local maxima

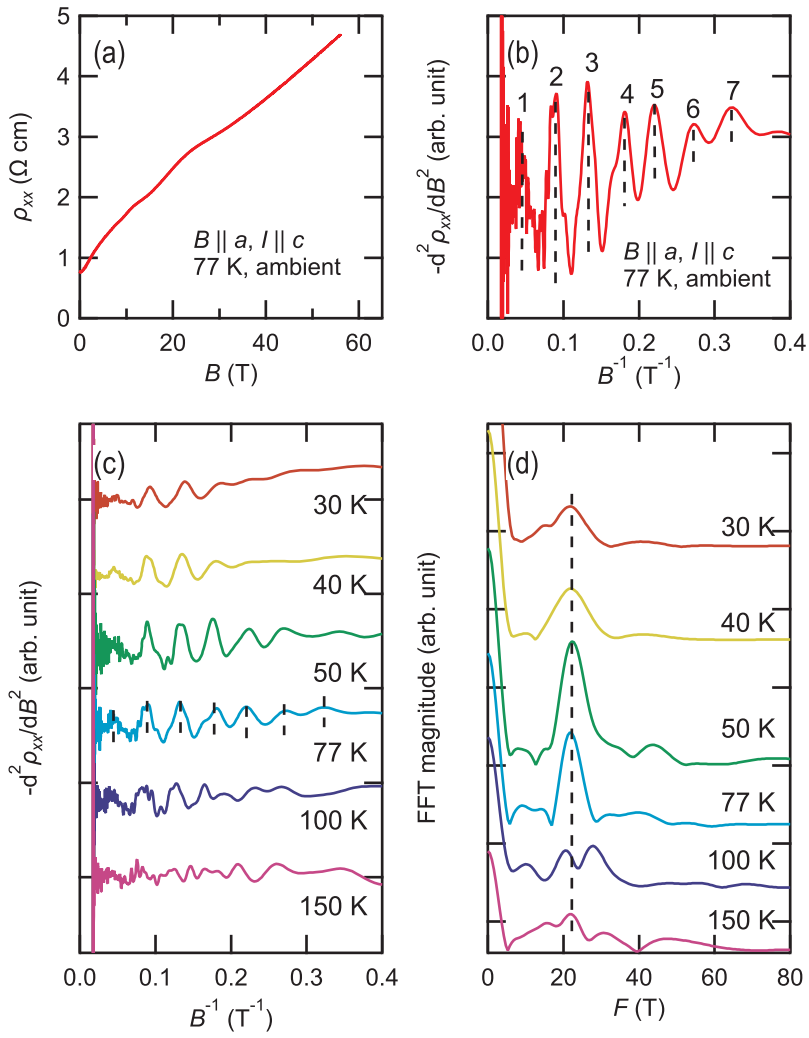

Figure 3.9: (a) Magnetoresistance ρ_{xx} at ambient pressure and temperature of 77 K. A magnetic field of up to 55 T was applied along the a-axis and current along the c-axis. (b) The second derivative of magnetoresistance $-d^2\rho_{xx}/dB^2$ as a function of inverse field B^{-1}. The numbers indicate the integer indices N of the magneto-phonon resonance (see text). (c) The temperature dependence of the magneto-phonon resonance in $-d^2\rho_{xx}/dB^2$. (d) The temperature dependence of the FFT spectra calculated from the data shown in (c).

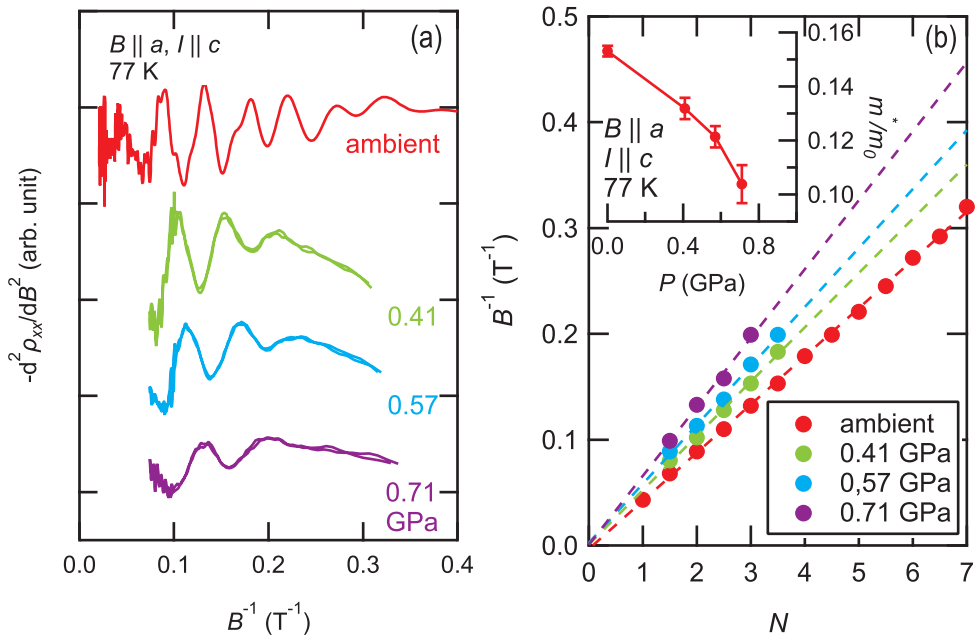

Figure 3.10: (a) Second derivatives of ρ_{xx} as a function of B^{-1} at several pressures. The magnetic field was applied along the a-axis and current along the c-axis. (b) Relationship between inverse peak/dip fields B^{-1} and the index N in Eq. (3.7) (see text in detail). The inset of (b) shows the pressure dependence of cyclotron mass estimated from the slopes of the B^{-1} vs. N plot.

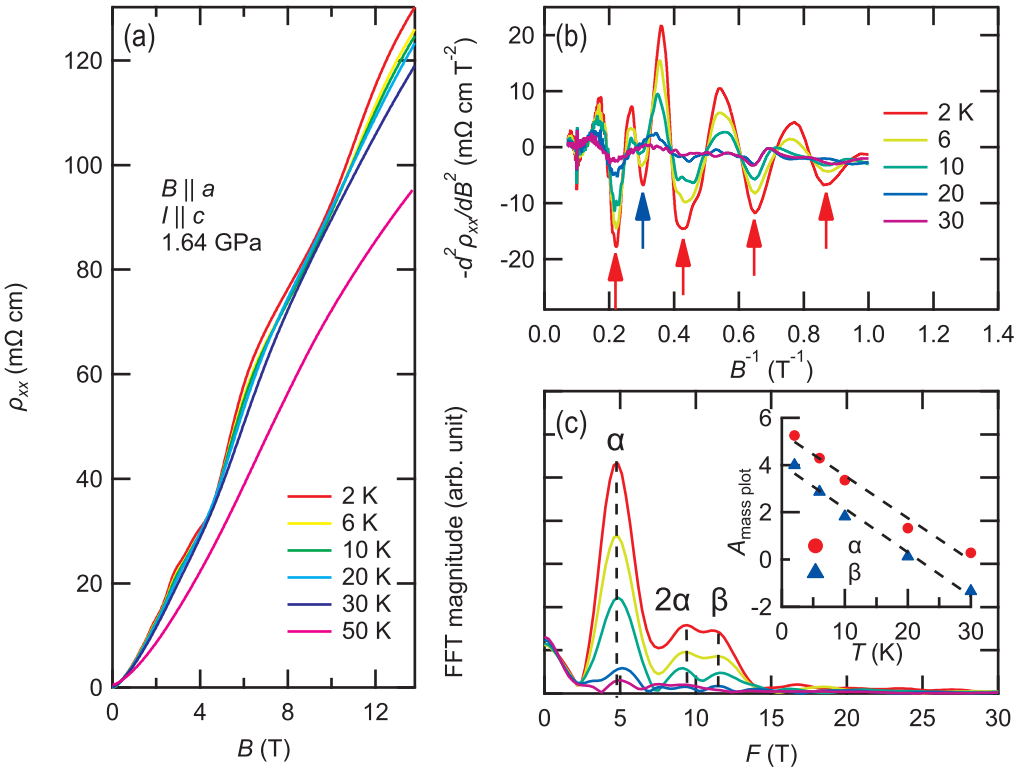

Figure 3.11: (a) Magnetoresistance ρ_{xx} at 1.64 GPa under magnetic fields along the a-axis. (b) Second derivatives of ρ_{xx} as a function of B^{-1}. The red and blue arrows correspond to α and β peaks in (c), respectively. (c) FFT spectrum calculated from the data shown in (b). The inset shows self-consistently linearized A_{massplot} at α and β peaks (see text for details). The broken lines shows the linear fits of each A_{massplot}.

(minima) in Fig. 3.10(a). We can recognize that B^{-1} is proportional to N and the slope of the line becomes steep with applied pressure. As is clear in Eq. (3.8), the change of slope by applying pressure is regarded as a change of coefficient $e/(m^*\omega_O)$. Generally, both m^* and ω_O in Eq. (3.8) can vary with applied pressure. In the case of BP, however, it has been shown in the previous report that the phonon energy was insensitive to the pressure, at least in the pressure range of this study (Fig. 3.6). Thus, the increase of the slopes in Fig. 3.10(b) can be regarded as the reduction of m^* by applying pressure assuming ω_O as a constant. According to the simple $\boldsymbol{k}\cdot\boldsymbol{p}$ perturbation introduced in Sec. 1.1, effective mass becomes small as the energy gap decreases. Hence, the reduction of m^* implies the suppression of the energy gap by pressure. By using $\omega_O = 2.60\times10^{13}$ s^{-1} (138 cm^{-1}), which is the frequency of the B_{1u} (L) mode optical phonon identified experimentally (Table 3.4), m^* estimated from Eq. (3.8) is 0.153 m_0 at ambient pressure, which is consistent with the previously reported values of 0.146 m_0 at 20 K [75] and 0.166 m_0 at 30 K [76] determined by experiments of cyclotron resonance (Table 3.3). The change of m^*/m_0 with applied pressure is summarized in the inset of Fig. 3.10(b).

3.3.3 Quantum Transport Phenomena in Semimetallic Black Phosphorus —Shubnikov-de Haas Oscillation—

Next, we focus on the electrical transport properties in semimetallic BP. We succeeded in observing the Shubnikov-de Haas (SdH) oscillations in the semimetallic BP. This section is mainly dedicated to the elucidation of the electronic state in semimetallic BP based on detailed analysis of the SdH oscillations.

Firstly, we focus on the transport properties under magnetic fields applied along the a-axis, in which the cyclotron mass m^* in the semiconducting state is smaller than those of other principal axes. Figure 3.11(a) shows ρ_{xx} at 1.64 GPa as a function of magnetic field at several temperatures. We observed non-saturating increase of ρ_{xx}, and the magnetoresistance normalized by the value at zero field reaches $[\rho_c(B) - \rho_c(0)]/\rho_c(0) \sim 1000$ at 14 T and 2 K. Such a marked change in magnetoresistance has been known in bismuth [97] and graphite [98], which are typical elemental semimetals, and attracts renewed interest in other semimetals [99]. The origin of the large magnetoresistance will be discussed in later part together with the in-plane transport properties.

In addition to this approximately linear magnetoresistance, we can identify the superposed modulation. The modulated components are clearly visible in their second derivatives shown in Fig. 3.11(b). Contrary to the MPR in the semiconducting state, the oscillating component periodic to B^{-1} grows up as the temperature decreases and is hardly visible at 50 K. Thus, this structure can be ascribed to the SdH oscillations. We can see a major oscillation (red arrows) and additional small structures (an blue arrow) in Fig. 3.11(b), suggesting that there are at least two frequency components. Since semimetallic BP is expected to have at least one electron and one hole Fermi pockets, above result is reasonable. The fast Fourier transform (FFT) spectrum and its temperature dependence are shown in Fig. 3.11(c). FFT was carried out for $-d^2\rho_{xx}/dB^2$ shown in Fig. 3.11(b) with Hanning window function. We can see two distinct peaks, α (4.9 T) and β (11 T), and the second harmonic 2α (9.8 T) as marked by broken lines. The frequency of the SdH oscillation (F) is proportional to the cross-sectional area (S) surrounded by the closed orbit in reciprocal space:

$$F = \frac{\hbar S}{2\pi e}. \tag{3.9}$$

The cross-sectional areas of each Fermi surface are 0.47×10^{-3} and 1.0×10^{-3}Å^{-2} for α and β, which are approximately 0.017 and 0.037% of those of the first Brillouin zone at the $k_z = 0$ plane, respectively. If we assume spherical Fermi surfaces, these small pockets roughly correspond to carrier densities of 10^{16} cm^{-3}, which is comparable to those in bismuth and graphite (c.f. Table 1.1). More detailed discussion about the Fermi surface will be made later in this section. Owing to such a small Fermi surfaces, the quantum limit state is expected to achieve above 11 T at this pressure.

The SdH oscillations are represented theoretically by the Lifshitz-Kosevich (LK) formula [100]. The cyclotron mass was determined by the temperature dependence of the SdH amplitude as described below. In the LK formula, the amplitude of the quantum oscillation $A(T)$ as a function of temperature T is represented by

$$A(T) = A_0 \frac{am^*T/B}{\sinh(am^*T/B)}. \tag{3.10}$$

Here, A_0 is a constant which is independent of the temperature, and $a = 2\pi^2 k_B/(e\hbar)$

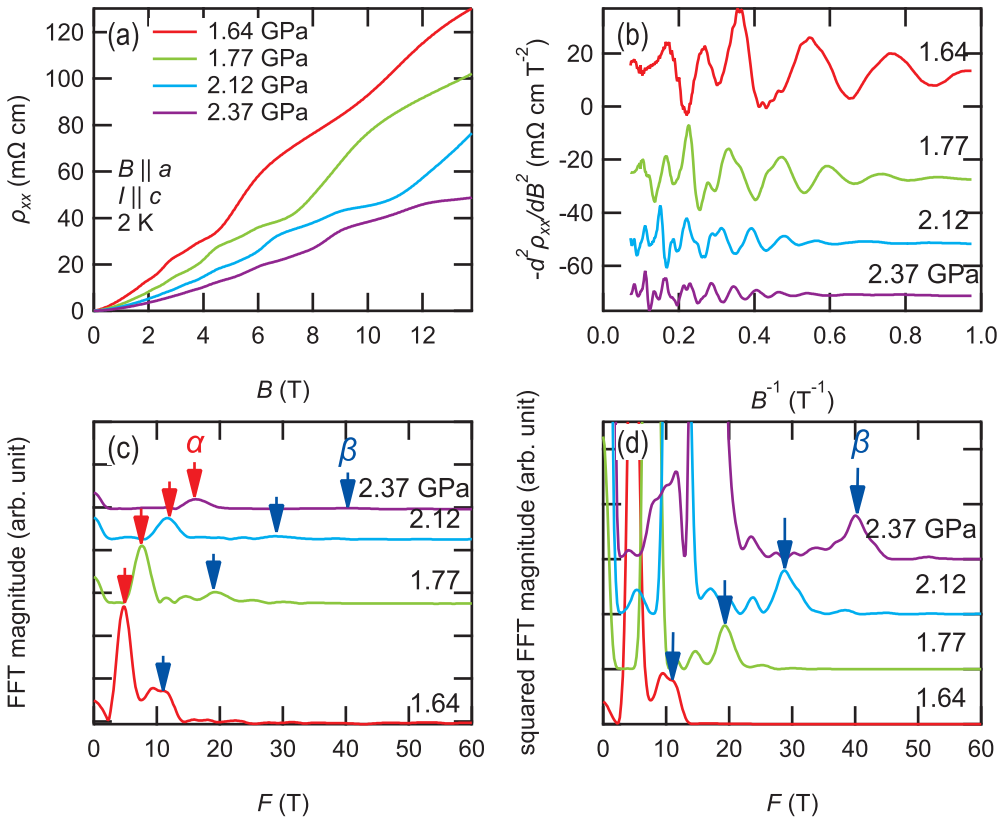

Figure 3.12: (a) Magnetoresistance ρ_{xx} at various pressures. B was applied along the a-axis. (b) $-d^2\rho_{xx}/dB^2$ calculated from the data shown in (a). (c) FFT spectrum calculated from the data shown in (b). The pressure dependence of α and β peaks are traced by red and blue allows, respectively. (d) Squared FFT magnitude. The pressure dependence of β peak is traced by blue arrows.

using Boltzmann constant k_{B}. Further, we can rearrange Eq. (3.10) to

$$\ln\left[A(T)\left[1-\exp\left(-2am^*T/B\right)\right]/T\right] = C - \frac{am^*T}{B}, \tag{3.11}$$

where C is a constant which is independent of temperature. We can see that the left hand side of Eq. (3.11) (referred as A_{massplot}) should be linear as a function of T. We firstly substitute appropriate m^*_{old} to m^* in A_{massplot}, and next, plot A_{massplot} as a function of T, and then, obtain the new m^*_{new} from the slope of A_{massplot} and update m^*_{old} to m^*_{new}. We recurred above procedure until the cyclotron mass sufficiently converges, more specifically, until $|m^*_{old}-m^*_{new}|/m^*_{old} < 10^{-6}$ is satisfied. m^* is determined from the final slope of the A_{massplot} after the recursive calculation. The inset of Fig.3.11(c) shows the most linearized A_{massplot} for α and β peaks, and $m^* \sim 0.02\ m_0$ is obtained for both peaks.

Next, we argue the magnetoresistance at various pressures. Figure 3.12(a) shows ρ_{xx} at 2 K under several pressures. Application of pressure significantly suppresses positive magnetoresistance and modifies superposed oscillating structure. The change of the SdH oscillation is more obvious in $-d^2\rho_{xx}/dB^2$ as shown in Fig. 3.12(b). As illustrated in the FFT spectra [Fig. 3.12(c)], the peaks α and β detected at 1.64 GPa move toward

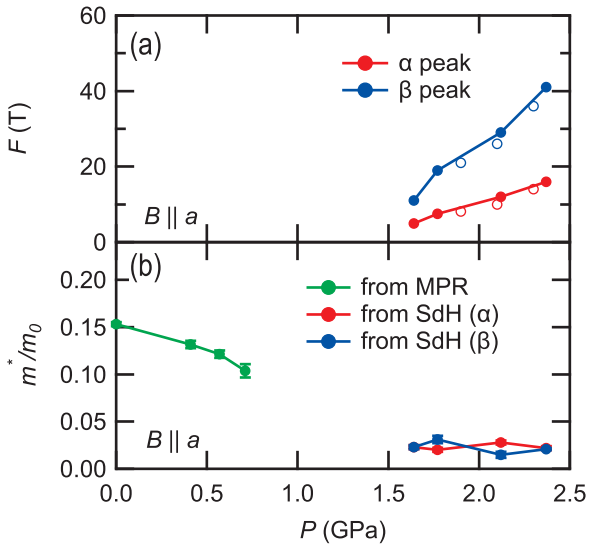

Figure 3.13: (a) Pressure dependence of the FFT frequencies for α and β peaks. The open markers represent the results of another sample piece, which shows good reproducibility. (b) Pressure dependence of the cyclotron mass obtained from the analyses of the MPR and SdH oscillations.

higher frequency, indicating the enlargement of the Fermi surfaces by applying pressure. This behavior can be understood by the increase of band overlap by pressure. Although the magnitude of β peak is considerably weaker than that of α peak as shown in Fig. 3.12(c), It can be clearly recognized in squared FFT magnitude and definable as shown in Fig. 3.12(d).

Figure 3.13(a) summarizes the pressure dependence of the SdH frequencies with the magnetic field applied along the a-axis. We investigated the pressure dependence of these peaks in another sample piece as shown by the open symbols in Fig. 3.13(a), and confirmed the reproducibility. The pressure dependence of m^* determined through the analyses of the MPR and the SdH is shown together in Fig. 3.13(b). In semimetallic state, m^* takes the value between 0.02 to 0.03 m_0, which indicates that the semimetallic BP has considerably light effective mass comparable to typical semimetals, bismuth and graphite (c.f. Table 1.1). In addition, it is approximately an order of magnitude smaller than that of the semiconducting state.

We also investigated the magnetoresistance in the longitudinal configuration ($B \parallel I \parallel a$), in which the cyclotron motion due to the Lorenz force is irrelevant to the charge current. Figure 3.14(a) shows the longitudinal magnetoresistance (ρ_{zz}) in magnetic field along the a-axis at 1.65 GPa. Even in this geometry, we clearly observed the SdH oscillations. The frequency was confirmed to be consistent with that in transverse geometry at 1.64 GPa. In addition, we observed large and non-saturating magnetoresistance also in this longitudinal configuration. At 2 K, the ratio $[\rho_{zz}(B)-\rho_{zz}(0)]/\rho_{zz}(0)$ reaches approximately 50 at 14 T. According to a conventional Drude-type formulation, $\sigma_{zz}(= 1/\rho_{zz})$ is independent of B and described by the following equation:

$$\sigma_{zz} = \frac{n_h e^2 \tau_h}{m_h} + \frac{n_e e^2 \tau_e}{m_e}. \tag{3.12}$$

In this equation, $\tau_{h(e)}$ and $m_{h(e)}$ represent the relaxation time and the effective mass of

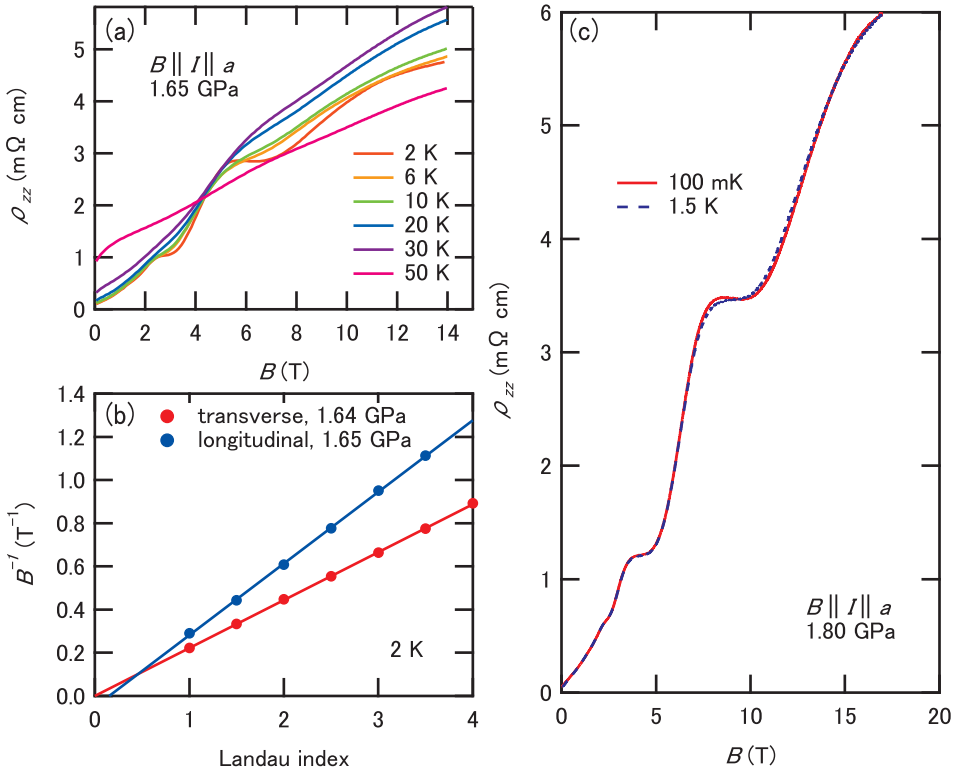

Figure 3.14: (a) ρ_{zz} in the longitudinal configuration ($B \parallel I \parallel a$, at 1.65 GPa). (b) The comparison of the Landau-level fan diagram for α peak between transverse ($B \perp I$) and longitudinal ($B \parallel I$) configurations. B was applied along the a-axis in both configurations. (c) ρ_{zz} at 1.5 K and 100 mK in the configuration of $B \parallel I \parallel a$ at 1.80 GPa.

the holes (electrons), respectively. Since the observed SdH oscillations can be analyzed using fixed values of $n_{h,e}$ and $m_{h,e}$, we have to introduce a field dependence of $\tau_{h,e}$ so as to reproduce the observed longitudinal magnetoresistance in this classical framework.

Here, let us comment on the phase of the SdH oscillations, *i.e.*, so-called Landau-level fan diagram analysis. In Fig. 3.14(b), we plot the relationship between the inverse fields showing peak/dip in ρ_{xx} ($B \parallel a$ and $I \parallel c$) and ρ_{zz} ($B \parallel I \parallel a$) against the Landau index. Similar analyses are frequently utilized in topological materials to evaluate the Berry's phases from the values of the horizontal intercept in this diagram. Here, only major oscillations from α peak were extracted by attenuating oscillations from β peak by digital filter, and dips were assigned to integer indices. Although whether peaks or dips should be assigned to integer indices is not trivial since semimetallic BP is multi-carrier system, we follow the case of graphite in which the dip of ρ_{xx} is known to correspond to the depopulation of Landau subbands [101]. The intercept for $\rho_{\rm c}$ is 0.00 ± 0.01 similar to a two-dimensional Dirac system, whereas that for $\rho_{\rm a}$ is 0.15 ± 0.02 even in the same field direction. The origin of above difference seems to come from the failure of the prerequisite $\sigma_{xx} \ll |\sigma_{xy}|$ for analysis in ρ_{xx} [45]. Actually, the occasion $\rho_{xx} \sim \rho_{yx}$ can realize in semimetallic BP as shown later. Therefore, we cannot make a reliable argument from the analyses of this diagram.

Further, we measured ρ_{zz} at lower temperature down to 100 mK and higher magnetic field up to 17 T to explore the existence of additional heavier carriers and field-induced exotic phases. Figure 3.14(c) shows ρ_{zz} at $T = 100$ mK and 1.5 K. The observed SdH oscillation at 100 mK is almost identical to that observed at $T = 1.5$ K, and no additional components in the oscillation can be identified down to this temperature. High-field studies on clean elemental semimetals of bismuth and graphite show anomalous behavior in the vicinity of the quantum limit state [19, 102–107], yet we do not find any features indicating a phase transition at least up to 17 T in the case of semimetallic BP.

Next, we show the pressure depencence of the SdH oscillations under magnetic field along the *b*- and *c*-axes. Figure 3.15(a) shows the pressure dependence of $-d^2\rho_{xx}/dB^2$ at 2 K from 1.28 to 2.24 GPa in magnetic fields applied along the *b*-axis. As the pressure increases, oscillatory structure becomes more prominent, and the frequency clearly becomes larger. Figure 3.15(b) shows the pressure dependence of the FFT spectra from 1.43 to 2.24 GPa at 2 K. FFT was carried out for $-d^2\rho_{xx}/dB^2$ shown in Fig. 3.15(a) with Hanning window function. We identified two frequency peaks marked with red (referred to as a major peak) and blue (referred to as a minor peak) arrows. The major peak first becomes discernible at 1.43 GPa with a frequency of about 5 T, while the minor peak appears at 1.75 GPa with a frequency of about 9.5 T. Both frequencies monotonically become larger as pressure increases. Although SdH oscillation-like structures can be seen in $-d^2\rho_{xx}/dB^2$ at 1.28 and 1.38 GPa, we cannot define the reliable frequency through FFT due to the limited number of cycles of the oscillations. We also note that there are some additional structures at higher frequencies than that of major peaks as marked by green arrows at 1.43 and 1.54 GPa in Fig. 3.15(b). Since these peaks do not show systematic dependence on temperature as shown in the inset of Fig. 3.15(a), we focus on the other two peaks in the following discussion. Figures 3.15(c) and (d) show the pressure dependence of $-d^2\rho_{xx}/dB^2$ and the FFT spectra, respectively, in magnetic fields applied along the *c*-axis. Similar with the results of the other directions, we can recognize two peak frequencies [red and blue branches in Fig. 3.15(d)], which monotonically increase as pressure increases. The frequency assigned by blue arrows has tiny amplitude compared to another one. We estimated the cyclotron masses of major peaks for all three principal axes, and obtained $m_a^* \sim 0.02m_0$, $m_b^* \sim 0.04m_0$, and $m_c^* \sim 0.14m_0$.

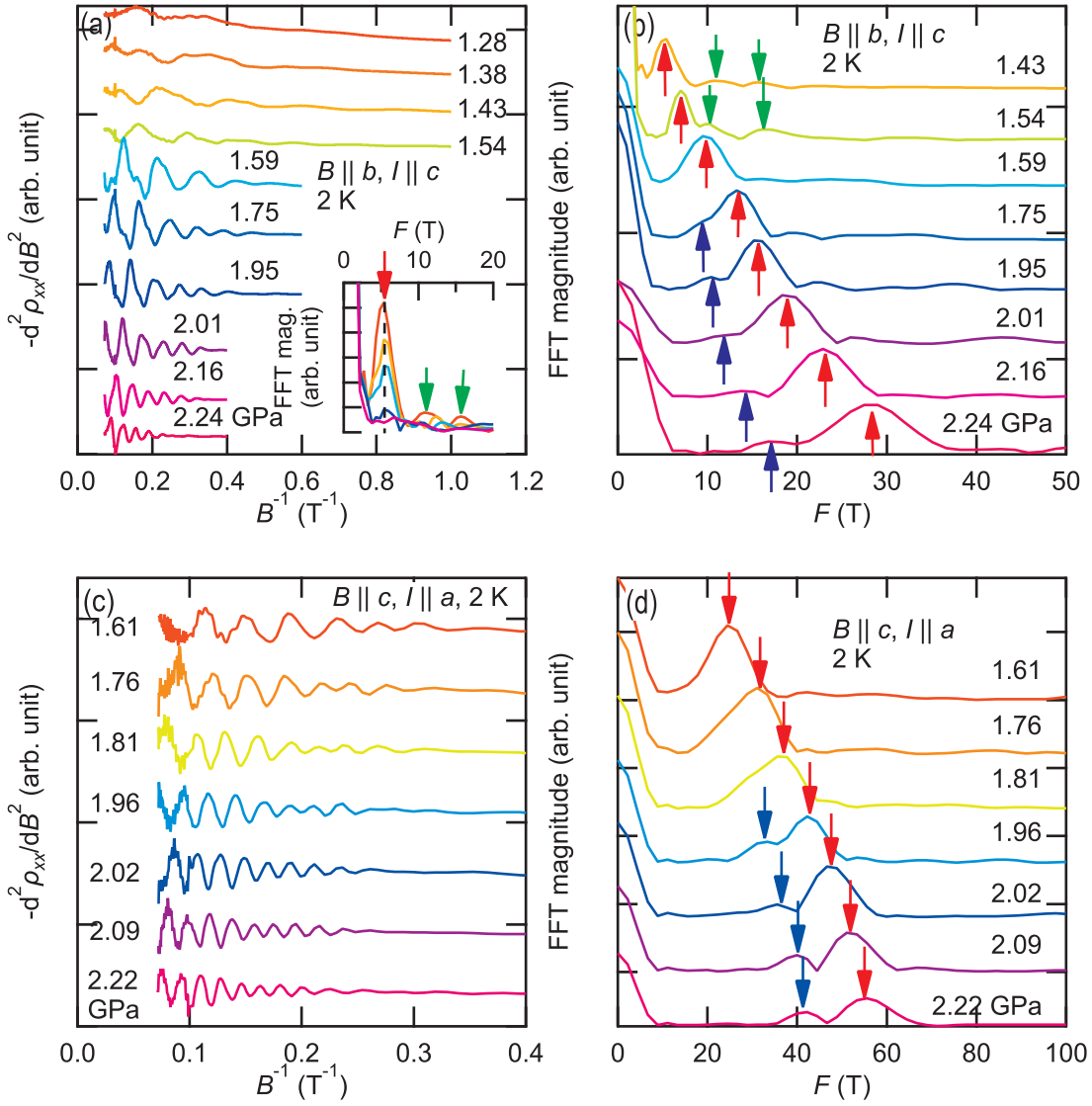

Figure 3.15: (a) $-d^2\rho_{xx}/dB^2$ from 1.28 to 2.24 GPa at 2 K in magnetic fields along the b-axis. The data were vertically offset for clarity. The inset shows the temperature dependence of the FFT spectra at 1.43 GPa. (b) FFT spectra of $-d^2\rho_{xx}/dB^2$ from 1.43 to 2.24 GPa in magnetic fields along the b-axis. The major and minor peaks are indicated by the red and blue arrows, respectively. Several additional peaks which appear at 1.43 and 1.54 GPa are indicated by the green arrows. Each magnitude of the spectrum is normalized by the amplitude of each major peak and vertically offset for clarity. (c) $-d^2\rho_{xx}/dB^2$ from 1.61 to 2.22 GPa at 2 K in magnetic fields along the c-axis. The data were vertically offset for clarity. (d) FFT spectra of $-d^2\rho_{xx}/dB^2$ from 1.61 to 2.22 GPa in magnetic fields along the c-axis. The major and minor peaks are indicated by the red and blue arrows, respectively.

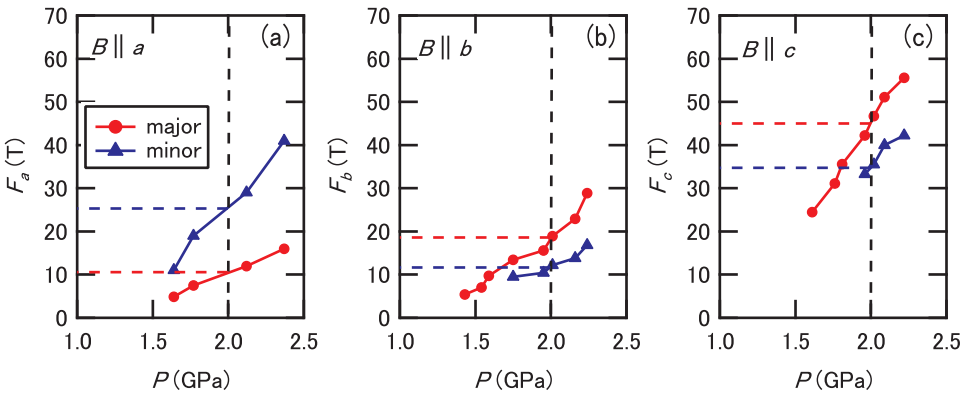

Figure 3.16: Pressure dependence of the SdH frequencies in magnetic fields along the (a) a-, (b) b-, and (c) c-axes. In all of the field directions, the major peak with a large FFT amplitude (red), and the minor peak with smaller one (blue), were observed.

These values are less sensitive to the pressure in the semimetallic states. We comment that the anisotropy of hole cyclotron mass in the semiconducting state, $m_a^* < m_b^* < m_c^*$ (Table 3.3) is also held in that of major peaks in the semimetallic state.

The results of the pressure dependence of the SdH frequencies are summarized in Figs. 3.16(a) to (c). As described above, two branches with larger (red) and smaller (blue) amplitudes are observed in all of the orientations. They will be also referred to as the major and minor peaks, respectively. We can estimate the SC-SM transition pressure as 1.2-1.4 GPa where FFT frequencies for the magnetic field along the three principal axes (F_{a-c}) becomes zero by extrapolating from the data shown in Figs. 3.16(a)-(c). Note that this roughly corresponds to the pressure where Δ_g and Δ_i becomes zero discussed in Figs. 3.8(b) and (c). Since we did not find any other peaks down to the lowest temperatures in this study as shown in Fig. 3.14(c), we attribute these two frequencies to that of the quantum oscillations from the electron and hole Fermi pockets. However, we cannot identify which frequency corresponds to the electron/hole pocket for all of the three field directions, only from the experimental results.

Finally, we introduce the results of the band calculation under pressure performed by Mr. H. Arai and Prof. Y. Fuseya (The University of Electro-Communications), and compare them with the experimental results. Figure 3.17(a) shows the band structure at a pressure of 2.0 GPa determined by the first-principles calculations within the generalized gradient approximation using the OpenMX code [108]. Corresponding first Brillouin zone and symmetric points are shown in Fig. 3.17(b). Two and one primitive orbitals for s- and p-orbitals are used for the pseudo-atomic orbitals basis functions, respectively. Crystal structure parameters at 2.0 GPa was determined by linear extrapolation of parameters at ambient pressure and 0.8 GPa shown in [68] Almost the same results as those in Fig. 3.17(a) was obtained even by using the crystal structure parameters given in [85]. At ambient pressure, the obtained band structure (not shown) is consistent with previous works, [68, 109] and the direct band gap at the Z point is 130 meV. At a pressure of 2.0 GPa, the band overlap between the conduction and valence bands at the Z point is 140 meV. Figure 3.17(c) shows the calculated Fermi surface. There are one hole pocket at around the Z point and four electron pockets located between the Γ-A lines (their energy minima are slightly off the Γ-A lines). Their calculation resulted in the indirect band overlap: the energy band other than near the Z point contributes

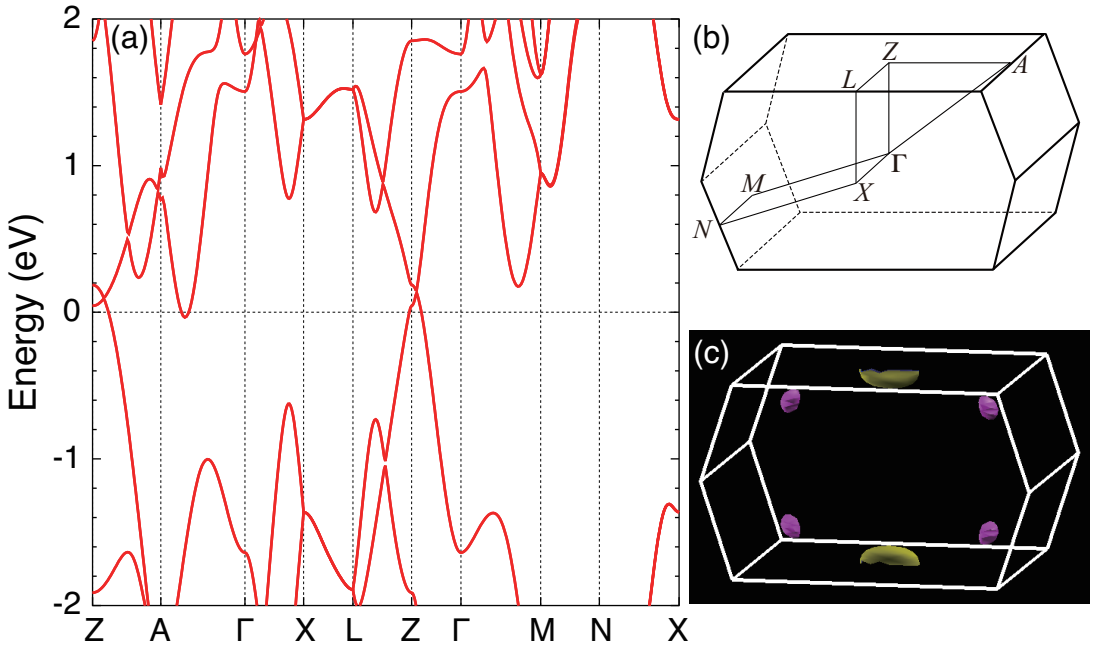

Figure 3.17: (a) Band structure at pressure of 2.0 GPa. (b) Brillouin zone and some of the symmetric points. (c) Fermi surfaces: one hole pocket at around the Z point and four electron pockets between the Γ-A lines. The a-, b-, and c-axes correspond to the Z-A, Γ-Z, and Γ-X directions, respectively.

to the semimetallizaton. Drop of the energy band on the $\Gamma - A$ path with pressure is explained by change of the in-plane hopping due to the shrinkage of the puckered honeycomb layers along the c-axis [110]. The hole pocket is highly anisotropic: the ratio of Fermi wave vectors is $k_{\rm F}^{Z-A} : k_{\rm F}^{Z-\Gamma} : k_{\rm F}^{Z-L} = 21 : 13 : 3$, while the electron pockets are rather isotropic. For the nearly compensated condition, which will be quantitatively validated in the next section, the total volume of the electron pockets should be equal to that of the hole pocket.

Now, we compare the theoretical results mentioned above with our experimental results. For the sake of simplicity, we approximate the Fermi surfaces as spheroids that are characterized by three axes, L_a, L_b, and L_c: *i.e.*, the Fermi surfaces are represented in the reciprocal space by $(k_a/L_a)^2 + (k_b/L_b)^2 + (k_c/L_c)^2 = 1$. Here the a-, b-, and c-directions in the real space correspond to the k_a-, k_b-, and k_c- directions in the reciprocal space. From the first-principles calculation, the anisotropy of the hole pocket is estimated as $L_a : L_b : L_c = 21 : 13 : 3$ at 2 GPa. As a result, the ratio of the cross-sections perpendicular to the a- (S_a), b- (S_b), and c- (S_c) axis is $S_a : S_b : S_c = 13 : 21 : 91$ based on the above theoretical estimation. By assuming that the major peaks originated from the hole pockets and using extrapolated $F_{a,b,c}$ at 2 GPa [indicated with red dashed lines in Figs. 3.16(a)-(c)], the hole density calculated from the volume of the spheroid is about 2.6×10^{17} cm^{-3}. In addition, this identification satisfies the relationship $S_c > S_b > S_a$, which was suggested by the theoretical calculation. In this case, however, the electron pocket constructed from $F_{a,b,c}$ of minor peaks [blue dashed lines in Fig. 3.16(a)-(c)], has an almost identical volume to that of the hole even for one pocket, which does not match the first-principles calculation. Recently, several theoretical studies reported different band structures of BP in the semimetallic state [111,112], which also could not reproduce

the observed SdH frequencies in the present study. For complete determination of the Fermi surfaces in semimetallic BP, additional information such as angle-resolved SdH measurements, and careful comparison with theoretical studies should be necessary.

3.3.4 Analyses of the In-Plane Transport Properties Based on the Two-Carrier Model

In this section, we quantitatively evaluate the carrier density and mobility based on the semiclassical two-carrier model. Firstly, we focus on the transport properties in the semiconducting state at 0.29 GPa. Figure 3.18(a) shows the magnetoresistance (ρ_{xx}) at T =2, 15, and 30 K with magnetic field applied parallel to the b-axis. ρ_{xx} first decreases below 2 T and then increases as the magnetic field increases at 2 K. The negative magnetoresistance below 2 T is ascribed to the suppression of the two-dimensional Anderson localization [113]. On the other hand, it monotonically increases with the magnetic field at 15 and 30 K. Figure 3.18(b) shows the Hall resistance (ρ_{yx}) at 2, 15, and 30 K. Nonlinear behavior becomes pronounced as the temperature increases, which is also reported in another report [114]. The nonlinear ρ_{yx} suggests that at least two kinds of carriers exists, and that they have different densities and mobilities. Since ρ_{yx} is always positive up to 14 T, the majority of the carriers is expected to be holes. Figure 3.18(c) shows the Hall conductivity (σ_{xy}) as calculated from both ρ_{xx} and ρ_{yx} as

$$\sigma_{xy} = \frac{\rho_{yx}}{\rho_{xx}^2 + \rho_{yx}^2}. \tag{3.13}$$

Here, Eq. (3.13) is for the isotropic case with $\rho_{xx} = \rho_{yy}$ and $\rho_{xy} = -\rho_{yx}$ in the original definition:

$$\sigma_{xy} = \frac{\rho_{yx}}{\rho_{xx}\rho_{yy} - \rho_{xy}\rho_{yx}}. \tag{3.14}$$

In the case of BP, It has been reported that the resistivity along the a-axis (ρ_a) is approximately 10 times larger than ρ_c at ambient pressure [73]. We actually observed the anisotropy in the semiconducting state, as shown in the Fig. 3.7(c). However, since ρ_a/ρ_c was confirmed to be nearly constant as functions of temperature and magnetic field, we utilized the isotropic two-carrier model and focus on qualitative change in the parameters in the semiconducting state. By assuming two kinds of carriers (labeled 1 and 2) with densities ($n_{1,2}$) and mobilities ($\mu_{1,2}$), we can obtain σ_{xy} [115]:

$$\sigma_{xy} = eB\left(\pm\frac{n_1\mu_1^2}{1+\mu_1^2B^2} \pm \frac{n_2\mu_2^2}{1+\mu_2^2B^2}\right). \tag{3.15}$$

In Eq. (3.15), $e > 0$ is the elementary charge and B is the magnetic flux density, respectively. The plus and minus signs in Eq. (3.15) should be taken into consideration when the corresponding carrier is a hole or electron, respectively. It should be noted that the signs of ρ_{yx} and σ_{xy} are the same in this formulation. Our discussion of the result in the semiconducting state assumes the coexistence of two kinds of hole carries [*i.e.*, plus signs are taken in Eq. (3.15)]. The dashed lines in Fig. 3.18(c) show the fitted curves of σ_{xy}, based on Eq. (3.15), and we adjust for the four fitting coefficients: namely, the densities ($n_{h1,h2}$) and mobilities ($\mu_{h1,h2}$) of the hole carriers. The temperature dependence of these coefficients is shown in Figs. 3.18(d) and (e). For simplicity, we ignored the effects of the Anderson localization that are observed at 2 K. We can see that the carrier densities ($n_{h1,h2}$) increase with increasing temperature, which can be explained by the thermal excitation of carriers from the impurity levels as discussed in earlier Sec.

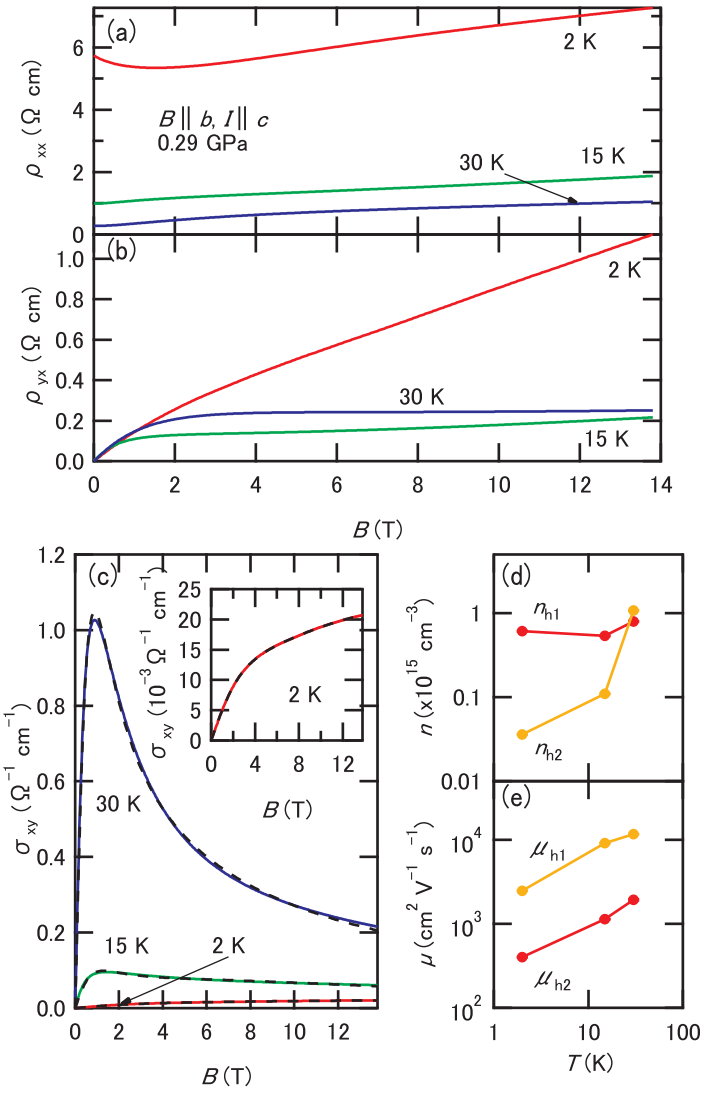

Figure 3.18: (a) Resistivity (ρ_{xx}) and (b) Hall resistivity (ρ_{yx}) as a function of the magnetic field that is applied along the b-axis at 0.29 GPa. (c) Hall conductivity (σ_{xy}) at 2, 15, and 30 K, as calculated from both ρ_{xx} and ρ_{yx} using Eq. (3.13). Dashed lines indicate the fitted curves based on the two-carrier model (see text). The inset shows the magnified view of σ_{xy} at 2 K. The temperature dependence of the (d) densities (n_{h1}, n_{h2}) and (e) mobilities (μ_{h1}, μ_{h2}) of the holes estimated by the two-carrier model fittings at 0.29 GPa. The error bars are smaller than the diameter of the circles.

3.3.1. The mobilities (μ_{h1} and μ_{h2}) also increase with increasing temperature, which is consistent with the positive temperature coefficient of the Hall mobility that had been observed at ambient pressure up to 20 K [Fig. 3.3(c)].

Here, we comment on the statistical error accompanying the two-carrier fit. Eguchi *et al.* recently pointed out that there is a large uncertainty in the fitting coefficients of the two-carrier model analyses of the resistivities (ρ_{xx} and ρ_{yx}) [116,117]. We also recognized that significant errors in the fitting coefficients occur in the analyses of resistivities, and thus, we adopted a fitting to the Hall conductivity (σ_{xy}). The parameters we obtained had a much lower error and resulted in physically reasonable behavior, as mentioned above. One important point to make is that, contrary to that of recent report on BP [114], our experimental results cannot be reproduced by assuming the coexistence of electrons and holes: our results indicate that the existence of two kinds of hole carriers with different densities and mobilities is crucial to reproduce the experimental results. Since semiconducting BP is assumed to be a direct band gap semiconductor and has no band degeneracy near the narrowest gap [the Z point, see Fig. 3.2(e)], the origin of the "two kinds of hole" is unclear.

Next, we show the in-plane magnetoresistance and Hall resistance ($B \parallel b$, $I \parallel c$) near and above the SC-SM transition pressure. Figure 3.19(a) shows $\rho_R(B) \equiv [\rho_{xx}(B) - \rho_{xx}(0\ \mathrm{T})]/\rho_{xx}(0\ \mathrm{T})$ at 2 K at several pressures from 1.01 to 2.24 GPa. The details about the SdH oscillation superposed on $\rho_R(B)$ has already been discussed in earlier Sec. 3.3.3. We do not see any tendency of saturation in $\rho_R(B)$ until at least 14 T in the semimetallic state. The magnetoresistance effect reaches its maximum value of $\rho_R(14\ \mathrm{T}) \cong 8000$ at 1.75 GPa and then decreases with increasing pressure, as shown in Fig. 3.19(e): meanwhile the ρ_c at 2 K is monotonically suppressed by pressure, as shown in Fig. 3.7(a). Figure 3.19(b) shows ρ_{yx} at 2 K from 1.01 to 2.24 GPa, which shows non-linear behavior at all pressures suggesting a contribution from multiple kinds of carriers also in this pressure region. The sign inversions of ρ_{yx} were observed at this pressure region below 2 T, as shown in the inset of Fig. 3.19(b), which agrees with the previous report [93]: this sign inversion in ρ_{yx}, however, cannot be recognized at 0.29 GPa, as shown in Fig. 3.18(b). In addition, the magnetic field where the sign inversion takes place systematically increases with increasing pressure. Thus, we regard this sign inversion as an important feature in this pressure region.

In order to discuss whether the large and non-saturating magnetoresistance in BP is explained within the semiclassical theory or not, careful analysis closely following the conventional Drude model is important. Thus, we analyzed σ_{xy} at 2 K based on the isotropic two-carrier model. As shown in Fig. 3.7(c), the anisotropy between ρ_a and ρ_c at 2 K becomes small above 1.2 GPa at zero field. In addition, the magnetoresistance along the a- and c-axes was reported to be less anisotropic in the semimetallic state [93]. We can reasonably reproduce σ_{xy} by assuming the coexistence of electron and hole carriers at pressures from 1.01 to 2.24 GPa [opposite signs between the first and second terms are taken in Eq. (3.15)]. Curve fittings were carried out in the magnetic field from 0 T to 4 T where the effect of the quantum oscillations is negligible. Figure 3.19(c) shows the pressure dependence of the electron (n_e) and hole (n_h) densities with vertical error bars: both n_e and n_h monotonically increase with increasing pressure, which indicates that the Fermi pockets become larger due to the enhancement of the band overlap. This result is consistent with the pressure dependence of the SdH frequencies (Fig. 3.16).

This result shows that carrier density is continuously controlled by hydrostatic pressure in semimetallic BP. It is also shown in Fig. 3.19(c) that n_e and n_h have similar values at all pressures, which indicates the nearly compensated semimetallic nature of

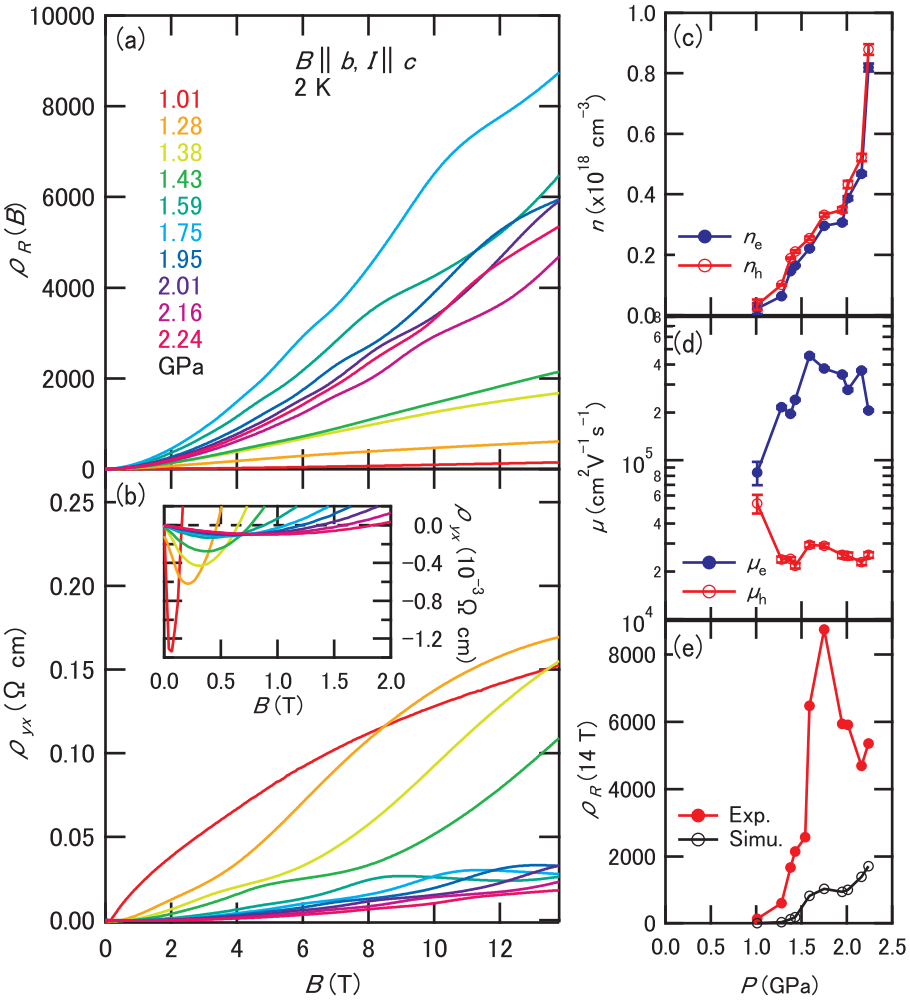

Figure 3.19: (a) $\rho_{\mathrm{R}}(B) = [\rho_{xx}(B) - \rho_{xx}(0\ \mathrm{T})]/\rho_{xx}(0\ \mathrm{T})$ from 1.01 to 2.24 GPa at 2 K. (b) Hall resistivity (ρ_{yx}) from 1.01 to 2.24 GPa at 2 K. The inset of (b) shows the magnified view of ρ_{yx} below 2 T. (c) Pressure dependence of the hole (n_h, red markers) and electron (n_e, blue markers) densities with vertical error bars. (d) The pressure dependence of the hole (μ_h, red markers) and electron (μ_e, blue markers) mobilities with vertical error bars. (e) The experimental (filled red circles) and simulated (open black circles) values of $\rho_{\mathrm{R}}(14\ \mathrm{T})$ using Eq. (3.19).

BP. Figure 3.19(d) shows the pressure dependence of the electron (μ_e) and hole (μ_h) mobilities with vertical error bars: The μ_e and μ_h have similar values at 1.01 GPa, while μ_e becomes more than 10 times larger than μ_h above 1.28 GPa. The coexistence of electrons and holes, and the large difference between μ_e and μ_h, reasonably explains the sign inversion of ρ_{yx} that is shown in the inset of Fig. 3.19(b). In the electron-hole two-carrier model, σ_{xy} is represented by Eq. (3.15):

$$\sigma_{xy} = eB\left(\frac{n_h}{\mu_h^{-2}+B^2} - \frac{n_e}{\mu_e^{-2}+B^2}\right). \tag{3.16}$$

In the strong-magnetic field limit ($\mu_{e,h}^{-1} \ll B$), Eq. (3.16) can be simplified:

$$\sigma_{xy} \sim \frac{e}{B}(n_h - n_e). \tag{3.17}$$

This equation indicates that the sign of σ_{xy} is only determined by the carrier imbalance, $n_h - n_e$. σ_{xy} is always positive in the strong-field limit in the present case, since $n_h > n_e$ holds at the all studied pressures. In the weak-magnetic field limit ($\mu_{e,h}^{-1} \gg B$), on the other hand, σ_{xy} is represented by the following equation:

$$\sigma_{xy} \sim eB(\mu_h^2 n_h - \mu_e^2 n_e). \tag{3.18}$$

As can be seen, the sign depends also on the mobilities. Since $n_e \simeq n_h$ and $\mu_e^2 > \mu_h^2$ in the present case, σ_{xy} is negative in a weak magnetic field. Therefore, the sign inversion takes place in a magnetic field where the first term is equal to the second term in Eq. (3.16). Above features well explain our results.

Here, we discuss the large and non-saturating magnetoresistance of semimetallic BP. Recently, several theoretical groups have suggested the possible realization of the Dirac electron system in semimetallic BP under pressure [111, 118]. In recent magneto-transport study of Cd_3As_2, which is a candidate of three-dimensional Dirac system, linear and no-saturating magnetoresistance originated from the non-trivial band topology has been suggested [33]. Whether the magnetoresistance effect obserbed in semimetallic BP contains such a non-trivial origin is of great interest. To clarify the above point, we analyze the magnetoresistance based on the two-carrier model. In the present model, $\rho_{\mathrm{R}}(B)$ is represented by the following equation [119]:

$$\rho_{\mathrm{R}}(B) = \frac{B^2 n_e n_h \mu_e \mu_h (\mu_e + \mu_h)^2}{(\mu_e n_e + \mu_h n_h)^2 + B^2 \mu_e^2 \mu_h^2 (n_e - n_h)^2}. \tag{3.19}$$

In the case of a completely compensated semimetal ($n_e = n_h$), $\rho_R(B)$ can be reduced to $\mu_e \mu_h B^2$: the resistance continuously increases without showing saturation within the classical model. In the present case, however, incomplete compensation leads to the saturation of $\rho_R(B)$ to a finite value. We calculated $\rho_R(14\ \mathrm{T})$ by Eq. (3.19) using $n_{e,h}$ and $\mu_{e,h}$ shown in Figs. 3.19(c) and (d). The open circles in Fig. 3.19(e) show that the calculated $\rho_R(14\ \mathrm{T})$ is much smaller than the experimental values at the all studied pressures, and it cannot reproduce the peak structure at 1.75 GPa. Therefore, the observed XMR in BP involves some additional physics beyond the conventional two-carrier model for nearly compensated semimetals. In addition, the observed large longitudinal magnetoresistance, which is shown in Fig. 3.14, cannot be explained through this semi-classical approach.

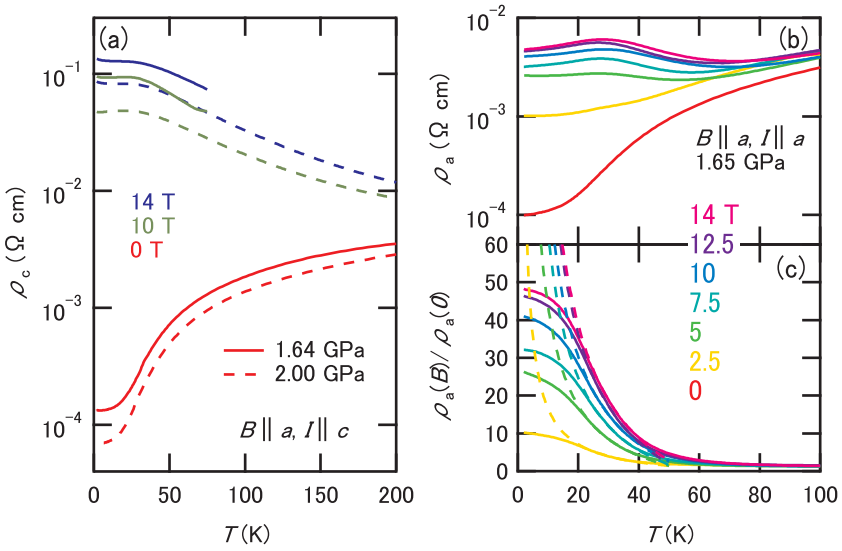

Figure 3.20: (a) The temperature dependence of ρ_c in several magnetic fields at 1.64 (solid lines) and 2.00 GPa (broken lines) in transverse configuration ($B \parallel a$ and $I \parallel c$). (b) The temperature dependence of ρ_a in several magnetic fields at 1.65 GPa in longitudinal configuration ($B \parallel I \parallel a$). (c) The temperature dependence of ρ_a normalized by the resistivity at zero field $\rho_a(0)$. Fitting curves based on Eq. (3.22) in the text are shown by broken lines.

3.3.5 Exploration of Unconventional Electronic Phases on the Boundary between Semiconducting and Semimetallic States

In the vicinity of the SC-SM transition pressure, the quantum limit state in which all the carriers are accommodated in the lowest Landau subband can be realized in order of 10 T as shown in earlier Sec. 3.3.3. Recent experimental studies of graphite suggested the emergence of an excitonic phase in the vicinity of the quantum limit state in high magnetic fields [19, 107]. Since semimetallic BP is an ideally clean low-carrier system, shielding of the Coulomb interaction will be weaker than that in ordinary metals. In order to look for anomalous quantum states caused by the charge correlation in this electron-hole system, we studied the temperature dependence of the resistivity, as shown in Fig. 3.20(a). The temperature dependence at zero field is metallic as mentioned above, while in magnetic fields, they become semiconductor-like ones at temperatures of up to 200 K. Although this kind of behavior is sometimes interpreted as a field-induced SM-SC transition, such apparent semiconductor-like behavior in semimetals can be explained by a simple two-carrier model [120]. The transverse resistivity (ρ_{xx}) is expressed as [121]

$$\rho_{xx}(B) = \frac{\rho_{\rm e}\rho_{\rm h}(\rho_{\rm e}+\rho_{\rm h}) + (\rho_{\rm e}R_{\rm h}^2 + \rho_{\rm h}R_{\rm e}^2)B^2}{(\rho_{\rm e}+\rho_{\rm h})^2 + (R_{\rm e}+R_{\rm h})^2B^2}, \tag{3.20}$$

where $R_{\rm e,h} = 1/(n_{\rm e,h}q_{\rm e,h})$ is the Hall coefficients of electron and hole carriers ($n_{\rm e,h}$ and $q_{\rm e,h}$ represent the density and charge of electron and hole carriers, respectively) and $\rho_{\rm e,h} = 1/(n_{\rm e,h}e\mu_{\rm e,h})$ is the resistivity of each carrier at zero field. For simplicity, we assume the completely compensated case. Then, we can set $-q_{\rm e} = q_{\rm h}$ and $n_{\rm e} = n_{\rm h}$, *i.e.*, $-R_{\rm e} = R_{\rm h} = R$. Further, we assume that $\rho_{\rm e}$ and $\rho_{\rm h}$ have the same metallic temperature

dependence, *i.e.*, $\rho_{\rm e}(T) = \rho_{\rm h}(T) = \rho_0(T)$ at zero field. Then, Eq. (3.20) is reduced to

$$\rho_{xx}(B,T) = \frac{\rho_0(T)}{2} + \frac{R^2B^2}{2\rho_0(T)}. \tag{3.21}$$

In low-carrier systems, the second term in Eq. (3.21) becomes dominant at high magnetic fields since R is generally large, and thus ρ_{xx} can show the superficial insulating-like behavior even in a metallic sample. Since transverse magnetoresistance shows this kind of artificial metal-insulator transition-like behavior, we next focus on the longitudinal magnetoresistance.

As shown in Fig. 3.20(b), the longitudinal magnetoresistance shows a peak structure at around 30 K as a function of temperature. Such nonmonotonic behavior, however, may not be ascribed to the emergence of a novel phase below this temperature. Figure 3.20(c) shows the temperature dependence of the $\rho_{\rm a}(B)$ normalized by the value at zero field $\rho_{\rm a}(0)$. The traces show monotonic behaviors at all the fields. According to a transport theory in the quantum limit state [122], the longitudinal resistivity $\rho_{\parallel}(B,\,T)/\rho_{\parallel}(0,\,T)$ for classical statistics, in which the Fermi energy is smaller than $k_{\rm B}T$, is represented by,

$$\frac{\rho_{\parallel}(B,\,T)}{\rho_{\parallel}(0,\,T)} = \frac{1}{3}\left(\frac{\hbar\omega_{\rm c}}{k_{\rm B}T}\right) = \frac{\hbar e}{3k_{\rm B}m^*}\frac{B}{T} \tag{3.22}$$

when the scattering mechanism is dominated by the δ-function impurity potential or acoustic phonon. As shown by broken lines in Fig. 3.20(c), $\rho_{\rm a}(B,\,T)/\rho_{\rm a}(0,\,T)$ is reasonably reproduced by Eq. (3.22) at all the fields by adjusting the single parameter $m^* = 0.005\ m_0$ above 20 K. Although the m^* used in this analysis is different from that estimated above, this discrepancy is not unusual considering the crudeness of the model and coexistence of electrons and holes. Therefore, the unusual temperature dependences of the transverse and longitudinal magnetoresistances in semimetallic BP do not show the emergence of a gapped phase at a high magnetic field, but can be simply understood as characteristic behavior in a high-mobility and low-carrier-density semimetal comparable to bismuth and graphite.

Finally, we focus on the magnetotransport properties at lower temperatures, which was achieved through the use of a dilution refrigerator. Figure 3.21 and its inset show the temperature dependence of ρ_a at 1.80 GPa in various fields that were applied along the a-axis. No anomalous features in the ρ_a-T curves were observed down to 43 mK.

We comment on the necessary condition to realize the excitonic insulator phase based on rough estimation. The energy ratio of the lowest Landau level at 10 T [$\hbar\omega_c/2 = \hbar eB/(2m^*) = 28.9$ meV] to exciton binding energy [$E^B_{e\text{-}h} = e^2/(8\pi\epsilon a^B_{e\text{-}h}) = 0.945$ meV] is estimated as $\gamma = \hbar\omega_c/(2E^B_{e\text{-}h}) \sim 30.6$, assuming the cyclotron and conversion masses are $m^* = 0.02m_0$ and $\mu = 0.01m_0$, respectively. Since we do not have exact ϵ in semimetallic state, we used $\epsilon \sim 12\epsilon_0$ determined at ambient pressure [123]. According to Yafet *et al.*, the binding energy is expected to become ~ 5 times larger than that in zero field at $\gamma \sim 30$ [124]. Thus, the exciton binding energy at 10 T is expected to be $5E^B_{e\text{-}h} \sim 4.73$ meV. Although we do not know the precise value of $|G|$ in present case, it is approximately the same order with $\hbar\omega_c = 57.9$ meV. Comparing $E^B_{e\text{-}h}$ at 10 T and $|G|$, we can expect the situation $E^B_{e\text{-}h} \gtrsim |G|$ in higher pulsed magnetic field. In addition, smaller $|G|$ is desirable, which can be controlled by hydrostatic pressure in case of semimetallic BP.

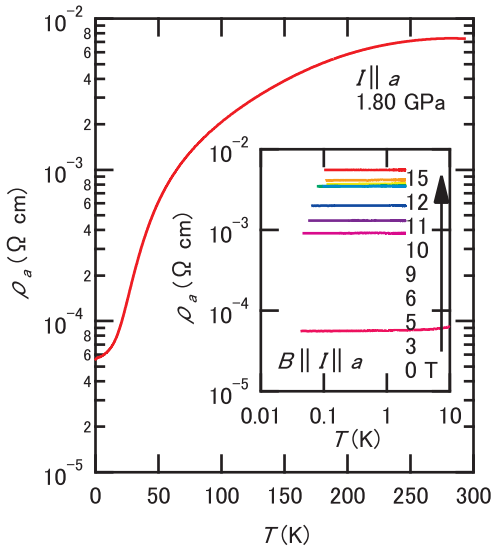

Figure 3.21: Temperature dependence of the resistivity along the a-axis (ρ_a) at 1.80 GPa down to 43 mK. The inset shows the temperature dependence of ρ_a below 1 K under various magnetic fields along the a-axis.

3.4 Summary

We investigated the electrical transport properties of black phosphorus under high magnetic fields and pressure. In semiconducting state, we observed the magneto-phonon resonance, which is marked by the high mobility nature of black phosphorus. The pressure dependence of the magneto-phonon resonance indicates that the cyclotron mass becomes lighter as pressure increases, which can be understood as a result of band gap closure. In semimetallic state above 1.4 GPa, we observed clear Shubnikov-de Haas oscillation and large magnetoresistance effect. From the analysis of Shubnikov-de Haas oscillations, we identified the light cyclotron mass and small carrier density in the vicinity of semiconductor-semimetal transition, which is comparable to bismuth and graphite. Further, Fermi surfaces become monotonically larger as pressure increases, which denotes that the carrier density is tunable by hydrostatic pressure. More detailed experiments such as angular dependence of the quantum oscillations and careful comparison with theoretical studies are necessary to completely determine the number and geometry of the Fermi surfaces. Also, we quantitatively determined the carrier densities and mobilities of electrons and holes based on the two-carrier model, which confirmed the nearly compensated nature in the semimetallic state, and large mobility difference between electrons and holes. The large magnetoresistance observed in the semimetallic phase cannot be fully reproduced by conventional two-carrier model, which suggests additional mechanisms beyond the semiclassical framework, such as magnetic field dependence of the relaxation time. To seek unconventional electronic states in the vicinity of the semiconductor-semimetal transition, we measured temperature dependence of the resistivity under magnetic field and temperature down to 43 mK. Temperature dependence of the resistivity apparently became semiconductor-like under magnetic field, yet this behavior can be explained within already-known conventional theory. Experiments in higher fields are desirable to explore exotic electronic phases in the semimetallic black phosphorus.

Chapter 4

Lead Telluride

4.1 Basic Properties of PbTe

PbTe is known as an degenerated narrow-gap semiconductors with high mobility carriers. Since before, PbTe have attracted attention as an optical and thermoelectric material owing to their tunable band gap by alloying and high thermoelectric figure of merit. Besides, they are now being recognized as a candidate for novel topological material called "topological crystalline insulator" and "three-dimensional Dirac electron system". In this section, we overview the fundamental properties of this system with related literatures and clarify the scope of this study.

4.1.1 Crystal and Energy Band Structure

PbTe, one of the IV-VI compounds, is known to form the NaCl-type face-centered cubic (FCC) crystal structure as shown in Fig. 4.1(a), which belongs to the space group $Fm\bar{3}m$. As shown in Fig. 4.1(b), PbTe is a semiconductor with the narrowest direct gap of approximately 0.18 eV at the L point of the first Brillouin zone shown in Fig. 4.1(c). Presence of the band gap has also been confirmed experimentally by optical measurements [125]. The band structure is considerably altered whether the spin-orbit interaction is taken into account or not [126,127], which implies the primary importance of the relativistic effect in this system.

Although stoichiometric PbTe should be an insulator at 0 K, real samples are either p- or n-type degenerated semiconductor (have moderate number of carries at low temperature) due to the natural defect or impurities. It has been known that Pb and Te vacancy introduces acceptor and donor levels, respectively [128]. The number of the Fermi surface depends on the doping amount. While the doping is very small, ellipsoidal Fermi pockets are located only at the L points. As the doping increases, additional Fermi pockets show up on the Γ–K path. This doping dependence is common to p- and n-type cases, since the band structure is approximately symmetric with respect to the ideal Fermi level as shown in Fig. 4.1(b).

4.1.2 Physical Properties of PbTe

Here, we overview the previous literatures related to pristine PbTe. In 1950s, Allgaier *et al.* investigated the carrier mobility of lead salts PbS, PbSe, and PbTe [131]. They found that the carrier concentrations are the order of 10^{18} cm^{-3} and carrier mobilities rapidly increase as temperature decreases. Extremely high mobility 10^5 cm^{2}V^{-1}s^{-1} at

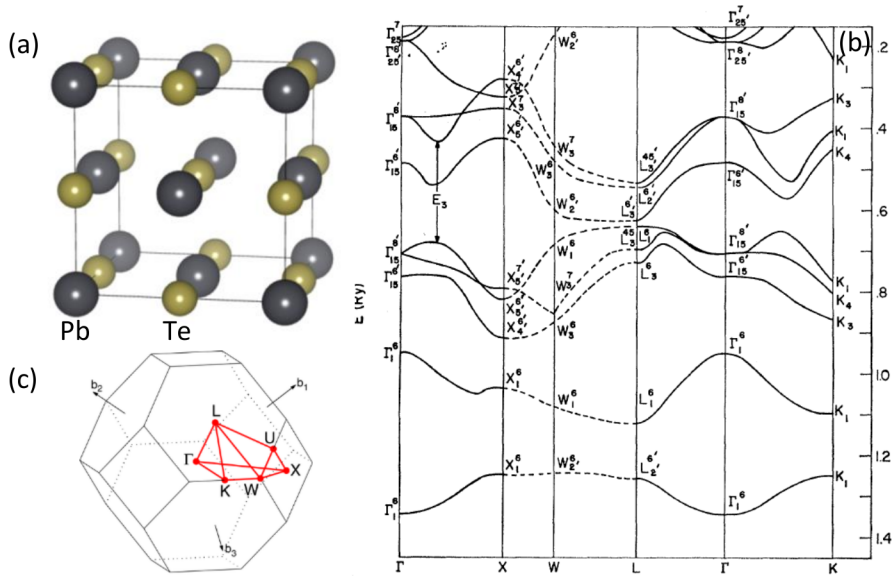

Figure 4.1: (a) Crystal structure of PbTe. (b) Energy band structure of PbTe [129]. (c) The first Brillouin zone of the FCC crystal [130].

4.2 K in PbTe is comparable with that in semimetallic BP [Fig. 3.19(d)]. Allgaier also investigated the magnetoresistance in lead salts up to 0.43 T at low temperature and reported anomalous behavior that longitudinal magnetoresistance (current $I \parallel$ magnetic fields B) is larger than transverse one ($I \perp B$) [132].

In the early 1960s, successive observations of the SdH oscillation [133, 134], dHvA oscillation [135], and cyclotron resonance [136, 137] has initiate the detailed Fermiology on PbTe. Owing to the high mobility and light effective mass, PbTe shows notable quantum oscillation even in relatively weak magnetic fields.

Burke *et al.* investigated the SdH oscillations and their angular dependence in p-type PbTe with hole density of 3.0×10^{18} cm^{-3} [138]. Figure 4.2(a) shows the SdH oscillation at 1.3 K. Clear oscillation was observed in a magnetic field less than 3.5 T, which reflects high mobility nature of PbTe. In this report, the elongated ellipsoidal Fermi pockets along the $\langle 111 \rangle$ directions are assumed to locate only at the L points as shown in Fig. 4.2(b). From the FFT spectrum of the SdH oscillation shown in Fig. 4.2(c), they assigned the peaks at 11.6, 21.8, and 39.6 T to the cross-sectional extrema originated from A, C, and B pockets in Fig. 4.2(b), respectively. Figure 4.2(d) shows the angular dependence of the SdH oscillation with the magnetic field swept from the [110] to [001] direction. The angular dependence of the fundamental SdH frequency F_{fund} (in unit of T) is analytically calculated from the cross-sectional area of ellipsoid cut by the plane perpendicular to the field direction as [138]:

$$F_{fund} = 31.5(n_p^{pocket}/10^{18})^{2/3} K^{1/6} [1 + (K-1)\cos^2\Theta]^{-1/2}. \tag{4.1}$$

Here, n_p^{pocket} (in unit of cm^{-3}) and Θ are hole density enclosed in the ellipsoid and angle between the $\langle 111 \rangle$ and magnetic field direction, respectively. $K = (b/a)^2$ represents the anisotropy of the ellipsoid with radii perpendicular (a) and parallel (b) to the $\langle 111 \rangle$ direction. They determined these parameters to reproduce the observed angular dependence as shown by solid lines in Fig. 4.2(d), and obtained $K \sim 13$ and $n_p^{pocket} = 0.75 \times 10^{18}$ cm^{-3}. Since there are 4 ellipsoids in the first Brillouin zone, the total hole density is

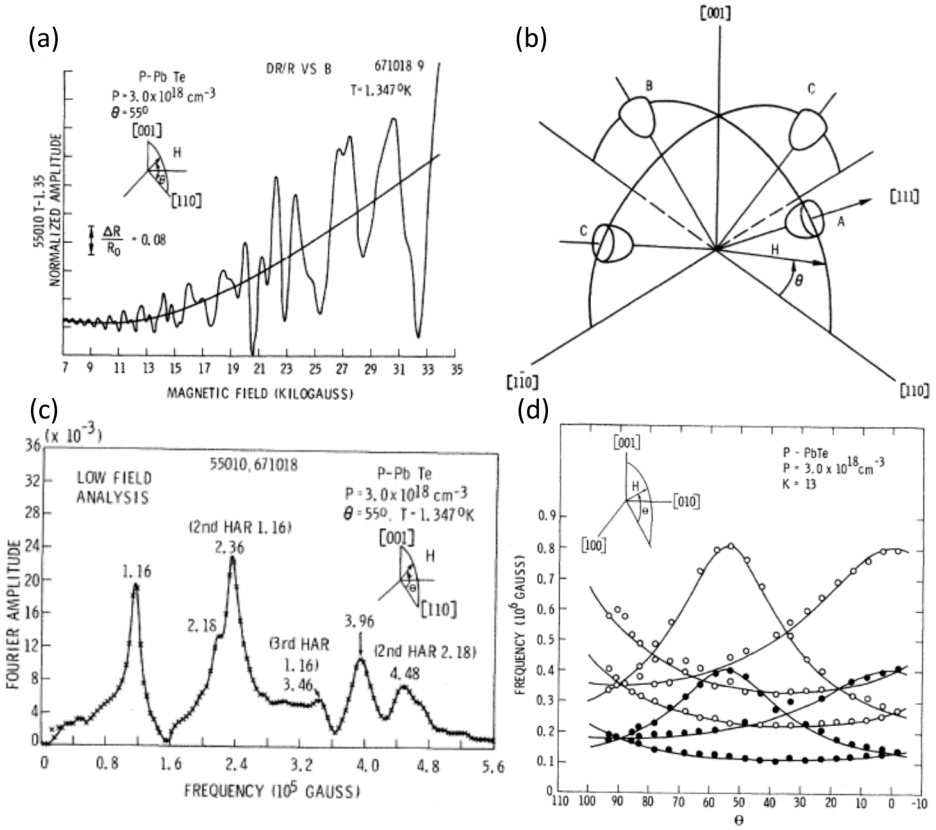

Figure 4.2: (a) SdH oscillation in PbTe [138]. (b) Fermi surfaces of PbTe assumed in [138]. (c) FFT spectrum of the SdH oscillation [138]. (d) Angular dependence of the SdH oscillation [138].

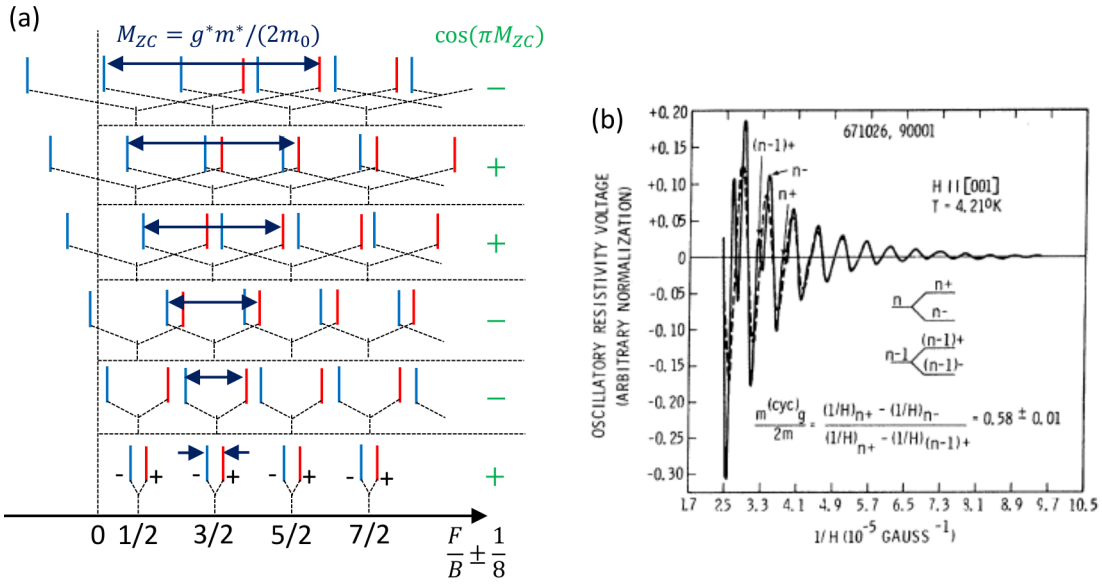

Figure 4.3: (a) Schematic Landau-level diagram with spin-splitting [100]. (b) SdH oscillation of PbTe with spin-splitting [138].

$4 \times n_p^{pocket} = 3 \times 10^{18}$ cm^{-3}, which showed good agreement with that estimated from the Hall coefficient. Note that relatively large second harmonic was also reported in the FFT spectrum of SdH oscillation as shown with open symbols in Fig. 4.2(d). As is clear in Fig. 4.2(c), the amplitude of the second harmonics at 23.6 T became even larger than that of fundamental one at 11.6 T. Although they pointed out the possible effect of spin-splitting for such a large harmonics, no quantitative explanation was made in their report. On the other hand, similar large second harmonic was also recently reported by Giraldo-Gallo *et al.* in their study of $Pb_{1-x}Na_xTe$, yet the reason for that was not attributed to the spin-splitting [139].

Burke *et al.* also revealed the effective g-factor (g^*) along several field directions. Here, we review how they deduced g^* from the experimental results. When a magnetic field B is applied to the materials, the electronic state is quantized into the Landau subbands, and they cross the Fermi level at the inversed magnetic field positions given by [100]

$$\frac{F}{B} = n + \gamma \pm \frac{1}{2} M_{ZC} \pm \frac{1}{8}, \tag{4.2}$$

including the effect of spin. $F = \hbar S_F/(2\pi e)$ is the fundamental frequency of quantum oscillation with cross-sectional extrema S_F. γ is identical with that introduced in Sec. 1.2, which stems from the Bohr-Sommerfeld quantization rule. $M_{ZC} = g^* \mu_B B/\hbar\omega_c = m^* g^*/(2m_0)$ is the ratio of the Zeeman splitting to the cyclotron energy, and we call it "ZC ratio", hereafter. The $\pm$ on the fourth term in Eq. (4.2) is chosen whether S_F is the maximum (+) or minimum (−) extremal cross-section. Figure 4.3(a) schematically shows the inverse magnetic field position of Landau levels described by Eq. (4.2), in which γ is set to 1/2 assuming the trivial case (Berry's phase $\Phi_B = 0$). In case that spin-splitting is pronounced, we can determine g^* from the SdH oscillation by following relationship [138]:

$$\frac{(1/B)_{n+} - (1/B)_{n-}}{(1/B)_{n+} - (1/B)_{(n-1)+}} = M_{ZC}, \tag{4.3}$$

field direction	m^*/m_0	M_{ZC}	g^*
$\langle 111 \rangle$	0.036 ± 0.002	0.58 ± 0.01	32 ± 3
$\langle 001 \rangle$	0.051 ± 0.008	0.58 ± 0.01	23 ± 5
$\langle 110 \rangle$	0.080 ± 0.014	0.27 ± 0.01	7 ± 2

Table 4.1: Cyclotron masses normalized by the electron mass (m^*/m_0), ZC ratios (M_{ZC}), and effective g-factors (g^*) of PbTe along the $\langle 111 \rangle$, $\langle 001 \rangle$, and $\langle 110 \rangle$ directions [138].

assuming that the cyclotron mass m^* is known from the temperature dependence of SdH oscillation. In Eq. (4.3), $(1/B)_{n+}$ *etc.* is the value of the inverse field at which the energy level $n+$ crosses the Fermi level. However, there remains ambiguity in determination of g^* only from Eq. (4.3). For example, all the cases shown in Fig. 4.3(a) result in quite similar oscillatory structures in small B, except phases of the oscillations.

To restrict the possible cases, they focused on the phase of SdH oscillation. According to the Lifshitz-Kosevich (LK) formula which describes the quantum oscillation phenomena, the quantum oscillation A_{osc} is represented as follows:

$$A_{osc} \propto \sum_{p=1}^{\infty} A(p) R_T(p) R_D(p) R_S(p) \cos\left[2\pi p \left(\frac{F}{B} + \gamma \pm \frac{1}{8p}\right)\right]. \tag{4.4}$$

Here, natural number p denotes the number of harmonics. The $\pm$ is chosen whether S_F is the minimum $(+)$ or maximum $(-)$ extremal cross-section. Since $A(p)$, $R_T(p)$, and $R_D(p)$ are all positive factors, they do not affect the phase of oscillation. Thus, only the factor $R_S(p) = \cos[\pi p m^* g^*/(2m_0)] = \cos(\pi M_{ZC})$ can alter the phase. For simplicity, they consider only $p = 1$ case:

$$A_{osc} \propto \cos(\pi M_{ZC}) \cos\left[2\pi \left(\frac{F}{B} + \gamma \pm \frac{1}{8}\right)\right]. \tag{4.5}$$

As is clear in Eq. (4.5), the apparent phase of oscillation changes whether $\cos(\pi M_{ZC})$ is plus or minus, the range of M_{ZC} can be restricted. The corresponding signs of $\cos(\pi M_{ZC})$ are shown in the right edge of Fig. 4.3(a). Burke *et al.* estimated g^* focusing on the $p = 1$ fundamental wave, and determined g^* along several crystal directions as shown in Table 4.1. An example of SdH oscillation is shown in Fig. 4.3(b), in which the magnetic field was applied along the [001] direction. Using doubled-peak positions observed in high magnetic field region and phases of the oscillations, they deduced $M_{ZC}^{[001]} = m_{[001]}^* g_{[001]}^*/(2m_0) = 0.58$. Here, $m_{[001]}^*$ and $g_{[001]}^*$ represent the cyclotron mass and effective g-factor with magnetic field along the [001] direction, respectively. We note that they reported remarkable anisotropy in M_{ZC}, namely, $M_{ZC}^{[110]}$ is smaller than those in other directions as shown in Table 4.1.

Jensen *et al.* investigated the angular dependence of the SdH oscillation on 9 p-type samples with different hole density [140]. They reported that the anisotropy of the ellipsoidal Fermi surface $K \sim 13$ and $M_{ZC}^{\langle 111 \rangle} \sim 0.6$ were almost independent of hole density from 4.0×10^{17} to 1.1×10^{19} cm^{-3}. Quantum oscillations with spin-splitting has also been reported in elastic properties and magnetostriction in magnetic fields [141,142].

Note that the M_{ZC} obtained above scheme is not unique but possible smallest value: to eliminate the possibility $M_{ZC} > 1$, magnetic field high enough to reach the quantum limit state is necessary to determine the M_{ZC} without any ambiguity. Yet, full Landau-indexing of the quantum oscillations over such a high magnetic field has not been reported.

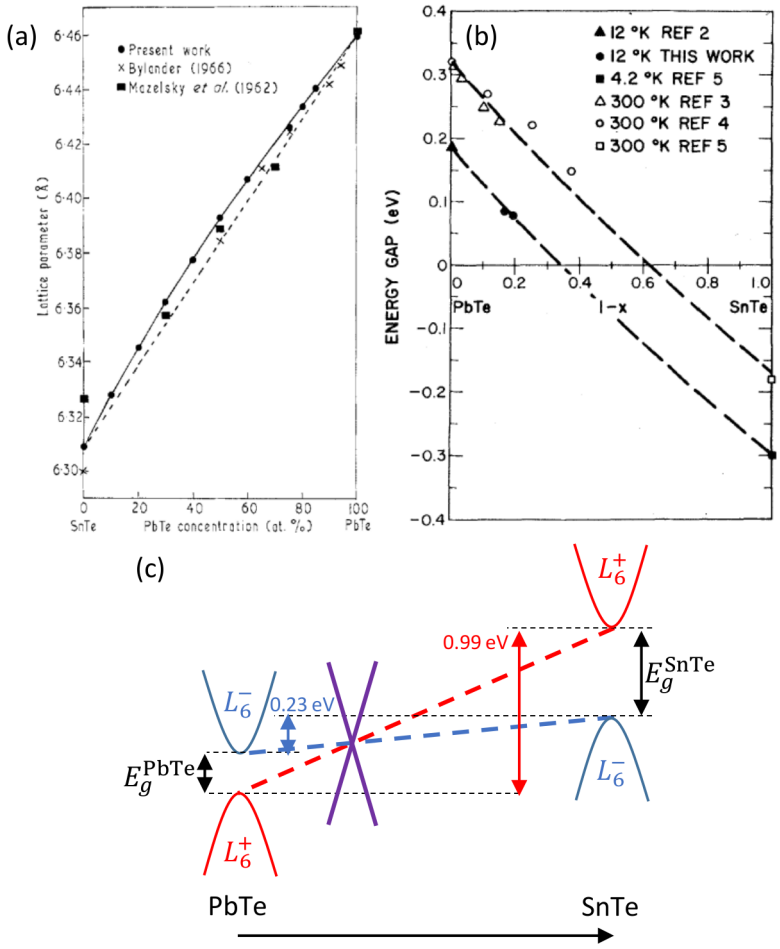

Figure 4.4: (a) Composition dependence of the lattice constant in $Pb_{1-x}Sn_xTe$ [143]. (b) Composition dependence of the band gap in $Pb_{1-x}Sn_xTe$ [144]. (c) Schematic band structure model in $Pb_{1-x}Sn_xTe$ [144].

4.1.3 Physical Properties of $Pb_{1-x}Sn_xTe$

Here, we review the change of the lattice constant and electronic structure by substitution of Sn for Pb. The composition dependence of the lattice constant has been investigated by X-ray diffraction [143, 145, 146]. The lattice constant of $Pb_{1-x}Sn_xTe$ ($a_{Pb_{1-x}Sn_xTe}$) monotonically decreases from PbTe ($a_{PbTe} = 6.46$ Å) to SnTe ($a_{SnTe} = 6.31$ Å) as shown in Fig. 4.4(a), which is qualitatively understood by empirical Vegard's law:

$$a_{Pb_{1-x}Sn_xTe} = (1-x)a_{PbTe} + xa_{SnTe}. \tag{4.6}$$

Similar effect is expected to be brought by applying hydrostatic pressure to pristine PbTe, which will be mentioned in Sec. 4.1.6.

The effect of Sn substitution for the band gap has also been investigated in several previous studies. Dimmock *et al.* investigated the photoluminescence of $Pb_{1-x}Sn_xTe$ at 12 K and found that the band gap was suppressed with increment of x as shown in Fig. 4.4(b) [144]. The similar tendency was reported by later experiment [147]. On the other hand, fully substituted material SnTe is also known as a narrow-gap semiconductor with a gap of 0.3 eV at the L point, which is larger than that of PbTe. Further, the band gap of SnTe is smaller at 300 K than that at low temperature, *i.e.*, the band

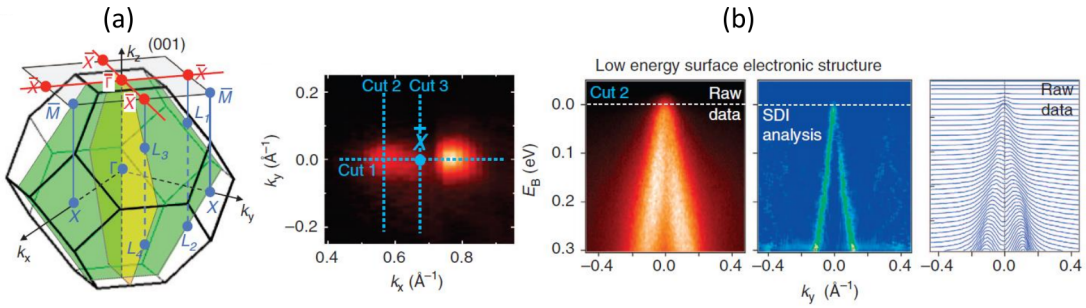

Figure 4.5: (a) The brillouin zone of FCC cubic lattice and Dirac surface states observed in $Pb_{0.6}Sn_{0.4}Te$ [151].

gap of SnTe has negative temperature coefficient, which is opposite to that of PbTe. From these facts, Dimmock *et al.* proposed a band structure model at the L point schematically shown in Fig. 4.4(c), in which the valence and conduction band in SnTe are inverted from those of PbTe. In PbTe, the valence and conduction band edges are group-theoretically belong to L_6^+ and L_6^- states, respectively. According to this model, the band gap decreases as L_6^+ and L_6^- states approach each other by Sn substitution, and becomes zero at specific composition with degeneration of these two states. At this band contact, the inversion of valence and conduction bands takes place. Then, the band gap increases as Sn substitution since the order of L_6^+ and L_6^- are inverted compared to that in PbTe. From Fig. 4.4(b), we can expect the realization of zero-gap state at a critical composition of $x_c \sim 0.35$. Such a composition-dependent band inversion is also known in $Bi_{1-x}Sb_x$ [148].

The composition dependence of the band gap mentioned above can be qualitatively understood by the difference between the relativistic effects in Pb and Sn atoms [144]. According to a band calculation, 36% of the valence L_6^+ state comes from a Pb s state and 31% of conduction L_6^- states comes from Pb p state. Comparing the difference of the relativistic effect between s (Pb $6s$ and Sn $5s$) and p (Pb $6p$ and Sn $5p$) states, the relativistic shift of the s and p states are estimated as 2.75 eV and 0.73 eV [149], respectively. Thus, the energy of L_6^+ and L_6^- states increase by $2.75 \times 0.36 = 0.99$ eV and $0.73 \times 0.31 = 0.23$ eV, respectively, with going from PbTe to SnTe. As is clear in schematic energy diagram shown in Fig. 4.4(c), L_6^+ and L_6^- should cross at a certain composition, which suggests the realization of a zero-gap state. Also, the reason why the energy gap of SnTe can be larger than that of PbTe is qualitatively explained by this model.

In order to clarify the change of electronic properties of $Pb_{1-x}Sn_xTe$ alloy system, quantum oscillations have been investigated through various physical properties in previous literature. Melngailis *et al.* investigated the Sn composition (x) dependence of the SdH oscillations in p-type $Pb_{1-x}Sn_xTe$ samples, and reported the decrease of ellipsoidal anisotropy K [150]. They also suggested that the spin-splitting of $x = 0.22$ sample is larger than that in previous result in pure PbTe.

4.1.4 Topological Properties of $Pb_{1-x}Sn_xTe$

Quite recently, the anomalous character of the energy band structure of $Pb_{1-x}Sn_xTe$ has attracted attention in a topological context. A novel class of topological materials "topological crystalline insulator" (TCI) was theoretically predicted by Fu [152], and

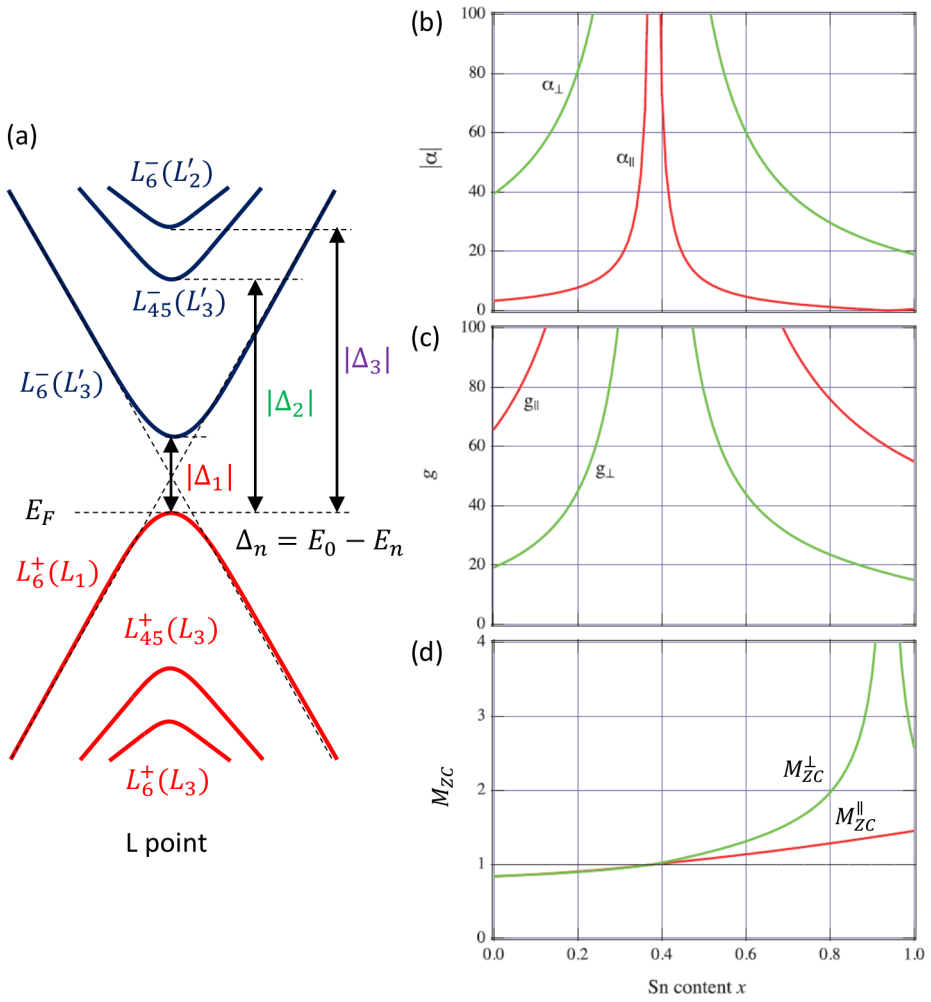

Figure 4.6: (a) Schematic energy band structure of PbTe at the L point. Carrier type is assumed to be hole, and Δ_{1-3} is the energy difference from the top of the valence band (E_0) defined as $\Delta_n = E_0 - E_n$. Calculated Sn content (x) dependence of the (b) inverse masses, (c) g-factors, and (d) ZC ratios [154]. $\parallel$ and $\perp$ indicates the magnetic field direction parallel and perpendicular to the $\langle 111 \rangle$ direction, respectively.

then, $Pb_{1-x}Sn_xTe$ system with $x > x_c \sim 0.35$ was shown as a candidate of TCI [153]. In other words, the electronic system of $Pb_{1-x}Sn_xTe$ undergoes topological phase transition at the critical composition x_c. TCI has metallic surface states with linear energy dispersion inside the bulk band gap. Unlike conventional topological insulator, in which metallic surface states protected by the time-reversal symmetry, surface states of TCIs are protected by its crystal symmetry. Recent ARPES study on $Pb_{1-x}Sn_xTe$ with inverted band structure reported observation of the surface states, which construct a Dirac cone in the vicinity of the Fermi level (Fig. 4.5) [151]. Although there are several recent reports which focus on the unconventional surface state, we do not introduce them since we focus on the bulk properties in this study.

Hayasaka *et al.* theoretically investigated the effect of spin-orbit interaction in $Pb_{1-x}Sn_xTe$ focusing on the ZC ratio [154], and deepened the understanding of relationship between the ZC ratio and Dirac electron system. The general formulae for inverse mass tensor and g-factor have been known according to the multiband $\boldsymbol{k} \cdot \boldsymbol{p}$

theory [155]. Hayasaka *et al.* applied above framework to the $Pb_{1-x}Sn_xTe$ system and obtained the exact formulae for the ZC ratio:

$$M_{ZC}^{\parallel} = \frac{1-\lambda|X|^2+\lambda'|Y|^2}{1+\lambda|X|^2+\lambda'|Y|^2}, \tag{4.7}$$

$$M_{ZC}^{\perp} = \frac{|1-\lambda' YZ^*|}{\sqrt{(1+\lambda'|Z|^2)(1+\lambda|X|^2+\lambda'|Y|^2)}}. \tag{4.8}$$

In this formulation, the carrier type is assumed to be hole, and the suffixes $\perp$ and $\parallel$ indicate the magnetic field direction perpendicular and parallel to the $\langle 111\rangle$ direction, respectively. $\lambda = \Delta_1/\Delta_2$ and $\lambda' = \Delta_1/\Delta_3$, and $\Delta_n = E_0 - E_n$ $(n = 1, 2, 3)$ is defined as the energy difference from the top of $L_6^+(L_1)$ valence band as shown in Fig. 4.6(a). X, Y, and Z are constants determined by the degree of interband couplings. Note that the contributions from the lower bands [$L_{45}^+(L_3)$ and $L_6^+(L_3)$] with the same parity vanish, and we can consider only upper bands [$L_6^-(L_3')$, $L_{45}^-(L_3')$, and $L_6^-(L_2')$] with different parity. When the band gap $|\Delta_1| \to 0$, namely, the Hamiltonian of this system is approximated to be two-band Dirac Hamiltonian, both $M_{ZC}^{\parallel}$ and $M_{ZC}^{\perp}$ become 1 since $\lambda, \lambda' \to 0$ in Eqs. (4.7) and (4.8). This means that M_{ZC} is unity regardless of magnetic field direction, which is known as a common consequence of the two-band Dirac system. When the contributions from the other band cannot be ignored, on the other hand, $M_{ZC}^{\parallel}$ and $M_{ZC}^{\perp}$ vary from unity, and can depend on the magnetic field direction. From these properties of M_{ZC}, they pointed out that the M_{ZC} can be an index to see how the system is close to the ideal two-band Dirac system, so to speak, "Diracness" of materials: we can estimate the "Diracness" of a material by the measurement of M_{ZC} and qualitatively evaluate similarity to the Dirac system. Compared to rather sensuous judgment of "Diracness" such as the appearance of the band dispersion based on calculations or ARPES measurements, or observation of the linear magnetoresistance, M_{ZC} provides quantitative framework to determine the "Diracness", and further enables us to compare the "Diracness" between different materials with each other. M_{ZC} can be estimated by the measurements of quantum oscillations, which indicates that M_{ZC} becomes a new experimental criterion to evaluate the "Diracness" of the system.

They also numerically calculated inverse mass ($\alpha_{\perp,\parallel}$), g-factor ($g_{\perp,\parallel}$), and ZC racio ($M_{ZC}^{\perp,\parallel}$) in whole x range from 0 to 1, which are shown in Figs. 4.6(b), (c), and (d), respectively. As we can see in Fig. 4.6(d), M_{ZC} gradually increases as x increases, and satisfy $M_{ZC}^{\perp} = M_{ZC}^{\parallel} = 1$ at $x = 0.381$, which is just the calculated band inversion point. This indicates that the zero-gap state realized in $Pb_{1-x}Sn_xTe$ can be regarded as an ideal "Dirac electron system".

There are several reports which investigate the bulk physical properties in the vicinity of topological phase transition. Assaf *et al.* reported the magneto-optical study of $Pb_{0.54}Sn_{0.46}Te$, which is assumed to be the TCI [156]. They reported absorption peaks originated both from the bulk and surface, and the Landau-level fan diagram constructed from the bulk absorption energy was explained by the massive Dirac model. The Landau-level fan diagram were well fitted by $\sqrt{B}$ dependence, which is characteristic of the Dirac system. Further, spin-split was missing in their report, which is ascribed to the situation that spin-splitting and cyclotron energy is almost equal. We note that similar magneto-optical properties were reported on $Pb_{1-x}Sn_xSe$ system [157].

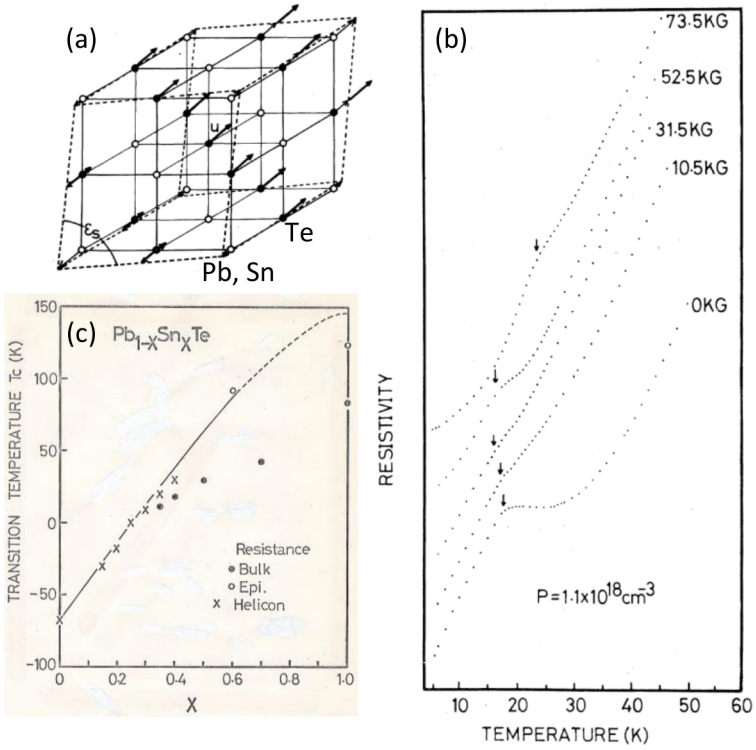

Figure 4.7: (a) Atomic displacement of the ferroelectric transition in $Pb_{1-x}Sn_xTe$ [158]. (b) Resistivity anomalies corresponding to the ferroelectric transition in $Pb_{0.6}Sn_{0.4}Te$ [159]. (c) Sn content (x) dependence of the ferroelectric transition temperature (T_c) in $Pb_{1-x}Sn_xTe$ [160].

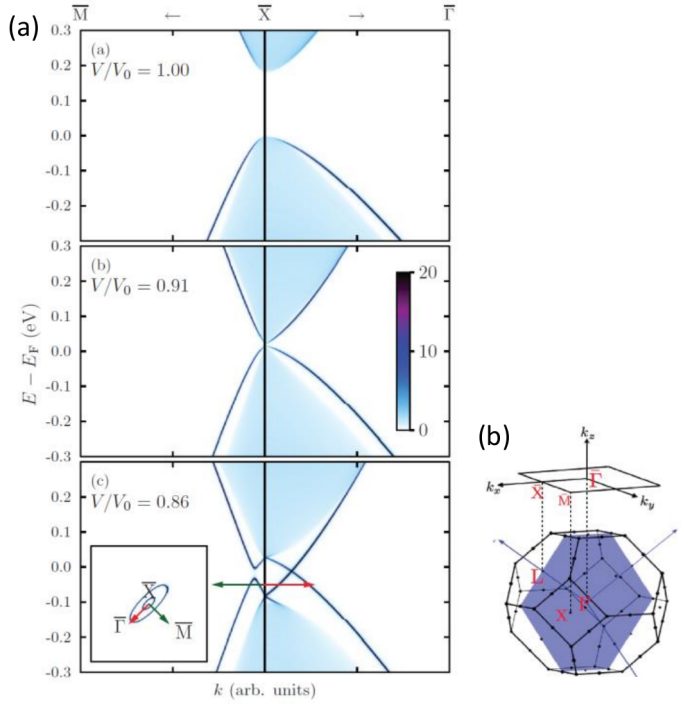

Figure 4.8: (a) Band structure calculations in PbTe under pressure. Upper, middle, and lower windows show the band structure at a volume ratio of $V/V_0 = 1.00$, 0.91, and 0.86, respectively. V_0 represents the volume at ambient pressure. (b) Corresponding representations of the high symmetry points in Brillouin zone [161].

4.1.5 Ferroelectric Transition in $Pb_{1-x}Sn_xTe$

SnTe is known to form the NaCl-type crystal structure at room temperature, while at low temperature, SnTe undergoes a structural phase transition to the rhombohedral $A7$ structure. This transition is explained by the relative displacement of sublattice along the $\langle 111 \rangle$ direction as shown in Fig. 4.7(a) [158]. As a result, rhombohedral SnTe is ferroelectric. On the other hand, PbTe forms NaCl-type structure down to 0 K and does not show any structural phase transition. Therefore, the critical temperature of the ferroelectric transition T_c^{FE}, which is ∼100 K in pure SnTe, decreases as x decreases, and reaches $T_c^{FE} = 0$ at a critical composition x_c^{FE}. The phase transition has been experimentally identified by an anomaly appeared in the temperature dependence of the resistivity. Figure 4.7(b) shows the resistivity anomaly observed in $Pb_{0.6}Sn_{0.4}Te$ corresponding to the ferroelectric transition. In this composition, T_c^{FE} is approximately 18 K, and it was found to increase by an application of a magnetic field. Takaoka *et al.* explained the magnetic field dependence of T_c^{FE} by a possible contribution of the interband electron-transverse optical phonon coupling [159]. Figure. 4.7(c) shows the Sn content dependence of T_c^{FE}. Although x_c^{FE} is regarded to be close to $x_c \sim 0.35$ at which the topological phase transition takes place, the relationship between band gap closure and ferroelectric transition remains unclear.

4.1.6 Physical Properties of Pressurized PbTe

In this section, we review the effect of another external parameter, hydrostatic pressure on PbTe. In earlier literature, the band gap at the L point was reported to decrease with applying pressure at a rate of -74 meV/GPa at room temperature [128]. The pressure dependence of the band gap at the L point was also investigated by calculation, in which the pressure coefficient of the band gap closure of ~ -40 meV/GPa was reported [162]. Based on these facts, we expect that the band gap of 0.18 eV becomes zero within a moderate pressure range below 10 GPa. Recent theoretical calculation predicted the pressure-induced topological phase transition from topologically trivial semiconductor to non-trivial TCI in IV-VI chalcogenides [161]. In case of PbTe, the band inversion at the L point was expected to realize at a volume ratio of $V/V_0 = 0.91$ (~ 4 GPa). Here, V_0 is the volume at ambient pressure. The crystal structure of PbTe under pressure was reported by several experimental groups [163–166]. PbTe undergoes the first structural phase transition to the *Pnma* structure with increment of the pressure. Although the reported transition pressure (4.5–7.5 GPa) varies with research groups, topological phase transition mentioned above can occur within the NaCl-type structure. However, there are few experimental investigation regarding to the electronic state of PbTe under pressure, the details remains unclear.

4.2 Purpose of the Study

In recent studies of topological materials, numbers of novel phenomena have been reported experimentally. However, the universal nature of topological materials are buried in their complex band structure, and hence, it is very hard to accurately extract the essence from the experimental results. PbTe and its alloy system can be one of the best candidates to solve the problem. In PbTe, the physical properties are expected to be governed by the carriers only in the vicinity of the narrow gap at the L point. This simplicity is notable compared to other topological materials with multiple kinds of carriers. Further, the manipulation of parameters such as composition or hydrostatic pressure enables us to continuously control the band structure of PbTe from degenerate semiconductor to TCI *via* the zero-gap state. This character posses great possibility to evaluate the true nature originated from the non-trivial band topology with precisely controlling the band topology.

Another problem in previous research of topological material is how to identify their non-trivial topology. Although the observation of linear band dispersion is commonly accepted as an evidence of topological materials, this criteria can bring sensuous discussion. Alternative criteria with firm quantitativity should be necessary. We thus focus on the possibility of the ZC ratio which quantitatively reflects the degree of "Diracness" of materials. However, determination of the ZC ratio accompanies ambiguities, and thus, high magnetic field measurements are necessary for precise determination. The firm methodology for determining the ZC ratio from the experimental data, and careful confirmation of its validity is firstly needed.

Based on this cognition, we investigated PbTe by tuning its band topology with Sn substitution and hydrostatic pressure.

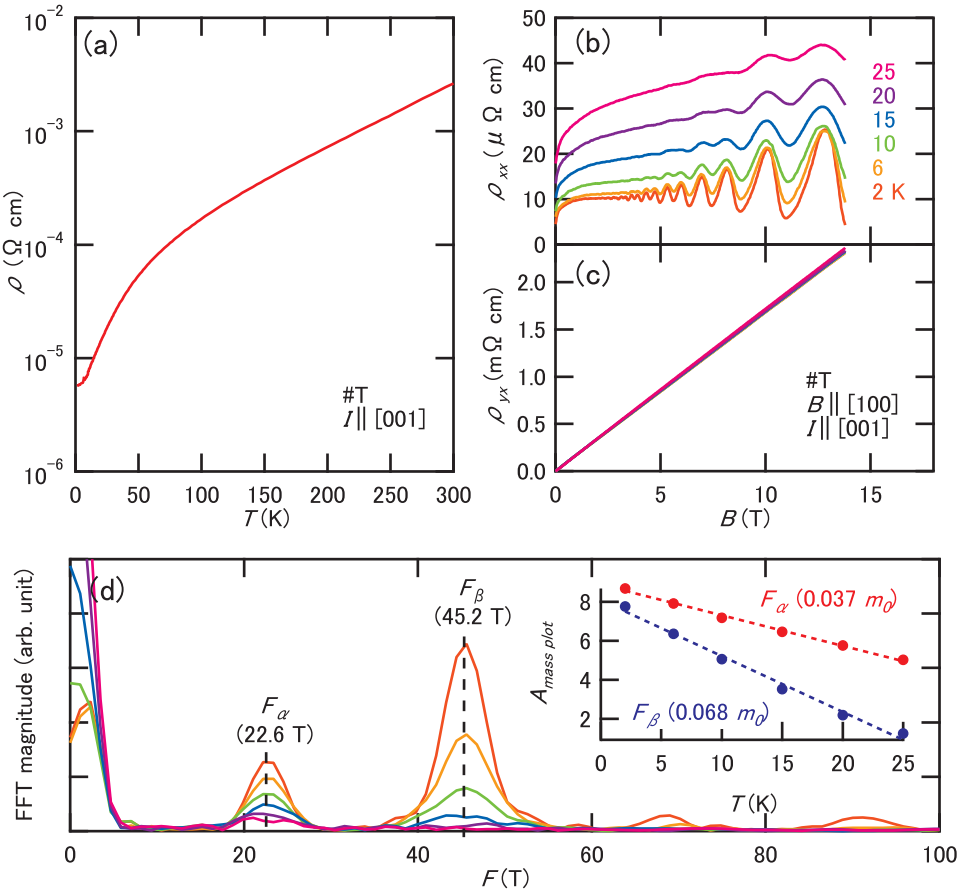

Figure 4.9: (a) Temperature dependence of the resistivity from 2 to 300 K. (b) Magnetoresistance ρ_{xx} and (c) Hall resistance ρ_{yx} up to 14 T. (d) FFT spectrum of SdH oscillation superimposed on ρ_{xx}. The inset of (d) shows the mass plot for cyclotron mass determination. The dashed lines are fitting results based on Eq. (3.11).

4.3 Results and Discussion

4.3.1 Pristine PbTe at Ambient Pressure

Firstly, we investigated the transport properties of PbTe at ambient pressure synthesized by the vapor transport method (referred as #T sample). As shown in Sec. 2.8, the #T sample has higher carrier density than those synthesized by the Bridgemann method. Figure 4.9(a) shows the temperature dependence of the resistivity with electric currents applied along the [001] direction. Resistivity showed metallic dependence in whole temperature range from 300 to 2 K, which indicates that the sample has finite number of degenerated carriers at low temperature. The RRR [ρ(300 K)/ρ(2 K)] is obtained as 453 from the data shown in Fig. 4.9(a). Figure 4.9(b) shows the magnetoresistance (ρ_{xx}) up to 14 T at various temperatures. In the following resistivity measurements, magnetic fields and currents were applied along the [100] and [001] directions, respectively, unless otherwise specified. Although [100], [010], and [001] are symmetrically equivalent, we use these notations to specify the relationship between applied magnetic field and electric current. Shubnikov-de Haas (SdH) oscillations are clearly observed at 2 K, which are damped with increasing temperature. In these experiments, the magnetoresistance

effect is less sensitive to magnetic flux density (B). However, it seems to vary with samples as will be mentioned later. Figure 4.9(c) shows the magnetic field dependence of Hall resistance (ρ_{yx}). The ρ_{yx} is positive and increases linearly as B increases up to 14 T, which suggest that a single kind of hole carriers are responsible to the transport properties. The slope of ρ_{yx} is almost independent of temperature up to 25 K, which indicates that the hole density (n_p) is insensitive to temperature. It is notable that ρ_{yx} is almost 100 times larger than ρ_{xx}. Hence, SdH oscillations are inconspicuous in ρ_{yx} owing to the huge linear background. The hole density ($n_p = 3.7 \times 10^{18}$ cm^{-3}) and mobility ($\mu_p = 3.8 \times 10^5$ cm^{2}V^{-1}s^{-1}) are estimated by the single carrier Drude model:

$$\rho_{xx} = \frac{1}{e\mu_p n_p}, \tag{4.9}$$

$$\rho_{yx} = \frac{B}{n_p e}. \tag{4.10}$$

We evaluated μ_p using ρ_{xx} at $B = 0$. Above values are consistent with the previous report [140]. Here, we comment on the magnitude relationship between σ_{xx} and σ_{xy}. Since $\rho_{xx} \ll \rho_{yx}$ in this case, conductivities are represented as $\sigma_{xx} \sim \rho_{xx}/\rho_{yx}^2$ and $\sigma_{xy} \sim 1/\rho_{yx}$. Thus, $\sigma_{xx} \ll \sigma_{xy}$ is satisfied, and the peak/dip relation between σ_{xx} and ρ_{xx} is almost identical. We actually confirm this by comparing ρ_{xx} and σ_{xx}.

Here, we focus on the frequency of the SdH oscillations superimposed on ρ_{xx}. Figure 4.9(d) shows the FFT spectra of the SdH oscillations. We can recognize two obvious peaks (labeled by F_α and F_β) showing systematical dumping as temperature increases. The inset of Fig. 4.9(d) shows the mass plots for F_α and F_β. Small cyclotron masses of 0.037 m_0 for F_α and 0.068 m_0 for F_β were identified. Existence of two kinds of Fermi pockets with different cross-section may result in this two-peak feature with different cyclotron masses, while it is inconsistent with the single-carrier-like ρ_{yx} shown in Fig. 4.9(c). Since $F_\beta \simeq 2F_\alpha$, we can alternatively interpret the β as the second harmonic of α. In this case, reasonable explanation is needed for why amplitudes of higher harmonics are larger than those of fundamental wave.

To obtain the insight into the origin of these frequency peaks, we investigated the angular dependence of the SdH oscillations. If F_α and F_β peaks originate from multiple Fermi pockets, these peaks vary independently; If F_β is the second harmonic of F_α, the relationship $F_\beta \simeq 2F_\alpha$ should be maintained regardless of a magnetic field direction. Figure 4.10(a) shows the angular dependence of the SdH oscillations superimposed on ρ_{xx}. Here, $\Delta\rho_{xx}$ indicates the oscillatory components obtained by subtraction of polynomial curve. Magnetic field was tilted between the [010] to [100] directions. SdH oscillation pattern complicatedly varied with the field direction. Detailed analysis and Landau indices for this oscillation pattern will be discussed later. Here, we focus on the angular dependence of oscillation frequencies. Figures 4.10(b) and (c) show the FFT spectra calculated from $\Delta\rho_{xx}$ in various field directions, and a contour plot based on (b), respectively. In Fig. 4.10(c), the left axis and color bar represent the frequency and amplitude of the SdH oscillations, respectively. It is clearly shown that the relationship $F_\beta \simeq 2F_\alpha$ is always satisfied, which supports that F_α and F_β stem from the same Fermi pocket at the L point. To quantitatively confirm this, we fitted the observed angular dependence of SdH frequencies by single Fermi pocket model. We assume that the Fermi pocket at the L point is simple ellipsoid aligned along the $\langle 111 \rangle$ direction, which is characterized by the length of short (a) and long (b) axes of the ellipsoid in the k-space [Fig. 4.10(d)]. In this case, the fundamental frequencies F_{fund} are calculated by Eq. (4.1). Solid lines overlayed on Fig. 4.10(c) show the angular dependence of fundamental

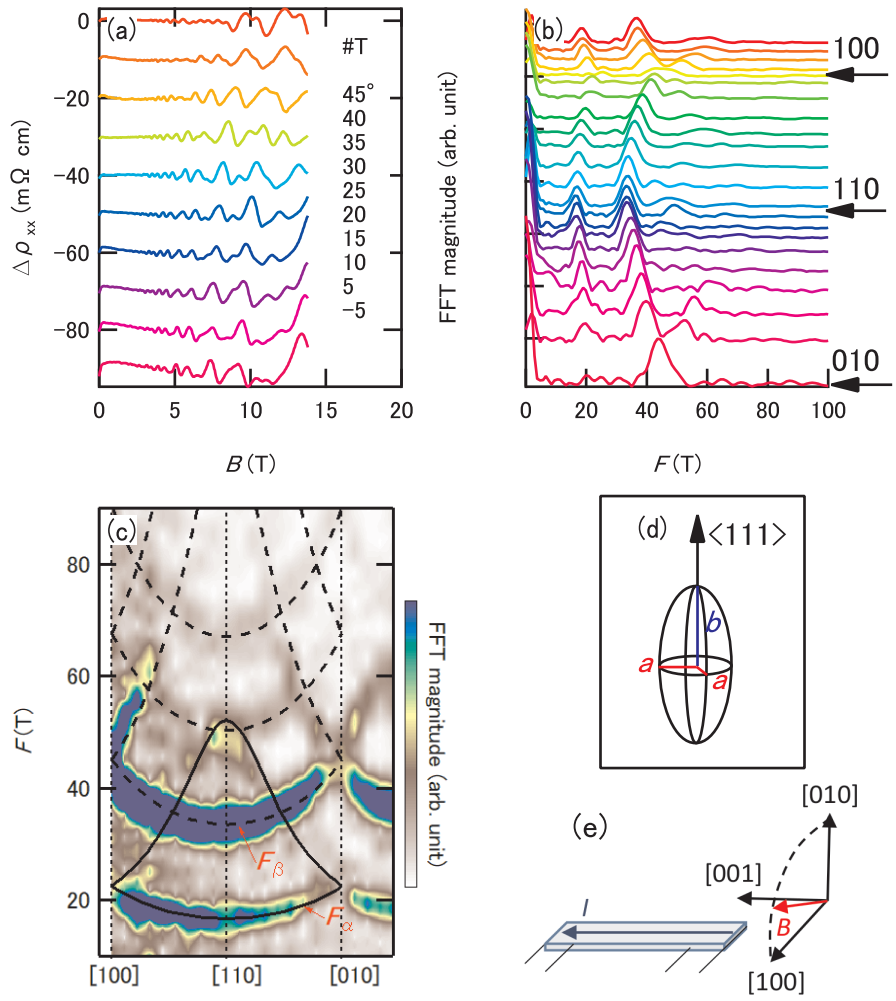

Figure 4.10: (a) Angular dependence of the $\Delta\rho_{xx}$. Magnetic field was swept between [100] and [110] in the plane perpendicular to the [001] direction, which is shown in (e). The angles from [110] direction are shown. (b) Angular dependence of the FFT spectrum calculated from $\Delta\rho_{xx}$. (c) The contour plot of SdH frequency with the direction of the magnetic field. The magnetic field is rotated between [010] and [100] directions in the plane perpendicular to [001] direction, which is shown in (e). The color bar indicates the magnitude of FFT spectra of the SdH oscillations. Solid and dashed curves shows the fundamental frequencies and higher harmonics, respectively, calculated by assuming the ellipsoidal Fermi pocket as shown in (d) (see text in detail). (d) The ellipsoidal Fermi surface assumed in the analysis. (e) The relationship between crystal axes and current directions. The magnetic field is always applied perpendicular to the current.

frequencies F_{fund} calculated from cross section of the ellipsoid perpendicular to the field direction. In this calculation, we set the carrier density which is enclosed inside the ellipsoid as 1.1×10^{18} cm^{-3} and the anisotropy of ellipsoid to be $K = (b/a)^2 = 13.7$. This anisotropy factor reproduces well the previous report [138, 140]. Since there are 4 ellipsoids in the first Brillouin zone, the total carrier density corresponds to 4.4×10^{18} cm^{-3}, which is in good agreement with $n_p = 3.7 \times 10^{18}$ cm^{-3} determined from ρ_{yx}. Moreover, we can reproduce whole angular dependence of SdH frequency up to 100 T by introducing higher harmonics $2F_{fund}$, $3F_{fund}$, and $4F_{fund}$ [shown with broken lines in Fig. 4.10(c)], which supports the validity of the above model. The difference of the cyclotron masses in F_α and F_β mentioned in the inset of Fig. 4.9(d) also supports this interpretation. Since ordinal cyclotron mass analysis, the contribution from the higher harmonics is ignored, and thus, Eq. (3.10) or (3.11) can be used only under the condition that the higher harmonics are sufficiently negligible compared to the fundamental one. The present case apparently violates this condition. If we intend to estimate accurate cyclotron mass from the peak of 2nd harmonic, m^* should be replaced by $2m^*$, which is evident in detailed LK formula [Eq. (4.11)]. Without this correction, m^* is overestimate by a factor of 2, which explains the difference of cyclotron masses shown in the inset of Fig. 4.9(d). From these results, we conclude that Fermi pockets are located only at the L points, and F_β is the second harmonic of F_α.

Next, we focus on the magnetization (M), which is a thermodynamic quantity. Figure 4.11(a) shows the magnetic field dependence of M up to 7 T. Here, B was applied along the [100] direction. Clear de Haas-van Alphen (dHvA) oscillations overlap on the diamagnetic linear slope. Such a linear diamagnetism is reported on elemental bismuth, graphite [167], and $Pb_{1-x}Sn_xSe$ [168]. For reference, the magnetization of bismuth, which is known to show titanic diamagnetism at low temperature, was also measured. Figure 4.11(b) shows the comparison of diamagnetism between the #T sample and bismuth. Here, M was normalized by the molar mass, 334.8 g/mol for PbTe and 418 g/mol for Bi_2. Although the magnitude of diamagnetism in PbTe is about 1/6 of that in bismuth, the significant diamagnetism is worth mentioning. Figure 4.11(c) shows the FFT spectrum of the dHvA oscillations. The positions of FFT peaks reproduce the result of transport measurements. Since the maximum magnetic field is lower than that in transport measurements, the magnitude of the second harmonic is smaller than the fundamental one. As we showed in the analysis of the SdH oscillation, the cyclotron masses approximately 2 times differ between F_α and F_β, which supports that F_β is the second harmonic of F_α.

Here, we consider the reason why the amplitude of $2F_\alpha$ can be larger than that of F_α by taking the effect of Zeeman-splitting into account. According to the Lifshitz-Kosevich (LK) theory, the oscillatory component of ρ_{xx} is represented by the following form including the ZC ratio $M_{ZC} = g^*\mu_B B/(\hbar\omega_c)$ [44, 122]:

$$\begin{aligned}\frac{\Delta\rho_{xx}}{\rho_0} \simeq \frac{5}{2}\sum_{p=1}^{\infty}\sqrt{\frac{B}{2pF_\alpha}} \\ \times R_T(T,p)R_D(T_D,p)R_S(M_{ZC},p) \\ \times \cos\left[2\pi p\left(\frac{F_\alpha}{B}+\frac{1}{2}\right)-\frac{\pi}{4}\right].\end{aligned} \tag{4.11}$$

Here, $\Delta\rho_{xx}$, ρ_0 and T_D are ρ_{xx} after subtracted background, resistivity at $B = 0$, and Dingle temperature, respectively. The natural number p represents the number of harmonics. The phase factor γ in Eq. (4.4) was set to 1/2 since PbTe is assumed

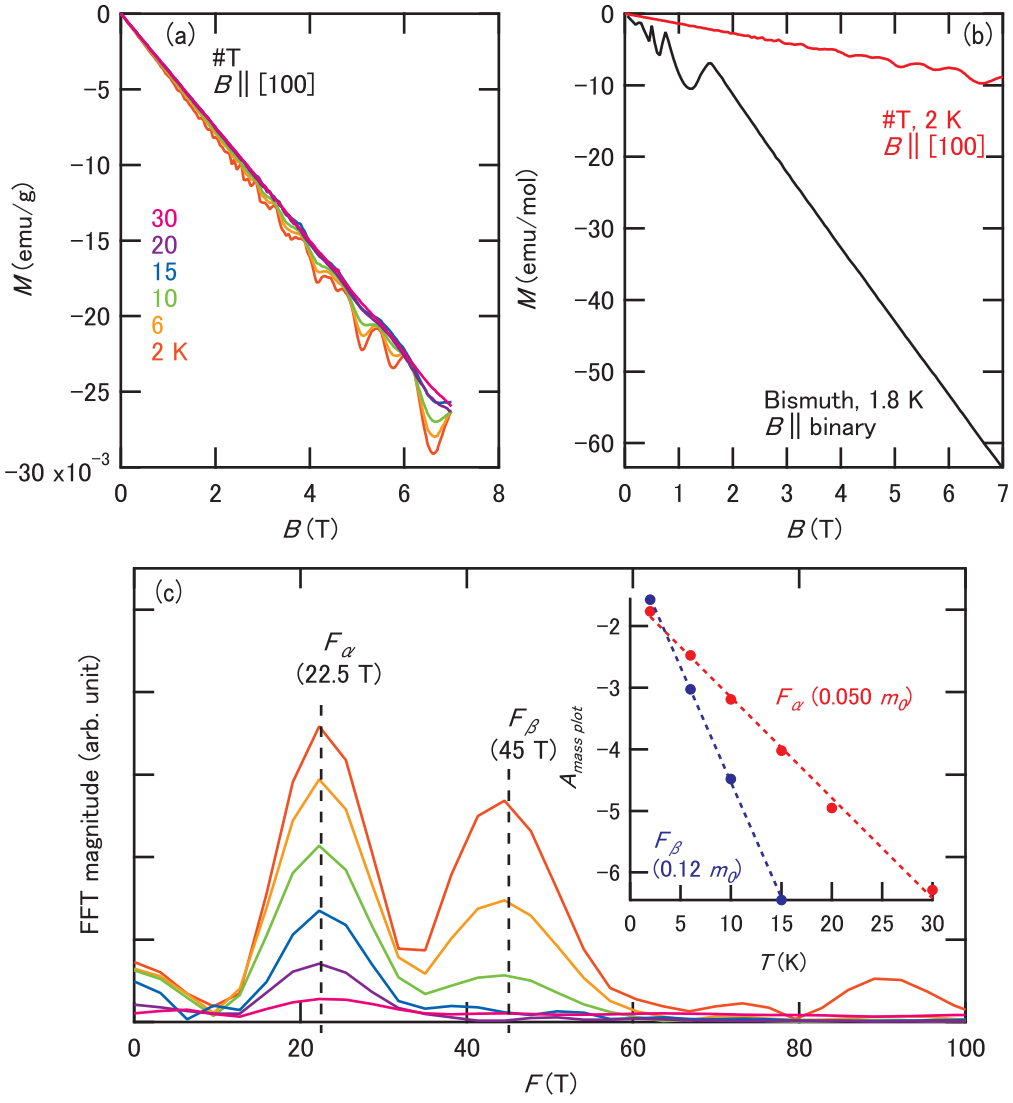

Figure 4.11: (a) Magnetic field dependence of the magnetization up to 7 T. (b) Comparison of diamagnetism between PbTe (red) and bismuth (black). (c) FFT spectra of the dHvA oscillations in #T. The inset of (c) shows the mass plot for cyclotron mass determination.

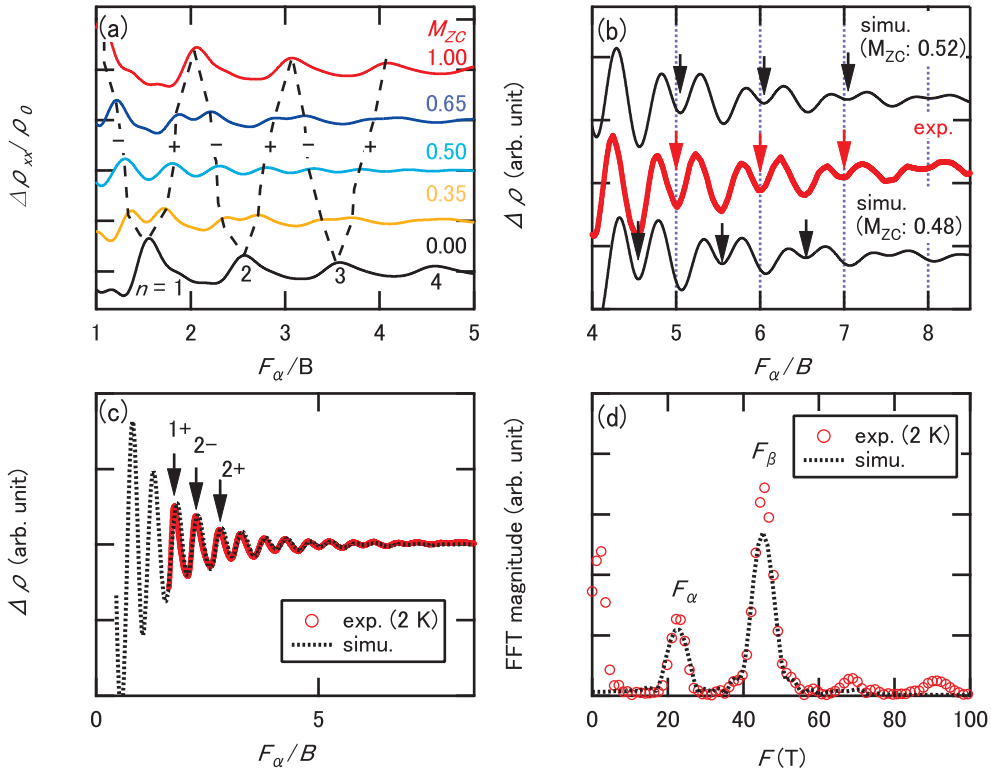

Figure 4.12: (a) Simulated oscillatory components in ρ_{xx} as a function of F_α/B at $M_{ZC} = 0.00$, 0.35, 0.50, 0.65, and 1.00. (b) Comparison of oscillatory components between the experiment (red) and simulation (black) in magnetic field region $F_\alpha/B > 4$. Simulation was performed for cases of $M_{ZC} = 0.52$ (upper) and 0.48 (lower). Shallower dips are indicated by arrows. (c) Comparison of whole SdH oscillation between the experiment at 2 K (red) and simulation (black). (d) Comparison of the FFT spectra between the experimental data at 2 K (red symbols) and simulated data (black broken line).

to be trivial semiconductor. In addition, the Fermi surface of PbTe was found to be simple ellipsoidal, and thus, double sign in the third terms inside cos function in Eq. (4.4) was set to −. Each cosine term has three damping factors: temperature factor $R_T(T,p) = 2\pi^2 p k_B T/(\hbar\omega_c)/\sinh[2\pi^2 p k_B T/(\hbar\omega_c)]$, Dingle factor $R_D(T_D,p) = \exp[-2\pi^2 p k_B T_D/\hbar\omega_c]$, and spin factor $R_S = \cos(pM_{ZC}\pi)$. We consider a case where $g^*\mu_B B$ is equal to a half of $\hbar\omega_c$, namely, $M_{ZC} = 0.5$. In this case, $R_S(0.5,p) = 0$ for odd p, while $R_S(0.5,p) = \pm 1$ for even p. Although the R_T and R_D exponentially decreases with increasing p, the second harmonics can dominate over the fundamental one when M_{ZC} is close to 0.5. Therefore, we can expect relatively large second harmonic in the vicinity of $M_{ZC} = 0.5$. Figure 4.12(a) shows the simulated modification of SdH oscillation by increment of M_{ZC} from 0 to 1. Each curve is simulated by Eq. (4.11) substituting appropriate values in m^*, F_α, and T_D. Peaks of resistivity initially split into two indicated by + and − in Fig. 4.12(a), and move to opposite directions with each other as M_{ZC} increases toward 1. Then, at $M_{ZC} = 1$, two peaks having different Landau indices merge into the same peak. Here, the phase of oscillation differs by π compared to that in $M_{ZC} = 0$. As expected above, the period of oscillation at $M_{ZC} = 0.5$ becomes just a half of that at $M_{ZC} = 0$ or 1. Then, we compare our experimental results with simulated SdH oscillation around $M_{ZC} = 0.5$, and find suitable M_{ZC}. Figure 4.12(b) shows the comparison between experimental result (red) and simulated curves (black) based on Eq. (4.11). These curves are vertically shifted for clarity. Simulation was performed for $M_{ZC} = 0.52$ and 0.48 assuming the parameters as $m^* = 0.05\ m_0$, $T_D = 10$ K, and $F_\alpha = 22.6$ T. Relatively small contributions from $p \geq 3$ are ignored. Although the wave forms of $M_{ZC} = 0.52$ and $M_{ZC} = 0.48$ look quite similar, we can see that the simulated curve with $M_{ZC} = 0.52$ better reproduce the experimental result than that with $M_{ZC} = 0.48$ [focus on the positions of the shallower dips indicated in Fig. 4.12(b)]. Figure 4.12(c) shows the comparison of whole SdH oscillation between experimental result (red) and simulated curves (black) with $M_{ZC} = 0.52$. Both the peak/dip structures and phase of oscillation agree well with the experimental result. Landau indices of the last three peaks are shown assuming $M_{ZC} = 0.52$. Figure 4.12(d) shows the FFT spectrum of experimental data at 2 K (red circles) and simulated curve (broken line). We can reasonably reproduce the amplitude ratio between F_α and F_β and anomalously large second harmonics.

Although the difference in the vicinity of $M_{ZC} = 0.5$ as shown in Fig. 4.12(b) may look insignificant, this can cause crucial change in the construction of Landau-level fan diagram as shown below. We assume typical system which have light carrier mass of $m^* = 0.08m_0$, fundamental frequency of $F_\alpha = 100$ T, and moderate Dingle temperature of $T_D = 10$ K. We performed the numerical simulation for above case based on the LK formula [Eq. (4.11)]. The results are shown in Figs. 4.13(a) and (b). Here, we assumed relatively high temperature $T = 20$ K, and showed the case of $M_{ZC} = 1$, 0.55, 0.45, and 0. As is clear in Figs. 4.13(a) and (b), the spin-splittings are discernible only for $F_\alpha/B < 10$. Thus, in both Figs. 4.13(a) and (b), the peak/dip positions look identical at a glance in magnetic fields with $F_\alpha/B > 10$. That is, in case that magnetic field is not strong enough to observe the spin-splitting effect, fan diagram analysis cannot distinguish $M_{ZC} = 1$ and 0.55, or $M_{ZC} = 0.45$ and 0 in spite of the significant difference of the ZC ratio. Further, we focus on the cases of $M_{ZC} = 0.45$ and 0.55 in Fig. 4.13. Although the difference of the ZC ratio is only 0.1 between these case, the phase of the oscillations differs by π. Consequently, fan diagram analysis may conclude the realization of non-trivial Berry's phase even in trivial materials with $M_{ZC} = 0.55$ when only the oscillation in the region $F_\alpha/B > 10$ is available. From this considerations, we have to be careful

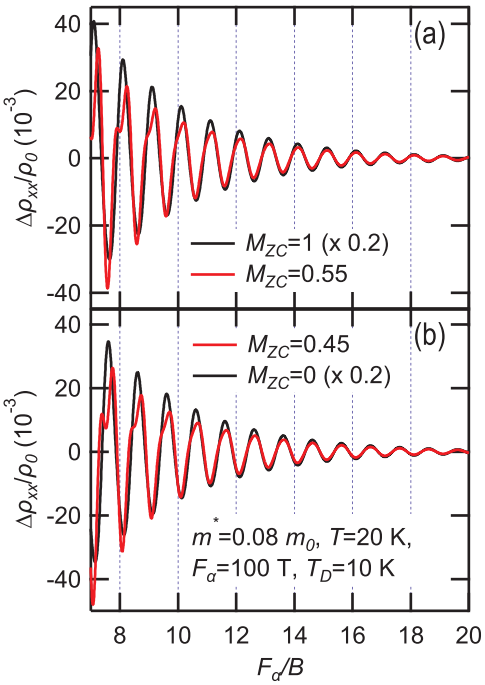

Figure 4.13: Comparison of the simulated oscillation structures between (a) $M_{ZC} = 1$ and $M_{ZC} = 0.55$ cases, and (b) $M_{ZC} = 0.45$ and $M_{ZC} = 0$ cases. Simulations were performed based on the LK formula, assuming $m^* = 0.08m_0$, $T = 20$ K, $F_\alpha = 100$ T, and $T_D = 10$ K.

in the fan diagram analysis in case that the effect of spin-splitting is smeared out in the quantum oscillations in lower field. This point is not necessarily considered in widely-adopted Landau-level fan diagram analysis. High-field experiments for $F_\alpha/B < 10$ are necessary to distinguish whether the spin-sprit exists or not in above situation.

As mentioned in Sec. 4.1, Burke *et al.* determined $M_{ZC} = 0.58$ from the spin-splitting and phase of SdH oscillation, which agree well with our result $M_{ZC} = 0.52$. In their result, distinct anisotropy is reported in M_{ZC} as shown in Table 4.1 [138]. To clarify this, we focus on the detailed structure of SdH oscillations. Figure 4.14(a) shows the $\Delta\rho_{xx}$ with the magnetic field rotated from [100] to [110] in the (001)-plane as shown in the inset in Fig. 4.14(b). The horizontal axis is normalized by each F_α obtained by the FFT. Starting from the indices for $B||[100]$ showin in Fig. 4.12(c), we can identify Landau indices at various field directions. If M_{ZC} has anisotropy as suggested by Burke *et al.*, peak positions should vary with field direction. However, Figure 4.14(a) shows that the peaks are almost independent of field direction, which indicates the isotropic M_{ZC}. We obtained the angular dependence of M_{ZC} based on Eq. (4.3). M_{ZC} shown in Fig. 4.14(b) is the averaged value over $n = 5, 4, 3$ cases in Eq. (4.3). M_{ZC} is almost independent of the field direction and shows the isotropic nature. The isotropy of M_{ZC} is consistent with recent theoretical prediction by Hayasaka *et al.* [154] The anisotropy of M_{ZC} reported in a previous report [138] was not identified in our results.

Up to here, we found that oscillation structure was well reproduced assuming $M_{ZC} = 0.52$, and M_{ZC} is almost independent of field direction. However, $M_{ZC} = 0.52$ and Landau indices shown in Figs. 4.12(c) and 4.14(a) is not unique as explained below. Figure 4.15 shows the Landau-level structures at several M_{ZC} up to 3.48 following Fig.

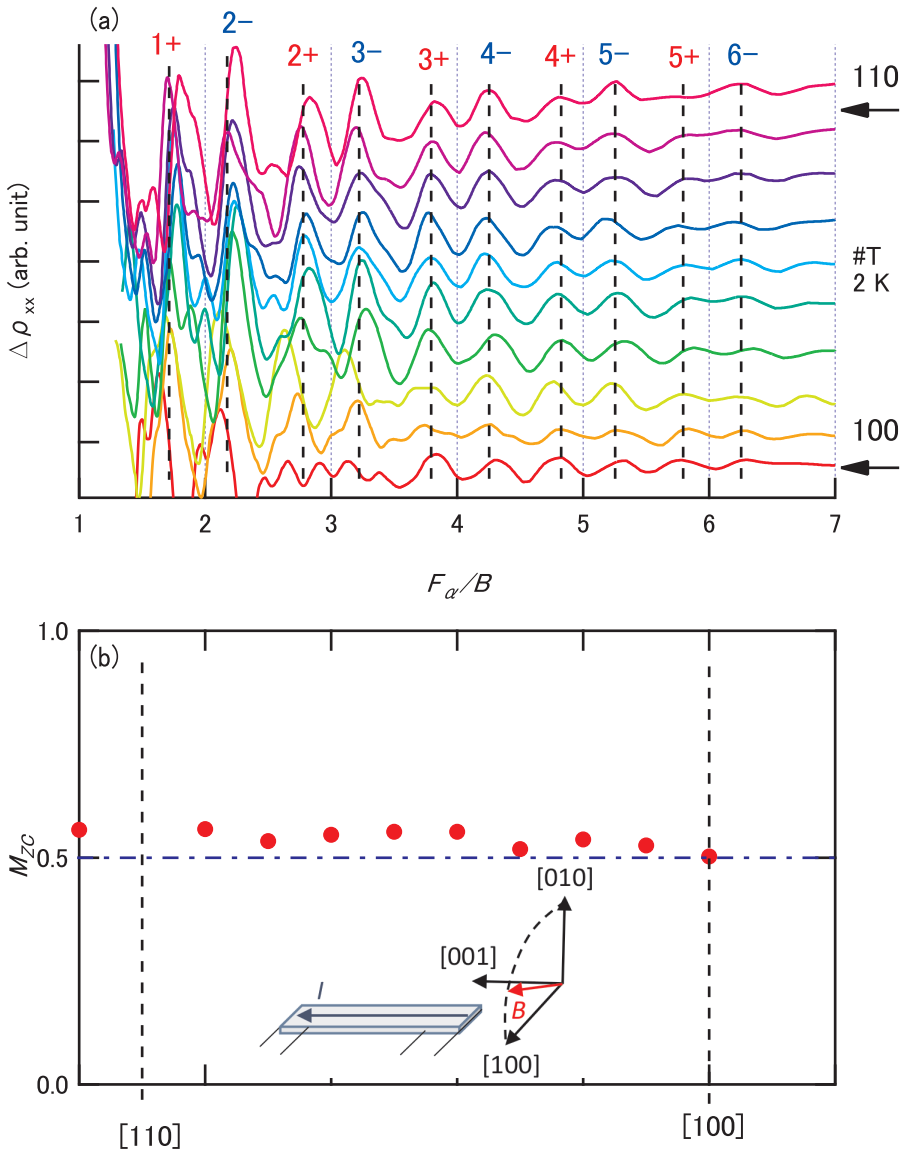

Figure 4.14: (a) Angular dependence of $\Delta\rho_{xx}$. Magnetic field was swept between [100] and [110] in the inset of (b). $\Delta\rho_{xx}$ are plotted as a function of F_α, and F_α was determined by the FFT of each curve. (b) Angular dependence of the ZC ratio from [100] to [110].

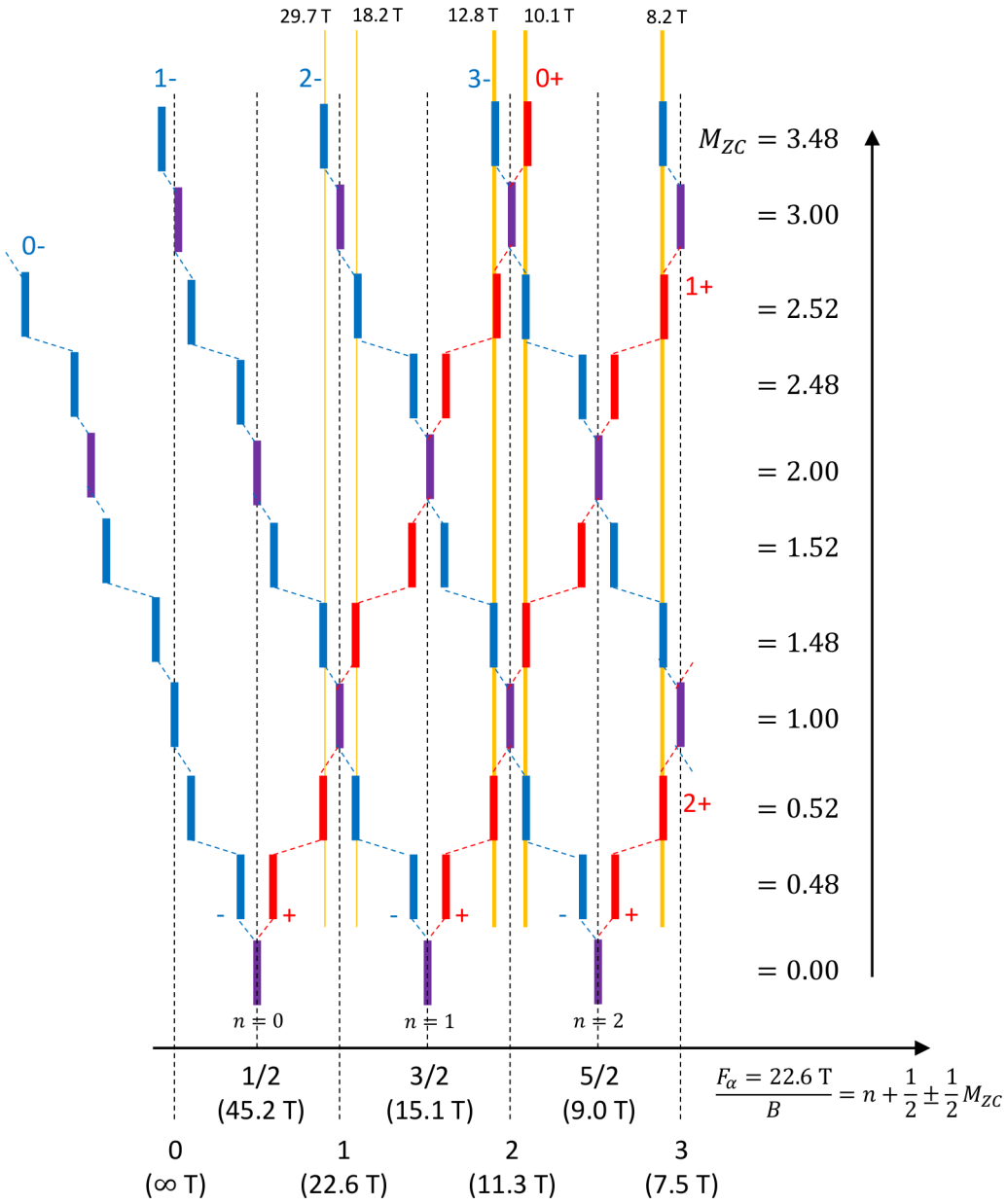

Figure 4.15: Landau-level structures at several ZC ratios. The horizontal and longitudinal axis represent the values of F_α/B and M_{ZC}, respectively.

4.3(a). Since the oscillation frequency was found to $F_\alpha = 22.6$ T, all the level-crossing field can be calculated. Observed peak position in ρ_{xx} up to 14 T are shown by the vertical bold lines. Cases with $M_{ZC} > 3.48$ apparently cannot explain the observed peak positions, and hence, not shown. Among the cases shown in Fig. 4.15, we can see that M_{ZC} =0.52, 1.48, 2.52, and 3.48 can reproduce the observed peak positions up to 14 T. We cannot eliminate this ambiguity by current data. To further restrict the possible cases, experiments up to higher magnetic fields is crucial. If two oscillations are observed at around 18 and 30 T (indicated by vertical thin lines in Fig. 4.15), M_{ZC} is 0.52 or 1.48. If only one oscillation is observed, M_{ZC} is 2.52 or 3.48. To clarify this point, we performed the quantum oscillation measurements in pulsed magnetic fields up to 55 T.

Figures 4.16(a) and (b) show the magnetic field dependence of resistivity and magnetization, respectively. The red and blue lines indicate the raw field dependences and oscillation components obtained by subtraction of backgrounds, respectively. We observed two local maxima (∼20 and 32 T) in both resistivity and magnetization, and no oscillation was found in higher fields up to 55 T. In addition, diamagnetism shown in Fig. 4.11(a) was found to continue to increase up to 55 T. We note that the field dependence of the background in ρ_{xx} is different from that in Fig. 4.9(a) measured in a different sample piece. Although the reason is not clear for us at present, the background tends to enhance in poor RRR samples. In spite of the difference in the underlying magnetoresistance, the peak/dip positions of the SdH oscillations are reproduced well between the samples with different background, and thus, the quantum oscillation itself is almost sample-piece-independent. Further, we measured elastic properties through ultrasound measurements in pulsed magnetic fields. Figures 4.16(c) and (d) show the ultrasonic attenuation coefficient and sound velocity, respectively, as a function of magnetic field up to 55 T. In both traces, clear acoustic quantum oscillations are observed with the higher S/N ratio compared to resistivity and magnetization, which is due to the absence of huge background in the elastic property measurements. Hence, ultrasonic measurements can be a powerful probe to investigate the quantum oscillations in pulsed magnetic fields. Also in ultrasonic attenuation coefficient and sound velocity, we recognize clear anomalies at approximately 18 and 30 T, and no noticeable structure was observed in higher field, which are consistent with the resistivity and magnetization measurements.

From these results, we identified the two quantum oscillations at around 18-20 T and 30-32 T, which certificate depopulations of the Landau subbands from the Fermi level at these magnetic fields. These values agree well with the expected values shown in Fig. 4.15. Therefore, we can restrict the possible M_{ZC} to 0.52 or 1.48. In both cases, the system enters the spin-polarized quantum limit state in which all conduction carriers are confined into the lowest 0− subband. The difference between these two cases is the order of spin + and −. To distinguish these two cases experimentally, we should perform a measurement to identify corresponding spins of each subbands. Since such a measurement is not available at the current stage, we finally adopt recent theoretical suggestion. According to [154], the analytic forms of $M_{ZC}^{\parallel}$ and $M_{ZC}^{\perp}$ are represented by Eqs. (4.7) and (4.8). Since $\Delta_{1\text{–}3} < 0$ in case of PbTe, $\lambda, \lambda' > 0$ is satisfied. Thus, the denominators are *always* larger than numerators in Eqs. (4.7) and (4.8), which leads to $M_{ZC} < 1$ for PbTe. Thus, we conclude that $M_{ZC} = 0.52$ is realized in our #T sample. Figure 4.16(e) shows the Landau-level fan diagram constructed from those in ρ_{xx} up to 55 T. The blue symbols are taken from the experiment up to 14 T, and red symbols in pulsed magnetic fields. Dashed line are averaged F_α/B of + and − subbands, which has x-intercept of ~ 0.47.

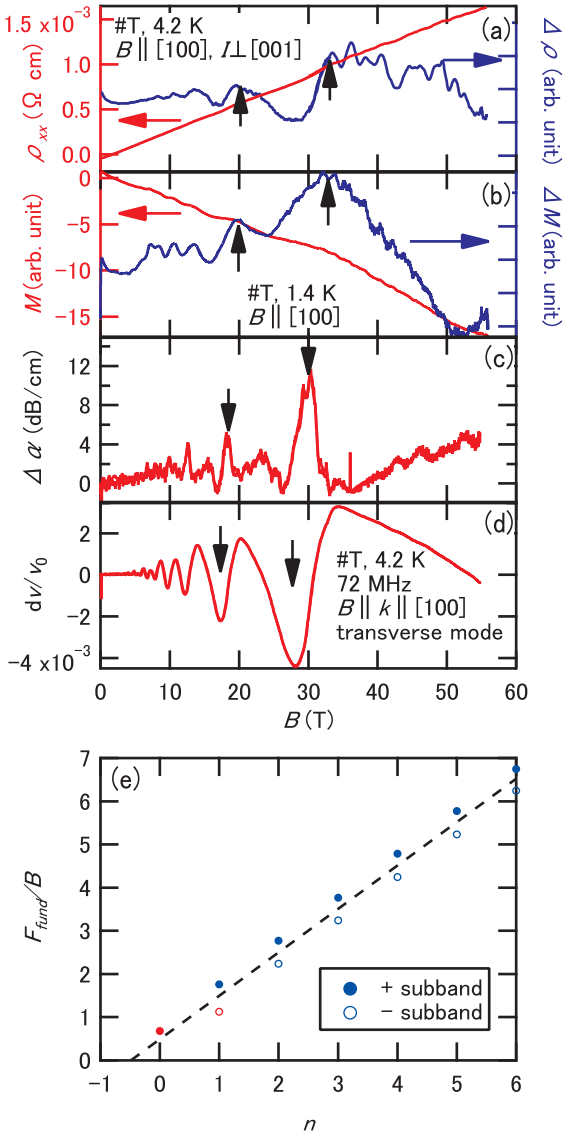

Figure 4.16: Magnetic field dependence of (a) magnetoresistance, (b) magnetization, (c) ultrasonic attenuation coefficient, and (d) sound velocity up to 55 T. In (a) and (b), blue traces are oscillatory components obtained by subtracting linear background from the red traces. In (a) to (d), newly identified structures in high-field measurements are indicated by solid arrows. (e) Landau-level fan diagram obtained experimentally from SdH oscillations in magnetoresistance. Closed and open symbols represent + and − subbands, respectively. Blue and red symbols were obtained from the measurements in static fields up to 14 T and pulsed magnetic fields up to 55 T, respectively. The broken lines represents the averaged F_α/B of + and − subbands.

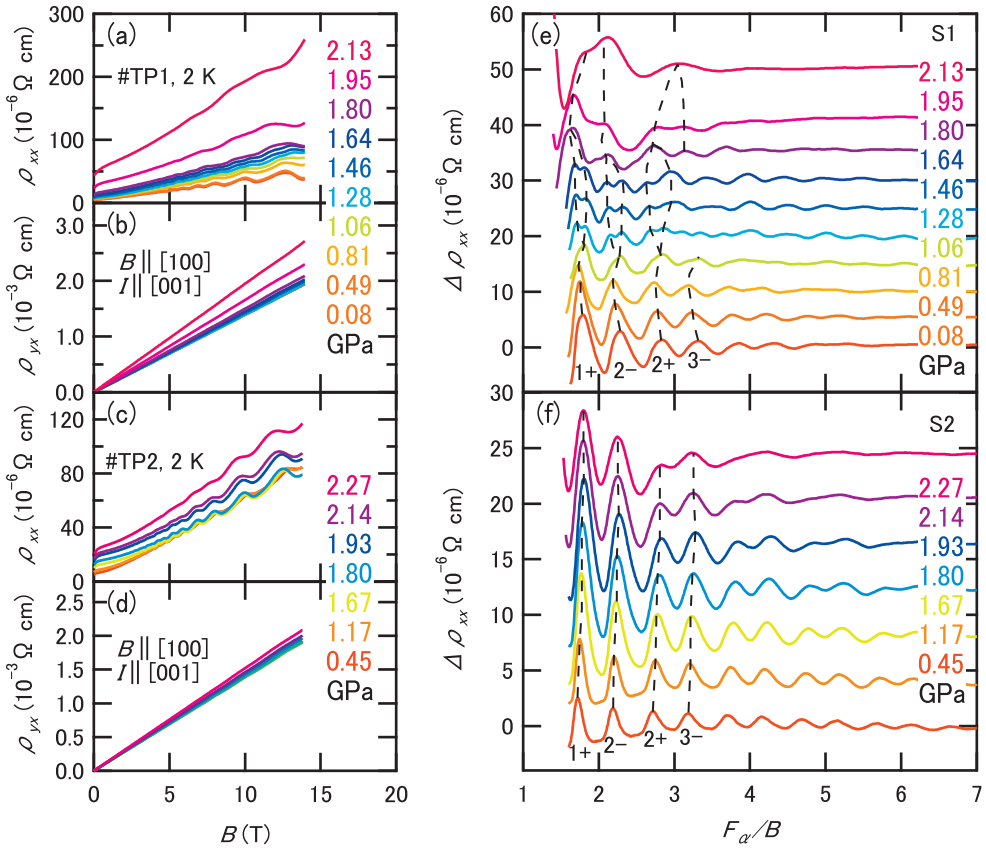

Figure 4.17: Pressure dependence of (a) magnetoresitance and (b) Hall resistance from 0.083 to 2.13 GPa in sample #TP1. Pressure dependence of (c) magnetoresitance and (d) Hall resistance from 0.45 to 2.27 GPa in another sample #TP2. Pressure dependence of SdH oscillation in (e) #TP1 and (f) #TP2. The changes of the peak positions are traced with broken lines in each spectrum.

Up to here, we have elucidated the SdH oscillation based on the LK formula which includes the effect of Zeeman-splitting and determined the value of M_{ZC} to 0.52 at ambient pressure. If the pressure-induced topological transition takes place as suggested in [161], we expect that M_{ZC} becomes unity at the critical pressure. Namely, systematic change in the SdH oscillation as shown in Fig. 4.12(a) should be detectable when applying hydrostatic pressure. Based on this prospect, we performed electronic transport measurements under high pressure environment. Here, we show the results of the electronic transport properties measured on two different sample pieces, which we refer as #TP1 and #TP2. These pieces were cut from the identical bulk of #T sample. Identical pressure medium (Daphne7373) was utilized in these measurements.

Figures 4.17(a) and (b) show the magnetic field dependence of ρ_{xx} and ρ_{yx} of #TP1 at 2 K and various pressures up to 2.2 GPa. Clear SdH oscillations were always observed in ρ_{xx} between 0.083 and 2.13 GPa. The resistivity monotonically increases with increasing pressure in the whole field region up to 14 T. The ρ_{yx} is always linear as a function of B up to 2.13 GPa, which indicates that no additional valleys contribute the transport properties by applying pressure. Slope of the ρ_{yx} gradually increases with applying pressure. The origin for this behavior is not clear at present since the carrier density is expected to be independent of pressure in single-carrier system due to the charge conservation. We confirmed the common tendency mentioned above in ρ_{xx} and ρ_{yx} of #TP2, as shown in Fig. 4.17(c) and (d). However, the pressure dependence of the SdH oscillation shows different behavior depending on the samples, as shown in Fig. 4.17(e) and (f). In #TP1, as shown in Fig. 4.17(e), the Zeeman-splitted peaks with different Landau indices observed near the ambient pressure basically approach each other as pressure increases. At 2.13 GPa, the peaks with $n = 1+$ and $n = 2-$ are almost being merged, and the double-peak structure can be hardly recognized in the other peaks. This can be regarded as the change of M_{ZC} toward unity as shown in Fig. 4.12(a), and thus, suggest that PbTe actually approaches the ideal 3D Dirac electron system by applying pressure. More quantitative analysis of ZC ratio at 1.95 and 2.13 GPa will be described later. Note that in this sample, there is additional split between 1.06 and 1.64 GPa. We regard that this may be caused by possible inhomogeneity of hydrostatic pressure, and do not enter the detailed discussion. On the other hand, we cannot observe such a behavior in #TP2, as shown in Fig. 4.17(f). In this sample, the peak positions are almost independent of the applied pressure, which indicates that the ZC ratio of #TP2 is almost unchanged by pressure.

In #TP1, we can determine the ZC ratio under pressure experimentally by comparing the experimental data with the numerical simulation based on Eq. (4.11). We varied the M_{ZC} in Eq. (4.11) to most satisfactorily reproduce the peak positions of experimental data as shown in Fig. 4.18(a) and (b). As a result, we obtained $M_{ZC} = 0.58$ at 1.95 GPa and 0.65 at 2.13 GPa. The overall pressure dependence of M_{ZC} is shown in Fig. 4.18(c) with red symbols. This result quantitatively indicate the enhancement of "Diracness" under pressure. In #TP1, the cyclotron mass (m^*) estimated from the temperature dependence of the SdH amplitude tends to decrease as shown in Fig. 4.18(d), which qualitatively agree with the sharpening of the energy dispersion near the L point. We can estimate the effective g-factor (g^*) from the relationship

$$g^* = \frac{2M_{ZC}}{m^*} \tag{4.12}$$

using M_{ZC} and m^* obtained from the measurements. As shown in Fig. 4.18(e), g^* monotonically increases as a function of pressure and reaches approximately 50 above

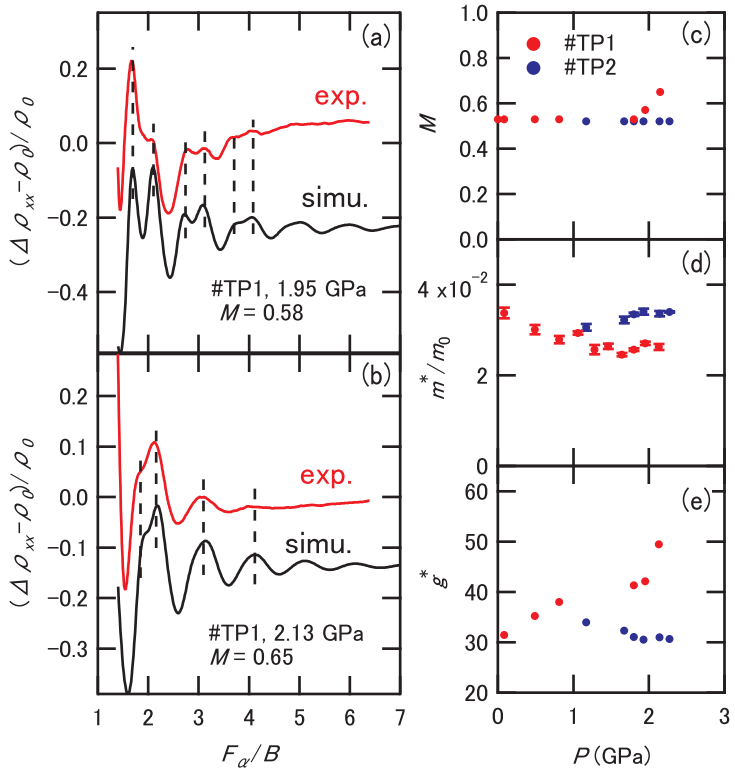

Figure 4.18: Comparison between experimental SdH oscillation (red) and simulation (black) based on Eq. (4.11) at (a) 1.95 GPa and (b) 2.13 GPa in #TP1. (c) ZC ratio estimated from the Zeeman-splitting, (d) the cyclotron mass estimated from the temperature dependence of the amplitude, and (e) effective g-factor calculated from Eq. (4.12). In (c)-(e), red (blue) marker represents #TP1 (#TP2), respectively.

2 GPa. In the case of #TP2, on the other hand, m^* tends to increase as pressure is applied in contrast to #TP1 [Fig. 4.18(d)], and therefore, calculated g^* does not show the increase at high pressure as shown in Fig. 4.18(e). Increase of the cyclotron mass is inconsistent with the expected band-gap closure. This difference may be caused by the sensitivity to the quality of hydrostatic pressure.

In the following, we mention the transport properties of the sample made by Bridgmann method (referred as #S sample), which has lower carrier density than that of #T (see Sec. 2.8). Figure 4.19(a) shows the temperature dependence with current along the [001] direction. The RRR [ρ(300 K)/ρ(2 K)] is 384, which is slightly lower than that of #T sample. The metallic behavior over the temperature range from 2 to 300 K is identical with that of #T. Figure 4.19(b) shows ρ_{xx} up to 14 T at several temperatures. The magnetoresistance is approximately linear unlike that of #T shown in Fig. 4.9(b). Also in #S, SdH oscillation was observed at wide temperature and magnetic field range, which reflect the light effective mass and high mobility nature of carriers in the #S sample. Figure 4.19(c) shows ρ_{yx} up to 14 T. The slope of ρ_{yx} is steeper than that of #T shown in Fig. 4.9(c) due to the less carrier density of #S, while the linearity and sign of ρ_{yx} is identical with those of #T. Then, we focus on the SdH oscillation on ρ_{xx} in detail. Figure 4.19(d) shows the FFT spectra at several temperatures from 2 to 50 K. We can identify two obvious peaks, at 9.5 and 19 T, and assume that the fundamental frequency F_α is 9.5 T, and the other frequency F_β with $9.5 \times 2 = 19$ T is the second harmonic due to the spin-splitting. Actually, the estimated cyclotron masses from F_β is approximately two times larger than that from F_α. As is clear in second derivative of ρ_{xx} shown in Fig. 4.19(e), the structures denoted by solid arrows in higher magnetic field region are not represented by single component. We performed the peak-position fitting based on the LK formula and successfully reproduced the experimental result by taking $M_{ZC} = 0.57$. Also in present case, we cannot distinguish $M_{ZC} = 0.57$ and 1.43 since corresponding spins of Landau levels cannot be distinguished experimentally. We assume, however, $M_{ZC} = 0.57$ by similar assumption made in the discussion on #T sample. This value is close to that in #T, and thus, we can regard that the carrier-density dependence of the ZC ratio is sufficiently weak at least from 0.99–3.7$\times 10^{18}$ cm^{-3}. These results indicate that the criterion for "Diracness" based on ZC ratio is less sensitive to the position of the Fermi level from the band-crossing point at least up to this carrier density.

Then, we studied transport properties of #S in high magnetic fields. Figure 4.20(a) shows ρ_{xx} up to 55 T. As shown in the inset of Fig. 4.20(a), the SdH oscillation was observed in lower field region, and the last two peaks correspond to the depopulation of 1− and 0+ subbands were observed at 7.1 and 10.8 T. Above 10.8 T, no oscillation was observed up to 55 T, which confirms the realization of spin polarized quantum limit state in which only 0− sate is occupied below the Fermi level. In the quantum limit state, ρ_{xx} continues to increase. The slope is steeper at 1.4 and 4.2 K than that of 20 K. ρ_{yx} was linear in the whole magnetic field range without showing non-linearity as shown in Fig. 4.20(b). Lastly, we show the longitudinal magnetoresistance ρ_{zz} (both B and I are parallel to the cubic axis) in pulsed high magnetic fields. Figure 4.20(c) represents the ρ_{zz} up to 55 T. The quantum oscillation was also observed in longitudinal configuration in lower field range as shown in the inset of Fig. 4.20(c).

We note that the peak at 10.8 T observed in ρ_{xx} is absent in ρ_{zz}, which seems to be related to the selection rules of carrier scattering between Landau subbands. Narita *et al.* [169] and Takafuji *et al.* [170] measured the SdH oscillation of n-type samples of $Pb_{1-x}Sn_xTe$ alloy, and found that the one-side peaks of spin-splitted pairs are absent in longitudinal configuration. They explained this behavior based on the selection rule

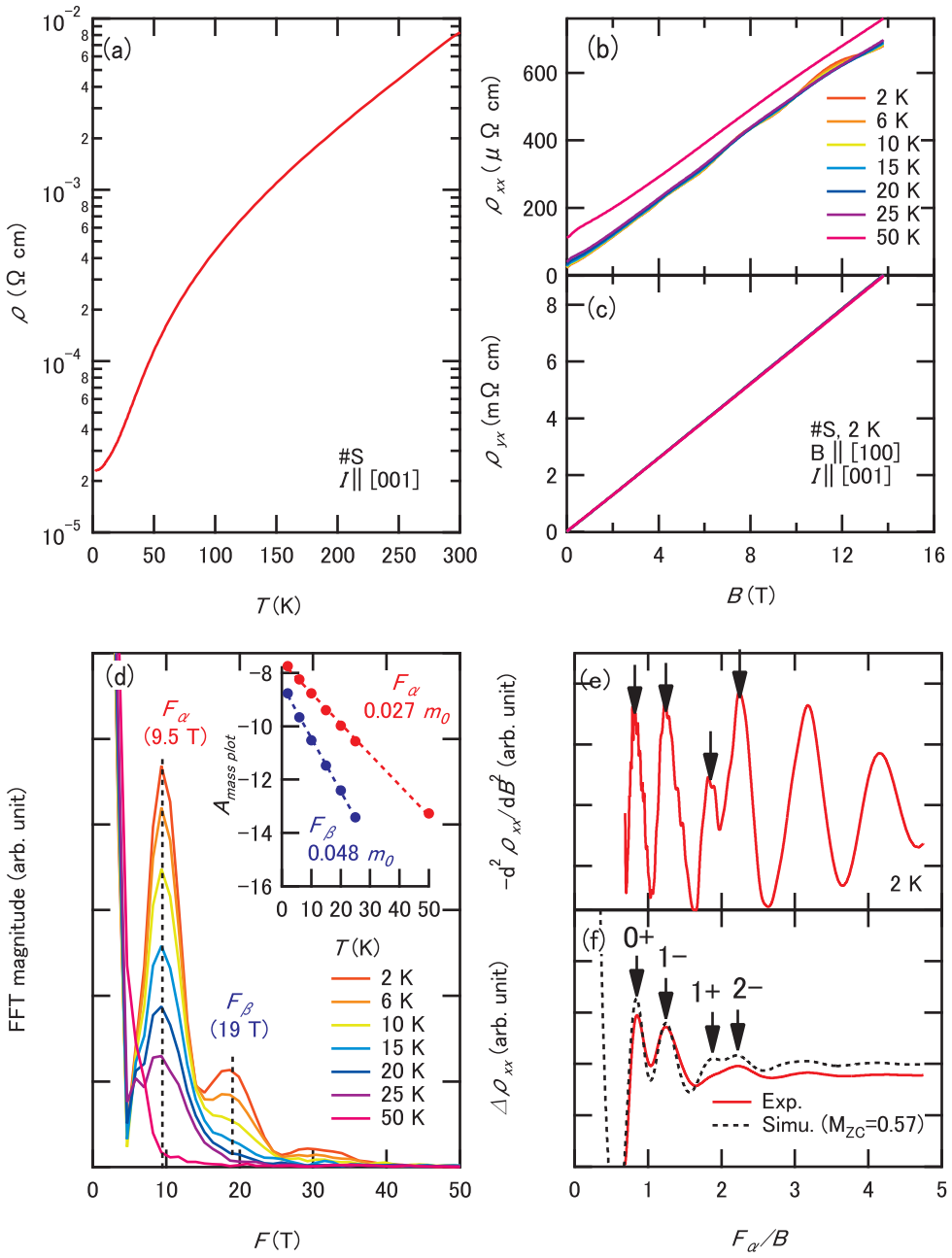

Figure 4.19: (a) Temperature dependence of the resistivity from 300 to 2 K in #S sample. Magnetic field dependence of (b) ρ_{xx} and (c) ρ_{yx} up to 14 T in #S sample. (d) FFT spectra at several temperatures. The inset shows the mass plot for determination of the cyclotron mass. (e) Second derivative of ρ_{xx} at 2 K in terms of B. (f) Comparison between experimental oscillation $\Delta\rho_{xx}$ and calculation based on the LK formula assuming $M_{ZC} = 0.57$.

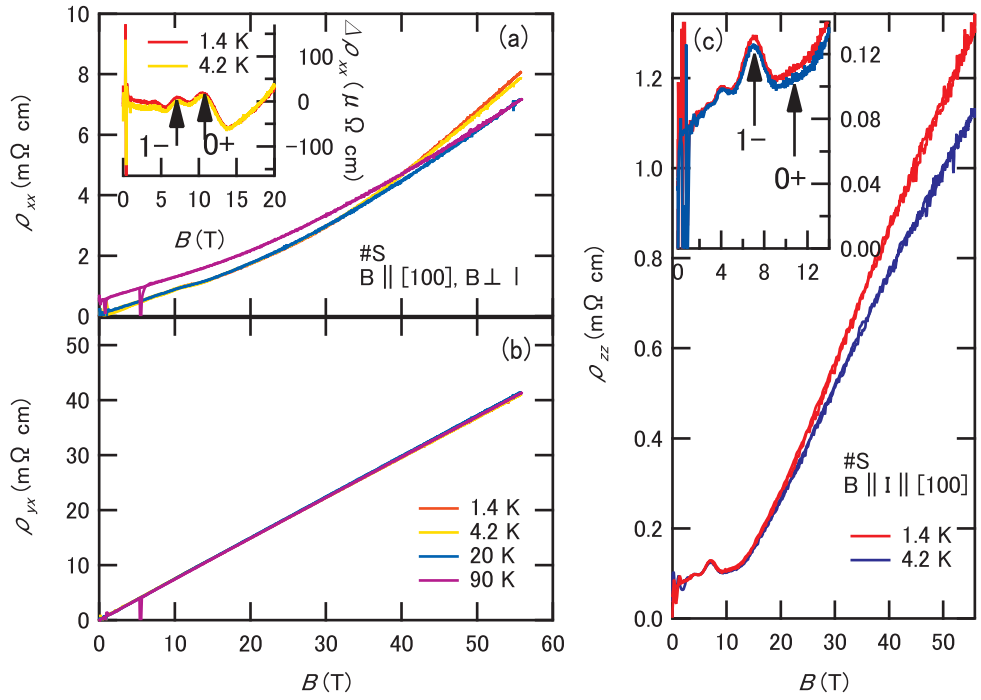

Figure 4.20: Magnetic field dependence of (a) ρ_{xx} and (b) ρ_{yx} up to 55 T under transverse configuration ($B \perp I$) in #S sample. The inset of (a) shows the magnified view of SdH oscillations observed on ρ_{xx}. (c) Magnetic field dependence of ρ_{zz} up to 55 T under longitudinal configuration ($B \parallel I$) in #S sample. The inset shows the magnified view of SdH oscillations observed in low-field region.

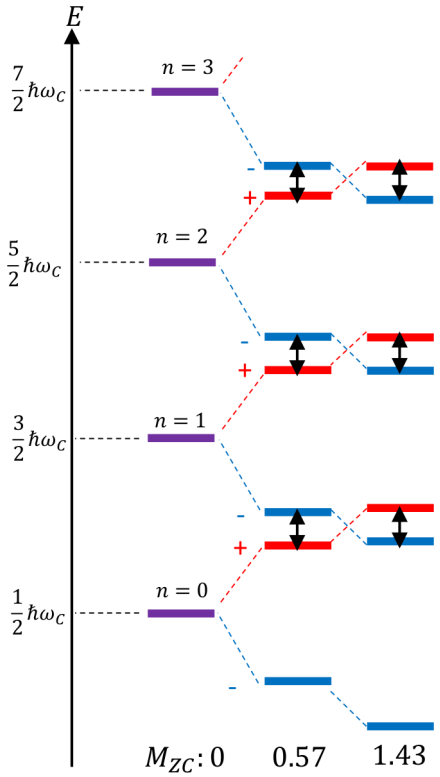

Figure 4.21: Landau-level structures at $M_{ZC} = 0.57$ and 1.43. Allowed carrier scattering in longitudinal configuration are shown in bidirectional arrows.

of the carrier scattering under strong spin-orbit interactions. According to [169], the selection rule of the carrier scattering in longitudinal magnetoresistance is represented as

$$n- \rightleftharpoons (n-1)+ . \tag{4.13}$$

Allowed carrier scattering is schematically shown in Fig. 4.21 with solid bidirectional arrows in cases of $M_{ZC} = 0.57$ and 1.43. We consider the present $M_{ZC} = 0.57$ case (the second column in Fig. 4.21). We assume that $n = 3-$ level crosses the Fermi level with increasing magnetic field. Since the scattering transition between $n = 3-$ and $n = 2+$ is allowed in this case, the resistivity is expected to increase at the depopulation of $n = 3-$ subband. On the other hand, when $n = 2+$ level cross the Fermi level, there is no available scattering transition, and thus, peak is almost absent in the resistivity. Since this situation is common in every Landau indices n, depopulations of spin+ subbands is not obvious in the SdH oscillation in longitudinal configuration at $M_{ZC} = 0.57$. This situation is identical in $M_{ZC} = 1.43$ (the third column in Fig. 4.21) except the order of subbands between $n-$ and $(n-1)+$, and therefore, we cannot experimentally distinguish the case of $M_{ZC} = 0.57$ and 1.43 from this phenomenon.

Above 10 T, ρ_{zz} is continuously and linearly increases as a function of magnetic field. The slope at high magnetic field region show slight temperature dependence, and is steeper at 1.4 K than that of 4.2 K. Such a drastic increase of ρ_{zz} is unusual since the electric current is not ideally affected by the magnetic field in the longitudinal configuration.

Although linear and non-saturating ρ_{xx} observed in #S sample resembles linear magnetoresistance in the quantum limit state as Abrikosov predicted [47, 48], the pristine

PbTe is found to have the M_{ZC} deviate from unity, and hence, such a mechanism seems not to fit in the present case. We also note that recent study on $SrTiO_3$ reported linear and non-saturating ρ_{xx} and non-linear I-V characteristic in the quantum limit regime [171]. In their study, possible realization of a field-induced charge density wave or Wigner crystal states stabilized by spacial inhomogeneity was suggested. On the other hand, temperature-dependent non-saturating magnetoresistance is believe to occur in the "Hall insulator" state expected in the quantum limit state [172, 173]. Hall insulator state is characterized by the diverging ρ_{xx} at $T \to 0$ in spite of the almost constant ρ_{yx}. In case of PbTe, however, the magnetoresistance seems to vary with samples as mentioned previously, and hence, further careful investigation for the origin of magnetoresistance in high magnetic field should be necessary. The origin for anomalous behavior observed in ρ_{xx} and ρ_{zz} in the quantum limit state is an open question at the present stage.

4.3.2 $Pb_{0.7}Sn_{0.3}Te$

As introduced in Sec. 4.1, Sn substitution also reduces the band gap, and is expected to induce topological phase transition at around $x = 0.35$. At this point, the ZC ratio is expected to be unity. In order to obtain the Sn-content dependence of the ZC ratio, we performed resistivity, magnetization, and ultrasonic measurements on $Pb_{0.7}Sn_{0.3}Te$. We refer this sample as #T30, hereafter. Figure 4.22(a) shows temperature dependence of the resistivity. The resistivity showed metallic dependence without showing anomalous behavior over the whole temperature range. From this measurement, we cannot identify any anomaly suggestive of the ferroelectric transition expected in this alloy system [159]. Figure 4.22(b) shows ρ_{xx} up to 14 T at several temperatures. The SdH oscillation is visible especially in the high-field region, and the background magnetoresistance slightly increases as B increases. Figure 4.22(c) shows ρ_{yx} up to 14 T. The ρ_{yx} is linear and positive, which suggests the existence of the single hole carrier. In #T30, the SdH oscillation is also visible in ρ_{yx}. We estimated the carrier density and mobility as 5.1×10^{19} cm^{-3} and 950 cm^{2}V^{-1}s^{-1}, respectively, based on the simple single-carrier model. The carrier density is more than 10 times larger, and the mobility is 100 times smaller than those of pristine one. Figure 4.22(d) shows the FFT spectra of SdH on ρ_{xx}. We can identify only single peak in this spectra, and no higher harmonics was observed. The annihilation of the large second harmonic stemming from the spin-splitting indicates the change of the ZC ratio. From the temperature dependence of the FFT spectra, the cyclotron mass of $0.11m_0$ was estimated, which is heavier than that of PbTe.

Since SdH oscillation showed no signature of spin-splitting, we cannot evaluate the ZC ratio in #T30 sample. Then, we constructed the Landau-level fan diagram and evaluated the phase of SdH oscillation. Figure 4.23(a) shows the oscillation components of resistivity ($\Delta\rho_{xx}$) and conductivity ($\Delta\sigma_{xx}$) subtracted their background. In case of #T30, ρ_{xx} and ρ_{yx} have comparable magnitude, and thus, the condition $\sigma_{xx} \ll \sigma_{xy}$ is not necessarily satisfied. Reflecting this circumstance, the peak/dip positions in σ_{xx} do not coincide with those of ρ_{xx}. Figure 4.23(b) shows the Landau-level fan diagram constructed from both resistivity and conductivity. In this diagram, the peak positions are assigned in integer indices, and hence, the x-intercept near -0.5 means $M_{ZC} = 0, 2, 4, \cdots$ case. Both diagrams take x-intercept near -0.5 as shown in the inset of Fig. 4.23(b), which suggests non-unity value of M_{ZC} in this system, although the band structure of #T30 is expected to be sufficiently close to the topological phase transition. At this point, however, there remains a possibility: since the obtained peak/dip is all far from

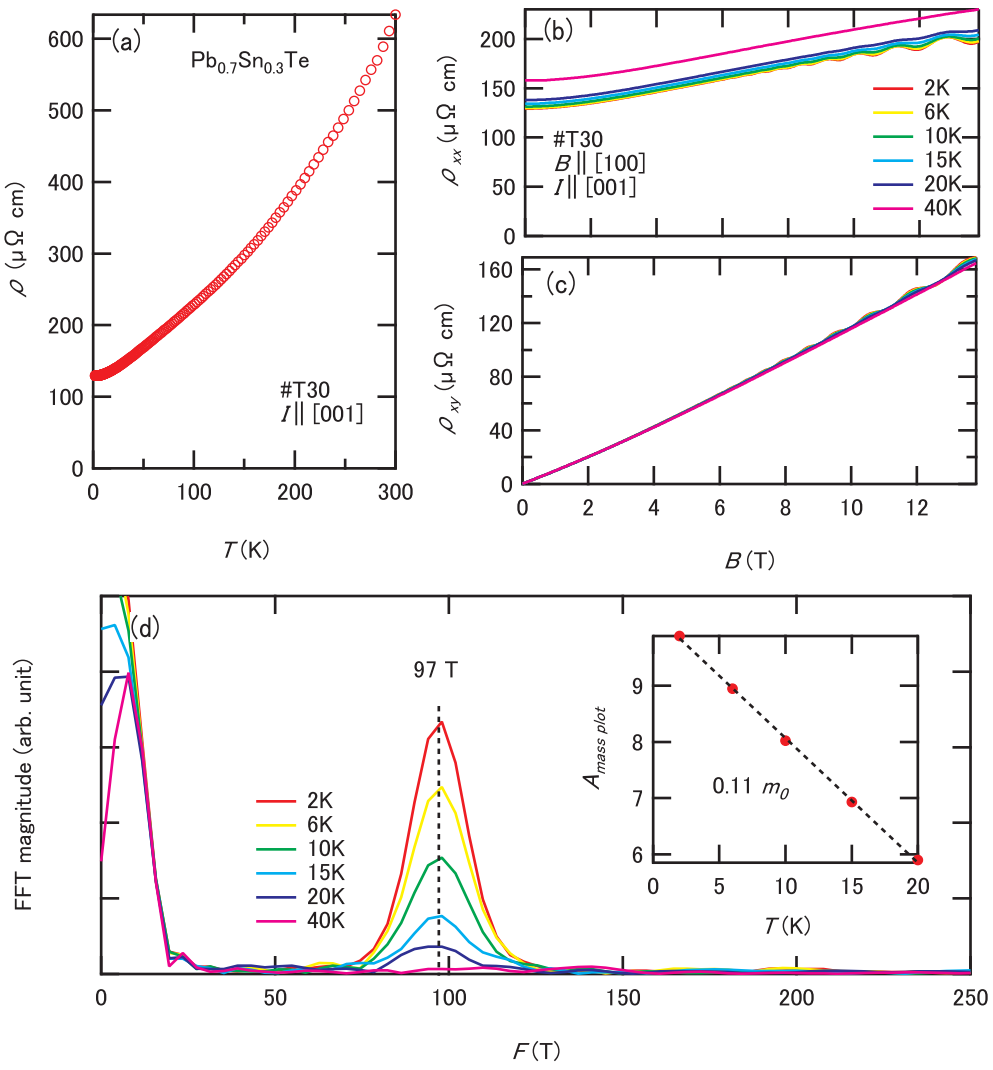

Figure 4.22: (a) Temperature dependence of the resistivity from 300 to 2 K in #T30 sample. (b) Magnetic field dependence of (b) ρ_{xx} and (c) ρ_{yx} up to 14 T in #T30 sample. (d) FFT spectra at several temperatures. The inset shows the mass plot for cyclotron mass determination.

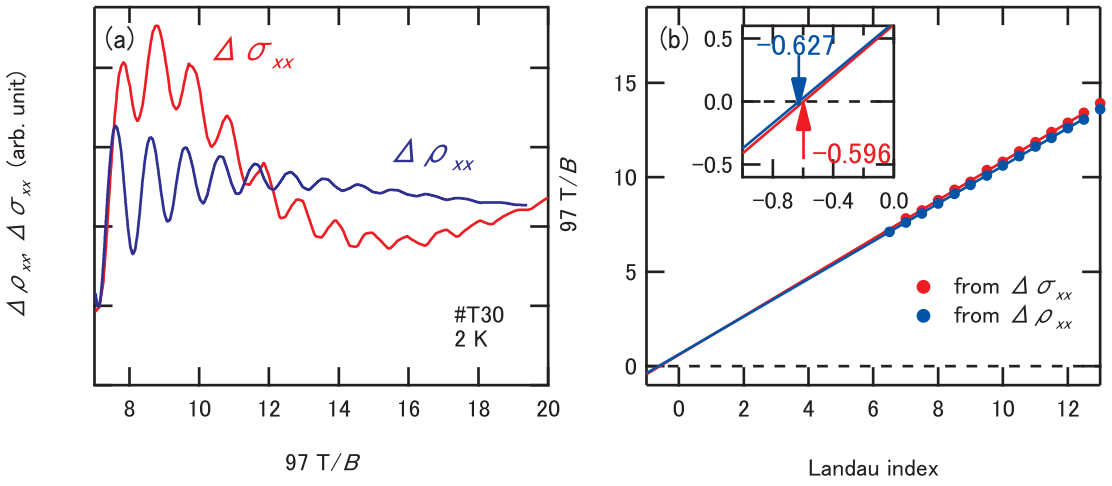

Figure 4.23: (a) Oscillation components on conductivity ($\Delta\sigma_{xx}$, red) and resistivity ($\Delta\rho_{xx}$, blue) in #T30 sample. (b) Landau-level fan diagram constructed from $\Delta\sigma_{xx}$ and $\Delta\rho_{xx}$ shown in (a). The peaks are assigned to integer indices in both plots.

the quantum limit, determined x-intercepts have possible uncertainty. In order to refine the fan diagram, we performed ultrasonic measurement under pulsed high magnetic field on #T30. In case of the acoustic dHvA oscillation in ultrasonic attenuation coefficient, the peak corresponds to the depopulation of the Landau subband since only carriers having velocity close to the Fermi velocity interact with the ultrasonic wave in metal [100]. Thus, ultrasonic attenuation coefficient is critical for determining the phase factor of the fan diagram.

Figures 4.24(a) and (b) show the acoustic dHvA oscillations in attenuation coefficient and sound velocity, respectively. In this measurement, the magnetic field and transverse ultrasound were applied along the [100] direction [propagation ($\boldsymbol{k}$) and displacement ($\boldsymbol{q}$) directions are $\boldsymbol{k} \parallel$ [100] and $\boldsymbol{q} \parallel$ [010], respectively]. In both quantity, quite large oscillations were observed. Focusing on the relatively low field region in sound velocity as shown in Fig. 4.24(b), the oscillation seems to have multiple component. To clarify this, we calculate the FFT spectrum from the data of sound velocity, which is shown in Fig. 4.24(c). The two peaks are identified in the spectrum, and these frequencies slightly differ with each other. This cannot be explained by the fundamental and second harmonic waves. One possibility for this spectrum is slight misalignment of the sample. If the field direction is slightly off from the [100] direction, more than two cross-sectional areas with slightly different value can arise. Another possibility is the ferroelectric transition. If the rhombohedral structure was realized at this temperature, the degeneracy at the L point will be solved. As a result, the two cross-sectional area can come up. In this case, however, we could not observed firm evidence for ferroelectric transition in transport measurement as shown in Fig. 4.22(a), and thus, we regard this FFT spectrum as a result of slight misalignment.

Finally, we summarize the fan diagram of #T30 in Fig. 4.25 including all physical quantities investigated in this study. The brown circles were plotted from the peaks of the attenuation coefficient shown in Fig. 4.24(a). In addition, we plotted the results from the ultrasound measurement with different field direction (green circles), transport measurements [red squares and blue triangles, identical with Fig. 4.23(b)], and magnetization measurement (black circles). As shown in the inset of Fig. 4.25, the x-intercepts

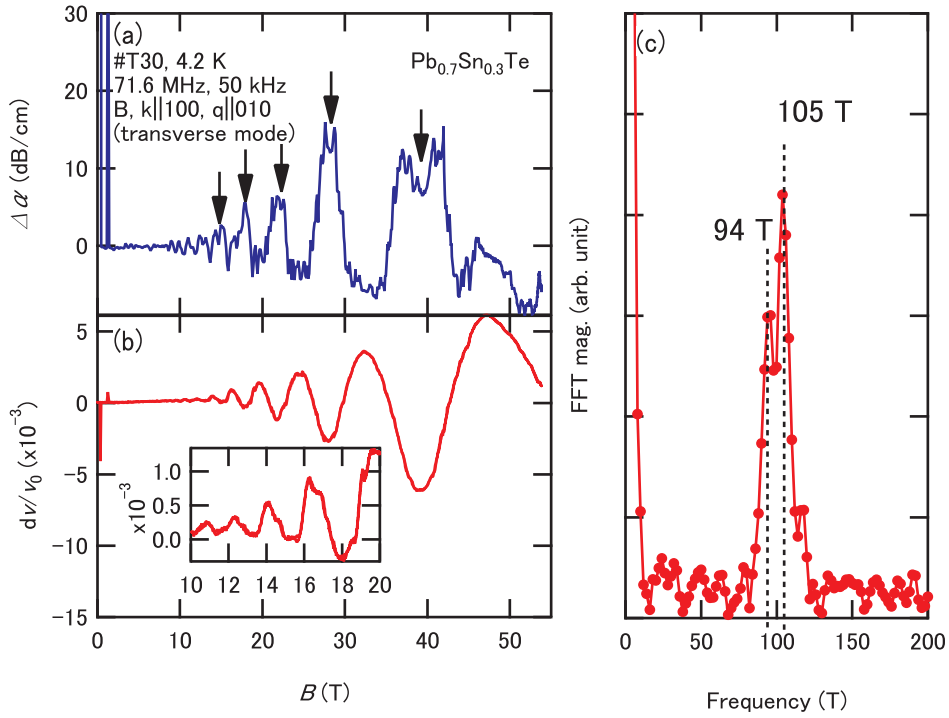

Figure 4.24: Magnetic field dependence of the (a) attenuation coefficient $\Delta\alpha$ and (b) sound velocity dv/v_0 in #T30 sample. (c) FFT spectrum of acoustic dHvA oscillation observed in (b). The field window was taken in low field region from 3.3 to 20 T.

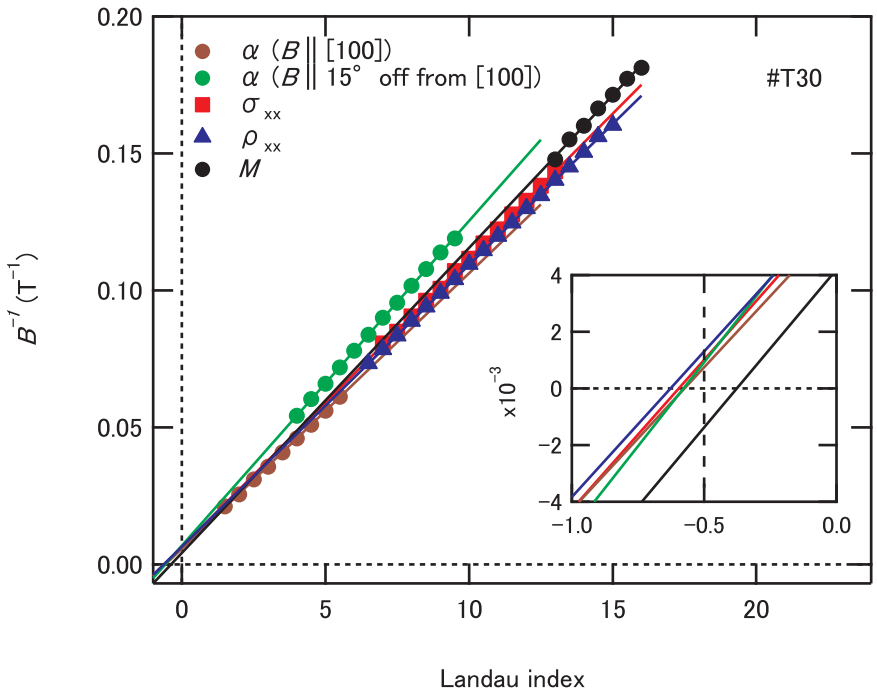

Figure 4.25: Landau-level fan diagrams constructed from various quantum oscillations in #T30 sample. See text for method of the construction. The inset shows the magnified view around the horizontal intersections.

are all close to -0.5, which indicates that #T30 has non-unity ZC ratio. We should further clarify how carrier density affects the experimental determination of ZC ratio. Since the carrier density is more than 10 times larger than pristine sample, this might influence the results. More investigations should be needed for samples with intermediate compositions between $x = 0$ and 0.3.

4.4 Summary

We investigated the electric transport, magnetization, and elastic properties in PbTe and $Pb_{0.7}Sn_{0.3}Te$. Pristine PbTe showed clear quantum oscillations on resistivity, magnetization, ultrasonic attenuation, and sound velocity. We identified large second harmonic in FFT spectra of the quantum oscillations, and pointed out that this is a firm evidence for large spin-splitting in PbTe. The simple band structure and distinct spin-splitting caused by strong spin-orbit interaction in PbTe enable us to testify the evaluation of the Zeeman-cyclotron ratio. By numerical simulation based on Lifshitz-Kosevich formula, we consistently explained the oscillation structure, and determined the Zeeman-cyclotron ratio to 0.52 in pristine PbTe. The Landau level indices are unambiguously determined by measurements in pulsed high magnetic fields, which takes PbTe to the spin-polarized quantum limit state. From the angular dependence of the Shubnikov-de Haas oscillations, we confirmed that the Zeeman-cyclotron ratio is almost independent of the field direction, which is consistent with the theoretical prediction. By the resistivity measurements under hydrostatic pressure, we obtained an indication that the Zeeman-cyclotron ratio in one sample approaches unity as pressure increases, which suggests that PbTe approaches the ideal Dirac electron system. On the other hand, above behavior was not reproduced in another sample, which suggests possible sensitivity to the inhomogeneity of pressure. In PbTe with relatively low carrier density, we observed large and non-saturating magnetoresitance in both transverse and longitudinal configurations. This behavior cannot be fully explained in the present stage, and was remained as an open question. We also investigated the electrical transport and ultrasonic measurements in $Pb_{0.7}Sn_{0.3}Te$ to obtain the Sn content dependence of the Zeeman-cyclotron ratio. We pointed out that too heavy carrier doping causes an inaccuracy in experimental determination of the Zeeman-cyclotron ratio.

Chapter 5

Concluding Remarks

5.1 Summary of This Thesis

In this thesis, we investigated two narrow gap semiconductors, black phosphorus (BP) and lead telluride (PbTe).

In Chap. 1, we reviewed the previous studies of unconventional electronic states in solids expected to realize in the vicinity of the metal–insulator transiton. Then, we specify the problems in those studies, and clarify our approach to solve these problems. We pointed out that BP and PbTe can be model materials to solve these problems owing to the simple and tunable electronic structure.

In Chap. 2, we explained the experimental techniques (the resistivity measurements under high pressure, generation of pulsed high magnetic fields, and several measurement techniques in pulsed high magnetic fields), and described the properties of BP, PbTe, and $Pb_{1-x}Sn_xTe$ samples investigated in this thesis.

In Chap. 3, we reviewed the fundamental properties of BP, and demonstrated our results. In the semiconducting state, we investigated magneto-phonon resonance and its pressure dependence. We showed that the cyclotron mass becomes lighter as pressure increases, which is ascribed to the narrowing of the band gap. Above 1.4 GPa, we observed clear Shubnikov-de Haas (SdH) oscillations and large magnetoresistance effect. From the analysis of SdH oscillations, we identified the light cyclotron masses and small densities of carriers in semimetallic BP. We also showed the monotonic enlargement of Fermi surfaceses, which indicates the tunability of the carrier density by controlling pressure. Two-carrier analysis affirmed the nearly compensated nature of semimetallic BP and enhancement of carrier density by pressure. Large and non-saturating magnetoresistance obserbed in semimetallic state was not fully reproduced by the two-carrier model, which suggests additional mechanism for this phenomena. To seek the unconventional electronic states in the vicinity of the semiconductor–semimetal transition, we investigated the temperature dependence of the resistivity under magnetic field. The apparent insulating-like temperature dependence of resistivity observed in magnetic fields was reasonably explained by the conventional theory. Thus, truly anomalous behavior stemming from the emergence of the excitonic insulator phase could not be observed in this study.

In Chap. 4, we introduced the fundamental properties of PbTe and $Pb_{1-x}Sn_xTe$, and demonstrated our results. We observed clear SdH oscillations in pristine PbTe, and identified anomalously large second harmonic in the Fourier spectra of SdH oscillations. We pointed out that the large second harmonic is originated from the large spin-splitting

in PbTe. We experimentally determined the ratio of Zeeman energy to cyclotron energy (ZC ratio) to 0.52. The ZC ratio and Landau indices for oscillation were unambiguously confirmed by pulsed high-field measurement. We performed resistivity measurements by controlling the band gap with pressure. We obtained an indication that the ZC ratio approaches unity as pressure increase in one sample, which suggests that PbTe approaches the Dirac electron system on the way to the topological phase transition. We also observed the large and non-saturating magnetoresistance in the quantum limit state of PbTe in both transverse and longitudinal magnetoresistance, which was remained as an open question. We also investigated the electrical transport and elastic properties in $Pb_{0.7}Sn_{0.3}Te$. We pointed out that too heavy carrier doping causes inaccuracy on the determination of ZC ratio.

We finally comment on the current position of this study from the global viewpoint.

One of our main results on the study of BP is successful observation of SdH oscillations, which revealed that semimetallic BP is band-tunable electron-hole system with low carrier density and high mobility comparable to bismuth and graphite. We should then establish the firm understanding of its Fermi surface to proceed our study. The present situation of BP is like that of bismuth about 90 years ago, when the SdH effect was discovered for the first time in bismuth. Looking back on the research history of bismuth, we can learn that how difficult the precise determination of the Fermi surface is: it took more than 30 years to consistently explain the whole experimental data by theory [174]. To deal with the Fermiology of semimetallic BP, we should then learn from the history of bismuth, in which the experimentalists and theorists closely worked and fed back their results with each other.

Within the scope of this study, we could not confirm the realization of unconventional electronic transition in BP. Although there are numerous semimetals and narrow-gap semiconductors, graphite is the only an example which shows obvious electronic transition in high magnetic fields at present, as far as we know. The problem of universal interest is that "what is the necessary condition for the emergence of such an electronic transition in high magnetic fields?". The dimensionality of the crystal and band structure is considered to be one of the important factors to tackle the problem. We now obtained the ideal electron-hole systems with different crystal dimensionality, graphite (two-dimensional nature), bismuth (three-dimensional nature), and BP (intermediate nature between two- and three- dimension). The similarity between ferroelectric $Pb_{1-x}Sn_xTe$ and bismuth is worth mentioning, which both form rhombohedral A7 structure. Comprehensive study for these materials posses great possibility to reveal the universal nature of electronic phase realized in the electron-hole systems in high magnetic fields.

In regards to PbTe, our main result is summarized to the successful determination of ZC ratio, namely, "Diracness" of this material. This established the new experimental criterion to evaluated the band topology of materials, and basis to investigated more detailed physical properties in the vicinity of the ideal Dirac system in PbTe by continuously tuning the band topology. Future advances of the quantitative study based on the ZC ratio can supply a guideline to organize the present chaotic situation on the transport studies of topological materials.

5.2 Future Prospects

There remains several open questions in our studies. In regards to BP, we compared the experimentally obtained SdH oscillations along the three principal axes with the Fermi surfaces estimated by calculation. However, we could not fully determine the geometry of the Fermi surface in semimetallic BP. In order to complete full mapping of the Fermi surface of semimetallic BP, we should perform the angular dependence measurements of SdH oscillations under magnetic fields and pressure.

Although such a measurement is expected to be technically difficult, a diamond anvil cell of small size (18 mm in diameter and less than 40 mm tall) and rotating mechanisms for the cell have been developed by Dr. A. Miyake, ISSP. Above system is all made of non-metallic materials to reduce the effect of eddy currents in measurements in pulsed magnetic fields. A wide-bore (64 mm diameter) pulse magnet, which is developed by Kindo group, ISSP, is now available for resistivity measurements up to $\sim$ 25 T using this system. We are dealing with the angular dependence of the resistivity in pulsed high magnetic fields with these equipments. Also, we could not obtain a firm evidence of realization of excitonic insulator phase in BP. To explore such phases, higher magnetic fields are preferable to increase the binding energy of excitons. Collaborating with Kindo group, we intend to increases the maximum magnetic fields up to $\sim$ 50 T in the near future.

In PbTe, we observed the increase of ZC ratio by applying pressure, yet this behavior was not reproduced in measurements in another sample piece. To confirm the enhancement of the "Diracness" in pressurized PbTe, we should perform some supplemental measurements. The possible effect from inhomogeneity of pressure or sample dependence should be carefully clarified in future. The large magnetoresistance in PbTe was also remained as an open question. We observed non-saturating magnetoresistance in the quantum limit state. While, we observed different magnetoresistance effect even in the same sample batch. To clarify the nature of the magnetoresistance in PbTe, we should carefully measure the transport properties avoiding geometrical effects such as current-jetting. Fabrication of PbTe thin-film can be possible solution to exclude the inhomogeneity of the electric current. In regards to $Pb_{1-x}Sn_xTe$, we pointed out that the heavy hole doping causes the deviation of ZC ratio from true value. In order to confirm the enhancement of the Diracness in $Pb_{1-x}Sn_xTe$, samples having less carrier density should be investigated. Further, if the critical temperature of ferroelectric transition (T_c^{FE}) satisfied $T_c^{FE} > 0$ in the vicinity of band gap closure as suggested in previous reports, the inversion symmetry of the crystal is broken below T_c^{FE}. As a results, the zero-gap state is Weyl electron system below T_c^{FE}, and is Dirac electron system above T_c^{FE}. This property means the possibility that Dirac and Weyl system can be switched by temperature in $Pb_{1-x}Sn_xTe$. To confirm this intriguing feature, we should investigate the relationship between ferroelectric transition and band gap closure in detail.

Publications

Original papers (peer reviewed)

- Y. Mizuguchi, A. Miyake, K. Akiba, M. Tokunaga, J. Kajitani, and O. Miura, *Anisotropic upper critical field of the BiS_2-based superconductor $LaO_{0.5}F_{0.5}BiS_2$*, Phys. Rev. B **89**, 174515 (2014).
- K. Akiba, A. Miyake, H. Yaguchi, A. Matsuo, K. Kindo, and M. Tokunaga, *Possible Excitonic Phase of Graphite in the Quantum Limit State*, J. Phys. Soc. Jpn. **84**, 054709 (2015).
- K. Akiba, A. Miyake, Y. Akahama, K. Matsubayashi, Y. Uwatoko, H. Arai, Y. Fuseya, and M. Tokunaga, *Anomalous Quantum Transport Properties in Semimetallic Black Phosphorus*, J. Phys. Soc. Jpn. **84**, 073708 (2015).
- K. Akiba, A. Miyake, Y. Akahama, K. Matsubayashi, Y. Uwatoko, and M. Tokunaga, *Two-carrier analyses of the transport properties of black phosphorus under pressure*, Phys. Rev. B **95**, 115126 (2017).
- M. Uchida, Y. Nakazawa, S. Nishihaya, K. Akiba, M. Kriener, Y. Kozuka, A. Miyake, Y. Taguchi, M. Tokunaga, N. Nagaosa, Y. Tokura, and M. Kawasaki, *Quantum Hall states observed in thin films of Dirac semimetal Cd_3As_2*, Nat. Commun. **8**, 2274 (2017).
- Y. Fujishiro, N. Kanazawa, T. Shimojima, A. Nakamura, K. Ishizaka, T. Koretsune, R. Arita, A. Miyake, H. Mitamura, K. Akiba, M. Tokunaga, J. Shiogai, S. Kimura, S. Awaji, A. Tsukazaki, A. Kikkawa, Y. Taguchi, and Y. Tokura, *Large magneto-thermopower in MnGe with topological spin texture*, Nat. Commun. **9**, 408 (2018).

Commentaries (peer reviewed)

- 秋葉和人, 三宅厚志, 徳永将史, 赤浜裕一, 圧力下の半金属黒燐における異常量子輸送現象, 固体物理 **51**, 249 (2016).

Appendix A

Computer Programs Composed for This Study

In this appendix, we show the source codes of the computer programs composed for this study. All programs are composed by the author, and implemented in Igor Pro language (WaveMetrics, Inc.).

A.1 Numerical Lock-In

```
#pragma rtGlobals=3             // Use modern global access method.
#pragma version=3.4

//20150819 AKB

Menu "Numerical Lockin"
        "Activate LOCKIN", LOCKIN_INIT()
End

Macro LOCKIN_INIT(sIpt0,sIpt1,sIpt2,sIpt3,sIpt4,sIpt5,vSamplerate,vTotalpoint,vFreq)
        String/G sgIpt0, sgIpt1, sgIpt2, sgIpt3, sgIpt4, sgIpt5
        String sIpt0=sgIpt0,sIpt1=sgIpt1,sIpt2=sgIpt2,sIpt3=sgIpt3,sIpt4=sgIpt4, sIpt5=sgIpt5
        Prompt sIpt0, "magnetic field (T):"
        Prompt sIpt1,"input1 (do not use = \"off\"):"
        Prompt sIpt2,"input2 (do not use = \"off\"):"
        Prompt sIpt3,"input3 (do not use = \"off\"):"
        Prompt sIpt4,"input4 (do not use = \"off\"):"
        Prompt sIpt5,"input5 (do not use = \"off\"):"
        Variable/G vgSamplerate
        Variable vSamplerate=vgSamplerate
        Prompt vSamplerate, "samplerate (/s):"
        Variable/G vgTotalpoint
        Variable vTotalpoint=vgTotalpoint
        Prompt vTotalpoint, "total data point:"
        Variable/G vgFreq
        Variable vFreq=vgFreq
        Prompt vFreq,"reference frequency (Hz):"

        Variable/G vgPhase=0
        Variable/G vgPointofcycle
        String/G sgFilename
        Variable/G vgPshift
        String/G sgTimestamp="timestamp_Lockin"
        String/G sgReference="refsignal", sgReferenceImg="refsignal_img"
        Variable/G vgActtime

        INITIALIZE(sIpt0,sIpt1,sIpt2,sIpt3,sIpt4,sIpt5,vSamplerate,vTotalpoint,vFreq)
End

Function INITIALIZE(sIpt0,sIpt1,sIpt2,sIpt3,sIpt4,sIpt5,vSamplerate,vTotalpoint,vFreq)
        String sIpt0,sIpt1,sIpt2,sIpt3,sIpt4, sIpt5
        Variable vSamplerate
        Variable vTotalpoint
        Variable vFreq
        Variable i

        Make/T/O/N=(6) Ipt
        Ipt[0]=sIpt0; Ipt[1]=sIpt1; Ipt[2]=sIpt2; Ipt[3]=sIpt3; Ipt[4]=sIpt4; Ipt[5]=sIpt5;

        Make/T/O/N=(6) Num
        Num[0]="0"; Num[1]="1"; Num[2]="2"; Num[3]="3"; Num[4]="4"; Num[5]="5";
```

```
Make/T/O/N=(6) IptTuned
i=0
Do
        IptTuned[i]="input"+Num[i]+"_t"
        i+=1
While (i<6)

Make/T/O/N=(6) IptTunedImg
i=0
Do
        IptTunedImg[i]="input"+Num[i]+"_tImg"
        i+=1
While (i<6)

Make/T/O/N=(6) IptLocked
i=0
Do
        IptLocked[i]="input"+Num[i]+"_locked"
        i+=1
While (i<6)

Make/T/O/N=(6) IptLockedImg
i=0
Do
        IptLockedImg[i]="input"+Num[i]+"_lockedImg"
        i+=1
While (i<6)

Make/T/O/N=(6) IptPhaseshift
i=0
Do
        IptPhaseshift[i]="input"+Num[i]+"_phaseshift"
        i+=1
While (i<6)

Make/T/O/N=(6) IptNorm
i=0
Do
        IptNorm[i]="input"+Num[i]+"_norm"
        i+=1
While (i<6)

Make/O/N=(6) Ampgain

Make/O/N=(6) Color1
Color1[1]=65280; Color1[2]=0; Color1[3]=0; Color1[4]=65280; Color1[5]=0;

Make/O/N=(6) Color2
Color2[1]=43520; Color2[2]=65280; Color2[3]=0; Color2[4]=0; Color2[5]=0;

Make/O/N=(6) Color3
Color3[1]=0; Color3[2]=0; Color3[3]=65280; Color3[4]=26112; Color3[5]=26112

Make/O/N=(6) Flag
i=1
Do
        Flag[i]=0
        i+=1
While (i<6)

NVAR vgActtime
if (vgActtime==0)
        Print "Send bug or error reports to: k_akiba@issp.u-tokyo.ac.jp"
endif

vgActtime+=1

SVAR sgIpt0
SVAR sgIpt1
SVAR sgIpt2
SVAR sgIpt3
SVAR sgIpt4
SVAR sgIpt5
NVAR vgSamplerate
NVAR vgTotalpoint
NVAR vgFreq
sgIpt0=sIpt0; sgIpt1=sIpt1; sgIpt2=sIpt2; sgIpt3=sIpt3; sgIpt4=sIpt4; sgIpt5=sIpt5
vgSamplerate=vSamplerate
vgTotalpoint=vTotalpoint
vgFreq=vFreq

i=1
Do
        Make/O/N=(vgTotalpoint) $IptTuned[i]
        i+=1
While (i<6)

i=1
Do
        Make/O/N=(vgTotalpoint) $IptTunedImg[i]
        i+=1
While (i<6)

SVAR sgReference
```

```
	SVAR sgReferenceImg
	SVAR sgTimestamp
	NVAR vgPshift
	NVAR vgPhase
	Make/O/N=(vgTotalpoint) $sgReference=sin(2*pi*vgFreq*(p-vgPshift)/vgSamplerate-vgPhase)
	Make/O/N=(vgTotalpoint) $sgReferenceImg=sin(2*pi*vgFreq*(p-vgPshift)/vgSamplerate-vgPhase-pi/2)
	Make/O/N=(vgTotalpoint) $sgTimestamp=p/vgSamplerate

	i=1
	Do
		if (cmpstr(Ipt[i],"off")==0)
			Flag[i]=0
		else
			Flag[i]=1
		endif
		i+=1
	While (i<6)

	if( (Flag[1]==0)*(Flag[2]==0)*(Flag[3]==0)*(Flag[4]==0)*(Flag[5]==0)==0)
		i=1
		Do
			DUPLICATE_IPT(Ipt[i],IptTuned[i],Flag[i])
			i+=1
		While (i<6)

		Display/N=phase_tuning $sgReference vs $sgTimestamp
		ModifyGraph/W=phase_tuning margin(top)=20

		i=1
		Do
			APPEND_IPT("phase_tuning",Ipt[i],sgTimestamp,Flag[i],Color1[i],Color2[i],Color3[i])
			i+=1
		While (i<6)

		Legend/W=phase_tuning/C/N=text0/A=RB
		Label/W=phase_tuning bottom "Time (sec)"
		Label/W=phase_tuning left "Raw input"

		SetVariable setpshift win=phase_tuning,size={100,20} ,value=vgPshift
		SetVariable setpshift proc=UPDATE_REFERENCE,title="point shift"
		SetVariable setfreq win=phase_tuning,size={100,20} ,value=vgFreq
		SetVariable setfreq proc=UPDATE_REFERENCE, title="freq"
		Button plus win=phase_tuning,size={50,20} ,proc=PLUS, title="+pi/2"
		Button minus win=phase_tuning,size={50,20} ,proc=MINUS, title="-pi/2"
		Button multiply win=phase_tuning,size={70,20} ,proc=MULTIPLY_REFERENCE, title="multiply"
	else
		Doalert 0, "There is no input data."
	endif
End

Function DUPLICATE_IPT(sIpt,sOpt,vFlag)
	String sIpt,sOpt
	Variable vFlag
	NVAR vgTotalpoint
	if (vFlag==1)
		Duplicate/O/R=(0,vgTotalpoint-1) $sIpt $sOpt
	endif
End

Function APPEND_IPT(sWinname,sIpt,sXwave,vFlag,vColor1,vColor2,vColor3)
	String sIpt ,sXwave,sWinname
	Variable vFlag,vColor1,vColor2,vColor3
	if (vFlag==1)
		AppendToGraph/W=$sWinname $sIpt vs $sXwave
		ModifyGraph/W=$sWinname rgb($sIpt)=(vColor1,vColor2,vColor3)
	endif
End

Function UPDATE_REFERENCE(ctrlName,varNum,varStr,varName) : SetVariableControl
	String ctrlName,varStr,varName
	Variable varNum
	svar sgReference, sgReferenceImg
	UPDATE_REFERENCE_SUB($sgReference, $sgReferenceImg)
End
Function UPDATE_REFERENCE_SUB(wName1, wName2)
	wave wName1, wName2
	nvar vgFreq, vgPshift, vgSamplerate, vgPhase
	wname1[]=sin(2*pi*vgFreq*(p-vgPshift)/vgSamplerate-vgPhase)
	wname2[]=sin(2*pi*vgFreq*(p-vgPshift)/vgSamplerate-vgPhase-pi/2)
End

Function PLUS(ctrlName):ButtonControl
	String ctrlName
	svar sgReference, sgReferenceImg
	PLUS_SUB($sgReference, $sgReferenceImg)
End
Function PLUS_SUB(wName1, wName2)
	wave wName1, wName2
	nvar vgFreq, vgPshift, vgSamplerate, vgPhase
	vgPhase+=pi/2
	wName1[]=sin(2*pi*vgFreq*(p-vgPshift)/vgSamplerate-vgPhase)
	wName2[]=sin(2*pi*vgFreq*(p-vgPshift)/vgSamplerate-vgPhase-pi/2)
End
```

```
Function MINUS(ctrlName):ButtonControl
        String ctrlName
        svar sgReference, sgReferenceImg
        MINUS_SUB($sgReference, $sgReferenceImg)
End
Function MINUS_SUB(wName1, wName2)
        wave wName1, wName2
        nvar vgFreq, vgPshift, vgSamplerate, vgPhase
        vgPhase+=-pi/2
        wName1[]=sin(2*pi*vgFreq*(p-vgPshift)/vgSamplerate-vgPhase)
        wName2[]=sin(2*pi*vgFreq*(p-vgPshift)/vgSamplerate-vgPhase-pi/2)
End

Function MULTIPLY_REFERENCE(ctrlName):ButtonControl
        String ctrlName
        Variable i
        NVAR vgSamplerate, vgFreq
        Wave Flag, Color1, Color2, Color3
        Wave/T Ipt, IptTuned, IptTunedImg
        SVAR sgReference, sgReferenceImg, sgTimestamp
        if (mod(vgSamplerate, vgFreq) != 0)
                Doalert 0, "Samplerate/Frequency is not integer."
        endif

        i=1
        Do
                TUNING(Flag[i], Ipt[i], IptTuned[i], sgReference)
                i+=1
        While (i<6)

        i=1
        Do
                TUNING(Flag[i], Ipt[i], IptTunedImg[i], sgReferenceImg)
                i+=1
        While (i<6)

        Killwindow phase_tuning
        Display/N=locked
        ModifyGraph/W=locked margin(top)=20
        i=1
        Do
                APPEND_IPT("locked",IptTuned[i],sgTimestamp,Flag[i],Color1[i],Color2[i],Color3[i])
                i+=1
        While (i<6)
        Legend/W=locked/C/N=text0/A=RB
        Label/W=locked bottom "Time (sec)"
        Label/W=locked left "Refsignal * Raw input"

        if (Flag[1]==1)
                SetVariable amp1 win=locked,size={80,20},value=Ampgain[1], title="amp1"
        endif
        if (Flag[2]==1)
                SetVariable amp2 win=locked,size={80,20},value=Ampgain[2], title="amp2"
        endif
        if (Flag[3]==1)
                SetVariable amp3 win=locked,size={80,20},value=Ampgain[3], title="amp3"
        endif
        if (Flag[4]==1)
                SetVariable amp4 win=locked,size={80,20},value=Ampgain[4], title="amp4"
        endif
        if (Flag[5]==1)
                SetVariable amp5 win=locked,size={80,20},value=Ampgain[5], title="amp5"
        endif

        Button calculate win=locked,size={60,20} ,proc=CALCULATION, title="calculate"
End

Function TUNING(vFlag, sIpt, sTuned, sRef)
        variable vFlag
        string sIpt, sTuned, sRef
        if (vFlag == 1)
                wave wIpt=$sIpt
                wave wTuned=$sTuned
                wave wRef=$sRef
                wTuned[]=wIpt[p]*wRef[p]
        endif
End

Function CALCULATION(ctrlName):ButtonControl
        String ctrlName
        Variable i
        NVAR vgPointofcycle, vgSamplerate, vgFreq, vgTotalpoint
        Wave/T IptLocked, IptLockedImg, IptPhaseshift, Ipt, IptTuned, IptTunedImg, IptNorm
        Wave Flag, Ampgain, Color1, Color2, Color3
        vgPointofcycle=vgSamplerate/vgFreq
        i=0
        Do
                Make/O/N=(vgTotalpoint/vgPointofcycle) $IptLocked[i]
                i+=1
        While (i < 6)

        i=1
        Do
                Make/O/N=(vgTotalpoint/vgPointofcycle) $IptLockedImg[i]
```

```
		i+=1
	While (i<6)

	i=1
	Do
		Make/O/N=(vgTotalpoint/vgPointofcycle) $IptPhaseshift[i]
		i+=1
	While (i<6)

	i=1
	Do
		Make/O/N=(vgTotalpoint/vgPointofcycle) $IptNorm[i]
		i+=1
	While (i<6)

	FIELD_CALC($Ipt[0], $IptLocked[0])

	i=1
	Do
		AVERAGE_IPT(Flag[i],$IptTuned[i],$IptLocked[i],Ampgain[i])
		i+=1
	While (i<6)

	i=1
	Do
		AVERAGE_IPT(Flag[i],$IptTunedImg[i],$IptLockedImg[i],Ampgain[i])
		i+=1
	While (i<6)

	i=1
	Do
		PHASESHIFT_CALC(Flag[i], $IptPhaseshift[i], $IptLockedImg[i], $IptLocked[i])
		i+=1
	While (i<6)

	i=1
	Do
		NORM_CALC(Flag[i], $IptNorm[i], $IptLockedImg[i], $IptLocked[i])
		i+=1
	While (i<6)

	Killwindow locked
	Display/N=result
	ModifyGraph/W=result margin(top)=20
	i=1
	Do
		APPEND_IPT("result",IptLocked[i],IptLocked[0],Flag[i],Color1[i],Color2[i],Color3[i])
		i+=1
	While (i<6)

	Legend/W=result/C/N=text0/A=RB
	Label/W=result bottom "Magnetic field (T)"
	Label/W=result left "Absolute value"
	Button savewaves win=result,size={60,20} ,proc=SAVE_WAVES, title="save"
	SetVariable setfilename win=result,size={200,20},value=sgFilename, title="filename"

	Display/N=phaseshift
	ModifyGraph/W=phaseshift margin(top)=20
	i=1
	Do
		APPEND_IPT("phaseshift",IptPhaseshift[i],IptLocked[0],Flag[i],Color1[i],Color2[i],Color3[i])
		i+=1
	While (i<6)
	Legend/W=phaseshift/C/N=text0/A=RB
	Label/W=phaseshift bottom "Magnetic field (T)"
	Label/W=phaseshift left "Phase shift (deg)"
	Button OK win=phaseshift,size={60,20} ,proc=OK, title="OK"
	TextBox/C/N=text1/F=0 "\\Z18Phase shift check"
End

Function AVERAGE_IPT(vFlag,sIpt,sOpt,vAmp)
	Variable vFlag, vAmp
	wave sIpt,sOpt
	NVAR vgPointofcycle
	NVAR vgTotalpoint
	Variable i
	i=0
	if(vFlag==1)
		do
			Wavestats/Q/R=(i*vgPointofcycle,i*vgPointofcycle+(vgPointofcycle-1)) sIpt
			sOpt[i]=2*V_avg/vAmp
			i+=1
		while(i<vgTotalpoint/vgPointofcycle)
	endif
End

Function FIELD_CALC(sIpt,sIptLocked)
	wave sIpt, sIptLocked
	NVAR vgPointofcycle
	NVAR vgTotalpoint
	Variable i

	i=0
		do
```

```
                        Wavestats/Q/R=(i*vgPointofcycle,i*vgPointofcycle+(vgPointofcycle-1)) sIpt
                        sIptLocked[i]=V_avg
                        i+=1
                while(i<vgTotalpoint/vgPointofcycle)
End

Function SAVE_WAVES(ctrlName):ButtonControl
        String ctrlName
        Variable i
        NVAR vgTotalpoint, vgPointofcycle
        SVAR sgFilename
        Wave/T IptLocked, Num
        Wave Flag, Color1, Color2, Color3
        Make/O/N=(vgTotalpoint/vgPointofcycle) $sgFilename+"_field"
        Duplicate/O/R=(0,vgTotalpoint/vgPointofcycle-1) $IptLocked[0],$sgFilename+"_field"

        i=1
        Do
                COPY_IPT(Flag[i],"_input"+Num[i],$IptLocked[i])
                i+=1
        While (i<6)

        Killwindow result
        Display/N=saved_waves
        i=1
        Do
                APPEND_IPT("saved_waves",sgFilename+"_input"+Num[i],sgFilename+"_field", Flag[i],Color1[i],
                     Color2[i],Color3[i])
                i+=1
        While (i<6)
        Legend/W=saved_waves/C/N=text0/A=RB

        SAVE_WAVES_FROM_GRAPH("saved_waves")
        Killwindow saved_waves
        Killwaves $sgFilename+"_field"
        i=1
        Do
                if (Flag[i]==1)
                        KILL_IPT($sgFilename+"_input"+Num[i])
                endif
                i+=1
        While(i<6)
End

Function PHASESHIFT_CALC(vFlag, sPhaseshift,sLockedImg,sLocked)
        variable vFlag
        wave sPhaseshift, sLockedImg, sLocked
        if (vFlag == 1)
        sPhaseshift[]=atan(sLockedImg[p]/sLocked[p])*180/pi
        endif
End

Function OK(ctrlName):ButtonControl
        string ctrlName
        Killwindow phaseshift
End

Function NORM_CALC(vFlag, sNorm, sLockedImg, sLocked)
        variable vFlag
        wave sNorm, sLockedImg, sLocked
        if (vFlag == 1)
        sNorm[]=sqrt(sLockedImg[p]^2+sLocked[p]^2)
        endif
End

Function SAVE_WAVES_FROM_GRAPH(graphName)
        String graphName
        String list, traceList, traceName
        SVAR sgFilename
        Variable index = 0
        list = ""
        traceList = TraceNameList(graphName, ";", 1)
        traceName=StringFromList(0,traceList,";")
        Wave refx=XWaveRefFromTrace(graphName, traceName)
        list+=GetWavesDataFolder(refx,2) + ";"

        do
                traceName = StringFromList(index, traceList, ";")
                if (strlen(traceName) == 0)
                        break
                endif
                Wave w = TraceNameToWaveRef(graphName, traceName)
                list += GetWavesDataFolder(w,2) + ";"
                index += 1
        while(1)

        if (strlen(list) > 0)
                Save/G/W/B/M="\r\n" list as sgFilename+".txt"
        endif
End

Function KILL_IPT(sIpt)
        Wave sIpt
        Killwaves sIpt
```

```
End

Function COPY_IPT(vFlag,sChar,sIpt)
        Variable vFlag
        String sChar
        wave sIpt
        NVAR vgTotalpoint
        NVAR vgPointofcycle
        SVAR sgFilename
        if (vFlag==1)
                Duplicate/O/R=(0,vgTotalpoint/vgPointofcycle-1) sIpt, $sgFilename+sChar
        endif
End
```

A.2 Data Acquisition with Tektronix DPO5104B

```
#pragma rtGlobals=3             // Use modern global access method.
#pragma version=2.0

//TEKTRONIX control
//real-time control
//all waves will be saved (not only active waves)
//160223 AKB (k_akiba@issp.u-tokyo.ac.jp)

Menu "TEKTRONIX"
        "Activate TEKTRONIX", TEKTRONIX()
End

function TEKTRONIX()
        newdatafolder/o/s root:TEKTRO

        variable/g vgSrate, vgDatalength, vgInterval, vgHorizPosition
        string/g sgAddress="TCPIP::169.254.88.181::INSTR"
        string/g sgDest1="TEKTRO_ch1", sgDest2="TEKTRO_ch2", sgDest3="TEKTRO_ch3", sgDest4="TEKTRO_ch4"

        variable/g vgSelect1, vgSelect2, vgSelect3, vgSelect4
        variable/g vgScale1, vgScale2, vgScale3, vgScale4
        variable/g vgPosition1, vgPosition2, vgPosition3, vgPosition4
        variable/g vgOffset1, vgOffset2, vgOffset3, vgOffset4
        variable/g vgUnit1, vgUnit2, vgUnit3, vgUnit4

        variable/g vgDig_unit1

        variable/g vgCom=0

        string/g sgAcq

        make/o TEKTRO_ch1=0
        make/o TEKTRO_ch2=0
        make/o TEKTRO_ch3=0
        make/o TEKTRO_ch4=0

        newpanel/w=(315,10,1000,250)/n=TEKTRONIX_MAIN_PANEL
        SetDrawEnv textrgb= (26368,0,52224),fname= "Times New Roman",fstyle= 1,fsize= 64
        DelayUpdate
        DrawText/w=TEKTRONIX_MAIN_PANEL 399,222,"Tektronix"

        SetDrawEnv linefgc= (65280,0,0),linethick= 3.00
        DrawLine/w=TEKTRONIX_MAIN_PANEL 643,210,626,238 //red line

        SetDrawEnv fname= "Times New Roman"
        DrawText 400,230,"DPO 5104B"

        SetDrawEnv linefgc= (65280,65280,0),linethick= 3.00
        DrawLine/w=TEKTRONIX_MAIN_PANEL 54,36,78,36

        SetDrawEnv linefgc= (0,43520,65280),linethick= 3.00
        DrawLine/w=TEKTRONIX_MAIN_PANEL 54,86,78,86

        SetDrawEnv linefgc= (65280,0,52224),linethick= 3.00
        DrawLine/w=TEKTRONIX_MAIN_PANEL 54,136,78,136

        SetDrawEnv linefgc= (0,65280,0),linethick= 3.00
        DrawLine/w=TEKTRONIX_MAIN_PANEL 54,186,78,186

        SetDrawEnv fillpat= 0
        drawrect/w=TEKTRONIX_MAIN_PANEL 6,25,374,71
        SetDrawEnv fillpat= 0
        drawrect/w=TEKTRONIX_MAIN_PANEL 6,75,374,121
        SetDrawEnv fillpat= 0
        drawrect/w=TEKTRONIX_MAIN_PANEL 6,125,374,171
        SetDrawEnv fillpat= 0
        drawrect/w=TEKTRONIX_MAIN_PANEL 6,175,374,221

        setvariable Address win=TEKTRONIX_MAIN_PANEL, size={300, 25}, value=sgAddress, pos={1,3}, title="
             Address: "
        button update win=TEKTRONIX_MAIN_PANEL, size = {60, 20}, proc = UPDATE, title = "receive", pos
             ={316,3}
        button apply win=TEKTRONIX_MAIN_PANEL, size = {60, 20}, proc = APPLY, title = "send", pos={386,3},
             disable=2
        button read win=TEKTRONIX_MAIN_PANEL, size = {70, 20}, proc = READ, title = "read data", pos={480,3}
```

```
        button graph win=TEKTRONIX_MAIN_PANEL, size = {70, 20}, proc=GRAPHPANEL, title = "graph", pos={590,3}

        checkbox Select1 size={80, 25}, title="Ch1", variable=vgSelect1, proc=STATE1, pos={10,30}
        setvariable Dest1 disable=2, win=TEKTRONIX_MAIN_PANEL, size={200, 25}, value=sgDest1, pos={100,30},
             title="Dest1: "
        setvariable Scale0 win=TEKTRONIX_MAIN_PANEL, size={125, 25}, value=vgScale1, title="Scale: ", pos
             ={10,50}, proc=APPLY_SETTING_SV
        setvariable Position0 win=TEKTRONIX_MAIN_PANEL, size={125, 25}, value=vgPosition1, title="Position:
             ", pos={140,50}, proc=APPLY_SETTING_SV
        setvariable Offset0 disable=2,win=TEKTRONIX_MAIN_PANEL, size={100, 25}, value=vgOffset1, title="
             Offset: ", pos={270,50}, proc=APPLY_SETTING_SV
        button stop win=TEKTRONIX_MAIN_PANEL, size = {60, 20}, proc = STOP, title = "stop", fcolor
             =(65280,0,0), pos={400,30}

        checkbox Select2 size={80, 25}, title="Ch2", variable=vgSelect2, proc=STATE2, pos={10,80}
        setvariable Dest2 disable=2, win=TEKTRONIX_MAIN_PANEL, size={200, 25}, value=sgDest2, pos={100,80},
             title="Dest2: "
        setvariable Scale1 win=TEKTRONIX_MAIN_PANEL, size={125, 25}, value=vgScale2, title="Scale: ", pos
             ={10,100}, proc=APPLY_SETTING_SV
        setvariable Position1 win=TEKTRONIX_MAIN_PANEL, size={125, 25}, value=vgPosition2, title="Position:
             ", pos={140,100}, proc=APPLY_SETTING_SV
        setvariable Offset1 disable=2, win=TEKTRONIX_MAIN_PANEL, size={100, 25}, value=vgOffset2, title="
             Offset: ", pos={270,100}, proc=APPLY_SETTING_SV
        button run win=TEKTRONIX_MAIN_PANEL, size = {60, 20}, proc = RUN, title = "run", fcolor=(0,65280,0),
             pos={400,50}

        checkbox Select3 size={80, 25}, title="Ch3", variable=vgSelect3, proc=STATE3, pos={10,130}
        setvariable Dest3 disable=2, win=TEKTRONIX_MAIN_PANEL, size={200, 25}, value=sgDest3, pos={100,130},
             title="Dest3: "
        setvariable Scale2 win=TEKTRONIX_MAIN_PANEL, size={125, 25}, value=vgScale3, title="Scale: ", pos
             ={10,150}, proc=APPLY_SETTING_SV
        setvariable Position2 win=TEKTRONIX_MAIN_PANEL, size={125, 25}, value=vgPosition3, title="Position:
             ", pos={140,150}, proc=APPLY_SETTING_SV
        setvariable Offset2 disable=2,  win=TEKTRONIX_MAIN_PANEL, size={100, 25}, value=vgOffset3, title="
             Offset: ", pos={270,150}, proc=APPLY_SETTING_SV
        button single win=TEKTRONIX_MAIN_PANEL, size = {60, 20}, proc = SINGLE, title = "single",fcolor
             =(0,65280,0), pos={400,80}

        checkbox Select4 size={80, 25}, title="Ch4", variable=vgSelect4, proc=STATE4, pos={10,180}
        setvariable Dest4 disable=2, win=TEKTRONIX_MAIN_PANEL, size={200, 25}, value=sgDest4, pos={100,180},
             title="Dest4: "
        setvariable Scale3 win=TEKTRONIX_MAIN_PANEL, size={125, 25}, value=vgScale4, title="Scale: ", pos
             ={10,200}, proc=APPLY_SETTING_SV
        setvariable Position3 win=TEKTRONIX_MAIN_PANEL, size={125, 25}, value=vgPosition4, title="Position:
             ", pos={140,200}, proc=APPLY_SETTING_SV
        setvariable Offset3 disable=2, win=TEKTRONIX_MAIN_PANEL, size={100, 25}, value=vgOffset4, title="
             Offset: ", pos={270,200}, proc=APPLY_SETTING_SV

        setvariable horizposition win=TEKTRONIX_MAIN_PANEL, size={175, 25}, value=vgHorizPosition, title="
             HorizPosition: ", pos={500,30}, proc=APPLY_SETTING_SV

        setvariable datalength win=TEKTRONIX_MAIN_PANEL, size={175, 25}, value=vgDatalength, title="
             Datalength: ", pos={500,60}, proc=APPLY_SETTING_SV

        setvariable srate win=TEKTRONIX_MAIN_PANEL, size={175, 25}, value=vgSrate, title="Samplerate: ", pos
             ={500,90}, proc=APPLY_SETTING_SV

        //valdisplay totaltime win=TEKTRONIX_MAIN_PANEL, size={175, 25}, value = #"vgDatalength/vgSrate",
             title = "totaltime: ", pos={500,120}

        //button NO win=TEKTRONIX_MAIN_PANEL, size = {150, 20}, noproc, title = "numerical ORPHEUS",pos
             ={470,215} //to access numerical ORPHEUS directly.

        popupmenu acq win=TEKTRONIX_MAIN_PANEL, size={150, 25}, value="SAMPLE;PEAKDETECT;HIRES;AVERAGE;WFMDB;
             ENVELOPE;", pos={385,140}, title="Acq. mode", proc=ACQ

        setvariable acq_string win=TEKTRONIX_MAIN_PANEL, size={100, 25}, value = sgAcq, title = "Acq: ", pos
             ={385,110}, disable=2
end

Function ACQ (ctrlName,popNum,popStr) : PopupMenuControl
        String ctrlName
        Variable popNum // which item is currently selected (1-based)
        String popStr           // contents of current popup item as string
        svar sgAcq

        sgAcq=popStr
        APPLY_SETTING()
End

Function STATE1 (ctrlName,checked) : CheckBoxControl
        String ctrlName
        Variable checked                // 1 if selelcted, 0 if not
        setdatafolder root:TEKTRO
        nvar vgSelect1
        vgSelect1=checked
        APPLY_SETTING()
End

Function STATE2 (ctrlName,checked) : CheckBoxControl
        String ctrlName
        Variable checked                // 1 if selelcted, 0 if not
        setdatafolder root:TEKTRO
        nvar vgSelect2
```

```
        vgSelect2=checked
        APPLY_SETTING()
End

Function STATE3 (ctrlName,checked) : CheckBoxControl
        String ctrlName
        Variable checked                // 1 if selelcted, 0 if not
        setdatafolder root:TEKTRO
        nvar vgSelect3
        vgSelect3=checked
        APPLY_SETTING()
End

Function STATE4 (ctrlName,checked) : CheckBoxControl
        String ctrlName
        Variable checked                // 1 if selelcted, 0 if not
        setdatafolder root:TEKTRO
        nvar vgSelect4
        vgSelect4=checked
        APPLY_SETTING()
End

function UPDATE(ctrlName) : ButtonControl
        string ctrlName
        setdatafolder root:TEKTRO
        nvar vgCom
        vgCom=1
        ASK_STATE()
        ASK_SCALE()
        ASK_POSITION()
        ASK_OFFSET()
        ASK_LENGTH()
        ASK_SRATE()
        ASK_HORIZPOSITION()
        ASK_ACQ()
        vgCom=0
end

function ASK_STATE()
        variable defaultRM, instr
        svar sgAddress
        nvar vgSelect1, vgSelect2, vgSelect3, vgSelect4
        viOpenDefaultRM(defaultRM)
        viOpen(defaultRM, sgAddress, 0, 0, instr)
                visawrite instr, "SELect:CH1?"
                visaread instr, vgSelect1
                visawrite instr, "SELect:CH2?"
                visaread instr, vgSelect2
                visawrite instr, "SELect:CH3?"
                visaread instr, vgSelect3
                visawrite instr, "SELect:CH4?"
                visaread instr, vgSelect4
        viClose(instr)
        viClose(defaultRM)
end

function ASK_SCALE()
        variable defaultRM, instr
        svar sgAddress
        nvar vgScale1, vgScale2, vgScale3, vgScale4
        viOpenDefaultRM(defaultRM)
        viOpen(defaultRM, sgAddress, 0, 0, instr)
                visawrite instr, "CH1:SCAle?"
                visaread instr, vgScale1
                visawrite instr, "CH2:SCAle?"
                visaread instr, vgScale2
                visawrite instr, "CH3:SCAle?"
                visaread instr, vgScale3
                visawrite instr, "CH4:SCAle?"
                visaread instr, vgScale4
        viClose(instr)
        viClose(defaultRM)
end

function ASK_POSITION()
        variable defaultRM, instr
        svar sgAddress
        nvar vgPosition1, vgPosition2, vgPosition3, vgPosition4
        viOpenDefaultRM(defaultRM)
        viOpen(defaultRM, sgAddress, 0, 0, instr)
                visawrite instr, "CH1:POSition?"
                visaread instr, vgPosition1
                visawrite instr, "CH2:POSition?"
                visaread instr, vgPosition2
                visawrite instr, "CH3:POSition?"
                visaread instr, vgPosition3
                visawrite instr, "CH4:POSition?"
                visaread instr, vgPosition4
        viClose(instr)
        viClose(defaultRM)
end

function ASK_OFFSET()
        variable defaultRM, instr
```

```
        svar sgAddress
        nvar vgOffset1, vgOffset2, vgOffset3, vgOffset4
        viOpenDefaultRM(defaultRM)
        viOpen(defaultRM, sgAddress, 0, 0, instr)
                visawrite instr, "CH1:OFFSet?"
                visaread instr, vgOffset1
                visawrite instr, "CH2:OFFSet?"
                visaread instr, vgOffset2
                visawrite instr, "CH3:OFFSet?"
                visaread instr, vgOffset3
                visawrite instr, "CH4:OFFSet?"
                visaread instr, vgOffset4
        viClose(instr)
        viClose(defaultRM)
end

function ASK_LENGTH()
        variable defaultRM, instr
        svar sgAddress
        nvar vgDatalength
        viOpenDefaultRM(defaultRM)
        viOpen(defaultRM, sgAddress, 0, 0, instr)
                visawrite instr, "HORizontal:MODE:RECOrdlength?"
                visaread instr, vgDatalength
        viClose(instr)
        viClose(defaultRM)
end

function ASK_SRATE()
        variable defaultRM, instr
        svar sgAddress
        nvar vgSrate
        viOpenDefaultRM(defaultRM)
        viOpen(defaultRM, sgAddress, 0, 0, instr)
                visawrite instr, "HORizontal:MODE:SAMPLERate?"
                visaread instr, vgSrate
        viClose(instr)
        viClose(defaultRM)
end

function ASK_HORIZPOSITION()
        variable defaultRM, instr
        svar sgAddress
        nvar vgHorizPosition
        viOpenDefaultRM(defaultRM)
        viOpen(defaultRM, sgAddress, 0, 0, instr)
                visawrite instr, "HORizontal:POSition?"
                visaread instr, vgHorizPosition
        viClose(instr)
        viClose(defaultRM)
end

function ASK_ACQ()
        variable defaultRM, instr
        svar sgAddress
        svar sgAcq
        viOpenDefaultRM(defaultRM)
        viOpen(defaultRM, sgAddress, 0, 0, instr)
                visawrite instr, "ACQuire:MODe?"
                visaread/T="\r\n" instr, sgAcq
        viClose(instr)
        viClose(defaultRM)
end

function APPLY(ctrlName) : ButtonControl
        string ctrlName
        setdatafolder root:TEKTRO
        nvar vgCom
        vgCom=1
        ASSIGN_STATE()
        ASSIGN_SCALE()
        ASSIGN_POSITION()
        ASSIGN_OFFSET()
        ASSIGN_LENGTH()
        ASSIGN_SRATE()
        ASSIGN_HORIZPOSITION()
        ASSIGN_ACQ()
        vgCom=0
end

function APPLY_SETTING()
        setdatafolder root:TEKTRO
        nvar vgCom
        vgCom=1
        ASSIGN_STATE()
        ASSIGN_SCALE()
        ASSIGN_POSITION()
        ASSIGN_OFFSET()
        ASSIGN_LENGTH()
        ASSIGN_SRATE()
        ASSIGN_HORIZPOSITION()
        ASSIGN_ACQ()
        vgCom=0
end
```

```
function APPLY_SETTING_SV(ctrlName,varNum,varStr,varName) : SetVariableControl
        String ctrlName
        Variable varNum // value of variable as number
        String varStr           // value of variable as string
        String varName  // name of variable
        setdatafolder root:TEKTRO
        nvar vgCom
        vgCom=1
        ASSIGN_STATE()
        ASSIGN_SCALE()
        ASSIGN_POSITION()
        ASSIGN_OFFSET()
        ASSIGN_LENGTH()
        ASSIGN_SRATE()
        ASSIGN_HORIZPOSITION()
        ASSIGN_ACQ()
        vgCom=0
end

function ASSIGN_STATE()
        variable defaultRM, instr
        svar sgAddress
        nvar vgSelect1, vgSelect2, vgSelect3, vgSelect4
        viOpenDefaultRM(defaultRM)
        viOpen(defaultRM, sgAddress, 0, 0, instr)
                visawrite instr, "SELect:CH1 "+num2str(vgSelect1)
                visawrite instr, "SELect:CH2 "+num2str(vgSelect2)
                visawrite instr, "SELect:CH3 "+num2str(vgSelect3)
                visawrite instr, "SELect:CH4 "+num2str(vgSelect4)
        viClose(instr)
        viClose(defaultRM)
end

function ASSIGN_SCALE()
        variable defaultRM, instr
        svar sgAddress
        nvar vgScale1, vgScale2, vgScale3, vgScale4
        viOpenDefaultRM(defaultRM)
        viOpen(defaultRM, sgAddress, 0, 0, instr)
                visawrite instr, "CH1:SCAle "+num2str(vgScale1)
                visawrite instr, "CH2:SCAle "+num2str(vgScale2)
                visawrite instr, "CH3:SCAle "+num2str(vgScale3)
                visawrite instr, "CH4:SCAle "+num2str(vgScale4)
        viClose(instr)
        viClose(defaultRM)
end

function ASSIGN_POSITION()
        variable defaultRM, instr
        svar sgAddress
        nvar vgPosition1, vgPosition2, vgPosition3, vgPosition4
        viOpenDefaultRM(defaultRM)
        viOpen(defaultRM, sgAddress, 0, 0, instr)
                visawrite instr, "CH1:POSition "+num2str(vgPosition1)
                visawrite instr, "CH2:POSition "+num2str(vgPosition2)
                visawrite instr, "CH3:POSition "+num2str(vgPosition3)
                visawrite instr, "CH4:POSition "+num2str(vgPosition4)
        viClose(instr)
        viClose(defaultRM)
end

function ASSIGN_OFFSET()
        variable defaultRM, instr
        svar sgAddress
        nvar vgOffset1, vgOffset2, vgOffset3, vgOffset4
        viOpenDefaultRM(defaultRM)
        viOpen(defaultRM, sgAddress, 0, 0, instr)
                visawrite instr, "CH1:OFFSet "+num2str(vgOffset1)
                visawrite instr, "CH2:OFFSet "+num2str(vgOffset2)
                visawrite instr, "CH3:OFFSet "+num2str(vgOffset3)
                visawrite instr, "CH4:OFFSet "+num2str(vgOffset4)
        viClose(instr)
        viClose(defaultRM)
end

function ASSIGN_LENGTH()
        variable defaultRM, instr
        svar sgAddress
        nvar vgDatalength
        viOpenDefaultRM(defaultRM)
        viOpen(defaultRM, sgAddress, 0, 0, instr)
                visawrite instr, "HORizontal:MODE MANual"
                visawrite instr, "HORizontal:MODE:RECOrdlength "+num2str(vgDatalength)
        viClose(instr)
        viClose(defaultRM)
end

function ASSIGN_SRATE()
        variable defaultRM, instr
        svar sgAddress
        nvar vgSrate
        viOpenDefaultRM(defaultRM)
        viOpen(defaultRM, sgAddress, 0, 0, instr)
```

```
                visawrite instr, "HORizontal:MODE MANual"
                visawrite instr, "HORizontal:MODE:SAMPLERate "+num2str(vgSrate)
        viClose(instr)
        viClose(defaultRM)
end

function ASSIGN_HORIZPOSITION()
        variable defaultRM, instr
        svar sgAddress
        nvar vgHorizPosition
        viOpenDefaultRM(defaultRM)
        viOpen(defaultRM, sgAddress, 0, 0, instr)
                visawrite instr, "HORizontal:POSition "+num2str(vgHorizPosition)
        viClose(instr)
        viClose(defaultRM)
end

function ASSIGN_ACQ()
        variable defaultRM, instr
        svar sgAddress
        svar sgAcq
        viOpenDefaultRM(defaultRM)
        viOpen(defaultRM, sgAddress, 0, 0, instr)
                visawrite instr, "ACQuire:MODe "+sgAcq
        viClose(instr)
        viClose(defaultRM)
end


function SINGLE(ctrlName) : ButtonControl
        string ctrlName
        setdatafolder root:TEKTRO
        variable defaultRM, instr
        svar sgAddress
        nvar vgCom
        vgCom=1
        viOpenDefaultRM(defaultRM)
        viOpen(defaultRM, sgAddress, 0, 0, instr)
                visawrite instr, "ACQuire:STOPAFTER SEQUENCE"
                visawrite instr, "ACQuire:STATE 1"
        viClose(instr)
        viClose(defaultRM)
        vgCom=0
end

function STOP(ctrlName) : ButtonControl
        string ctrlName
        setdatafolder root:TEKTRO
        variable defaultRM, instr
        svar sgAddress
        nvar vgCom
        vgCom=1
        viOpenDefaultRM(defaultRM)
        viOpen(defaultRM, sgAddress, 0, 0, instr)
                visawrite instr, "ACQuire:STOPAFTER RUNSTOP"
                visawrite instr, "ACQuire:STATE STOP"
        viClose(instr)
        viClose(defaultRM)
        vgCom=0
end

function RUN(ctrlName) : ButtonControl
        string ctrlName
        setdatafolder root:TEKTRO
        variable defaultRM, instr
        svar sgAddress
        nvar vgCom
        vgCom=1
        viOpenDefaultRM(defaultRM)
        viOpen(defaultRM, sgAddress, 0, 0, instr)
                visawrite instr, "ACQuire:STOPAFTER RUNSTOP"
                visawrite instr, "ACQuire:STATE RUN"
        viClose(instr)
        viClose(defaultRM)
        vgCom=0
end

function READ(ctrlName) : ButtonControl
        string ctrlName
        setdatafolder root:TEKTRO
        Variable defaultRM, instr
        variable vDatalength, vInterval, vDig_unit, vOffset, vPosition
        nvar vgSelect1, vgSelect2, vgSelect3, vgSelect4
        svar sgAddress
        nvar vgCom
        vgCom=1

        //UPDATE
        ASK_STATE()
        ASK_SCALE()
        ASK_POSITION()
        ASK_OFFSET()
        ASK_LENGTH()
        ASK_SRATE()
```

```
ASK_HORIZPOSITION()
ASK_ACQ()
//UPDATE

viOpenDefaultRM(defaultRM)
viOpen(defaultRM, sgAddress, 0, 0, instr)
        visawrite instr, "HORizontal:MODE:RECOrdlength?"//ask the record length.
        visaread instr, vDatalength

        visawrite instr, "HORizontal:MODE:SAMPLERate?"//ask the time interval.
        visaread instr, vInterval
        vInterval=1/vInterval
viClose(instr)
viClose(defaultRM)

//make/o/n=(vDatalength) TEKTRO_time
//TEKTRO_time=p*vInterval

viOpenDefaultRM(defaultRM)
viOpen(defaultRM, sgAddress, 0, 0, instr)

        make/o/n=(vDatalength) TEKTRO_ch1=0
        make/o/n=(vDatalength) TEKTRO_ch2=0
        make/o/n=(vDatalength) TEKTRO_ch3=0
        make/o/n=(vDatalength) TEKTRO_ch4=0

        if (vgSelect1 == 1)
                vDig_unit=0
                vOffset=0
                vPosition=0
                visawrite instr, "DATa:SOUrce CH1"
                visawrite instr, "DATa:ENCdg SRIbinary"
                visawrite instr, "DATa:START 1"
                visawrite instr, "DATa:STOP "+num2str(vDatalength)
                visawrite instr, "WFMOutpre:BYT_Nr 1"

                string vNop_wfm
                visawrite instr, "WFMOutpre?"
                visaread/T=",\r\t" instr, vNop_wfm
                print vNop_wfm

                visawrite instr, "WFMOUTpre:YMUlt?"//ask the convert coefficient.
                visaread instr, vDig_unit

                visawrite instr, "WFMOUTpre:YZEro?"//ask the offset.
                visaread instr, vOffset

                visawrite instr, "WFMOUTpre:YOFf?"//ask the position.
                visaread instr, vPosition

                visawrite instr, "CURVe?"
                visareadbinarywave/type=(0x08)/b/y={-vPosition+vOffset/vDig_unit, vDig_unit} instr,
                     TEKTRO_ch1
        endif

        if (vgSelect2 == 1)
                vDig_unit=0
                vOffset=0
                vPosition=0
                visawrite instr, "DATa:SOUrce CH2"
                visawrite instr, "DATa:ENCdg SRIbinary"
                visawrite instr, "DATa:START 1"
                visawrite instr, "DATa:STOP "+num2str(vDatalength)
                visawrite instr, "WFMOutpre:BYT_Nr 1"

                //string vNop_wfm
                visawrite instr, "WFMOutpre?"
                visaread/T=",\r\t" instr, vNop_wfm
                print vNop_wfm

                visawrite instr, "WFMOUTpre:YMUlt?"//ask the convert coefficient.
                visaread instr, vDig_unit

                visawrite instr, "WFMOUTpre:YZEro?"//ask the offset.
                visaread instr, vOffset

                visawrite instr, "WFMOUTpre:YOFf?"//ask the position.
                visaread instr, vPosition

                visawrite instr, "CURVe?"
                visareadbinarywave/type=(0x08)/b/y={-vPosition+vOffset/vDig_unit, vDig_unit} instr,
                     TEKTRO_ch2
        endif

        if (vgSelect3 == 1)
                vDig_unit=0
                vOffset=0
                vPosition=0
                visawrite instr, "DATa:SOUrce CH3"
                visawrite instr, "DATa:ENCdg SRIbinary"
                visawrite instr, "DATa:START 1"
                visawrite instr, "DATa:STOP "+num2str(vDatalength)
                visawrite instr, "WFMOutpre:BYT_Nr 1"
```

```
                        //string vNop_wfm
                        visawrite instr, "WFMOutpre?"
                        visaread/T=",\r\t" instr, vNop_wfm
                        print vNop_wfm

                        visawrite instr, "WFMOUTpre:YMUlt?"//ask the convert coefficient.
                        visaread instr, vDig_unit

                        visawrite instr, "WFMOUTpre:YZEro?"//ask the offset.
                        visaread instr, vOffset

                        visawrite instr, "WFMOUTpre:YOFf?"//ask the position.
                        visaread instr, vPosition

                        visawrite instr, "CURVe?"
                        visareadbinarywave/type=(0x08)/b/y={-vPosition+vOffset/vDig_unit, vDig_unit} instr,
                             TEKTRO_ch3
                endif

                if (vgSelect4 == 1)
                        vDig_unit=0
                        vOffset=0
                        vPosition=0
                        visawrite instr, "DATa:SOUrce CH4"
                        visawrite instr, "DATa:ENCdg SRIbinary"
                        visawrite instr, "DATa:START 1"
                        visawrite instr, "DATa:STOP "+num2str(vDatalength)
                        visawrite instr, "WFMOutpre:BYT_Nr 1"

                        //string vNop_wfm
                        visawrite instr, "WFMOutpre?"
                        visaread/T=",\r\t" instr, vNop_wfm
                        print vNop_wfm

                        visawrite instr, "WFMOUTpre:YMUlt?"//ask the convert coefficient.
                        visaread instr, vDig_unit

                        visawrite instr, "WFMOUTpre:YZEro?"//ask the offset.
                        visaread instr, vOffset

                        visawrite instr, "WFMOUTpre:YOFf?"//ask the position.
                        visaread instr, vPosition

                        visawrite instr, "CURVe?"
                        visareadbinarywave/type=(0x08)/b/y={-vPosition+vOffset/vDig_unit, vDig_unit} instr,
                             TEKTRO_ch4
                endif

        viClose(instr)
        viClose(defaultRM)
        vgCom=0
end

function graphpanel(ctrlName):ButtonControl
        string ctrlName
        setdatafolder root:TEKTRO
        variable/g vgIntOffset, vgCh, vgFpc, vgXch
        variable/g vgDisp1, vgDisp2, vgDisp3, vgDisp4
        wave TEKTRO_ch1, TEKTRO_ch2, TEKTRO_ch3, TEKTRO_ch4
        dowindow TEKTRO_CH
        if (V_flag == 1)
                dowindow/f TEKTRO_CH
                setaxis/a
        else
                display/w=(201,157,740,528)/n=TEKTRO_CH TEKTRO_ch1, TEKTRO_ch2, TEKTRO_ch3, TEKTRO_ch4
                ModifyGraph/w=TEKTRO_CH margin(left)=120,margin(top)=35, gbRGB= (0,0,0), grid=1,gridStyle=1

                ModifyGraph/w=TEKTRO_CH rgb(tektro_ch1)=(65280,65280,0)
                ModifyGraph/w=TEKTRO_CH rgb(tektro_ch2)=(0,43520,65280)
                ModifyGraph/w=TEKTRO_CH rgb(tektro_ch3)=(65280,0,52224)
                ModifyGraph/w=TEKTRO_CH rgb(tektro_ch4)=(0,65280,0)

                checkbox disp1 win=TEKTRO_CH, size = {70, 25}, value=1, variable=vgDisp1, proc=checkboxproc,
                      title = "TEKTRO_ch1", pos={100,15}
                checkbox disp2 win=TEKTRO_CH, size = {70, 25}, value=1, variable=vgDisp2, proc=checkboxproc,
                      title = "TEKTRO_ch2", pos={250,15}
                checkbox disp3 win=TEKTRO_CH, size = {70, 25}, value=1, variable=vgDisp3, proc=checkboxproc,
                      title = "TEKTRO_ch3", pos={400,15}
                checkbox disp4 win=TEKTRO_CH, size = {70, 25}, value=1, variable=vgDisp4, proc=checkboxproc,
                      title = "TEKTRO_ch4", pos={550,15}

                button  datasave win=TEKTRO_CH, size = {70, 20}, proc=DATASAVE, title="save", pos={20, 50}
                button  dataload win=TEKTRO_CH, size = {70, 20}, proc=DATALOAD, title="load", pos={20, 100}
                button  integ win=TEKTRO_CH, size = {70, 20}, proc=INTEG, title="integrate", pos={20, 150}
                button  detect_max win=TEKTRO_CH, size = {70, 20}, proc=DETECT_MAX, title="detectmax", pos
                     ={20, 200}
                button  buildyx win=TEKTRO_CH, size = {70, 20}, proc=BUILD_YX, title="Y-X", pos={20, 250}

                SetDrawEnv linefgc= (65280,65280,0),linethick= 3.00, xcoord= abs,ycoord= abs;DelayUpdate
                DrawLine/w=TEKTRO_CH 140,17,155,17

                SetDrawEnv linefgc= (0,43520,65280),linethick= 3.00, xcoord= abs,ycoord= abs;DelayUpdate
                DrawLine/w=TEKTRO_CH 255,17,270,17
```

```
                SetDrawEnv linefgc= (65280,0,52224),linethick= 3.00, xcoord= abs,ycoord= abs;DelayUpdate
                DrawLine/w=TEKTRO_CH 370,17,385,17

                SetDrawEnv linefgc= (0,65280,0),linethick= 3.00, xcoord= abs,ycoord= abs;DelayUpdate
                DrawLine/w=TEKTRO_CH 485,17,500,17

        endif
end

function checkboxproc(name, checked):CheckBoxControl
        string name
        variable checked
        setdatafolder root:TEKTRO
        variable vCh
        string sWavename

        make/o/n=(4, 3) ColorParam
        ColorParam[0][0]=65280; ColorParam[0][1]=65280;ColorParam[0][2]=0;
        ColorParam[1][0]=0;ColorParam[1][1]=43520;ColorParam[1][2]=65280;
        ColorParam[2][0]=65280;ColorParam[2][1]=0;ColorParam[2][2]=52224;
        ColorParam[3][0]=0;ColorParam[3][1]=65280;ColorParam[3][2]=0;

        strswitch (name)
                case "disp1":
                        vCh=1
                        break
                case "disp2":
                        vCh=2
                        break
                case "disp3":
                        vCh=3
                        break
                case "disp4":
                        vCh=4
                        break
        endswitch

        sWavename="TEKTRO_ch"+num2str(vCh)

        if (exists(sWavename) == 0)
                checkbox $name, value = 0
        else
                if (checked == 1)
                        appendtograph/w=TEKTRO_CH $sWavename
                        modifygraph/w=TEKTRO_CH rgb($sWavename)=(ColorParam[vCh-1][0],ColorParam[vCh-1][1],
                             ColorParam[vCh-1][2])

                else
                        removefromgraph/w=TEKTRO_CH $sWavename
                endif
        endif
end

function DATASAVE(ctrlName):ButtonControl
        string ctrlName
        setdatafolder root:TEKTRO
        string sSavelist=""
        nvar vgDisp1, vgDisp2, vgDisp3, vgDisp4
        //if (vgDisp1 == 1)
                sSavelist+="TEKTRO_ch1;"
        //endif
        //if (vgDisp2 == 1)
                sSavelist+="TEKTRO_ch2;"
        //endif
        //if (vgDisp3 == 1)
                sSavelist+="TEKTRO_ch3;"
        //endif
        //if (vgDisp4 == 1)
                sSavelist+="TEKTRO_ch4"
        //endif
        Save/G/W/B/M="\r\n" sSavelist
        print ssavelist
end

function INTEG(ctrlName):ButtonControl
        string ctrlName
        setdatafolder root:TEKTRO
        variable vCh
        prompt vCh, "Channel", popup "TEKTRO_ch1;TEKTRO_ch2;TEKTRO_ch3;TEKTRO_ch4"
        doprompt "Integrate", vCh
        nvar vgCh
        vgCh=vCh
        string sWavename="TEKTRO_ch"+num2str(vgCh)

        duplicate/o $sWavename, Int_wave
        duplicate/o Int_wave Int_wave_copy

        nvar vgIntOffset

        Int_wave=Int_wave_copy+vgIntOffset/1e5
        integrate Int_wave

        display/w=(201,157,740,528)/n=FIELD_PROP Int_wave
        ModifyGraph/w=FIELD_PROP margin(top)=35, gbRGB= (0,0,0), grid=1,gridStyle=1
```

```
        setvariable offset_op win=FIELD_PROP, size={160, 25}, value=vgIntOffset, proc=INTEGRATE_OP, pos
             ={1,3}, title="Offset (x10E-5): "
        setvariable fpc win=FIELD_PROP, size={100, 25}, value=vgFpc, noproc, pos={250,3}, title="F.P.C.: "
        button  integrate_op win=FIELD_PROP, size = {50, 20}, proc=OK_TEKTRO, title="OK", pos={500, 3}

end

Function INTEGRATE_OP (ctrlName,varNum,varStr,varName) : SetVariableControl
        String ctrlName
        Variable varNum
        String varStr
        String varName

        setdatafolder root:TEKTRO

        nvar vgIntOffset, vgCh
        wave Int_wave, Int_wave_copy

        Int_wave=Int_wave_copy+vgIntOffset/1e5
        integrate Int_wave

End


proc OK_TEKTRO(ctrlName):ButtonControl
        string ctrlName
        setdatafolder root:TEKTRO
        string sWavename="TEKTRO_ch"+num2str(vgCh)
        $sWavename=Int_wave*vgFpc
        killwindow FIELD_PROP
        killwaves Int_wave, Int_wave_copy
end

function DETECT_MAX(ctrlName):ButtonControl
        string ctrlName
        setdatafolder root:TEKTRO
        variable vCh
        prompt vCh, "Channel", popup "TEKTRO_ch1;TEKTRO_ch2;TEKTRO_ch3;TEKTRO_ch4"
        doprompt "detect max", vCh
        nvar vgCh
        vgCh=vCh
        string sWavename="TEKTRO_ch"+num2str(vgCh)

        silent 1

        wavestats/q $sWavename
        Doalert 0, "Max = "+num2str(V_max)+" (Min = "+num2str(V_min)+")"
        printf "Max = "+num2str(V_max)+" (Min = "+num2str(V_min)+")\r"
end

function DATALOAD(ctrlName):ButtonControl
        string ctrlName
        setdatafolder root:TEKTRO
        loadwave/q/g/n=TEKTRO_LOAD
        string sDestwave="TEKTRO_ch"
        string sSourcewave="TEKTRO_LOAD"

        variable i=0
        do
                sDestwave+=num2str(i+1)
                sSourcewave+=num2str(i)
                duplicate/o $sSourcewave $sDestwave
                sDestwave="TEKTRO_ch"
                sSourcewave="TEKTRO_LOAD"
                i+=1
                if (i+1 > V_flag)
                        break
                endif
        while (i < 4)

        i=0
        do
                sSourcewave+=num2str(i)
                killwaves $sSourcewave
                sSourcewave="TEKTRO_LOAD"
                i+=1
        while (i < V_flag)
        print "TEKTRO LOAD "+S_fileName
end

function BUILD_YX(ctrlName):ButtonControl
        string ctrlName
        setdatafolder root:TEKTRO
        variable vXch
        prompt vXch, "X wave", popup "TEKTRO_ch1;TEKTRO_ch2;TEKTRO_ch3;TEKTRO_ch4"
        doprompt "Build YX" vXch
        string sXch="TEKTRO_CH"
        nvar vgXch
        wave TEKTRO_ch1, TEKTRO_ch2, TEKTRO_ch3, TEKTRO_ch4

        vgXch=vXch

        sXch+=num2str(vXch)
```

```
	nvar vgIntOffset, vgCh, vgFpc
	dowindow YX_PROP
	if (V_flag == 1)
		dowindow/f YX_PROP
		setaxis/a
	else
		display/w=(201,157,740,528)/n=YX_PROP TEKTRO_ch1, TEKTRO_ch2, TEKTRO_ch3, TEKTRO_ch4 vs $sXch
		ModifyGraph/w=YX_PROP margin(left)=120,margin(top)=35, gbRGB= (0,0,0), grid=1,gridStyle=1

		ModifyGraph/w=YX_PROP rgb(tektro_ch1)=(65280,65280,0)
		ModifyGraph/w=YX_PROP rgb(tektro_ch2)=(0,43520,65280)
		ModifyGraph/w=YX_PROP rgb(tektro_ch3)=(65280,0,52224)
		ModifyGraph/w=YX_PROP rgb(tektro_ch4)=(0,65280,0)

		checkbox yxdisp1 win=YX_PROP, size = {70, 25}, value=1, proc=yxcheckboxproc,  title = "
		     TEKTRO_ch1", pos={100,15}
		checkbox yxdisp2 win=YX_PROP, size = {70, 25}, value=1, proc=yxcheckboxproc,  title = "
		     TEKTRO_ch2", pos={250,15}
		checkbox yxdisp3 win=YX_PROP, size = {70, 25}, value=1, proc=yxcheckboxproc,  title = "
		     TEKTRO_ch3", pos={400,15}
		checkbox yxdisp4 win=YX_PROP, size = {70, 25}, value=1, proc=yxcheckboxproc,  title = "
		     TEKTRO_ch4", pos={550,15}

		SetDrawEnv linefgc= (65280,65280,0),linethick= 3.00, xcoord= abs,ycoord= abs;DelayUpdate
		DrawLine/w=YX_PROP 140,17,155,17

		SetDrawEnv linefgc= (0,43520,65280),linethick= 3.00, xcoord= abs,ycoord= abs;DelayUpdate
		DrawLine/w=YX_PROP 255,17,270,17

		SetDrawEnv linefgc= (65280,0,52224),linethick= 3.00, xcoord= abs,ycoord= abs;DelayUpdate
		DrawLine/w=YX_PROP 370,17,385,17

		SetDrawEnv linefgc= (0,65280,0),linethick= 3.00, xcoord= abs,ycoord= abs;DelayUpdate
		DrawLine/w=YX_PROP 485,17,500,17
	endif
end

function yxcheckboxproc(name, checked):CheckBoxControl
	string name
	variable checked
	setdatafolder root:TEKTRO
	variable vCh
	string sWavename
	nvar vgXch
	string sXwavename="TEKTRO_ch"+num2str(vgXch)

	make/o/n=(4, 3) ColorParam
	ColorParam[0][0]=65280; ColorParam[0][1]=65280;ColorParam[0][2]=0;
	ColorParam[1][0]=0;ColorParam[1][1]=43520;ColorParam[1][2]=65280;
	ColorParam[2][0]=65280;ColorParam[2][1]=0;ColorParam[2][2]=52224;
	ColorParam[3][0]=0;ColorParam[3][1]=65280;ColorParam[3][2]=0;

	strswitch (name)
		case "yxdisp1":
		   vCh=1
		   break
		case "yxdisp2":
		   vCh=2
		   break
		case "yxdisp3":
		   vCh=3
		   break
		case "yxdisp4":
		   vCh=4
		   break
	endswitch

	sWavename="TEKTRO_ch"+num2str(vCh)

	if (exists(sWavename) == 0)
		checkbox $name, value = 0
	else
		if (checked == 1)
			appendtograph/w=YX_PROP $sWavename vs $sXwavename
			modifygraph/w=YX_PROP rgb($sWavename)=(ColorParam[vCh-1][0],ColorParam[vCh-1][1],
			     ColorParam[vCh-1][2])

		else
			removefromgraph/w=YX_PROP $sWavename
		endif
	endif
end
```

A.3 Numerical Analysis of Ultrasonic Measurements

```
#pragma TextEncoding = "UTF-8"
#pragma rtGlobals=3 // Use modern global access method and strict wave access.

//Ultrasonic measurement in pulsed magnetic fields.
//AKB (k_akiba@issp.u-tokyo.ac.jp)
```

```
Menu "Numerical ORPHEUS"
        "Activate NUMERICAL_ORPHEUS", NO_INIT()
End

macro NO_INIT()
        newdatafolder/o/s root:TEKTRO
        NUMERICAL_ORPHEUS()
end

macro NUMERICAL_ORPHEUS(vSrate_NO, vDatalength_NO, vUsfreq_NO, vPulsefreq_NO, sEcho, sField)
        variable/g vgSrate_NO, vgDatalength_NO, vgUsfreq_NO, vgPulsefreq_NO //fundamental parameters
        string/g sgEcho, sgField //input waves
        variable vSrate_NO=vgSrate_NO, vDatalength_NO=vgDatalength_NO, vUsfreq_NO=vgUsfreq_NO, vPulsefreq_NO=
             vgPulsefreq_NO //load parameters
        string sEcho=sgEcho, sField=sgField //load input wave names
        prompt vSrate_NO, "Sampling rate (Hz)"
        prompt vDatalength_NO, "Data length"
        prompt vUsfreq_NO, "Ultrasonic freq (Hz)"
        prompt vPulsefreq_NO, "Pulse freq (Hz)"
        prompt sEcho, "Echo signal"
        prompt sField, "dBdt"

        silent 1

        //begin of save parameters
        vgSrate_NO=vSrate_NO
        vgDatalength_NO=vDatalength_NO
        vgUsfreq_NO=vUsfreq_NO
        vgPulsefreq_NO=vPulsefreq_NO
        sgEcho=sEcho
        sgField=sField
        //end of save parameters

        variable/g vgPointofcycle_p_NO
        vgPointofcycle_p_NO=vSrate_NO/vPulsefreq_NO //number of points in a cycle of repetition
        if (mod(vSrate_NO,vPulsefreq_NO)!=0)
                doalert/t="warnig" 0, "mod(sampling freq./repetition freq.) is non-zero.\r I recommend
                     changing the parameters."
        endif

        make/o/n=(vgPointofcycle_p_NO) Signal_NO=0 //single snapshot of signal
        setscale/p x, 0, 1/vgsrate_NO, "s", Signal_NO

        FRAME_SUB() //for acceleration

        wavestats/q Signal_NO
        variable/g vgRefampl
        vgRefampl=V_max/12 //amplitude of reference wave

        variable/g vgPhase_NO=0, vgZero_NO=0
        make/d/o/n=(vgPointofcycle_p_NO) Ref_NO=vgRefampl*REFERENCE(p, vgUsfreq_NO, vgFrame,
             vgPointofcycle_p_NO, vgSrate_NO, vgPhase_NO, vgZero_NO, 0)
        //reference wave to calculate Re
        setscale/p x, 0, 1/vgsrate_NO, "s", Ref_NO

        dowindow Phase_determination
        if (V_flag == 1)
                dowindow/f Phase_determination
                setaxis/a
        else
                display/n=Phase_determination Ref_NO, Signal_NO
                ModifyGraph/w=Phase_determination margin(top)=45, grid=1,gridStyle=1
                ModifyGraph/w=Phase_determination rgb(Ref_NO)=(0,0,65280)
                setvariable phase win=Phase_determination,size={80,20} ,value=vgPhase_NO, proc=SHIFT_REF,
                     title="phase"
                button SET_ZERO win=Phase_determination, size={70,20}, proc=SET_ZERO, title="set zero"
                setvariable frame win=Phase_determination,size={80,20} ,value=vgFrame, proc=FRAME_SELECT,
                     title="frame"
                variable/g vgFrom=0, vgTo=vgPointofcycle_p_NO-1, vgTo_mod, vgfrom_mod
                //setvariable from win=Phase_determination,size={90,20} ,value=vgFrom, title="from", disable
                     =2
                //setvariable to win=Phase_determination,size={70,20} ,value=vgTo, title="to", disable=2
                //button region win=Phase_determination, size={50,20}, proc=CUR, title="cursor"
                variable/g vgEPB=0.1e6, vgSRB=1e6, vgfilcoef=101
                setvariable EPB win=Phase_determination,size={85,20} ,value=vgEPB, title="EPB"
                setvariable SRB win=Phase_determination,size={85,20} ,value=vgSRB, title="SRB"
                setvariable filcoef win=Phase_determination,size={70,20} ,value=vgfilcoef, title="coef"
                button MULT win=Phase_determination, size={70,20}, proc=MULT, title="calculate", fcolor
                     =(65280,0,0)
                variable/g vgParallel=1
                checkbox para win=Phase_determination, size={40,20}, variable=vgParallel, title="parallel
                     algorithm", proc=PARALLEL
        endif

end

Function FRAME_SUB()
        setdatafolder root:TEKTRO
        svar sgEcho
        wave Echo=$sgEcho, Signal_NO
        nvar vgPointofcycle_p_NO
        variable/g vgFrame=0

        variable i
```

```
        for (i=0;i<trunc(vgPointofcycle_p_NO);i+=1)
                Signal_NO[i]=Echo[vgFrame*vgPointofcycle_p_NO+i]
        endfor
end

Function PARALLEL (ctrlName,checked) : CheckBoxControl
        String ctrlName
        Variable checked                        // 1 if selected, 0 if not
        nvar vgParallel
        vgParallel=checked
End

Function FRAME_SELECT (ctrlName,varNum,varStr,varName) : SetVariableControl //update when vgFrame is changed
        String ctrlName
        Variable varNum
        String varStr
        String varName

        setdatafolder root:TEKTRO

        svar sgEcho
        wave Echo=$sgEcho, Signal_NO, Ref_NO
        nvar vgFrame, vgSrate_NO, vgPointofcycle_p_NO, vgRefampl, vgUsfreq_NO, vgPhase_NO, vgZero_NO

        variable i
        for (i=0;i<trunc(vgPointofcycle_p_NO);i+=1)
                Signal_NO[i]=echo[vgFrame*vgPointofcycle_p_NO+i]
        endfor
        Ref_NO=vgRefampl*REFERENCE(p, vgUsfreq_NO, vgFrame, vgPointofcycle_p_NO, vgSrate_NO, vgPhase_NO,
             vgZero_NO, 0)
end

function SET_ZERO(ctrlName):buttoncontrol //set the origin of phase
        string ctrlName
        setdatafolder root:TEKTRO
        nvar vgPhase_NO, vgZero_NO
        vgZero_NO+=vgPhase_NO
        vgPhase_NO=0
end

Function SHIFT_REF (ctrlName,varNum,varStr,varName) : SetVariableControl //update when vgPhase_NO is changed
        String ctrlName
        Variable varNum
        String varStr
        String varName

        setdatafolder root:TEKTRO

        wave Ref_NO
        nvar vgFrame, vgUsfreq_NO, vgSrate_NO, vgPhase_NO, vgRefAmpl, vgZero_NO, vgPointofcycle_p_NO

        Ref_NO=vgRefampl*REFERENCE(p, vgUsfreq_NO, vgFrame, vgPointofcycle_p_NO, vgSrate_NO, vgPhase_NO,
             vgZero_NO, 0)
end

function CUR(ctrlName) : ButtonControl
        String ctrlName
        nvar vgfrom, vgto
        variable vtemp
        vgfrom=hcsr(A)
        vgto=hcsr(B)

        if (vgfrom > vgto)
                vtemp=vgfrom
                vgfrom=vgto
                vgto=vtemp
        endif
        return 0
end

function MULT(ctrlName):buttoncontrol //main body of calculation
        string ctrlName
        setdatafolder root:TEKTRO
        svar sgEcho, sgField
        wave Echo=$sgEcho, Field=$sgField
        nvar vgSrate_NO, vgPulsefreq_NO, vgDatalength_NO, vgUsfreq_NO, vgPhase_NO, vgRefAmpl, vgFrame,
             vgZero_NO, vgPointofcycle_p_NO, vgDatalength
        nvar vgfrom, vgto
        nvar vgParallel
        nvar vgEPB, vgSRB, vgfilcoef

        killwindow Phase_determination

        make/d/o/n=(vgDatalength_NO) Re_NO=0 //real part
        setscale/p x, 0, 1/vgsrate_NO, "s", Re_NO

        make/d/o/n=(vgDatalength_NO) Im_NO=0 //imaginary part
        setscale/p x, 0, 1/vgsrate_NO, "s", Im_NO

        variable t_0, t_1, t_s, t_f //for benchmark
        t_0=stopMSTimer(-2)

        variable i, j
```

```
if (vgParallel==1)
        //begin of parallel processing
        printf "applying reference and low-pass filter... "

        variable nthreads=ThreadProcessorCount

        for (i=0; i<nthreads;i+=1) //create working waves
                make/o/n=(vgPointofcycle_p_NO) $"work_re"+num2str(i)
                make/o/n=(vgPointofcycle_p_NO) $"work_im"+num2str(i)
        endfor


        variable mt=ThreadGroupCreate(nthreads)
        variable col
        variable waittime=50
        for (col=0; col < vgDatalength_NO/vgPointofcycle_p_NO;)
                for(i=0;i<nthreads;i+=1)
                        //ThreadStart mt,i,APPL_REF(col, vgSrate_no, vgPulsefreq_no, vgDatalength_no,
                              vgUsfreq_no, vgPhase_no, vgFrame, vgZero_no, vgPointofcycle_p_no, Echo,
                              Re_NO, Im_NO)
                        ThreadStart mt,i,APPL_REFv6(col, vgSrate_no, vgPulsefreq_no, vgDatalength_no,
                              vgUsfreq_no, vgPhase_no, vgFrame, vgZero_no, vgPointofcycle_p_no, Echo,
                              Re_NO, Im_NO, vgEPB/vgSrate_NO, vgSRB/vgSrate_NO, vgfilcoef, $"work_re
                             "+num2str(i), $"work_im"+num2str(i))
                        col+=1
                        if( col >= vgDatalength_NO/vgPointofcycle_p_NO)
                                break
                        endif
                endfor
                do
                        variable tgs= ThreadGroupWait(mt,waittime)
                while( tgs != 0 )
        endfor
        variable dummy= ThreadGroupRelease(mt)

        for (i=0; i<nthreads;i+=1) // kill working waves
                killwaves $"work_re"+num2str(i)
                killwaves $"work_im"+num2str(i)
        endfor

//end of parallel processing
t_1=stopMSTimer(-2)
printf "done (time = %g s, parallel)\r", (t_1-t_0)/1e6

else
        printf "applying ferefence... "
        //begin of non-parallel processing
        for (j=0;j<vgDatalength_NO;j+=1)
                Re_NO[j]=Echo[j]*REFERENCE(j, vgUsfreq_NO, 0, vgPointofcycle_p_NO, vgSrate_NO,
                     vgPhase_NO, vgZero_NO, 0)
                Im_NO[j]=Echo[j]*REFERENCE(j, vgUsfreq_NO, 0, vgPointofcycle_p_NO, vgSrate_NO,
                     vgPhase_NO, vgZero_NO, 1)
        endfor
        //end of non-parallel processing
        t_1=stopMSTimer(-2)
        printf "done (time = %g s, serial)\r", (t_1-t_0)/1e6

t_0=stopMSTimer(-2)
printf "applying low-pass filter... "

make/o/d/n=0 coefs_NO
make/o/d coefsMag
setscale/p x, 0, 1/vgSrate_NO, "s", coefs_NO
FilterFIR/COEF/LO={vgEPB/vgSrate_NO, vgSRB/vgSrate_NO, vgfilcoef} coefs_NO
FFT/OUT=3/WINF=Hanning/PAD={(2*numpnts(coefs_NO))}/DEST=coefsMag coefs_NO
coefsMag= 20*log(coefsMag)
setscale d, 0, 0, "dB", coefsMag

//begin of applying low-pass filter
FILTER( Re_NO, vgEPB/vgSrate_NO, vgSRB/vgSrate_NO, vgfilcoef)
FILTER( Im_NO, vgEPB/vgSrate_NO, vgSRB/vgSrate_NO, vgfilcoef)
//end of applying low-pass filter
t_1=stopMSTimer(-2)
printf "done (time = %g s, serial)\r", (t_1-t_0)/1e6

endif

make/d/o/n=(vgSrate_NO/vgPulseFreq_NO) Signal_gating
make/d/o/n=(vgSrate_NO/vgPulseFreq_NO) Gate_gating=0

for (i=0; i<trunc(vgSrate_NO/vgPulseFreq_NO); i+=1)
        Signal_gating[i]=sqrt(Re_NO[vgFrame*(vgSrate_NO/vgPulseFreq_NO)+i]^2+Im_NO[vgFrame*(
             vgSrate_NO/vgPulseFreq_NO)+i]^2)
endfor

dowindow Gating
if (V_flag == 1)
        dowindow/f Gating
        setaxis/a
else
        display/n=Gating Signal_gating, Gate_gating
        ModifyGraph/w=Gating margin(top)=35, grid=1,gridStyle=1
        ModifyGraph/w=Gating rgb(Gate_gating)=(0,0,65280)
        button determ_gate win=Gating, size={70,20}, proc=APPL_GATE, title="gate"
```

```
                setvariable frame_gate win=Gating,size={100,20} ,value=vgFrame, proc=FRAME_SELECT_GATE, title
                    ="frame"
                button save_gate win=Gating, size={70,20}, proc=SAVE_GATE, title="save"
                variable/g vgConnect=0
                checkbox connect_gate  win=Gating, size={70,20}, variable=vgConnect, title="connection
                    algorithm", proc=CONNECT
        endif

end

Function FRAME_SELECT_GATE (ctrlName,varNum,varStr,varName) : SetVariableControl
        String ctrlName
        Variable varNum
        String varStr
        String varName
        nvar vgFrame, vgUsfreq_NO, vgPulseFreq_NO, vgSrate_NO
        wave Signal_gating, Re_NO, Im_NO
        setdatafolder root:TEKTRO

        variable i
        for (i=0; i<trunc(vgSrate_NO/vgPulseFreq_NO); i+=1)
                Signal_gating[i]=sqrt(Re_NO[vgFrame*(vgSrate_NO/vgPulseFreq_NO)+i]^2+Im_NO[vgFrame*(
                    vgSrate_NO/vgPulseFreq_NO)+i]^2)
        endfor
end

Function CONNECT (ctrlName,checked) : CheckBoxControl
        String ctrlName
        Variable checked                        // 1 if selected, 0 if not
        nvar vgConnect
        vgConnect=checked
End

function APPL_GATE(ctrlName):buttoncontrol
        string ctrlName
        setdatafolder root:TEKTRO
        svar sgField
        wave Gate_gating, Signal_gating, Re_NO, Im_NO, Field=$sgField
        variable vS_int, vE_int, d, i, vInvcoef=0
        nvar vgDatalength_NO, vgUsfreq_NO, vgPulsefreq_NO, vgSrate_NO, vgConnect, vgPointofcycle_P_NO

        vS_int=hcsr(A)
        vE_int=hcsr(B)

        if (vS_int > vE_int)
                d=vS_int
                vS_int=vE_int
                vE_int=d
        endif

        Gate_gating=0

        wavestats/q/r=(vS_int,vE_int) Signal_gating

        for(i=0; vS_int+i < vE_int+1; i+=1)
                Gate_gating[vS_int+i]=V_max/2
        endfor

        make/d/o/n=(vgDatalength_NO/vgPointofcycle_P_NO) Avg_Re
        make/d/o/n=(vgDatalength_NO/vgPointofcycle_P_NO) Avg_Im

        make/d/o/n=(vgDatalength_NO/vgPointofcycle_P_NO) Result_ampl=0
        make/d/o/n=(vgDatalength_NO/vgPointofcycle_P_NO) Result_phase=0
        make/d/o/n=(vgDatalength_NO/vgPointofcycle_P_NO) Result_dBdt=0

        for(i=0; i < trunc(vgDatalength_NO/vgPointofcycle_P_NO); i+=1)
                wavestats/q/r=[vgSrate_NO/vgPulseFreq_NO*i+vS_int, vgSrate_NO/vgPulseFreq_NO*i+vE_int] Re_NO
                Avg_Re[i]=V_avg
                wavestats/q/r=[vgSrate_NO/vgPulseFreq_NO*i+vS_int, vgSrate_NO/vgPulseFreq_NO*i+vE_int] Im_NO
                Avg_Im[i]=V_avg
                wavestats/q/r=[vgSrate_NO/vgPulseFreq_NO*i+vS_int, vgSrate_NO/vgPulseFreq_NO*i+vE_int] Field
                Result_dBdt[i]=V_avg
        endfor

        Result_ampl=sqrt(Avg_Re[x]^2+Avg_Im[x]^2)
        Result_phase=atan2(Avg_Im[x],Avg_Re[x])

        duplicate/o Result_phase, Result_phase_N_connect

        if (vgConnect==1)
                variable vThreshold=3.5
                for(i=1; i < trunc(vgDatalength_NO/vgPointofcycle_P_NO); i+=1)
                        //=====attempt connecting phase
                        if((Result_phase[i-1]>0)*(Result_phase[i]<0)*(abs(Result_phase[i-1]-Result_phase[i])>
                            vThreshold)==1)
                                vInvcoef+=2*pi
                        elseif((Result_phase[i-1]<0)*(Result_phase[i]>0)*(abs(Result_phase[i-1]-Result_phase[
                            i])>vThreshold)==1)
                                vInvcoef-=2*pi
                        endif
                        //=====attempt connecting phase
                        Result_phase_N_connect[i]=Result_phase[i]+vInvcoef
                endfor
        endif
```

```
        duplicate/o Result_ampl, Result_ampl_N
        duplicate/o Result_phase, Result_phase_N

        wavestats/q/r=(0, 24) Result_ampl
        //wavestats/q/r=(1400, 1500) Result_ampl
        Result_ampl_N=Result_ampl/V_avg

        wavestats/q/r=(0, 24) Result_phase_N_connect
        //wavestats/q/r=(1400, 1500) Result_phase_N_connect
        Result_phase_N=(Result_phase_N_connect-V_avg)/(pi/2)

        dowindow results_gated
        if (V_flag == 1)
                dowindow/f results_gated
                setaxis/a
        else
                Display/n=results_gated Result_dBdt,Result_ampl_N,Result_phase_N
                ModifyGraph/w=results_gated rgb(Result_dBdt)=(0,0,0),rgb(Result_phase_N)=(0,0,65280)
                Legend/C/N=text0/J/A=MC/w=results_gated "\\s(Result_dBdt) dBdt\r\\s(Result_ampl_N) ampl_N (in
                      units of ampl(B=0))\r\\s(Result_phase_N) phase_N (in units of pi/2)"
        endif
end

function SAVE_GATE(ctrlName):buttoncontrol
        string ctrlName
        setdatafolder root:TEKTRO
        wave Result_ampl_N, Result_Phase_N, Result_dBdt, Result_ampl

        Save/G/W Result_ampl_N, Result_Phase_N, Result_dBdt, Result_ampl
        killwindow Gating
        killwindow results_gated
end

function REFERENCE(i, f, frame, poc_p, srate, phase, zero, dig)
        variable i, f, frame, poc_p, srate, phase, zero, dig
        return sin(2*pi*f*(frame*poc_p+i)/srate-(phase+zero)/180*pi-pi/2*dig)
end

Function FILTER(wOpt, vEPB_n,vSRB_n, vCoef)
        wave wOpt
        variable vEPB_n, vSRB_n, vCoef
        nvar vgSate_NO
        FilterFIR/DIM=0/LO={vEPB_n,vSRB_n, vCoef} wOpt
End

threadsafe Function FILTER_TS(wOpt, vEPB_n,vSRB_n, vCoef)
        wave wOpt
        variable vEPB_n, vSRB_n, vCoef
        nvar vgSate_NO
        FilterFIR/DIM=0/LO={vEPB_n,vSRB_n, vCoef} wOpt
End

threadsafe function APPL_REF(col, Srate, Pulsefreq, Datalength, Usfreq, Phase, Frame, Zero, Pointofcycle_p,
     TEKTRO_ch1, Re_NO, Im_NO)
        variable col, Srate, Pulsefreq, Datalength, Usfreq, Phase, Frame, Zero, Pointofcycle_p
        wave TEKTRO_ch1, Re_NO, Im_NO

        //String pathre = "root:TEKTRO:Work_Re_NO"+num2str(ind)
        //make/d/o/n=(Pointofcycle_p) $pathre
        //wave wr=$pathre

        //String pathim = "root:TEKTRO:Work_Im_NO"+num2str(ind)
        //make/d/o/n=(Pointofcycle_p) $pathim
        //wave wi=$pathim

        variable j
        for (j=0;j<Pointofcycle_p;j+=1)
                Re_NO[col*Pointofcycle_p+j]=TEKTRO_ch1[col*Pointofcycle_p+j]*REFERENCE_TS(j, Usfreq, col,
                     Pointofcycle_p, Srate, Phase, Zero, 0)
                Im_NO[col*Pointofcycle_p+j]=TEKTRO_ch1[col*Pointofcycle_p+j]*REFERENCE_TS(j, Usfreq, col,
                     Pointofcycle_p, Srate, Phase, Zero, 1)
        endfor
end

threadsafe function APPL_REFv6(col, Srate, Pulsefreq, Datalength, Usfreq, Phase, Frame, Zero, Pointofcycle_p,
      TEKTRO_ch1, Re_NO, Im_NO, EPB, SRB, coef, wr, wi)
        variable col, Srate, Pulsefreq, Datalength, Usfreq, Phase, Frame, Zero, Pointofcycle_p, EPB, SRB,
             coef
        wave TEKTRO_ch1, Re_NO, Im_NO, wr, wi

        variable j
        for (j=0;j<Pointofcycle_p;j+=1)
                wr[j]=TEKTRO_ch1[col*Pointofcycle_p+j]*REFERENCE_TS(j, Usfreq, col, Pointofcycle_p, Srate,
                     Phase, Zero, 0)
                wi[j]=TEKTRO_ch1[col*Pointofcycle_p+j]*REFERENCE_TS(j, Usfreq, col, Pointofcycle_p, Srate,
                     Phase, Zero, 1)
        endfor

        FILTER_TS(wr, EPB,SRB, Coef)
        FILTER_TS(wi, EPB,SRB, Coef)

        for (j=0;j<Pointofcycle_p;j+=1)
                Re_NO[col*Pointofcycle_p+j]=wr[j]
```

```
                Im_NO[col*Pointofcycle_p+j]=wi[j]
        endfor
end

threadsafe function REFERENCE_TS(i, f, frame, poc_p, srate, phase, zero, dig)
        variable i, f, frame, poc_p, srate, phase, zero, dig
        return sin(2*pi*f*(frame*poc_p+i)/srate-(phase+zero)/180*pi-pi/2*dig)
end
```

References

[1] R. N. Bhargava, Phys. Rev. **156**, 785 (1967). Link.

[2] Z. Zhu, B. Fauqué, Y. Fuseya, and K. Behnia, Phys. Rev. B **84**, 115137 (2011). Link.

[3] H. Yaguchi and J. Singleton, J. Phys.: Condens. Matter **21**, 344207 (2009). Link.

[4] D. E. Soule, J. W. McClure, and L. B. Smith, Phys. Rev. **134**, A453 (1964). Link.

[5] W. S. Boyle and A. D. Brailsford, Phys. Rev. **107**, 903 (1957). Link.

[6] S. Bermon, Phys. Rev. **158**, 723 (1967). Link.

[7] L. W. Shubnikov and W. J. de Haas, Proc. Netherlands Roy. Acad. Sci. **33**, 130 (1930).

[8] L. W. Shubnikov and W. J. de Haas, Proc. Netherlands Roy. Acad. Sci. **33**, 163 (1930).

[9] W. J. de Haas and P. M. van Alphen, Proc. Netherlands Roy. Acad. Sci. **33**, 680 (1930).

[10] W. J. de Haas and P. M. van Alphen, Proc. Netherlands Roy. Acad. Sci. **33**, 1106 (1930).

[11] H. Fukuyama, Solid State Commun. **26**, 783 (1978). Link.

[12] D. Jérome, T. M. Rice, and W. Kohn, Phys. Rev. **158**, 462 (1967). Link.

[13] 倉本義夫, "半金属中の電子・正孔相関と超音波の巨大量子減衰", in **物理学最前線** *2*, ed. 大槻義彦, 共立出版, 東京 (1982).

[14] N. F. Mott, Phil. Mag. **6**, 287 (1961). Link.

[15] R. J. Elliott and R. Loudon, J. Phys. Chem. Solids. **8**, 382 (1959). Link.

[16] R. J. Elliott and R. Loudon, J. Phys. Chem. Solids **15**, 196 (1960). Link.

[17] E. W. Fenton, Phys. Rev. **170**, 816 (1968). Link.

[18] 秋葉和人, "パルス強磁場を用いた量子極限下グラファイトの電子相に関する研究", Master's thesis, 東京大学 (2015).

[19] K. Akiba, A. Miyake, H. Yaguchi, A. Matsuo, K. Kindo, and M. Tokunaga, J. Phys. Soc. Jpn. **84**, 054709 (2015). Link.

[20] Z. Zhu, R. D. McDonald, A. Shekhter, B. J. Ramshaw, K. A. Modic, F. F. Balakirev, and N. Harrison, Sci. Rep. **7**, 1733 (2017). Link.

[21] S. Mase and T. Sakai, J. Phys. Soc. Jpn. **31**, 730 (1971). Link.

[22] T. Sakai, N. Goto, and S. Mase, J. Phys. Soc. Jpn. **35**, 1064 (1973). Link.

[23] E. W. Fenton, Solid State Commun. **13**, 815 (1973). Link.

[24] Y. Wakisaka, T. Sudayama, K. Takubo, T. Mizokawa, M. Arita, H. Namatame, M. Taniguchi, N. Katayama, M. Nohara, and H. Takagi, Phys. Rev. Lett. **103**, 026402 (2009). Link.

[25] K. Seki, Y. Wakisaka, T. Kaneko, T. Toriyama, T. Konishi, T. Sudayama, N. L. Saini, M. Arita, H. Namatame, M. Taniguchi, N. Katayama, M. Nohara, H. Takagi, T. Mizokawa, and Y. Ohta, Phys. Rev. B **90**, 155116 (2014). Link.

[26] T. Pillo, J. Hayoz, H. Berger, F. Lévy, L. Schlapbach, and P. Aebi, Phys. Rev. B **61**, 16213 (2000). Link.

[27] H. Cercellier, C. Monney, F. Clerc, C. Battaglia, L. Despont, M. G. Garnier, H. Beck, P. Aebi, L. Patthey, H. Berger, and L. Forró, Phys. Rev. Lett. **99**, 146403 (2007). Link.

[28] C. Monney, E. F. Schwier, M. G. Garnier, N. Mariotti, C. Didiot, H. Cercellier, J. Marcus, H. Berger, A. N. Titov, H. Beck, and P. Aebi, New. J. Phys. **12**, 125019 (2010). Link.

[29] B. Bucher, P. Steiner, and P. Wachter, Phys. Rev. Lett. **67**, 2717 (1991). Link.

[30] K. Yoshioka, E. Chae, and M. K. Gonokami, Nat. Commun. **2**, 328 (2011). Link.

[31] Z. K. Liu, J. Jiang, B. Zhou, Z. J. Wang, Y. Zhang, H. M. Weng, D. Prabhakaran, S.-K. Mo, H. Peng, P. Dudin, T. Kim, M. Hoesch, Z. Fang, X. Dai, Z. X. Shen, D. L. Feng, Z. Hussain, and Y. L. Chen, Nat. Mater. **13**, 677 (2014). Link.

[32] Z. Wang, H. Weng, Q. Wu, X. Dai, and Z. Fang, Phys. Rev. B **88**, 125427 (2013). Link.

[33] T. Liang, Q. Gibson, M. N. Ali, M. Liu, R. J. Cava, and N. P. Ong, Nat. Mater. **14**, 280 (2015). Link.

[34] J. Xiong, S. K. Kushwaha, T. Liang, J. W. Krizan, M. Hirschberger, W. Wang, R. J. Cava, and N. P. Ong, Science **350**, 413 (2015). Link.

[35] L. Fu and C. L. Kane, Phys. Rev. B **76**, 045302 (2007). Link.

[36] D. Hsieh, D. Qian, L. Wray, Y. Xia, Y. S. Hor, R. J. Cava, and M. Z. Hasan, Nature (London) **452**, 970 (2008). Link.

[37] Z. K. Liu, B. Zhou, Y. Zhang, Z. J. Wang, H. M. Weng, D. Prabhakaran, S.-K. Mo, Z. X. Shen, Z. Fang, X. Dai, Z. Hussain, and Y. L. Chen, Science **343**, 864 (2014). Link.

[38] S.-Y. Xu, I. Belopolski, N. Alidoust, M. Neupane, G. Bian, C. Zhang, R. Sankar, G. Chang, Z. Yuan, C.-C. Lee, S.-M. Huang, H. Zheng, J. Ma, D. S. Sanchez, B. Wang, A. Bansil, F. Chou, P. P. Shibayev, H. Lin, S. Jia, and M. Z. Hasan, Science **349**, 613 (2015). Link.

[39] Y. YWu, D. Mou, N. H. Jo, K. Sun, L. Huang, S. L. Bud'ko, P. C. Canfield, and A. Kaminski, Phys. Rev. B **94**, 121113 (2016). Link.

[40] K. Deng, G. Wan, P. Deng, K. Zhang, S. Ding, E. Wang, M. Yan, H. Huang, H. Zhang, Z. Xu, J. Denlinger, A. Fedorov, H. Yang, W. Duan, H. Yao, Y. Wu, S. Fan, H. Zhang, X. Chen, and S. Zhou, Nat. Phys. **12**, 1105 (2016). Link.

[41] M. Neupane, S. Y. Xu, R. Sankar, N. Alidoust, G. Bian, C. Liu, I. Belopolski, T. R. Chang, H. T. Jeng, H. Lin, A. Bansil, F. Chou, and M. Z. Hasan, Nat. Commun. **5**, 3786 (2014). Link.

[42] Z. Wang, Y. Sun, X.-Q. Chen, C. Franchini, G. Xu, H. Weng, X. Dai, and Z. Fang, Phys. Rev. B **85**, 195320 (2012). Link.

[43] G. P. Mikitik and Y. V. Sharlai, Phys. Rev. Lett. **82**, 2147 (1999). Link.

[44] H. Murakawa, M. S. Bahramy, M. Tokunaga, Y. Kohama, C. Bel, Y. Kaneko, N. Nagaosa, H. Y. Hwang, and Y. Tokura, Science **342**, 1490 (2013). Link.

[45] Y. Ando, J. Phys. Soc. Jpn. **82**, 102001 (2013). Link.

[46] C. M. Wang, H.-Z. Lu, and S.-Q. Shen, Phys. Rev. Lett. **117**, 077201 (2016). Link.

[47] A. A. Abrikosov, Phys. Rev. B **58**, 2788 (1998). Link.

[48] A. A. Abrikosov, Phys. Rev. B **61**, 7770 (2000). Link.

[49] C. M. Wang and X. L. Lei, Phys. Rev. B **86**, 035442 (2012). Link.

[50] M. M. Parish and P. B. Littlewood, Nature (London) **426**, 162 (2003). Link.

[51] F. Kisslinger, C. Ott, and H. B. Weber, Phys. Rev. B **95**, 024204 (2017). Link.

[52] H. B. Nielsen and M. Ninomiya, Phys. Lett. B **130**, 389 (1983). Link.

[53] F. Arnold, C. Shekhar, S. C. Wu, Y. Sun, R. D. dos Reis, N. Kumar, M. Naumann, M. O. Ajeesh, M. Schmidt, A. G. Grushin, J. H. Bardarson, M. Baenitz, D. Sokolov, H. Borrmann, M. Nicklas, C. Felser, E. Hassinger, and B. Yan, Nat. Commun. **7**, 11615 (2016). Link.

[54] ed. 箕村茂, **超高圧** *(***実験物理学講座** *18)*. 共立出版, 東京 (1988).

[55] M. Garfinkel and D. E. Mapother, Phys. Rev. **122**, 459 (1961). Link.

[56] 松尾晶, 坂井義和, 川口孝志, and 金道浩一, 高圧力の科学と技術 **25**, 308 (2015). Link.

[57] P. Sun, Y. Nakanishi, T. Kono, H. Sugawara, D. Kikuchi, H. Sano, and M. Yoshizawa, J. Phys.: Conf. Ser. **51**, 243 (2006). Link.

[58] T. K. Fujita, M. Yoshizawa, R. Kamiya, H. Mitamura, T. Sakakibara, K. Kindo, F. Iga, I. Ishii, and T. Suzuki, J. Phys. Soc. Jpn. **80**, SA084 (2011). Link.

[59] S. Endo, Y. Akahama, S. Terada, and S. Narita, J. Appl. Phys. **21**, L482 (1982). Link.

[60] P. W. Bridgmann, J. Am. Chem. Soc. **36**, 1344 (1914). Link.

[61] A. Brown and S. Rundqvist, Acta Cryst. **19**, 684 (1965). Link.

[62] R. Hultgren, N. S. Gingrich, and B. E. Warren, J. Chem. Phys. **3**, 351 (1935). Link.

[63] L. Li, Y. Yu, G. J. Ye, Q. Ge, X. Ou, H. Wu, D. Feng, X. H. Chen, and Y. Zhang, Nat. Nanotechnol. **9**, 372 (2014). Link.

[64] A. Morita, Appl. Phys. A **39**, 227 (1986). Link.

[65] S. Fukuoka, T. Taen, and T. Osada, J. Phys. Soc. Jpn. **84**, 121004 (2015). Link.

[66] L. Li, J. Kim, C. Jin, G. J. Ye, D. Y. Qiu, F. H. da Jornada, Z. Shi, L. Chen, Z. Zhang, F. Yang, K. Watanabe, T. Taniguchi, W. Ren, S. G. Louie, X. H. Chen, Y. Zhang, and F. Wang, Nat. Nanotechnol. **12**, 21 (2017). Link.

[67] Y. Takao, H. Asahina, and A. Morita, J. Phys. Soc. Jpn. **50**, 3362 (1981). Link.

[68] H. Asahina, K. Shindo, and A. Morita, J. Phys. Soc. Jpn. **51**, 1193 (1982). Link.

[69] R. W. Keyes, Phys. Rev. **92**, 580 (1953). Link.

[70] D. Warschauer, J. Appl. Phys. **34**, 1853 (1963). Link.

[71] Y. Maruyama, S. Suzuki, K. Kobayashi, and S. Tanuma, Physica B&C **105**, 99 (1981). Link.

[72] 城谷一民, 馬庭亮, 佐藤宏行, 露沢朗, 佐藤直樹, 丸山有成, 梶原峻, 井口洋夫, and 秋本俊一, 日本化学会誌 **1981**, 1604 (1981). Link.

[73] Y. Akahama, S. Endo, and S. Narita, J. Phys. Soc. Jpn. **52**, 2148 (1983). Link.

[74] D. M. Brown and R. Bray, Phys. Rev. **127**, 1593 (1962). Link.

[75] S. Narita, S. Terada, S. Mori, K. Muro, Y. Akahama, and S. Endo, J. Phys. Soc. Jpn. **52**, 3544 (1983). Link.

[76] S. Takeyama, N. Miura, Y. Akahama, and S. Endo, J. Phys. Soc. Jpn. **59**, 2400 (1990). Link.

[77] S. Sugai, T. Ueda, and K. Murase, J. Phys. Soc. Jpn. **50**, 3356 (1981). Link.

[78] S. Sugai and I. Shirotani, Solid State Commun. **53**, 753 (1985). Link.

[79] C. Kaneta, H. K. Yoshida, and A. Morita, J. Phys. Soc. Jpn. **55**, 1213 (1986). Link.

[80] C. Kaneta and A. Morita, J. Phys. Soc. Jpn. **55**, 1224 (1986). Link.

[81] J. C. Jamieson, Science **139**, 1291 (1963). Link.

[82] M. H. Cohen, L. M. Falicov, and S. Golin, IBM J. Res. Dev. **8**, 215 (1964). Link.

[83] Y. Akahama, M. Kobayashi, and H. Kawamura, Phys. Rev. B **59**, 8520 (1999). Link.

[84] H. Kawamura, I. Shirotani, and K. Tachikawa, Solid State Commun. **49**, 879 (1984). Link.

[85] L. Cartz, S. R. Strinivasa, R. J. Riedner, J. D. Jorgensen, and T. G. Worlton, J. Chem. Phys. **71**, 1718 (1979). Link.

[86] T. Kikegawa and H. Iwasaki, Acta Cryst. **B39**, 158 (1983). Link.

[87] M. Okajima, S. Endo, Y. Akahama, and S. Narita, Jpn. J. Appl. Phys. **23**, 15 (1984). Link.

[88] Y. Akahama, S. Endo, and S. Narita, Physica B+C **139-140**, 397 (1986). Link.

[89] Y. Akahama and H. Kawamura, Phys. Status Solidi B **223**, 349 (2001). Link.

[90] C. A. Vanderborgh and D. Schiferl, Phys. Rev. B **40**, 9595 (1989). Link.

[91] K. Akiba, A. Miyake, Y. Akahama, K. Matsubayashi, Y. Uwatoko, H. Arai, Y. Fuseya, and M. Tokunaga, J. Phys. Soc. Jpn. **84**, 073708 (2015). Link.

[92] K. Akiba, A. Miyake, Y. Akahama, K. Matsubayashi, Y. Uwatoko, and M. Tokunaga, Phys. Rev. B **95**, 115126 (2017). Link.

[93] Z. J. Xiang, G. J. Ye, C. Shang, B. Lei, N. Z. Wang, K. S. Yang, D. Y. Liu, F. B. Meng, X. G. Luo, L. J. Zou, Z. Sun, Y. Zhang, and X. H. Chen, Phys. Rev. Lett. **115**, 186403 (2015). Link.

[94] C. H. Li, Y. J. Long, L. X. Zhao, L. Shan, Z. A. Ren, J. Z. Zhao, H. M. Weng, X. Dai, Z. Fang, C. Ren, and G. F. Chen, Phys. Rev. B **95**, 125417 (2017). Link.

[95] T. Strutz, N. Miura, and Y. Akahama, Physica B **201**, 387 (1994). Link.

[96] R. J. Nicholas, Prog. Quantum Electron. **10**, 1 (1985). Link.

[97] P. Kapitza, Proc. R. Soc. A **119**, 358 (1928). Link.

[98] J. W. McClure and W. J. Spry, Phys. Rev. **165**, 809 (1968). Link.

[99] M. N. Ali, J. Xiong, S. Flynn, J. Tao, Q. D. Gibson, L. M. Schoop, T. Liang, N. Haldolaarachchige, M. Hirschberger, N. P. Ong, and R. J. Cava, Nature (London) **514**, 205 (2014). Link.

[100] D. Shoenberg, *Magnetic Oscillations in Metals*. Cambridge University Press, Cambridge (1984).

[101] J. A. Woollam, Phys. Rev. Lett. **25**, 810 (1970). Link.

[102] N. B. Brandt and S. M. Chudinov, J. Low Temp. Phys. **8**, 339 (1972). Link.

[103] R. Küchler, L. Steinke, R. Daou, M. Brando, K. Behnia, and F. Steglich, Nat. Mater. **13**, 461 (2014). Link.

[104] S. Tanuma, R. Inada, A. Furukawa, O. Takahashi, Y. Iye, and Y. Onuki, "Electrical Properties of Layered Materials at High Magnetic Fields", in *Physics in High Magnetic Fields*, eds. S. Chikazumi and N. Miura, Springer, Berlin (1981).

[105] Y. Iye, P. M. Tedrow, G. Timp, M. Shayegan, M. S. Dresselhaus, G. Dresselhaus, A. Furukawa, , and S. Tanuma, Phys. Rev. B **25**, 5478 (1982). Link.

[106] H. Yaguchi and J. Singleton, Phys. Rev. Lett. **81**, 5193 (1998). Link.

[107] B. Fauqué, D. LeBoeuf, B. Vignolle, M. Nardone, C. Proust, and K. Behnia, Phys. Rev. Lett. **110**, 266601 (2013). Link.

[108] For the OpenMX package, code, pseudo-atomic basis functions, and pseudopotentials, see `http://www.openmx-square.org/`.

[109] J. Qiao, X. Kong, Z.-X. Hu, F. Yang, and Q. Ji, Nat. Commun. **5**, 4475 (2014). Link.

[110] Y. Fuseya, private communication.

[111] P.-L. Gong, D.-Y. Liu, K.-S. Yang, Z.-J. Xiang, X.-H. Chen, Z. Zeng, S.-Q. Shen, and L.-J. Zou, Phys. Rev. B **93**, 195434 (2016). Link.

[112] J. Zhao, R. Yu, H. Weng, and Z. Fang, Phys. Rev. B **94**, 195104 (2016). Link.

[113] M. Baba, F. Izumida, Y. Takeda, K. Shibata, A. Morita, Y. Koike, and T. Fukase, J. Phys. Soc. Jpn. **60**, 3777 (1991). Link.

[114] Z. Hou, B. Yang, Y. Wang, B. Ding, X. Zhang, Y. Yao, E. Liu, X. Xi, G. Wu, Z. Zeng, Z. Liu, and W. Wang, Sci. Rep. **6**, 23807 (2016). Link.

[115] D. E. Soule, Phys. Rev. **112**, 698 (1958). Link.

[116] G. Eguchi, K. Kuroda, K. Shirai, Y. Ando, T. Shinjo, A. Kimura, and M. Shiraishi, Phys. Rev. B **91**, 235117 (2015). Link.

[117] G. Eguchi and S. Paschen, arXiv:1609.04134. Link.

[118] R. Fei, V. Tran, and L. Yang, Phys. Rev. B **91**, 195319 (2015). Link.

[119] S. Sun, Q. Wang, P.-J. Guo, K. Liu, and H. Lei, New J. Phys. **18**, 082002 (2016). Link.

[120] X. Du, S.-W. Tsai, D. L. Maslov, and A. F. Hebard, Phys. Rev. Lett. **94**, 166601 (2005). Link.

[121] J. M. Ziman, *Principles of the Theory of Solids.* Cambridge University Press, Cambridge 2nd ed. (1972).

[122] L. M. Roth and P. N. Argyres, "Magnetic Quantum Effects", in *Semiconductors and Semimetals*, eds. R. K. Willardson and A. C. Beer, **1**, Academic Press, New York (1966).

[123] T. Nagahama, M. Kobayashi, Y. Akahama, S. Endo, and S. ichiro Narita, J. Phys. Soc. Jpn. **54**, 2096 (1985). Link.

[124] Y. Yafet, R. W. Keyes, and E. N. Adams, J. Phys. Chem. Solids **1**, 137 (1956). Link.

[125] P. M. Nikolic, Brit. J. Appl. Phys. **16**, 1075 (1965). Link.

[126] J. B. Conklin, L. E. Johnson, and G. W. Pratt, Phys. Rev. **137**, A1282 (1965). Link.

[127] T. Kuraya and Y. Fuseya, J. Phys.: Conf. Ser. **603**, 012025 (2015). Link.

[128] G. Nimtz and B. Schlicht, "Narrow-Gap Lead Salts", in *Narrow-Gap Semiconductors*, Springer, Berlin (1983).

[129] P. J. Lin and L. Kleinman, Phys. Rev. **142**, 478 (1966). Link.

[130] W. Setyawan and S. Curtarolo, Comp. Mater. Sci. **49**, 299 (2010). Link.

[131] R. S. Allgaier and W. W. Scanlon, Phys. Rev. **111**, 1029 (1958). Link.

[132] R. S. Allgaier, Phys. Rev. **112**, 828 (1958). Link.

[133] Y. Kanai, R. Nii, and N. Watanabe, J. Phys. Soc. Jpn. **15**, 1717A (1960). Link.

[134] K. F. Cuff, M. R. Ellett, and C. D. Kuglin, J. Appl. Phys. **32**, 2179 (1961). Link.

[135] P. J. Stiles, E. Burstein, and D. N. Langenberg, Phys. Rev. Lett. **6**, 667 (1961). Link.

[136] P. J. Stiles, E. Burstein, and D. N. Langenberg, Phys. Rev. Lett. **9**, 257 (1962). Link.

[137] R. Nii, J. Phys. Soc. Jpn. **18**, 456 (1963). Link.

[138] J. R. Burke, B. Houston, and H. T. Savage, Phys. Rev. B **2**, 1977 (1970). Link.

[139] P. Giraldo-Gallo, B. Sangiorgio, P. Walmsley, H. J. Silverstein, M. Fechner, S. C. Riggs, T. H. Geballe, N. A. Spaldin, and I. R. Fisher, Phys. Rev. B **94**, 195141 (2016). Link.

[140] J. D. Jensen, B. Houston, and J. R. Burke, Phys. Rev. B **18**, 5567 (1978). Link.

[141] W. Schilz, J. Phys. Chem. Solids **30**, 893 (1969). Link.

[142] T. E. Thompson, P. R. Aron, B. S. Chandrasekhar, and D. N. Langenberg, Phys. Rev. B **4**, 518 (1971). Link.

[143] N. R. Short, J. Phys. D: Appl. Phys. **1**, 129 (1968). Link.

[144] J. O. Dimmock, I. Melngailis, and A. J. Strauss, Phys. Rev. Lett. **16**, 1193 (1966). Link.

[145] R. Mazelsky, M. S. Lubell, and W. E. Kramer, J. Chem. Phys. **37**, 45 (1962). Link.

[146] E.G.Bylander, Mater. Sci. Eng. **1**, 190 (1966). Link.

[147] I. Melngailis and A. R. Calawa, Appl. Phys. Lett. **9**, 304 (1966). Link.

[148] S. Golin, Phys. Rev. **176**, 830 (1968). Link.

[149] F. Herman and S. Skillman, *Atomic Structure Calculations.* Prentice-Hall, New Jersey (1963).

[150] J. Melngailis, T. C. Harman, J. G. Mavroides, and J. O. Dimmock, Phys. Rev. B **3**, 370 (1971). Link.

[151] S.-Y. Xu, C. Liu, N. Alidoust, M. Neupane, D. Qian, I. Belopolski, J. D. Denlinger, Y. J. Wang, H. Lin, L. A. Wray, G. Landolt, B. Slomski, J. H. Dil, A. Marcinkova, E. Morosan, Q. Gibson, R. Sankar, F. C. Chou, R. J. Cava, A. Bansil, and M. Z. Hasan, Nat. Commun. **3**, 1192 (2012). Link.

[152] L. Fu, Phys. Rev. Lett. **106**, 106802 (2011). Link.

[153] T. H. Hsieh, H. Lin, J. Liu, W. Duan, A. Bansil, and L. Fu, Nat. Commun. **3**, 982 (2012). Link.

[154] H. Hayasaka and Y. Fuseya, J. Phys.: Condens. Matter **28**, 31LT01 (2016). Link.

[155] Y. Fuseya, Z. Zhu, B. Fauqué, W. Kang, B. Lenoir, and K. Behnia, Phys. Rev. Lett. **115**, 216401 (2015). Link.

[156] B. A. Assaf, T. Phuphachong, V. V. Volobuev, A. Inhofer, G. Bauer, G. Springholz, L. A. de Vaulchier, and Y. Guldner, Sci. Rep. **6**, 20323 (2016). Link.

[157] T. Phuphachong, B. A. Assaf, V. V. Volobuev, G. Bauer, G. Springholz, L.-A. de Vaulchier, and Y. Guldner, Crystals **7**, 29 (2017). Link.

[158] S. Takaoka and K. Murase, J. Phys. Soc. Jpn. **51**, 1857 (1982). Link.

[159] S. Takaoka and K. Murase, Phys. Rev. B **20**, 2823 (1979). Link.

[160] S. Takaoka, *Investigation of Electronic Properties under the Phase Transition in $Pb_{1-x}Ge_xTe$ and $Pb_{1-x}Sn_xTe$ Semiconductors.* PhD thesis, Osaka University (1978).

[161] P. Barone, T. Rauch, D. D. Sante, J. Henk, I. Mertig, and S. Picozzi, Phys. Rev. B **88**, 045207 (2013). Link.

[162] Z. Nabi, B. Abbar, S. Méçabih, A. Khalfi, and N. Amrane, Comp. Mater. Sci. **18**, 127 (2000). Link.

[163] G. A. Samara and H. G. Drickamer, J. Chem. Phys. **37**, 1159 (1962). Link.

[164] A. N. Mariano and K. L. Chopra, Appl. Phys. Lett. **10**, 282 (1967). Link.

[165] I. Wakabayashi, H. Kobayashi, H. Nagasaki, and S. Minomura, J. Phys. Soc. Jpn. **25**, 227 (1968). Link.

[166] G. Rousse, S. Klotz, A. M. Saitta, J. Rodriguez-Carvajal, M. I. McMahon, B. Couzinet, and M. Mezouar, Phys. Rev. B **71**, 224116 (2005). Link.

[167] G. Chouteau and A. Briggs, Solid State Commun. **21**, 785 (1977). Link.

[168] F. Orbanić, M. Novak, M. Baćani, and I. Kokanović, Phys. Rev. B **95**, 035208 (2017). Link.

[169] S. Narita and Y. Takafuji, Solid State Commun. **20**, 357 (1976). Link.

[170] Y. Takafuji and S. Narita, Jpn. J. Appl. Phys. **21**, 1315 (1982). Link.

[171] A. Bhattacharya, B. Skinner, G. Khalsa, and A. V. Suslov, Nat. Commun. **7**, 12974 (2016). Link.

[172] S. Kivelson, D.-H. Lee, and S.-C. Zhang, Phys. Rev. B **46**, 2223 (1992). Link.

[173] S. V. Kravchenko, J. E. Furneaux, and V. M. Pudalov, Phys. Rev. B **49**, 2250 (1994). Link.

[174] 伏屋雄紀, 物性研究 **90**, 537 (2008). Link.